



TECHNISCHE UNIVERSITÄT WIEN

Dissertation

Exotic phenomena in the phase behaviour of soft matter systems

ausgeführt zum Zwecke der Erlangung
des akademischen Grades eines Doktors
der technischen Wissenschaften unter der Leitung von

Ao. Univ.-Prof. Dr. Gerhard Kahl
Institut für Theoretische Physik
Technische Universität Wien

und

Ao. Univ.-Prof. Dr. Martin Neumann
Fakultät für Physik
Universität Wien

eingereicht an der Technischen Universität Wien
Fakultät für Physik

von

Mag. Bianca M. Mladek
9806245
Ospelgasse 1-9/2/25, 1200 Wien

Wien, im September 2007

Kurzfassung

Für bestimmte Systeme der weichen Materie, wie etwa Makromoleküle mit niedriger Monomerdichte in ihrem Inneren, kann man die effektiven Wechselwirkungen zwischen den Molekülen durch rein abstoßende, beschränkte Potentiale darstellen. Für das Phasenverhalten solcher Systeme wurden zwei unterschiedliche Szenarien vorausgesagt: einerseits “re-entrant melting”, wo eine Flüssigkeit bei Kompression zuerst friert und schließlich wieder schmilzt, und andererseits das “clustering” Phänomen, wo überlappende Teilchen Klumpen bilden, die sich an den Gitterplätzen von Kristallen anordnen. Das erste Szenario wurde sowohl theoretisch als auch experimentell an zahlreichen Systemen der weichen Materie untersucht und bestätigt. Der Bildung von Cluster-Phasen ist hingegen bislang noch wenig Interesse geschenkt worden. In dieser Arbeit wird dieses Phänomen daher eingehend studiert: einerseits wird aufgezeigt, wie man geeignete Makromoleküle, die dieses Phasenverhalten zeigen, synthetisieren kann. Andererseits wird eine eingehende Analyse der Eigenschaften und Thermodynamik dieser exotischen Systeme präsentiert. Somit werden in dieser Arbeit sowohl die mikroskopischen als auch die mesoskopischen Aspekte dieses Phänomens behandelt.

Abstract

Effective interactions in particular soft matter systems, such as macromolecules of low inner monomer concentration, can be described by purely repulsive, bounded potentials. For such systems, two different phase behaviours have been predicted: re-entrant melting, where a fluid freezes and re-melts again upon compression, and clustering, where particles agglomerate in groups at the lattice sites of perfect crystals. The former has been studied and confirmed by both theory and experiments for a wide range of soft matter systems. Clustering, however, has not yet received due attention despite its intriguing and counterintuitive character. Our investigations range from tailoring suitable macromolecules—demonstrating that clustering can indeed be realised in certain soft matter systems—to an thorough examination of the properties and thermodynamics of such exotic systems. In our detailed study of this phenomenon we thus bridge the scales between the microscopic and the mesoscopic level.

In any field, find the strangest thing and then explore it.

John Archibald Wheeler

Contents

1	Introduction	1
2	Models	5
2.1	System parameters	5
2.2	Phase behaviour of bounded, purely repulsive potentials	5
2.3	The Gaussian core model	7
2.4	The double Gaussian core model	8
2.5	The generalised exponential model	10
3	Statistical mechanics in a nutshell	13
3.1	Basic concepts	13
3.2	The canonical ensemble	14
3.3	The isobaric-isothermal ensemble	16
4	Theory	19
4.1	The fluid - integral equation theories	19
4.1.1	The radial distribution function and its connection to thermodynamic properties	19
4.1.2	The Ornstein-Zernike equation and integral equation theories	20
4.1.3	The mean field approximation	21
4.1.4	The hypernetted chain closure	22
4.1.5	The Percus-Yevick approximation	22
4.1.6	The self-consistent Ornstein-Zernike approximation	23
4.1.7	Integro-differential equation SCOZA approach	24
4.1.8	HNC-based SCOZA	25
4.2	The solid at zero temperature - genetic algorithms	26
4.3	The solid at finite temperatures - density functional theory	27
5	Monte Carlo simulations	31
5.1	Conventional Monte Carlo simulations	31
5.1.1	Master equation	31

5.1.2	Equilibrium and expectation values	32
5.1.3	Importance sampling	33
5.1.4	Markov chains	34
5.1.5	Ergodicity	35
5.1.6	Detailed balance	35
5.1.7	Acceptance probabilities	36
5.1.8	Metropolis Monte Carlo	36
5.2	Monte Carlo simulations in the isobaric-isothermal ensemble	37
5.3	Tricks of the trade	39
5.3.1	Boundary conditions, minimum image convention and tail corrections . . .	39
5.3.2	Cell lists	40
5.4	Lattice Monte Carlo simulations	41
5.4.1	Canonical Lattice Monte Carlo simulations	42
5.4.2	The radial distribution function in <i>NVT</i> -LMC	44
5.4.3	Discretisation errors	45
5.4.4	Comparison conventional MC - LMC	46
5.4.5	Isobaric-isothermal Lattice Monte Carlo simulations	49
5.5	Free energies and phase equilibria in MC simulations	50
5.5.1	Widom or particle insertion method	50
5.5.2	Overlapping distribution method in the <i>NVT</i> ensemble	51
5.5.3	Overlapping distribution method in the <i>NPT</i> ensemble	53
5.5.4	Non-Boltzmann sampling	54
5.5.5	Thermodynamic integration for cluster solids	56
5.5.6	The Gibbs ensemble	59
5.6	Data analysis	61
5.6.1	Cluster analysis	61
5.6.2	Bond order parameters	63
6	Re-entrant melting	67
6.1	The Gaussian core model as effective interaction	68
6.2	The MFA for the GCM	68
6.3	The MFA-based SCOZA for the GCM	70
6.3.1	Energy and compressibility route	71
6.3.2	Virial and compressibility route	72
6.4	IDE SCOZA approach for the GCM	73
6.5	Results of the different SCOZA approaches for the GCM	73

7 Clustering	83
7.1 Real systems - dendrimers	83
7.1.1 Effective interactions	86
7.1.2 Athermal dendrimers	87
7.1.3 Amphiphilic Dendrimers	88
7.2 On the thermodynamics of cluster crystals	110
7.3 Clustering model systems by example of the GEM-4	117
8 Conclusion	139
A The Polylogarithm	141
B Overlapping distribution method in the NPT ensemble	143
C Monte Carlo simulation data for the GEM-4	147

Chapter 1

Introduction

Soft-matter physics is a rapidly developing and challenging field for both experimentalists and theoreticians. Due to several reasons, particular effort has been dedicated in recent years to investigations on this topic. The applied aspect is undoubtedly based on the fact that we are surrounded by soft matter in our daily lives. Everyday examples of soft-matter systems range from food and food additives, through paints, rubbers, foams, gels and liquid crystals to cosmetics and pharmaceuticals. Therefore, soft matter plays a key role in many technological applications and processes. From the academic point of view, soft matter offers a broad range of possibilities where experiment and theory can cooperate in a very constructive and complementary manner. The fact that soft-matter particles are considerably larger than particles in atomic systems makes experimental investigations much easier, using modern tools such as video microscopy or optical tweezers (for an overview see [1]). Moreover, by suitably changing, on the one hand, relevant properties of the suspension such as solvent quality, salt concentration and temperature, or, on the other hand, the number, structure and length of the constituent polymer chains, it is possible to tune the effective interactions in a well defined way, leading to the freedom to *tailor* potentials. This brings a direct comparison between theory and experiment within reach.

In the present work, we will focus on a particular class of soft-matter systems, i.e., suspensions of mesoscopic particles (ranging in size from 1 μm to 1 nm) immersed in a solvent formed by particles of atomic size. The mesoscopic particles, in turn, are usually complex aggregates built up from a large number of atoms or molecules.

The huge number of constituent entities is one of the key problems in theoretical investigations of soft-matter systems. It is impossible to use concepts based on statistical mechanics that take all the degrees of freedom of these building particles explicitly into account. It is therefore more appropriate to focus rather on a simplified representation of the interaction between two macromolecules which may be obtained by applying suitable coarse graining procedures [2]. These techniques average over the internal degrees of freedom of the constituent particles of the macromolecules, leading to “effective” spherical particles. These are identified by their centre of

mass position and momentum and the interaction between two such effective particles is modelled by an effective pair potential. For a few colloidal dispersions such effective interactions have been proposed or derived in the literature, sometimes even in closed, analytical form: neutral and charged star polymers and microgels [3–5] are a few examples (for an overview see [2]).

In the special case of polymeric macromolecules of low inner monomer concentration, such as polymer chains [6–8], dendrimers [9, 10], microgels [4, 5, 11, 12] or block copolymers [13, 14], it is conceivable that—as a consequence of their complex internal structure—these particles may overlap, mutually penetrate, or even intertwine when being compressed. As apparent from Fig. 1.1, the centres of mass of two such macromolecules might even coincide as long as their constituent monomers do not overlap and still obey the excluded volume conditions at the microscopic level. Thus, since full overlaps between these effective particles are possible, the resulting effective interaction remains finite, i.e., bounded, at zero separation.

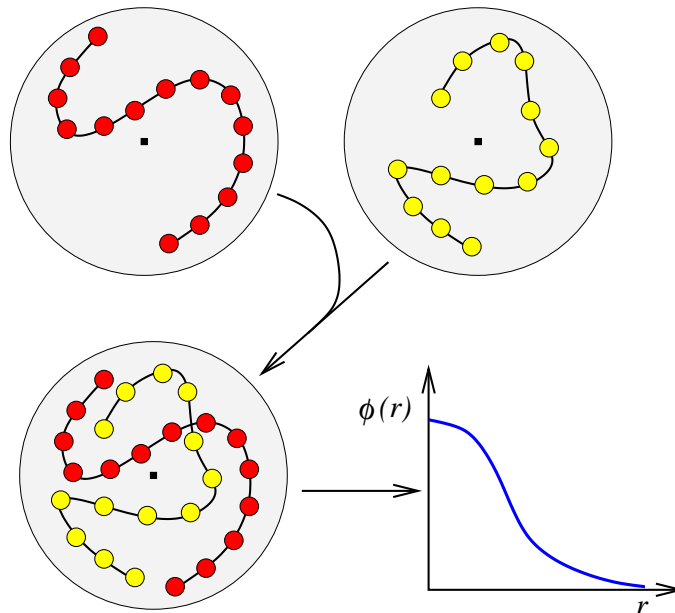


Figure 1.1: Top row: two macromolecules of low inner monomer density. The centers of mass are indicated by black squares. The coarse-grained effective particle is represented by the spherical shape. Bottom row: two effective macromolecules, which can even fully overlap without any monomers violating the excluded volume conditions. This leads to a bounded effective interaction $\phi(r)$.

In striking contrast to the harshly repulsive interatomic potentials typically known from atomic systems, the effective potentials characteristic of soft-matter systems lead to completely new features and a richer variety of ordered phases. Among those are not only the face-centred cubic arrangement assumed by colloidal spheres at high concentrations [15–17] and low-symmetry crystals formed by soft spheres [18], but also a variety of alloys observed for charged colloidal mixtures [19] and the gyroid phases assembled in block copolymer solutions [20–22]. Furthermore, in the phase diagram of star polymers and charged microgels a new and completely unexpected feature was encountered, namely re-entrant melting processes [11, 23], where the liquid freezes and re-melts

again upon incessant compression.

In this thesis, the thermodynamics of materials with soft, bounded effective interactions is studied using simulation and theory. After classifying the different types of phase behaviour expected for these systems in Chap. 2, their physics is quantitatively investigated. To this end, we give a short introduction to the concepts of statistical mechanics in Chap. 3, and then present the theoretical apparatus adequate to study such systems in Chap. 4. In Chap. 5, we present the various Monte Carlo simulation techniques that are used to test the theoretical predictions on the one hand, and to investigate the connection between a system's microscopic details and its mesoscopic properties on the other hand. In Chapters 6 and 7, we consider soft-matter systems that we predict to effectively interact via soft, bounded interactions, and discuss in detail the properties of the different anticipated types of phase behaviour. Finally, we present a summary of our findings and the most relevant conclusions of our work in Chap. 8.

Chapter 2

Models

2.1 System parameters

In this thesis, we consider one-component systems, i.e., systems consisting of only one species of particles interacting via a radially symmetric, density-independent pair potential $\phi(\mathbf{r}) = \phi(r)$, where $|\mathbf{r}| = r$ is the interparticle distance. We study classes of potentials which can be written as $\phi(r) = \varepsilon f(r/\sigma)$ with ε being an energy and σ a length scale. $f(r/\sigma)$ is a dimensionless function. Let N denote the number of particles in the system and V the volume to which these particles are confined, then the number density ϱ is defined by

$$\varrho = \frac{N}{V}. \quad (2.1)$$

To fix the thermodynamic state of the system it is also necessary to specify its temperature T or, equivalently, its inverse

$$\beta = \frac{1}{k_{\text{B}}T}, \quad (2.2)$$

where k_{B} is Boltzmann's constant.

2.2 Phase behaviour of bounded, purely repulsive potentials

In the following, we are going to present the two most frequently studied examples for bounded, purely repulsive model interactions. The first one is the penetrable sphere model (PSM) [24], defined by

$$\phi(r) = \begin{cases} \varepsilon & r < \sigma \\ 0 & \text{else} \end{cases}. \quad (2.3)$$

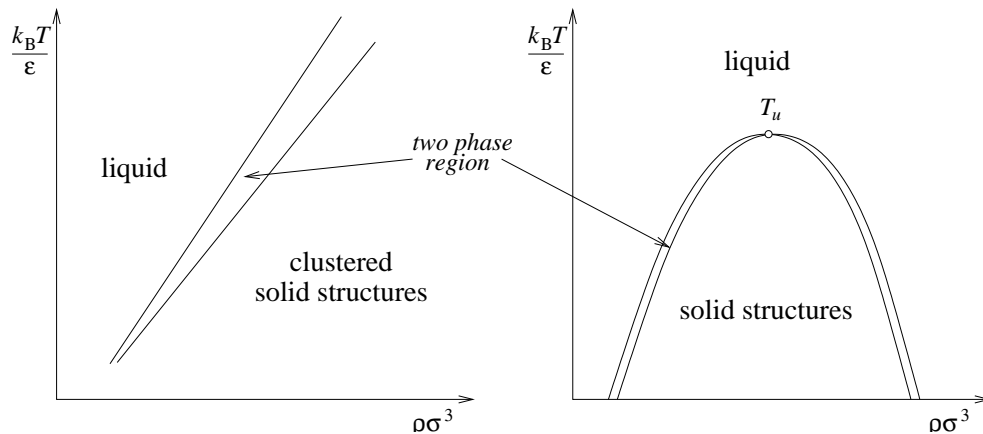


Figure 2.1: Schematic representation of the topology of the phase diagrams of the PSM (left) and the GCM (right): while the PSM freezes at all temperatures into crystals with multiply occupied lattice sites, the GCM shows re-entrant melting below an upper freezing temperature T_u .

The other is the Gaussian core model (GCM), defined as

$$\phi(r) = \varepsilon e^{-(r/\sigma)^2}, \quad (2.4)$$

which was introduced by Stillinger in the 1970s [25]. Both models were extensively studied by both computer simulations and different theoretical approaches (see [24, 26–34] for the PSM and [25, 35–42] for the GCM).

In these studies, the phase diagrams of both systems were investigated and discussed in detail. Surprisingly, the phase diagrams of the two models show a qualitatively very different topology schematised in Fig. 2.1. Upon increasing the density at fixed temperature in a system interacting by the PSM, homogeneously sized clusters of overlapping particles begin to form which arrange themselves in an ordered phase. This phenomenon is referred to as “clustering”. On the other hand, compressing a GCM-system at constant T , one observes below an upper freezing temperature a first order phase transition from the fluid to a crystalline cubic phase with singly occupied lattice sites. Upon further increase of the density, the system might undergo a structural phase transition, which depends on the temperature, but eventually, the solid will melt again. Therefore, this behaviour is called “re-entrant melting”. Above the upper freezing temperature, the fluid phase is stable at all densities.

Since both these model potentials are non-negative, bounded and monotonically decaying¹, their fundamentally different phase behaviour gives rise to the simple question: what is the essential difference between the PSM and the GCM?

The answer was given by Likos *et al.* [43]. Based on an analysis of the behaviour of the structure factor within the mean field approximation (MFA), these authors established a criterion that determines whether clustering or re-entrant melting behaviour will be observed in systems inter-

¹Note that the discontinuity of the PSM has no effect on the following considerations.

acting via bounded, non-negative potentials. For the criterion to be applicable, these interactions have to decay sufficiently fast to zero for large distances so that they are integrable and their Fourier transforms exist. Then, there are two possibilities for the functional behaviour of the Fourier transform $\tilde{\phi}(q)$, where q is the wave number:

- $\tilde{\phi}(q)$ is a non-negative and monotonically decaying function, i.e., $\tilde{\phi}(q) \geq 0$ for all q . Such potentials are called Q^+ -potentials and a system of such particles will show re-entrant melting. Since the Fourier transform of Eq. (2.4) is of Gaussian shape, the GCM obviously belongs to this kind of potentials (cf. Sec. 2.3).
- The Fourier transform $\tilde{\phi}(q)$ oscillates, i.e., it attains negative values for certain ranges of the wave number q . Such potentials are called Q^\pm -potentials and are expected to lead to clustering behaviour. The PSM is a representative of this class.

To find out to which class a potential belongs, an explicit evaluation of $\tilde{\phi}(q)$ is not required. A sufficient condition can be deduced along the following lines. We start from the inverse Fourier transform of a (bounded) potential $\phi(r)$

$$\phi(r) = \frac{1}{2\pi^2} \int_0^\infty dq q^2 \tilde{\phi}(q) \frac{\sin qr}{qr}. \quad (2.5)$$

Then, the second derivative of $\phi(r)$ at $r = 0$ is given by

$$\phi''(r = 0) = -\frac{1}{6\pi^2} \int_0^\infty dq q^4 \tilde{\phi}(q). \quad (2.6)$$

Thus, if $\phi''(r = 0) \geq 0$, then $\tilde{\phi}(q)$ *must* necessarily have negative parts and hence $\phi(r)$ is a Q^\pm -potential [44].

2.3 The Gaussian core model

The GCM has been introduced in Sec. 2.2. Its Fourier transform reads

$$\tilde{\phi}(q) = \pi^{3/2} \varepsilon \sigma^3 e^{-q^2 \sigma^2 / 4}. \quad (2.7)$$

As already mentioned before and as can be seen from above equation, $\tilde{\phi}(q) \geq 0$ for all q .

Due to the absence of an infinitely repulsive core of $\phi(r)$ we have to address the question of thermodynamic stability against collapse, i.e., the existence of the thermodynamic limit. According to Ruelle [45], the total interaction energy, $\Phi(\mathbf{r}^N)$, of a system of N particles positioned at $\{\mathbf{r}_1, \dots, \mathbf{r}_N\} = \mathbf{r}^N$ enclosed in a fixed volume V and interacting via a pair or higher order potential

is stable if there exists a constant $B \geq 0$ so that

$$\Phi(\mathbf{r}^N) \geq -NB, \quad (2.8)$$

for all N and all possible particle configurations \mathbf{r}^N in V .

In the case of pair potentials $\phi(r)$, the total potential energy of the system is given by

$$\Phi(\mathbf{r}^N) = \sum_{i < j} \phi(|\mathbf{r}_i - \mathbf{r}_j|). \quad (2.9)$$

For purely repulsive potentials, such as the GCM, Eq. (2.8) is trivially satisfied with $B = 0$, implying that the thermodynamic limit exists.

2.4 The double Gaussian core model

To generalise the GCM, we introduce a family of model potentials which we call double Gaussian core model (DGCM). Its functional form $\phi(r)$ is defined as the difference between two Gaussians, i.e.,

$$\phi(r) = \varepsilon \left[e^{-(r/\sigma)^2} - \eta e^{-(r/\zeta\sigma)^2} \right], \quad (2.10)$$

where η and ζ are dimensionless real parameters and $\eta \geq 0$ and $\zeta > 0$. Depending on the values of η and ζ , this potential can develop locally or globally attractive regions² (see Figs. 2.2 and 2.3).

The Fourier transform of this potential is given by

$$\tilde{\phi}(q) = \pi^{3/2} \varepsilon \sigma^3 \left(e^{-q^2 \sigma^2 / 4} - \eta \zeta^3 e^{-\zeta^2 q^2 \sigma^2 / 4} \right). \quad (2.11)$$

Since the DGCM develops negative parts for certain combinations of η and ζ , it is not obvious that Ruelle's stability criterion Eq. (2.8) is fulfilled. To avoid these complications, we restrict our studies to potentials of this family that are non-negative, i.e.,

$$\phi(r) \geq 0, \quad \forall r \quad (2.12)$$

to guarantee thermodynamic stability, which is fulfilled for

$$0 < \zeta \leq 1 \quad \text{and} \quad 0 \leq \eta \leq 1. \quad (2.13)$$

To find out for which pairs of parameters the potentials of the DGCM-class show re-entrant

²Here, locally attractive is defined by $\phi''(r_m) > 0$, $\phi'(r_m) = 0$ and $\phi(r_m) > 0$ while globally attractive corresponds to $\phi''(r_m) > 0$, $\phi'(r_m) = 0$ and $\phi(r_m) < 0$, r_m being the location of the minimum of the attractive region.

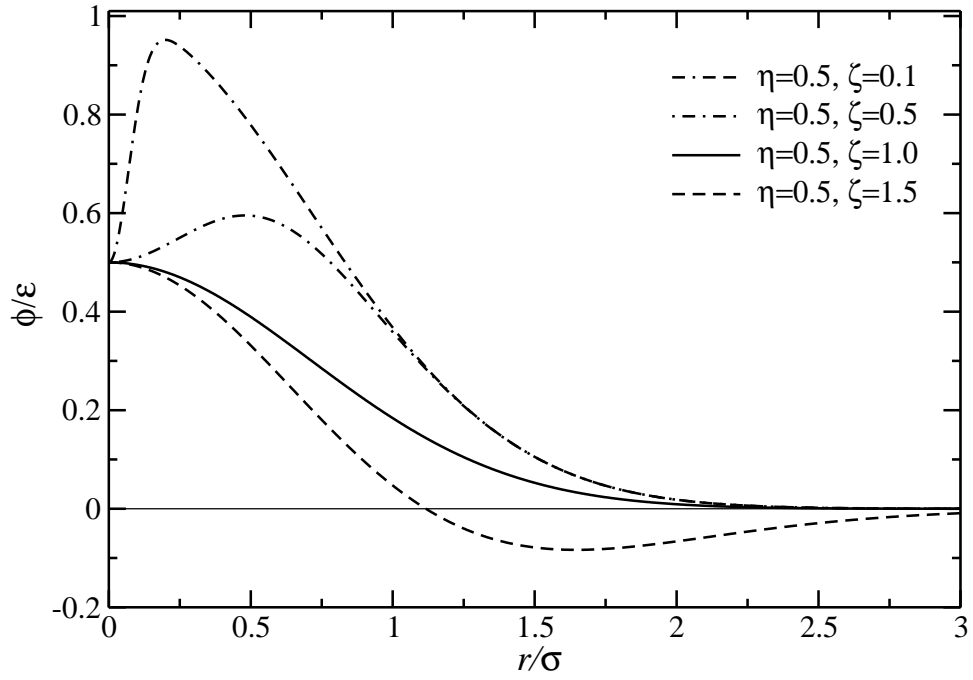


Figure 2.2: Four members of the DGCM family of potentials for fixed η and varying ζ .

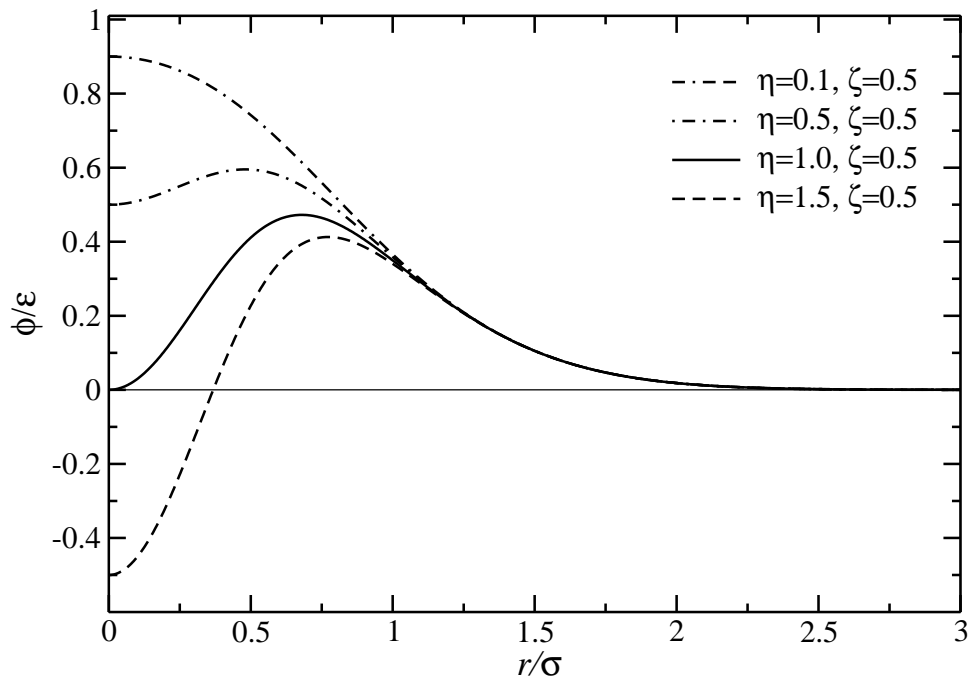


Figure 2.3: Four members of the DGCM family of potentials for fixed ζ and varying η .

melting, we have to select those members for which

$$e^{-q^2\sigma^2/4} - \eta\zeta^3 e^{-\zeta^2 q^2\sigma^2/4} \geq 0, \quad \forall q. \quad (2.14)$$

We can reformulate this condition as two inequalities, i.e.,

$$q^2\sigma^2 \leq 4 \frac{\log(\eta\zeta^3)}{\zeta^2 - 1}, \quad \text{if } \zeta < 1, \quad (2.15)$$

and

$$q^2\sigma^2 \geq 4 \frac{\log(\eta\zeta^3)}{\zeta^2 - 1}, \quad \text{if } \zeta > 1. \quad (2.16)$$

These conditions have to be fulfilled *for all* q . However, since q can attain arbitrarily large values, the first inequality can never be fulfilled. On the other hand, the second condition does not meet our stability requirement Eqs. (2.12) and (2.13). Thus, the DGCM potentials will show clustering for $0 < \zeta < 1$ and $0 < \eta \leq 1$. For the special cases $\zeta = 1$ or $\eta = 0$, the DGCM reduces to a single Gaussian and will show re-entrant melting.

2.5 The generalised exponential model

A different generalisation of the GCM is given by the family of bounded, strictly repulsive potentials termed the generalised exponential model of index n (GEM- n) [46–48],

$$\phi(r) = \varepsilon e^{-(r/\sigma)^n}, \quad (2.17)$$

where $n > 0$ is a real parameter. For $n = 2$, the GCM is recovered, whereas the limit $n \rightarrow \infty$ yields the special case of the PSM. Since $\phi(r) > 0$ in Eq. (2.17) for all n and r , Ruelle's stability criterion (2.8) is automatically fulfilled.

In Sec. 2.3 it was already shown that the GCM, which is identical to the GEM-2, belongs to the Q^+ -class. On the other hand, the PSM, which corresponds to the GEM- ∞ , is known to belong to the Q^\pm -class. Thus, there has to be a threshold value for the index n , where the phase behaviour of the GEM potentials changes from re-entrant melting to clustering. As no closed expression of the Fourier transform exists for the potential of the GEM- n for arbitrary index n , we rather study the second derivative of the potential given by

$$\phi''(r) = \frac{\varepsilon n}{\sigma^2} e^{-(r/\sigma)^n} \left[n \left(\frac{r}{\sigma}\right)^{2(n-1)} - (n-1) \left(\frac{r}{\sigma}\right)^{n-2} \right]. \quad (2.18)$$

We find that for the GEM- n family, $\phi''(r=0) = 0$ for $n > 2$. Therefore, it follows that the threshold value of the index is 2 and that for $n > 2$, the GEM- n potentials belong to the class of Q^\pm -interactions [44, 46, 49].

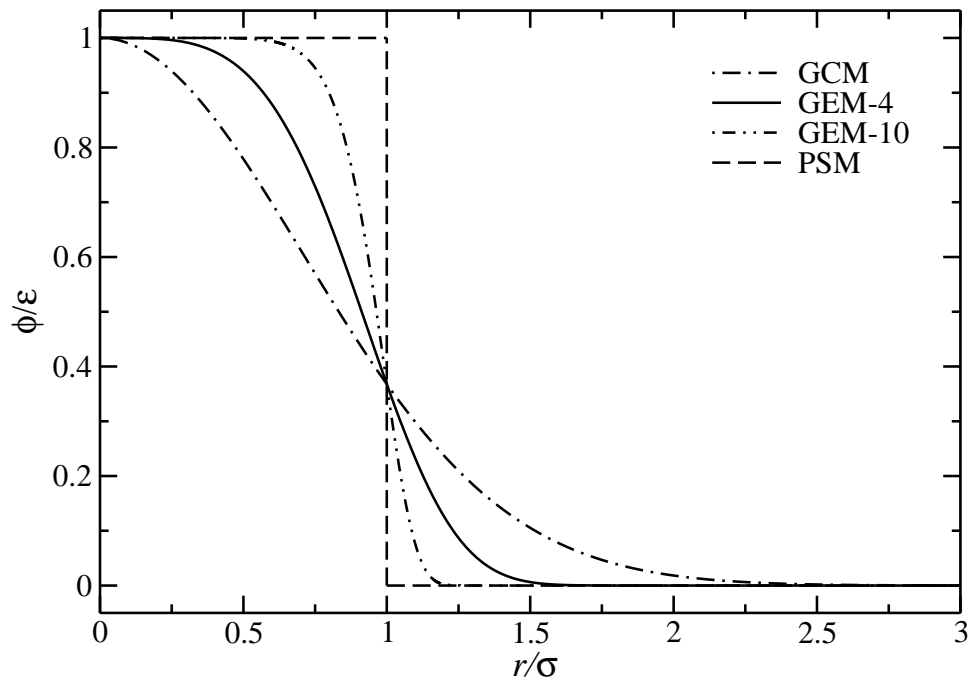


Figure 2.4: Four members of the GEM- n family: the GCM ($n = 2$), the GEM-4, GEM-10, and the PSM ($n = \infty$).

Chapter 3

Statistical mechanics in a nutshell

Statistical mechanics [50–53] provides the mathematical framework to derive the macroscopic properties of materials, which are accessible in experiments, from the knowledge of the microscopic properties and dynamics of its constituent entities, such as atoms, molecules or macromolecules. Statistical mechanics thus forms the basis for thermodynamics, which otherwise would just be a phenomenological theory. It also allows for the calculation of static and dynamical properties using the formalism of spatial and time correlation functions.

3.1 Basic concepts

At any time, the microscopic state of a classical system of N spherical particles is fully determined by the $3N$ coordinates $\mathbf{r}_1, \mathbf{r}_2, \dots, \mathbf{r}_N$ and $3N$ momenta $\mathbf{p}_1, \mathbf{p}_2, \dots, \mathbf{p}_N$ of the particles, presenting a point in the $6N$ -dimensional phase space. The dynamics of the system is governed by the Hamilton function $\mathcal{H}(\mathbf{r}^N, \mathbf{p}^N)$ and the equations of motion read

$$\frac{\partial \mathcal{H}(\mathbf{r}^N, \mathbf{p}^N)}{\partial \mathbf{p}_i} = \dot{\mathbf{r}}_i \quad (3.1)$$

and

$$\frac{\partial \mathcal{H}(\mathbf{r}^N, \mathbf{p}^N)}{\partial \mathbf{r}_i} = -\dot{\mathbf{p}}_i, \quad (3.2)$$

where the dot denotes a time derivative. These differential equations have to be solved with suitable initial conditions.

Since typical macroscopic systems usually consist of a huge number of particles of the order of $N \sim 10^{23}$, it is impossible to determine the trajectory of the system through phase space, even with the most modern computers. Fortunately, we do not need the details of the specific behaviour of every single particle. It is more convenient to introduce the concept of an “ensemble”, i.e., a large number of realisations of one and the same system where each member of the ensemble is compatible with fixed macroscopic parameters which describe the thermodynamic state of the

system. At the same time, however, each member is assumed to evolve under the microscopic laws of motion from its particular initial condition, i.e., its specific time evolution will be different from that of all other members in the ensemble. Nevertheless, we can determine macroscopic properties common to all members of the ensemble by performing so-called “ensemble averages”. Let $A = A(\mathbf{r}^N, \mathbf{p}^N)$ denote a macroscopic, time-independent property. Then, the ensemble average of A , denoted as $\langle A \rangle_{\text{ens}}$, is obtained by calculating the value of A in each member of the ensemble and performing an average over all these values:

$$\langle A \rangle_{\text{ens}}^M = \frac{1}{M} \sum_{i=1}^M A_i, \quad (3.3)$$

where M is the number of realisations of the system in the ensemble and A_i is the value of A in the i^{th} realisation. Usually, only a single system is considered and measurements are made at different points in time and we can determine a time average given by

$$\langle A \rangle_{\text{time}}^t = \frac{1}{t} \int_0^t dt' A(t'). \quad (3.4)$$

A system is called ergodic if

$$\langle A \rangle_{\text{ens}}^{M \rightarrow \infty} = \langle A \rangle_{\text{time}}^{t \rightarrow \infty}, \quad (3.5)$$

i.e., given an infinite amount of time, such a system will visit all possible microscopic states available to it in phase space.

3.2 The canonical ensemble

We consider a system of identical particles with fixed particle number N confined in a fixed volume V and in thermal equilibrium with an infinite large heat reservoir, thereby assuring that the system will have fixed temperature T .

The partition function $Q(N, V, T)$ of this so-called canonical or NVT ensemble is given by

$$Q(N, V, T) = \frac{h^{-3N}}{N!} \iint d\mathbf{r}^N d\mathbf{p}^N e^{-\beta \mathcal{H}(\mathbf{r}^N, \mathbf{p}^N)}, \quad (3.6)$$

where h is the Planck constant and the factor $N!$ accounts for the indistinguishability of the particles. This function links statistical mechanics to thermodynamics via the relation

$$F = -k_B T \log Q(N, V, T), \quad (3.7)$$

where F is the Helmholtz free energy, which is the appropriate thermodynamic potential for a system of fixed N , V and T .

If $F = F(N, V, T)$ were known, all other thermodynamic state functions could be obtained by

differentiation with respect to its variables. Thus, the free energy or equivalently the partition function contain essentially the entire information about the macroscopic thermodynamic properties of the system. For instance, it can be shown [54] that the internal energy U can be calculated via

$$U = \langle \mathcal{H} \rangle = - \left[\frac{\partial \log Q(N, V, T)}{\partial \beta} \right]_{V, N} = \left(\frac{\partial \beta F}{\partial \beta} \right)_{V, N}. \quad (3.8)$$

Further, the pressure P of the system is given by

$$P = k_B T \left[\frac{\partial \log Q(N, V, T)}{\partial V} \right]_{N, T} = - \left(\frac{\partial F}{\partial V} \right)_{N, T} \quad (3.9)$$

and the chemical potential μ by

$$\mu = -k_B T \left[\frac{\partial \log Q(N, V, T)}{\partial N} \right]_{T, V} = \left(\frac{\partial F}{\partial N} \right)_{V, T}. \quad (3.10)$$

Also, second derivatives of the free energy can be determined, like the bulk modulus B , which is given by

$$B = V \left(\frac{\partial^2 F}{\partial V^2} \right)_{N, T} = \kappa_T^{-1}, \quad (3.11)$$

where κ_T is the isothermal compressibility.

For the systems considered in this thesis, the Hamilton function \mathcal{H} can be separated into two contributions due to the kinetic and potential energy, thereby allowing for an explicit integration over the momenta in Eq. (3.6), which then can be rewritten as

$$Q(N, V, T) = \frac{\Lambda^{-3N}}{N!} z_N(V, T), \quad (3.12)$$

where

$$z_N(V, T) = \int d\mathbf{r}^N e^{-\beta \Phi(\mathbf{r}^N)} \quad (3.13)$$

is the configurational integral, $\Phi(\mathbf{r}^N)$ is the total potential energy (cf. Eq. 2.9) and

$$\Lambda = \sqrt{\frac{2\pi\beta\hbar^2}{m}} \quad (3.14)$$

is the de Broglie thermal wavelength. Here, m is the mass of the particles and $\hbar = \frac{h}{2\pi}$. For an ideal gas, $\Phi(\mathbf{r}^N) = 0$ and $z_N(T, V) = V^N$. Therefore, the partition function of the ideal gas is given by

$$Q^{\text{id}}(N, V, T) = \frac{\Lambda^{-3N}}{N!} V^N. \quad (3.15)$$

Based on this result, we can rewrite the partition function of a system of interacting particles as

$$Q(N, V, T) = Q^{\text{id}} \frac{z_N(V, T)}{V^N}, \quad (3.16)$$

which upon taking the logarithm of both sides naturally separates the free energy into an ideal and an excess part

$$F = F^{\text{id}} + F^{\text{ex}}. \quad (3.17)$$

Here, the excess part takes into account all contributions to the free energy that stem from interactions between the particles.

Using Stirling's approximation for large N

$$\log N! \sim N \log N - N, \quad (3.18)$$

F^{id} is given by

$$\frac{\beta F^{\text{id}}}{N} = \log \varrho + 3 \log \Lambda - 1 \quad (3.19)$$

and the excess part F^{ex} of the free energy is

$$F^{\text{ex}} = -k_{\text{B}}T \log \frac{z_N(V, T)}{V^N}. \quad (3.20)$$

In a similar manner, the internal energy can also be separated according to

$$U = U^{\text{id}} + U^{\text{ex}}, \quad (3.21)$$

where $U^{\text{id}} = \frac{3}{2}Nk_{\text{B}}T$ and

$$U^{\text{ex}} = \frac{1}{z_N(T, V)} \int d\mathbf{r}^N \Phi(\mathbf{r}^N) e^{-\beta\Phi(\mathbf{r}^N)} = \langle \Phi \rangle. \quad (3.22)$$

3.3 The isobaric-isothermal ensemble

Experiments are usually performed at constant *pressure* and temperature rather than constant *volume* and temperature, leading thus to the isobaric-isothermal or NPT ensemble. Similar to the canonical ensemble we can imagine the system being in contact with a heat reservoir at temperature T , and in addition the system will also be put under the action of a piston which is controlled by an external pressure P .

Following similar lines as before, a partition function $Q(N, P, T)$ can be introduced which is related to the one of the canonical ensemble via a Laplace transform

$$Q(N, P, T) = \beta P \int_0^{\infty} dV e^{-\beta PV} Q(N, V, T). \quad (3.23)$$

The thermodynamic potential of the isobaric-isothermal ensemble is the Gibbs free energy,

$G(N, P, T)$, which can then be calculated via

$$G(N, P, T) = -k_{\text{B}}T \log Q(N, P, T). \quad (3.24)$$

It can also be obtained by performing a Legendre transformation of the Helmholtz free energy

$$G(N, P, T) = F[N, V(P), T] - V(P) \frac{\partial F}{\partial V} = F[N, V(P), T] + PV(P). \quad (3.25)$$

Again, $Q(N, P, T)$ and $G(N, P, T)$ contain all the information about the macroscopic behaviour of the system. The volume is now given by

$$V = -k_{\text{B}}T \left[\frac{\partial \log Q(N, P, T)}{\partial P} \right]_{N, T} = \left(\frac{\partial G}{\partial P} \right)_{N, T}. \quad (3.26)$$

and the chemical potential μ can be obtained by

$$\mu = -k_{\text{B}}T \left[\frac{\partial \log Q(N, P, T)}{\partial N} \right]_{P, T} = \left(\frac{\partial G}{\partial N} \right)_{P, T}. \quad (3.27)$$

Chapter 4

Theory

To be able to study the phase behaviour of the systems under consideration, we have to choose theories suitable to describe the different states of matter. In this effort, we decided to investigate the fluid state by integral equation theories (cf. Sec. 4.1) and the solid state via genetic algorithms (cf. Sec. 4.2) and density functional theory (cf. Sec. 4.3).

4.1 The fluid - integral equation theories

4.1.1 The radial distribution function and its connection to thermodynamic properties

The key element of integral equation theories (IETs) is the pair distribution function which for a system of N spherical particles confined in volume V at constant temperature T is defined as

$$g_N(\mathbf{r}_1, \mathbf{r}_2) = \frac{N(N-1)}{\varrho^2 z_N(V, T)} \int \dots \int d\mathbf{r}_3 \dots d\mathbf{r}_N e^{-\beta\Phi(\mathbf{r}^N)}, \quad (4.1)$$

where $z_N(V, T)$ is the configurational integral given by Eq. (3.13).

On physical grounds, $g_N(\mathbf{r}_1, \mathbf{r}_2)d\mathbf{r}_1d\mathbf{r}_2$ can be understood as a measure for the probability to find particle 1 within a volume $d\mathbf{r}_1$ at \mathbf{r}_1 while particle 2 is located in a volume $d\mathbf{r}_2$ at \mathbf{r}_2 , irrespective of the positions of all other particles in the systems.

For isotropic systems, $g_N(\mathbf{r}_1, \mathbf{r}_2)$ only depends on the distance $|\mathbf{r}_1 - \mathbf{r}_2| = r$ between the particles and can be written as an ensemble average over pairs [54, 55]

$$g(r) = \frac{V}{N^2} \left\langle \sum_{i \neq j} \delta(\mathbf{r} - \mathbf{r}_{ij}) \right\rangle. \quad (4.2)$$

$g(r)$ is called radial distribution function (RDF) represents the ratio of the probability to find a particle at a certain distance from a given particle compared to the same probability in an ideal gas. The fundamental importance of $g(r)$ stems from the fact that the knowledge of this function

is sufficient to calculate all thermodynamic properties of the system under study [54].

Provided that all particles in a system interact only via pairwise additive interactions $\phi(r)$ and that $\phi(r)$ is density independent, the equation of state can be expressed as

$$\frac{\beta P}{\varrho} = 1 - \frac{2\pi}{3}\beta\varrho \int_0^\infty dr r^2 g(r) \left[r \frac{d\phi(r)}{dr} \right]. \quad (4.3)$$

This equation is commonly referred to as virial equation, since it expresses the pressure as an ensemble average of the virial.

There are two further routes to determine the pressure. The so-called energy route is based on the excess (over ideal) pressure, P^{ex} , which can be determined by rewriting Eq. (3.9) as

$$P^{\text{ex}} = - \left(\frac{\partial F^{\text{ex}}}{\partial V} \right)_T. \quad (4.4)$$

The excess free energy, F^{ex} , on the other hand, is given by

$$\frac{\beta F^{\text{ex}}}{N}(\varrho) = \int_0^\beta d\beta' \frac{U^{\text{ex}}}{N}(\beta', \varrho). \quad (4.5)$$

Here, the integral is evaluated along an isochore and the excess internal energy, U^{ex} , is related to $g(r)$ via

$$\frac{U^{\text{ex}}}{N} = 2\pi\varrho \int_0^\infty dr r^2 g(r) \phi(r). \quad (4.6)$$

The last route leads to the so-called compressibility equation, which in contrast to the two routes presented above is also valid for systems where particles interact through more general than pairwise additive forces. In this approach, the pressure can be obtained by integrating

$$\kappa_T = -\frac{1}{V} \left(\frac{\partial V}{\partial P} \right)_T = \left[\varrho \left(\frac{\partial P}{\partial \varrho} \right)_T \right]^{-1}, \quad (4.7)$$

along an isotherm with respect to ϱ or V , where the isothermal compressibility κ_T is obtained from the RDF according to

$$\varrho k_B T \kappa_T = 1 + 4\varrho \int d\mathbf{r} [g(\mathbf{r}) - 1]. \quad (4.8)$$

4.1.2 The Ornstein-Zernike equation and integral equation theories

In 1914, Ornstein and Zernike [56] introduced in a heuristic way the so-called direct correlation function $c(r)$ via the following equation

$$h(r) = c(r) + \varrho \int d\mathbf{r}' c(|\mathbf{r} - \mathbf{r}'|) h(r'). \quad (4.9)$$

This equation is valid for translationally invariant and isotropic fluids and is referred to as Ornstein-Zernike equation (OZE). It expresses the total correlation $h(r) = g(r) - 1$ between two particles in the fluid separated by distance r as the sum over the direct correlation $c(r)$ between those two particles and all indirect correlations mediated by $c(r)$ through an infinite number of many-body correlations over the other particles of the fluid.

The pair and direct correlation function can be systematically analysed in terms of configurational integrals over clusters of particles. Within the scope of this cluster expansion it can be shown that [54]

$$g(r) = e^{-\beta\phi(r)+h(r)-c(r)+B(r)}, \quad (4.10)$$

where the bridge function $B(r)$ is the sum of an infinite number of terms, each consisting of integrals whose kernels are products of increasing order of correlation functions and simple functions of the potential. Since the exact $B(r)$ is not known for any system, approximations have to be made, thereby giving rise to IETs. Then, Eq. (4.10) can be used as a so-called closure to the OZE. Whereas in an exact closure the virial, compressibility and energy routes to the equation of state would provide identical results [54], the approximate nature of the various IETs leads to different ones, i.e., they suffer from thermodynamic inconsistency.

In the following sections we will present the IETs considered in this thesis.

4.1.3 The mean field approximation

The mean field approximation (MFA) [57] was originally proposed for systems interacting via pair potentials consisting of a hard sphere interaction

$$\phi(r) = \infty, \quad \text{for } r < \sigma, \quad (4.11)$$

with diameter σ plus a tail for $r > \sigma$ that can take different functional forms. For such potentials, the MFA is based on an ansatz for $c(r)$,

$$c(r) = -\beta\phi(r), \quad \text{for } r > \sigma, \quad (4.12)$$

along with the so-called core condition that expresses the impenetrability of the particles

$$g(r) = 0, \quad \text{for } r < \sigma. \quad (4.13)$$

The relation (4.12) is motivated by a detailed investigation of the long-range behaviour of $c(r)$. Thereby, it can be generally shown that

$$c(r) \cong -\beta\phi(r), \quad \text{for } r \rightarrow \infty, \quad (4.14)$$

which implies that the MFA is correct in the limit $r \rightarrow \infty$ and can be considered as an extension of the realm of validity of Eq. (4.14) to short distances. This feature will be further discussed in Sec. 6.5.

As bounded potentials lack a hard core, Eq. (4.13) is not applicable and the MFA reduces to

$$c(r) = -\beta\phi(r), \quad \forall r. \quad (4.15)$$

Supplementing the OZE with this closure, Eqs. (4.12) and (4.13), or (4.15), respectively, yield an integral equation for the RDF.

Despite the simple form assumed for $c(r)$, the MFA provides reasonable results for many model systems, both with harshly repulsive and soft interactions. The most attractive feature of the MFA, however, is the fact that it can be solved analytically for a number of model potentials of physical interest, including the hard core Yukawa potential [58] and the charged hard sphere model [54]. In the case of soft potentials, however, the MFA suffers from some deficiencies, like, e.g., yielding negative values for the RDF at low densities (cf. Sec. 6.5), which is unphysical. This effect does not occur in the case of hard core potentials, as such a behaviour is then explicitly ruled out by Eq. (4.13).

4.1.4 The hypernetted chain closure

The hypernetted chain closure (HNC) [59] is obtained by setting

$$B(r) = 0. \quad (4.16)$$

Then, Eq. (4.10) becomes

$$g(r) = e^{-\beta\phi(r)+h(r)-c(r)}, \quad (4.17)$$

which is equivalent to

$$c(r) = -\beta\phi(r) + h(r) - \log[h(r) + 1]. \quad (4.18)$$

For the HNC, no analytical solutions are available. Usually, this approximation yields good results for bounded potentials [44, 47] and for long-ranged interactions such as in ionic systems [54].

4.1.5 The Percus-Yevick approximation

The Percus-Yevick approximation (PY), proposed in 1958 by Percus and Yevick [60], assumes that

$$c(r) = \left[1 - e^{\beta\phi(r)}\right] g(r), \quad (4.19)$$

so that $c(r)$ equals zero wherever the potential vanishes.

In this case, the RDF is given by

$$g(r) = e^{-\beta\phi(r)}[1 + h(r) - c(r)]. \quad (4.20)$$

Since expanding the HNC expression (4.17) with respect to $[h(r) - c(r)]$ up to the first order gives

$$\begin{aligned} g(r) &= e^{-\beta\phi(r)+h(r)-c(r)} = \\ &= e^{-\beta\phi(r)}e^{h(r)-c(r)} \simeq \\ &\simeq e^{-\beta\phi(r)}[1 + h(r) - c(r)], \end{aligned} \quad (4.21)$$

we see that the PY approximation is the result of linearising the HNC closure. A cluster analysis of both closures shows that the HNC approximation is obtained by summing up a higher number of terms than the PY closure [54]. In most cases, the solution of the OZE in combination with Eq. (4.19) has to be found numerically, but in some cases, e.g., for the hard sphere fluid or for adhesive hard spheres, it can be obtained analytically [54].

In particular for systems with short-ranged, steeply repulsive potentials, the PY equation is very successful. Its better performance for this kind of potentials in comparison to other conventional IETs might to some extent be due to the cancellation of errors while summing up the terms of the cluster expansion. On the other hand, as will be demonstrated in Sec. 7.3 and as was shown in [46], the PY approximation is usually not a good choice for bounded potentials.

4.1.6 The self-consistent Ornstein-Zernike approximation

Over the past decades, considerable effort has been devoted to the formulation of thermodynamically self-consistent liquid state theories, which, in turn, have most of all led to an improved description of the structural and thermodynamic properties of liquids with harshly repulsive potentials. In the first generation of these concepts, such as the Rogers-Young (RY) [61], the modified hypernetted chain (MHNC) [62], or the Zerah-Hansen approach (HMSA) [63,64], simple functions were introduced in the respective closure relations to the OZE which use an adjustable but not explicitly state-dependent parameter to interpolate between two conventional closures (such as, e.g., between PY and HNC in the case of the RY approach). Since self-consistency was enforced for each state point independent of the neighbouring ones, we shall call this approach *locally self-consistent*. The concepts of the second generation of the self-consistent liquid state theories were based on more sophisticated ideas. The self-consistent Ornstein-Zernike approximation (SCOZA), introduced in 1984 by Høye and Stell [65], proposed an explicitly state-*dependent* function in the MFA closure relation in order to enforce thermodynamic self-consistency between different thermodynamic routes [65,66]. The hierarchical reference theory (HRT) [67–69], on the other hand, successfully merged ideas of microscopic liquid state theory and renormalisation group concepts.

In both these advanced liquid state approaches thermodynamic consistency was enforced in the *entire* space of system parameters, which we shall call *global self-consistency*. In the following, we focus on the extension of SCOZA to soft systems.

The original formulation of the SCOZA for hard core systems [65, 66] is based on the MFA (cf. Sec. 4.1.3). Both concepts require the RDF to vanish inside the core and set the direct correlation function proportional to the potential for distances larger than the core diameter. In SCOZA, the proportionality factor now contains a state-dependent function that imposes global thermodynamic consistency. Following the lines of generalising the MFA to soft potentials (cf. Sec. 4.1.3), we extend the original SCOZA ansatz:

$$c(r) = \beta K_i(\varrho, \beta) \phi(r), \quad \forall r, \quad i = \text{EC or VC}, \quad (4.22)$$

where $K_i(\varrho, \beta)$ are as yet undetermined, state-dependent functions and the subscripts EC and VC specify whether thermodynamic consistency is enforced between the energy and the compressibility or between the virial and the compressibility routes (cf. Sec. 4.1.1). For the formulas common to both cases, the generic subscript i will be used. Since the MFA is recovered for $K_i(\varrho, \beta) \equiv -1$, deviations from this value are a measure of thermodynamic inconsistency in the MFA.

Applications of the SCOZA concept [65, 66, 70] to liquid systems were up to now restricted to those cases where the respective interactions can be expressed as a hard core plus a linear combination of Yukawa tails outside the core (HCY systems) [71, 72]. This restriction can be traced to the fact that the rather elaborate SCOZA formalism is intricately linked to the availability of the analytic solution of the MFA for such a system [73, 74]. From this point of view the obvious counterpart of HCY systems in soft matter is the GCM [25], which also can be treated semi-analytically within MFA [40, 41, 46]. The formalism of the SCOZA applied to the GCM will be presented in Sec. 6.3.

4.1.7 Integro-differential equation SCOZA approach

The availability of a semi-analytical framework provided by the MFA for specific systems, such as hard core Yukawa systems or the GCM, represents a rather singular exception and therefore, straightforward applications of SCOZA are limited. In an effort to overcome these restrictions one may ask whether the SCOZA concept may be formulated for the case of a *general* system, i.e., when a semi-analytic solution to the MFA is not at hand. This is indeed possible as we show in the following. Let us assume a SCOZA-type closure relation, i.e.,

$$c(r) = \beta \bar{K} \phi(r), \quad \forall r, \quad (4.23)$$

with a state-dependent function $\bar{K}(\varrho, \beta)$. Once \bar{K} is specified, this leads in combination with the OZE directly to the RDF $g(r) = g(r; \varrho, \beta; \bar{K})$, which is thus also a function of \bar{K} . Since \bar{K} is explicitly state-dependent, i.e., $\bar{K} = \bar{K}(\varrho, \beta)$, the compressibility as determined by the virial

route, i.e., differentiating Eq. (4.3), is given by

$$\begin{aligned} [\rho k_B T \kappa_T^Y]^{-1} &= 1 - \frac{4\pi}{3} \rho \int_0^\infty dr r^3 \frac{d\beta\phi(r)}{dr} g(r; \rho, \beta; \bar{K}) - \frac{2\pi}{3} \rho^2 \int_0^\infty dr r^3 \frac{d\beta\phi(r)}{dr} \frac{\partial g(r; \rho, \beta; \bar{K})}{\partial \rho} \\ &\quad - \frac{2\pi}{3} \rho^2 \frac{\partial \bar{K}}{\partial \rho} \int_0^\infty dr r^3 \frac{d\beta\phi(r)}{dr} \frac{\partial g(r; \rho, \beta; \bar{K})}{\partial \bar{K}}. \end{aligned} \quad (4.24)$$

Thermodynamic self-consistency between the virial and the compressibility route is now enforced by choosing \bar{K} such that κ_T^C , given by the compressibility equation (4.8), is equal to κ_T^Y , i.e., by finding at fixed temperature T a root of the function

$$f(\bar{K}) = \kappa_T^C - \kappa_T^Y. \quad (4.25)$$

Here, derivatives with respect to ρ and \bar{K} have to be calculated numerically. We call this the integro-differential equation (IDE) approach to SCOZA.

It was exactly this idea that was realised in previous applications of parameterised closure relations such as RY [61], HMSA [63,64], or MHNC [62]. There, however, consistency was achieved only *locally*, i.e., considering each state point in isolation and neglecting the state dependence of \bar{K} . This corresponds to setting $\partial \bar{K} / \partial \rho = 0$ and dropping the last term in Eq. (4.24). In the present approach, in contrast, we consider \bar{K} to be explicitly state-dependent and thus this term is retained. Consequently, the consistency criterion involves not only isolated state points but also neighbouring state points via the density derivative. Therefore, we have decided to call our criterion a *global* one. The quantitative difference between the local and the global approaches will be discussed in Sec. 6.5.

4.1.8 HNC-based SCOZA

The above approach to thermodynamic consistency represents an IDE based re-formulation of the SCOZA. It is now not only entirely independent of the semi-analytic solution provided by the MFA for the GCM. More importantly, it has become completely *general* in the sense that in the present formulation self-consistency can be enforced for systems with *arbitrary* (soft) potentials and in combination with other, parameterised closure relations.

To demonstrate the power of this idea we introduce a HNC-based SCOZA (for clarity we will refer to the SCOZA approaches introduced above as ‘‘MFA-based SCOZA’’). This particular choice is motivated by the fact that the HNC has been found to work very well for the GCM and other soft potentials [40, 41, 44, 47]. For the closure relation of our HNC-based SCOZA we propose

$$g(r) = \exp [\beta \bar{K}_{\text{HNC}}(\rho, \beta) \phi(r) + h(r) - c(r)], \quad (4.26)$$

where the unknown, state-dependent function $\bar{K}_{\text{HNC}}(\rho, \beta)$ is determined such as to make the right

hand side of the consistency requirement (4.25) vanish, i.e., by enforcing equality between the compressibility and the virial route. Numerically, this is achieved by solving Eq. (4.24), where $g(r; \varrho, \beta; \bar{K}_{\text{HNC}})$ is obtained from the solution of the OZE along with the closure relation (4.26).

4.2 The solid at zero temperature - genetic algorithms

Compared to the liquid state, the description of the properties of the solid phases is more delicate. Due to the many exotic structures that can form in soft matter systems (cf. Chap. 1), we do not know *a priori* which ordered structures our systems will form in equilibrium. The conventional approach is to select a set of possible lattices, based on more or less plausible arguments, and to calculate their respective free energies. The one with the lowest free energy is then *assumed* to be the stable structure. While this strategy is in general successful in hard (atomic) systems, the situation is entirely different in soft matter systems. Due to the arbitrariness involved, this pre-selection process is highly unsatisfactory, a problem that we solve by using a genetic algorithm (GA) [75], i.e., a tool which searches among *all* possible lattices for the equilibrium structure. On several occasions, this approach turned out to be a very reliable and convenient means to determine the equilibrium structures of different soft matter systems in an unbiased and parameter-free search [11, 12, 75].

The basic idea of the GA is to mimic the concepts of evolution, which can be outlined as follows. In an initial step we consider a large number of randomly generated possible candidate structures which are denoted as individuals. The collection of these individuals forms a so-called (first) generation. A fitness value is assigned to each individual which is a measure of its aptness for survival and reproduction in the sense that a better solution has a higher fitness value. Since in our case we search for the thermodynamically most favourable arrangement of particles in a crystalline structure, we associate a lower free energy of a given lattice with a higher fitness value. Among the individuals of the current generation suitable pairs of parents are chosen according to their fitness and via recombination they create the individuals (i.e., lattice structures) of the subsequent generation. With a certain probability, these individuals are then subject to a mutation process which avoids inbreeding and introduces new or previously lost genetic material. We proceed in this way for a sufficiently long sequence of generations, keeping track of the individual with the highest fitness value, i.e., the lattice structure with the lowest free energy so far. In general, the algorithm converges rapidly towards the equilibrium structure for a given state point. For conceptual details we refer to [75, 76].

The GA is used to search for the energetically most favourable ordered structures at $T = 0$, which are then considered as candidates for the phase diagram at finite temperatures. This search is particularly challenging for systems that show clustering behaviour. At $T = 0$, these solids behave ideally: all clusters are populated by the same number of particles, denoted by n_c , which sit perfectly on top of each other at the positions of an ideal lattice. Our measure of fitness is

related to the free energy, F , which at $T = 0$ is identical to the internal energy, U , and is given by

$$\frac{F(T=0)}{N} = \frac{U}{N} = \frac{n_c - 1}{2} \phi(\mathbf{R} = 0) + \frac{n_c}{2} \sum_{\mathbf{R} \neq 0} \phi(\mathbf{R}), \quad (4.27)$$

where $\{\mathbf{R}\}$ denotes the set of Bravais lattice vectors of a candidate structure for the cluster phase. Here, the first term is the interaction energy of a particle with the $(n_c - 1)$ particles of the same cluster, while the second one describes the particle's interaction with all other clusters of the crystal. In employing the GA, we minimise the lattice sum per particle, U/N , with respect to both the Bravais lattice and the cluster occupation number n_c .

Strictly speaking, at $T = 0$, n_c can only assume integer values, if we insist that each site is occupied by an identical number of particles. However, rational values of n_c arising from populating different sub-lattices with different integer occupation numbers and periodically repeating the pattern, are in principle also allowed. In our calculation, we avoid these cases by employing a kind of mean-field approach. Possible corrections to the lattice sum from short-range correlations that lead to differently populated sub-lattices are ignored, and the occupation number of all sites is set equal to the average value $\langle n_c \rangle$, a general real number. In reality, irrational occupations are, of course, forbidden for a ground state, pointing to the possibility of phase separation between optimally occupied states with rational occupation. However, at finite temperatures, it is expected that hopping processes will allow for the migration of particles and lead to an equalisation of the average number $\langle n_c \rangle$ of particles on every site. Our approximation of setting $n_c = \langle n_c \rangle$ is expected to be valid for temperatures that are low enough so that the entropic contribution, $-TS$, associated with the hopping processes can be ignored in comparison with the lattice energy, U , in the expression $F = U - TS$ for the free energy F . Moreover, since we do not expect sub-lattices to be populated by vastly different particle numbers even at $T = 0$, the error in replacing n_c by $\langle n_c \rangle$ is very small and the approach offers reliable information on the possible crystal structures at $T = 0$.

4.3 The solid at finite temperatures - density functional theory

With the possible candidate structures predicted by the GA at hand we can now proceed to finite temperatures where it is most convenient to describe the ordered phases within the framework of classical density functional theory (DFT) [77]. For the systems considered in this work we use a mean-field format for the free energy functional $\mathcal{F}[\varrho]$,

$$\mathcal{F}[\varrho] = \mathcal{F}_{\text{id}}[\varrho] + \mathcal{F}_{\text{ex}}[\varrho], \quad (4.28)$$

where the ideal part $\mathcal{F}_{\text{id}}[\varrho]$ is given by

$$\mathcal{F}_{\text{id}}[\varrho] = k_{\text{B}}T \int d\mathbf{r} \varrho(\mathbf{r}) \{ \log[\varrho(\mathbf{r})\Lambda^3] - 1 \}. \quad (4.29)$$

Λ is given by Eq. (3.14). Further, the excess part, $\mathcal{F}_{\text{ex}}[\varrho]$, is obtained via

$$\mathcal{F}_{\text{ex}}[\varrho] = \frac{1}{2} \iint d\mathbf{r}_1 d\mathbf{r}_2 \varrho(\mathbf{r}_1) \varrho(\mathbf{r}_2) \phi(|\mathbf{r}_1 - \mathbf{r}_2|). \quad (4.30)$$

This choice of the functional is explicitly justified in [44].

In the case of clustering systems, where particles can overlap or even sit on top of each other, we use a periodic array of Gaussian cluster density profiles,

$$\varrho_{\text{cl}}(\mathbf{r}) = n_c \left(\frac{\alpha}{\pi} \right)^{3/2} e^{-\alpha \mathbf{r}^2}, \quad (4.31)$$

localised at the lattice sites $\{\mathbf{R}\}$ as an ansatz for the inhomogeneous density field, $\varrho(\mathbf{r})$, i.e.,

$$\varrho(\mathbf{r}) \equiv \sum_{\{\mathbf{R}\}} \varrho_{\text{cl}}(\mathbf{r} - \mathbf{R}) = n_c \left(\frac{\alpha}{\pi} \right)^{3/2} \sum_{\{\mathbf{R}\}} e^{-\alpha(\mathbf{r} - \mathbf{R})^2}. \quad (4.32)$$

Our choice of this particular shape for the density profiles was anticipated in [44] and will be justified *a posteriori* when comparing the theoretical data with the simulation results (cf. Sec. 7.3). The inhomogeneous density field $\varrho(\mathbf{r})$ is uniquely determined by two parameters characterising the cluster density profiles, i.e., the width α of the profile and the cluster occupancy number or cluster size, n_c . To find the *equilibrium* density field, the functional given by Eqs. (4.28) to (4.30) has to be minimised with respect to both α and n_c , at fixed ϱ and T , giving us the theoretical predictions for the equilibrium values of α and n_c at the state point under consideration.

Inserting the ansatz (4.32) into the functional (4.28) to (4.30), $\mathcal{F}[\varrho]/N$ reduces to a function $f = f(n_c, \alpha)$ that can be split into an ideal, an inter-, and an intra-cluster contribution

$$f(n_c, \alpha) = f_{\text{id}}(n_c, \alpha) + f_{\text{inter}}(n_c, \alpha) + f_{\text{intra}}(n_c, \alpha). \quad (4.33)$$

For the ideal contribution, we find

$$f_{\text{id}}(n_c, \alpha) = k_{\text{B}}T \left[\log n_c + 3/2 \log(\alpha\sigma^2/\pi) - 5/2 + 3 \log(\Lambda/\sigma) \right], \quad (4.34)$$

which is an excellent approximation to the ideal free energy, provided that the Gaussians in Eq. (4.32) do not overlap, which is the case for $\alpha\sigma^2 \gtrsim 30$, representing thus a physically reasonable lower bound for α [78]. Further, it is easy to see from Eqs. (4.29) and (4.32) that for $\alpha \rightarrow 0$ the ideal free energy per particle tends to $k_{\text{B}}T [\log(\varrho\Lambda^3) - 1]$, the *finite* free energy of the ideal gas, whereas the approximate expression of Eq. (4.34) has a negative, logarithmic *divergence* there, signalling the breakdown of the approximation for low α -values.

For the other two terms in Eq. (4.33) we find

$$f_{\text{inter}}(n_c, \alpha) = n_c \sqrt{\frac{\alpha}{8\pi}} \sum_{\mathbf{R} \neq 0} \int_0^{\infty} dr \frac{r}{R} \left[e^{-\alpha(r-R)^2/2} - e^{-\alpha(r+R)^2/2} \right] \phi(r) \quad (4.35)$$

and

$$f_{\text{intra}}(n_c, \alpha) = (n_c - 1) \sqrt{\frac{\alpha^3}{2\pi}} \int_0^{\infty} dr r^2 e^{-\alpha r^2/2} \phi(r), \quad (4.36)$$

where R denotes the modulus of the Bravais lattice vector \mathbf{R} . For a given density ϱ , the modulus of the lattice vectors depends on the degree of clustering n_c , since the elementary cell can expand by accumulating more particles per lattice site.

Chapter 5

Monte Carlo simulations

Monte Carlo (MC) methods are special kinds of computer simulations that are based on stochastic algorithms, i.e., by using random numbers a wide variety of problems spanning from finance and economics through mathematics to chemistry and physics become numerically tractable.

5.1 Conventional Monte Carlo simulations

We explain the idea of Monte Carlo simulations [55,79–81] for the canonical ensemble (cf. Sec. 3.2). Via suitable modifications, the formulas presented in the following can readily be generalised to other ensembles.

5.1.1 Master equation

A system of N particles confined in a simulation box of volume V at temperature T is assumed to be in a state τ characterised by the positions of the particles. At time span dt later the system will be in state ν with probability $P(\tau \rightarrow \nu) dt$. Statistical mechanics allows to define transition probabilities for all states that are accessible to the system.

Let $\{w_\tau(t)\}$ be the set of weights which represent the probability that the system will be in state τ at fixed time t . Then, we can write the master equation which governs the time evolution of $w_\tau(t)$

$$\frac{dw_\tau(t)}{dt} = \sum_\nu [w_\nu(t)P(\nu \rightarrow \tau) - w_\tau(t)P(\tau \rightarrow \nu)]. \quad (5.1)$$

The first term on the right hand side describes transitions of the system from states ν *into* state τ , while the second one takes into account transitions *leaving* state τ for other states ν . Since the system has to be in *some* state at a given time t , the probabilities $w_\tau(t)$ have to obey the sum rule

$$\sum_\tau w_\tau(t) = 1, \quad \forall t. \quad (5.2)$$

Now, the ensemble average at time t , $\langle A \rangle_t$, of some arbitrary macroscopic property A of the system can be calculated with the help of these weights via

$$\langle A \rangle_t = \sum_{\tau} A_{\tau} w_{\tau}(t), \quad (5.3)$$

where A_{τ} is the value that A takes in state τ .

5.1.2 Equilibrium and expectation values

In equilibrium, the weights $\{w_{\tau}(t)\}$ converge with time towards time-independent values p_{τ} , called equilibrium occupation probabilities. They are defined by

$$p_{\tau} = \lim_{t \rightarrow \infty} w_{\tau}(t). \quad (5.4)$$

Consequently, $dw_{\tau}(t)/dt = 0$ for $t \rightarrow \infty$.

For a canonical ensemble

$$p_{\tau} = \frac{1}{Q(N, V, T)} e^{-\beta \mathcal{H}_{\tau}}, \quad (5.5)$$

where \mathcal{H}_{τ} is the Hamilton function of the system being in state τ and $Q(N, V, T)$ is the partition function defined by Eq. (3.6). Using this distribution of the p_{τ} , which is commonly referred to as Boltzmann distribution, we can rewrite the ensemble average for a macroscopic quantity A of the system as

$$\langle A \rangle = \frac{1}{Q} \sum_{\tau} A_{\tau} e^{-\beta \mathcal{H}_{\tau}}. \quad (5.6)$$

For instance, the internal energy U , i.e., the expectation value of the Hamilton function, can be obtained as

$$U = \langle \mathcal{H} \rangle = \frac{1}{Q(N, V, T)} \sum_{\tau} \mathcal{H}_{\tau} e^{-\beta \mathcal{H}_{\tau}}. \quad (5.7)$$

MC simulations allow us to steer a model system through a variety of states in such a way that the probability that the system is in state τ is equal to p_{τ} . This is achieved by choosing the rules for changing from one state to another so that the equilibrium solution to the master equation is precisely the Boltzmann distribution given by Eq. (5.5).

The idea of MC simulations is that only relatively few, representative states but not all possible states have to be sampled to gather good estimates of physical quantities of the system. Due to the limited number of states in this simulating procedure, the results are of course subject to statistical noise, which is one of the main disadvantages of this method. Taking derivatives of functions affected by statistical fluctuations leads to significant errors, so that the calculation of expectation values of, e.g., derivatives of $Q(N, V, T)$ as discussed in Sec. 3.2 is problematic. Therefore, it is highly recommendable to calculate as many quantities as possible directly via expectation values.

For instance, the pressure P can be obtained via

$$P = \rho k_B T - \frac{\langle W \rangle}{3V}, \quad (5.8)$$

where the virial W is defined as

$$W = \sum_{i < j} r_{ij} \left. \frac{\partial \phi(r)}{\partial r} \right|_{r=r_{ij}}. \quad (5.9)$$

Further, the bulk modulus B , which measures the resistance of the system against uniform compression, is given by (cf. Eq. 3.11)

$$B = \kappa^{-1} = -V \left(\frac{\partial P}{\partial V} \right). \quad (5.10)$$

In [82, 83], it was shown that B can be calculated directly in simulations via

$$B = \frac{2P + \rho kT}{3} + \langle \Theta \rangle - \frac{N}{\rho kT} \langle \delta(\Pi)^2 \rangle. \quad (5.11)$$

$$\Pi = \rho kT - \frac{W}{3V} \quad (5.12)$$

is the pressure function, while the pressure P is the canonical average of Π (cf. Eq. 5.8)

$$P = \langle \Pi \rangle. \quad (5.13)$$

The pressure fluctuations are given by

$$\delta(\Pi)^2 = \langle \Pi^2 \rangle - \langle \Pi \rangle^2. \quad (5.14)$$

Further, in the case of pairwise additive potentials the function Θ is given by

$$\Theta = \frac{1}{9V} \sum_{i < j} r_{ij}^2 \frac{\partial^2 \phi_{ij}}{\partial r_{ij}^2}. \quad (5.15)$$

5.1.3 Importance sampling

As already explained before, the aim of MC simulations is the calculation of the ensemble average $\langle A \rangle$ of some observable quantity A given by Eq. (5.3). The ideal route to determine such an expectation value is to average the weighted quantity of interest over *all* states τ of the system. In reality, the “true” average has to be replaced by the average over a *finite* sample, introducing necessarily some statistical inaccuracies in the calculation.

While a naive approach would be to choose states at random with uniform probability and then multiply the contributions A_τ to $\langle A \rangle$ by p_τ , the idea of importance sampling is to right away

select a subset of states according to their probability p_τ . Then, the given system will spend most of the simulation time in a representative number of states and the relative frequency with which a configuration is chosen corresponds to the amount of time a real system would spend there, limiting the evaluation of A to those states that make important contributions to it.

Supposing that the system has visited M such states $\{\tau_1, \dots, \tau_M\}$ during the course of the simulation, the estimator A_M of quantity A is then simply given by the arithmetic mean of the values of A_{τ_i} in states τ_i (cf. Eq. 3.3):

$$A_M = \frac{1}{M} \sum_{i=1}^M A_{\tau_i}. \quad (5.16)$$

with

$$\lim_{M \rightarrow \infty} A_M = \langle A \rangle. \quad (5.17)$$

Therefore, it is decisive to find an algorithm that selects states according to the probability distribution p_τ . This can be achieved by using a Markov chain [55, 79, 80].

5.1.4 Markov chains

A naive way to generate states according to the Boltzmann distribution (5.5) would be to choose states at random and accept or reject them with a probability $\exp(-\beta\mathcal{H}_\tau)$. Since nearly all configurations would be rejected due to their acceptance probabilities being exponentially small, this is a very slow algorithm. Instead, a time-homogeneous Markov chain [84–86] is commonly used, which consists of Markov transitions generating a new state ν of the system from a given system state τ by a random walk. The probability of generating the state ν from a given τ is called transition probability $P(\tau \rightarrow \nu)$. In the case of a time-homogeneous Markov chain, all transition probabilities have to satisfy the following three criteria:

- They do not vary with time.
- They only depend on the properties of the states τ and ν and not on any other states the system has visited in the past.
- They satisfy the sum rule

$$\sum_{\nu} P(\tau \rightarrow \nu) = 1, \quad (5.18)$$

since the system has to end up in *some* state ν .

Note that the probability that the system will remain in its current state, i.e., $P(\tau \rightarrow \tau)$, does not need to be zero.

MC simulations make repeated use of Markov transitions to generate a chain of states, i.e., a Markov chain. Starting from an arbitrary state of the system, these transitions are chosen such that when the Markov chain is sufficiently long it will come to equilibrium and will then produce

a sequence of states which appear with the probabilities given by the Boltzmann distribution. To achieve this, the Markov transitions have to fulfil two further conditions, i.e., ergodicity and detailed balance.

5.1.5 Ergodicity

The requirement that the Markov chain has to be able to reach any state of the system from any other state in a finite number of steps is called ergodicity. Let ν be a state with some non-zero probability in the Boltzmann distribution. If this state were inaccessible from another state τ no matter how long the Markov chain is continued, then the probability of finding state ν in the simulation will be equal to zero, and not p_ν , as required. Consequently, the sampled states would follow a different distribution function. The condition of ergodicity allows for some of the direct transition probabilities to be equal to zero, as long as there is always at least one compound path of non-zero transition probabilities between any arbitrary states τ and ν .

5.1.6 Detailed balance

The condition of detailed balance is the second condition imposed on the Markov transitions which ensures that we sample the Boltzmann distribution once the systems has reached equilibrium.

Equilibrium implies that the rate at which the system makes transitions out of a given state τ must be equal to the number of transitions into that state [cf. Eqs. (5.1) and (5.4)]

$$\sum_{\nu} p_{\tau} P(\tau \rightarrow \nu) = \sum_{\nu} p_{\nu} P(\nu \rightarrow \tau). \quad (5.19)$$

Using Eq. (5.18), this relation can be simplified to

$$p_{\tau} = \sum_{\nu} p_{\nu} P(\nu \rightarrow \tau). \quad (5.20)$$

Commonly, an even stronger criterion, called detailed balance, is imposed on the transition probabilities

$$p_{\tau} P(\tau \rightarrow \nu) = p_{\nu} P(\nu \rightarrow \tau), \quad (5.21)$$

In other words, the system should switch from state τ to ν just as often as from ν to τ . If the chosen Markov chain fulfils Eq. (5.21), then the probability distribution of the states tends to the Boltzmann distribution p_{τ} and Eq. (5.21) becomes

$$\frac{P(\tau \rightarrow \nu)}{P(\nu \rightarrow \tau)} = \frac{p_{\nu}}{p_{\tau}} = e^{-\beta(\mathcal{H}_{\nu} - \mathcal{H}_{\tau})}. \quad (5.22)$$

This relation along with Eq. (5.18) are the constraints imposed on the transition probabilities $P(\tau \rightarrow \nu)$. If they are satisfied, and the condition of ergodicity is met, then the equilibrium distribution of states sampled by the Markov chain will be the Boltzmann distribution.

5.1.7 Acceptance probabilities

As long as Eqs. (5.18) and (5.21) are fulfilled, there are several possibilities to choose the transition probabilities $P(\tau \rightarrow \nu)$. Since contriving an algorithm for the Markov chain to directly generate the correct transition ratios would be quite intricate, the following trick is used: at first, consider the probability that the system stays in its current state. If $\nu = \tau$ in Eq. (5.21), the equation simplifies to the tautology $1 = 1$, i.e., detailed balance is always satisfied for every $P(\tau \rightarrow \tau)$, no matter what its actual value. Furthermore, $P(\tau \rightarrow \nu)$ and $P(\nu \rightarrow \tau)$ can be adjusted arbitrarily without violating detailed balance as long as the original ratio $\frac{P(\tau \rightarrow \nu)}{P(\nu \rightarrow \tau)}$ is preserved. As only this ratio but not the absolute values are needed during the course of a simulation, the transition probabilities do not even have to be normalised, allowing for violation of the sum rule (5.18).

Next, the transition probabilities are split into two factors

$$P(\tau \rightarrow \nu) = s(\tau \rightarrow \nu) a(\tau \rightarrow \nu), \quad (5.23)$$

where $s(\tau \rightarrow \nu)$ denotes the selection probability, i.e., the probability that the algorithm generates a new state ν given an initial state τ , and $a(\tau \rightarrow \nu)$ is the acceptance probability, which indicates the probability with which the change from τ to ν will be accepted as a new state. In case of rejection, the system stays in state τ .

Using Eq. (5.23), relation (5.21) now becomes

$$\frac{P(\tau \rightarrow \nu)}{P(\nu \rightarrow \tau)} = \frac{s(\tau \rightarrow \nu) a(\tau \rightarrow \nu)}{s(\nu \rightarrow \tau) a(\nu \rightarrow \tau)}. \quad (5.24)$$

Since Eq. (5.24) only fixes the ratio $\frac{a(\tau \rightarrow \nu)}{a(\nu \rightarrow \tau)}$, it allows to simply set the larger of the two acceptance probabilities to 1 while the other one takes the required value in order to satisfy the condition of detailed balance. This guarantees that when switching between states τ and ν , moves will always be accepted for at least one direction, resulting in a so-called asymmetric rule¹.

5.1.8 Metropolis Monte Carlo

In 1953, Metropolis *et al.* proposed an algorithm [87] fulfilling all the requirements discussed in the preceding subsections. While the selection probabilities $s(\tau \rightarrow \nu)$ for all those states ν that can be reached from state τ are chosen to be equal, the selection probabilities for all other states are set to zero.

This is done in the following way. At first, the N particles of the system are placed within a box of volume V . This starting configuration can be arbitrary or some regular arrangement. Repeatedly, a particle i is chosen at random and moved according to

$$\mathbf{r}_i \rightarrow \mathbf{r}_i + \Delta \boldsymbol{\xi}_i, \quad (5.25)$$

¹Symmetric rules, where $a(\tau \rightarrow \nu) = a(\nu \rightarrow \tau)$ and $a(\tau \rightarrow \nu) \neq 1$, are often used in the simulation of spin systems.

Δ is the maximum allowed displacement. It is arbitrary, has a fixed value and is limited by the constraint that $\Delta \leq L/2$, where L is the length of the (cubic) simulation box. It is chosen to produce an acceptance ratio of 30 to 50 % [55]. Further, the ξ_i are some vectors of uniformly distributed random numbers in the interval $[-1, 1]$. After such a move, the particle is with equal probability expected to be anywhere in a cube of side 2Δ centred around its original position.

As $s(\tau \rightarrow \nu) = s(\nu \rightarrow \tau)$, Eqs. (5.22) and (5.24) simplify to

$$\frac{P(\tau \rightarrow \nu)}{P(\nu \rightarrow \tau)} = \frac{s(\tau \rightarrow \nu) a(\tau \rightarrow \nu)}{s(\nu \rightarrow \tau) a(\nu \rightarrow \tau)} = \frac{a(\tau \rightarrow \nu)}{a(\nu \rightarrow \tau)} = e^{-\beta(\mathcal{H}_\nu - \mathcal{H}_\tau)}. \quad (5.26)$$

Therefore, to choose the acceptance ratios $a(\tau \rightarrow \nu)$, we need to calculate the change in energy $\Delta\mathcal{H} = \mathcal{H}_\nu - \mathcal{H}_\tau$ of the system due to the displacement of the particle. If the move leads to a decrease in the energy, i.e., $\Delta\mathcal{H} < 0$, the trial move is accepted and the particle left at its new position. On the other hand, if $\Delta\mathcal{H} > 0$, the trial move is only accepted with a probability of $\exp(-\beta\Delta\mathcal{H})$, which is achieved by generating another uniformly distributed random number $\hat{\xi}$ between 0 and 1. Then, if $\hat{\xi} > \exp(-\beta\Delta\mathcal{H})$ the particle remains at its old position, while it is moved to the new coordinates if $\hat{\xi} < \exp(-\beta\Delta\mathcal{H})$ (see Fig. 5.1). No matter whether the new configuration has been accepted or not (i.e., the system is still in the old configuration), it is considered to be in a new configuration for the purpose of taking averages according to Eq. (5.16). This procedure is repeated with another randomly chosen particle, and so forth, thereby generating a random walk through phase space.

To summarise, the algorithm chooses the acceptance ratios to be

$$a(\tau \rightarrow \nu) = \min \left[1, e^{-\beta(\mathcal{H}_\nu - \mathcal{H}_\tau)} \right]. \quad (5.27)$$

Since Eq. (5.27) satisfies the condition of detailed balance (5.24), the Metropolis algorithm generates states according to the Boltzmann distribution. Due to its efficiency, it has become *the* algorithm of choice in the majority of MC studies of simple statistical models.

5.2 Monte Carlo simulations in the isobaric-isothermal ensemble

Simulations in the isobaric-isothermal (NPT) ensemble [88, 89] are often more convenient than in the NVT ensemble since they allow to mimic exactly the conditions given in the laboratory. The basic concepts of this ensemble were already described in Sec. 3.3.

In NPT simulations, the volume V adjusts in such a way as to keep the pressure fixed. Thus, apart from the standard trial moves of the particles, described in Sec. 5.1.8, we additionally have to carry out trial moves in V that have to obey detailed balance.

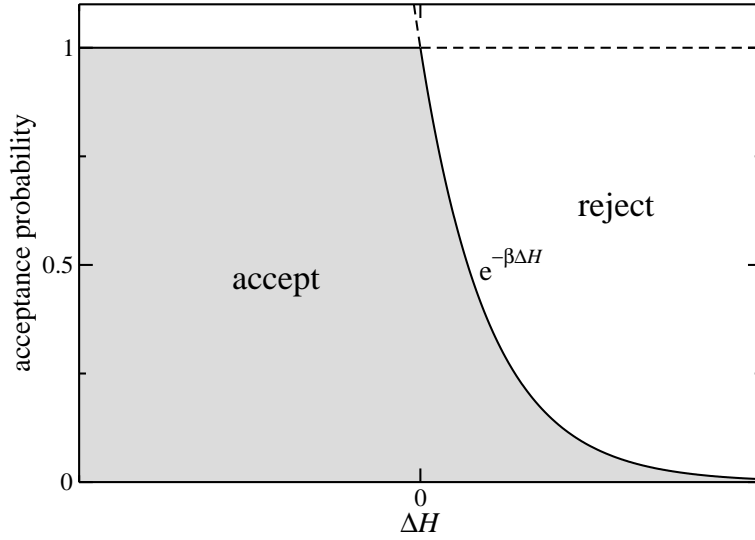


Figure 5.1: Acceptance probabilities in the Metropolis MC simulation. Moves with $\Delta\mathcal{H} < 0$ are always accepted, while for $\Delta\mathcal{H} > 0$, moves are accepted with a probability of $\exp(-\beta\Delta\mathcal{H})$.

Let us assume a trial move in volume, i.e., a change of volume

$$V_\tau \rightarrow V_\nu = V_\tau + \Delta V, \quad (5.28)$$

where ΔV is a uniformly distributed random number in the interval $[-\Delta V_{\max}, +\Delta V_{\max}]$. Here, V_{\max} depends on the state point under consideration and is chosen to produce an acceptance ratio of 30 to 50 percent [55, 89]. Note that such a move also re-scales all particle positions. Then, the Metropolis rule for acceptance of this attempted volume change is given by

$$a(\tau \rightarrow \nu) = \min \left[1, e^{-\beta(\mathcal{H}_\nu - \mathcal{H}_\tau) + P(V_\nu - V_\tau) - Nk_B T \log(V_\nu/V_\tau)} \right]. \quad (5.29)$$

A more convenient sampling might be achieved by conducting trial moves in the logarithm of the volume instead of the volume itself [90]. Then, the acceptance rule changes slightly to

$$a(\tau \rightarrow \nu) = \min \left[1, e^{-\beta(\mathcal{H}_\nu - \mathcal{H}_\tau) + P(V_\nu - V_\tau) - (N+1)k_B T \log(V_\nu/V_\tau)} \right]. \quad (5.30)$$

For most potentials, volume moves are computationally very expensive to analyse [79]. Since all particle positions have to be rescaled after such a move, all interaction energies have to be recomputed, rendering one volume move as expensive as N positional particle moves. Therefore, it is common practice to alternate randomly between the two types of moves, such that volume moves are attempted with a probability of $1/N$, while standard particle moves are carried out with a probability of $1 - 1/N$.

5.3 Tricks of the trade

5.3.1 Boundary conditions, minimum image convention and tail corrections

While MC simulations aim at providing information about the thermodynamic and structural properties of a *macroscopic* sample of the system of interest, only rather small systems can be handled in reality by present-day computers. Thus, most simulations only probe the behaviour of systems that contain several hundreds to few thousands of particles, which is by many orders of magnitude smaller than realistic systems. For such small systems the choice of boundary conditions does have a significant effect on the properties of the system. For instance, in a three-dimensional N -particle system, the fraction of particles located at the surface is proportional to $N^{-1/3}$. Especially in simulations of small systems, this fact makes it decisive to choose boundary conditions in a way that the surface effects are minimised.

In order to correctly simulate bulk phases, we require boundary conditions which mimic the presence of an infinite bulk surrounding the simulation box. One strategy is to impose periodic boundary conditions. Here, the simulation box is treated as the primitive cell of an infinite periodic lattice of identical cells. There are no walls at the boundary of the central box and therefore, no surface particles. As we move a particle in the original box, all its images in the cells of this infinite lattice will move in a coherent way. Therefore, when a particle leaves the box, one of its images is going to enter at the opposite side of the box. As a consequence of the infinite array of surrounding cells, particle i in the central box interacts not only with all other particles in the same cell, but also with all the other particles, including its own periodic image, in all other cells (cf. Fig. 5.2). When calculating the potential energy, we would thus need to sum up an infinite amount of terms. However, MC simulations often only deal with short-range interactions, where the pair potential decays faster than r^{-3} for $r \rightarrow \infty$. Therefore, the potential energy of a given particle i is dominated by interactions with neighbouring particles that are closer than some cutoff distance r_c . In particular, if $r_c \leq L/2$ only interactions of a given particle with the nearest periodic image of (at most) all other particles j have to be considered. This so-called minimum image convention is schematised in Fig. 5.3.

If the intermolecular potential is not rigorously zero for $r > r_c$, truncation of $\phi(r)$ at r_c will result in a systematic bias in the calculation of thermodynamic properties. This bias can be corrected to some extent by adding so-called tail corrections. For instance, for the expression for the potential energy, we find

$$\Phi \simeq \sum_{i < j} \phi_c(r_{ij}) + \frac{N\rho}{2} \int_{r_c}^{\infty} dr 4\pi r^2 \phi(r), \quad (5.31)$$

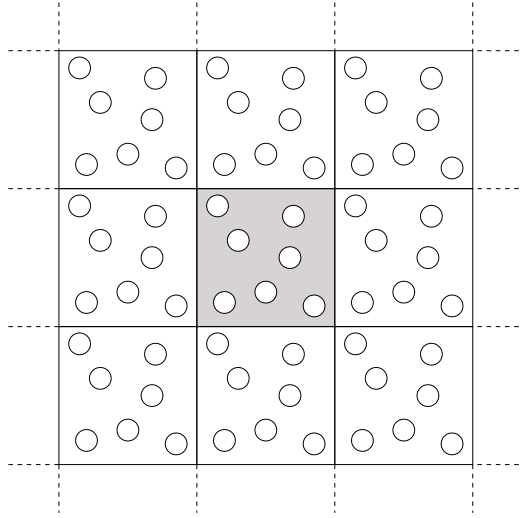


Figure 5.2: Schematic representation of periodic boundary conditions. The system of interest (grey) is surrounded by an infinite amount of identical copies of itself.

where $\phi_c(r)$ denotes the truncated potential energy function

$$\phi_c(r) = \begin{cases} \phi(r) & r \leq r_c \\ 0 & r > r_c \end{cases}, \quad (5.32)$$

with the spherical cutoff r_c . The second term in Eq. 5.31 follows from the assumption that

$$g(r) = 1 \quad \text{for } r > r_c, \quad (5.33)$$

i.e., for $r \geq r_c$, the tail correction replaces the discrete particle system by an infinite continuum.

In a similar way, a correction term is added to the expression for the virial

$$W \simeq \sum_{i < j} r_{ij} \left. \frac{\partial \phi_c(r)}{\partial r} \right|_{r=r_{ij}} + \frac{N\rho}{2} \int_{r_c}^{\infty} dr 4\pi\rho r^2 r \frac{\partial \phi(r)}{\partial r}. \quad (5.34)$$

5.3.2 Cell lists

To speed up simulations of systems with a large number of particles, Quentrec and Brot [91] developed the so-called cell list method. Assuming a cubic simulation cell of length L , the box is divided into $M \times M \times M$ sub-cells with size $r_m = L/M > r_c$. Further, it is assumed that each particle in a given cell only interacts with particles in the same or in the surrounding cells. A two dimensional visualisation of this idea is shown in Fig. 5.4. Using this method, we only need to consider $27NN_m$ pairs of particles in the calculation of Φ instead of $\frac{1}{2}N(N-1)$ (cf. Sec. 5.1). Here, $N_m = N/M^3$ is the average number of particles per cell.

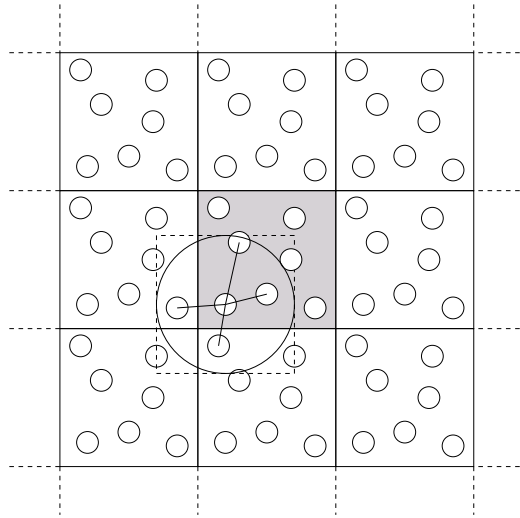


Figure 5.3: Schematic representation of the minimum image convention. The dashed box around one of the particles contains the same number and relative configuration of particles as the central one. The dashed circle represents a potential cutoff of $L/2$, i.e., only those particles lying within the circle interact directly with the particle in the centre.

To realise this method, linked lists can be used [79]. At the beginning of the simulation, all particles have to be assigned to their respective cells, which is a rapid process. In an array called “head-of-chain”, the identification number of one particle of each cell is stored. This number is then used to address the element of a linked list array which contains the identification number of the next particle in the cell. In turn, the array element for this particle is the index of the next one, and so forth. Using this method, one can address all the particles in a cell until the element ‘zero’ is reached, which signals the end of the list. Then, one has to move on to the head of chain of the next cell. After each accepted MC move, there is the possibility that the moved particle has left its cell. Instead of the time-consuming creation of a new list after every accepted move, the existing linked list can instead be updated at the cost of some extra book-keeping.

5.4 Lattice Monte Carlo simulations

In simulations of systems that freeze into singly occupied crystals ~ 500 particles often provide sufficiently reliable results. However, the situation is completely different in systems where particles agglomerate to clusters at the lattice sites of perfect crystals. This behaviour is observed for the PSM and also expected for the GEM- n introduced in 2.5. In this case, to guarantee a sufficiently large number of *clusters*, we need considerably more *particles* in our simulation volume, rendering the use of conventional MC techniques computationally rather expensive. In particular it is the determination of the distance between particles and the evaluation of the potential energy of a given particle configuration which is the most time consuming part. Therefore, a significant speed-up of the MC simulations is needed to make them feasible for systems that show clustering

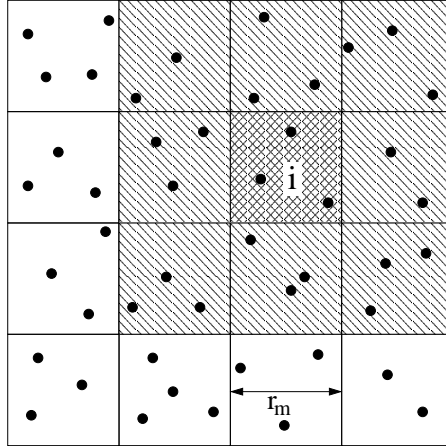


Figure 5.4: Schematic representation of the cell list method in two dimensions: the simulation box is divided into $M \times M$ cells of length r_m . A particle in cell i interacts only with particles of its cell (cross hatched) or of the neighbouring cells (hatched).

transitions.

5.4.1 Canonical Lattice Monte Carlo simulations

Motivated by previous work [49, 92, 93], we use Lattice Monte Carlo (LMC) simulations, a technique originally proposed by Panagiotopoulos [94]. The central idea of LMC is to transform the continuous system into a lattice model by restricting the possible particle positions within the simulation box to a finite number of discrete coordinates, as illustrated in Fig. 5.5.

Consider a particle with a characteristic diameter σ . We construct a series of lattice models, where we restrict allowed particle positions to the sites of a simple cubic grid of some characteristic spacing. The lattice discretisation parameter ζ specifies the number of grid sites per particle diameter σ and measures how closely the lattice model mimics the continuum behaviour. It can easily be seen from the upper panels of Fig. 5.5 that choosing a small value of ζ will have a strong effect on the structural as well as the thermodynamic properties of the system. However, artefacts due to the lattice discretisation are bound to decrease as ζ is increased.

For our implementation of the LMC method, we use a cubic box of length L (in units of σ). The box is discretised via a grid of 2^b (i.e., b bits) possible positions in each dimension. Thus, the discretisation parameter takes the form

$$\zeta = \frac{2^b}{L}. \quad (5.35)$$

It should be noted that the product $L \times \zeta$ has to be an integer (even though L and ζ can take any real value individually) so that we can use periodic boundary conditions for the LMC simulations.

Due to the discretisation there is now only a finite number of possible distances between two particles. Assuming that the interaction potential between any two sites is translationally

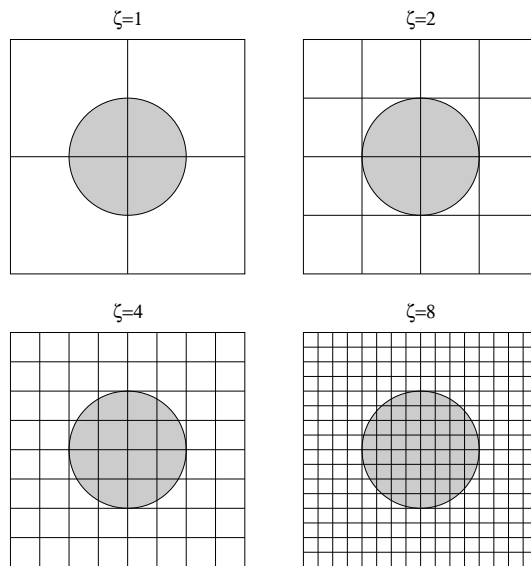


Figure 5.5: Schematic representation of the refinement process of the lattice model with increasing lattice discretisation parameter $\zeta = 1, 2, 4$ and 8 as described in the text. For clarity, a two dimensional system is shown, but the generalisation to three dimensions is straightforward. Note that the number of grid points per particle (grey sphere) grows as ζ increases.

invariant, we can write the potential energy as

$$\Phi(\mathbf{r}^N) = \sum_{i < j} \phi(r_{ij}), \quad (5.36)$$

where r_{ij} is the modulus of the vector connecting sites i and j

$$r_{ij} = \sqrt{(x_j - x_i)^2 + (y_j - y_i)^2 + (z_j - z_i)^2}. \quad (5.37)$$

The particle positions x_i , y_i and z_i , etc., are integers between 0 and $2^b - 1$. Since there is only a reasonably small, finite number of distances r_{ij} , it is obvious from Eq. (5.36) that we need to calculate interactions $\phi(r_{ij})$ for all these possible distances only *once*, at the beginning of the simulation, storing them as function of r^2 .

Depending on the functional form of the potential studied, the LMC method allows for a speed-up by a factor of ~ 20 compared to the conventional MC scheme [49, 92, 93]. This considerable reduction in computational time is due to the elimination of the time consuming evaluations of the potential for every pair of interacting particles. If—as in our case—we use a power of 2 as the number of grid sites per dimension, a further speed-up can be achieved since periodic boundary conditions reduce to a bit operation. As soon as a particle leaves the box, its coordinates will need more than b bits to be represented as a binary number. Truncating this to the lowest b bits, periodic boundary conditions are automatically fulfilled (see Fig. 5.6). Since computers use the binary representation of numbers, bit operations are extremely fast.

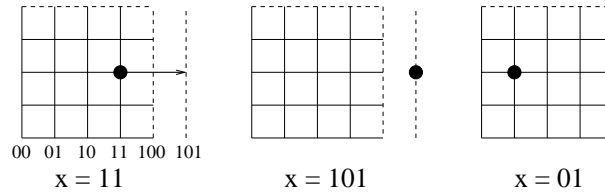


Figure 5.6: Schematic representation of periodic boundary conditions within the LMC simulations using a discretisation of 2 bits per dimension. Before the move (left panel), the particle has the x -coordinate $x=11$ in the binary representation. During the move (central panel), the particle leaves the simulation box. To store the new coordinates ($x=101$) on the computer, 3 bits are needed. Truncating the coordinates to 2 bits leads to the correct new coordinates within the box (right panel).

5.4.2 The radial distribution function in *NVT*-LMC

In liquid state theory [54], the RDF is defined by Eq. (4.1). In conventional MC simulations, $g(r)$ is obtained from a histogram of all observed particle distances, which, at the end of the simulation, has to be scaled according to the pre-factors in Eq. (4.1) and accounting for the volumes of the spherical shells in which we measured the histogram. The bin size Δr of this histogram (i.e., the thickness of the spherical shells) has to be chosen small enough to obtain $g(r)$ with sufficient resolution, but large enough to minimise the statistical error per bin. By measuring a histogram, the RDF is averaged per bin which leads to a significant statistical error at short distances since the small volumes of the spherical shells over which we average allow only for few events in this regime.

In LMC simulations, this problem is even more pronounced due to the fact that short distances are only represented by a few grid points and that the number of available grid points representing a certain distance interval is not exactly proportional to the volume of a corresponding spherical shell. Fortunately, one can measure the RDF in a different, more efficient and accurate way by not calculating a histogram but recording, for every possible interparticle separation on the grid, how often that distance was observed in the simulation and normalising by the number of times this separation can occur [92].

The advantage of this approach is that the RDF measured in LMC contains valuable qualitative information on the state of the system compared to the RDFs measured in conventional MC. In the fluid phase, particles can—in principle—occupy any distance relative to each other. During the course of the simulation, most possible distances on the grid will be realised, giving the impression that the RDF is a continuous curve. If, on the other hand, the system is in the solid phase and the amplitude of the particles' vibrations around their (physical) lattice sites is comparable to the spacing of the computational grid, only a small set of specific interparticle distances will be observed. In this case, the RDF will show pronounced peaks at the corresponding distances, so that it is easy to tell when crystallisation has occurred (see Fig. 5.7). By averaging, the RDF can be smoothed and reduced to the form usually obtained by conventional MC [92].

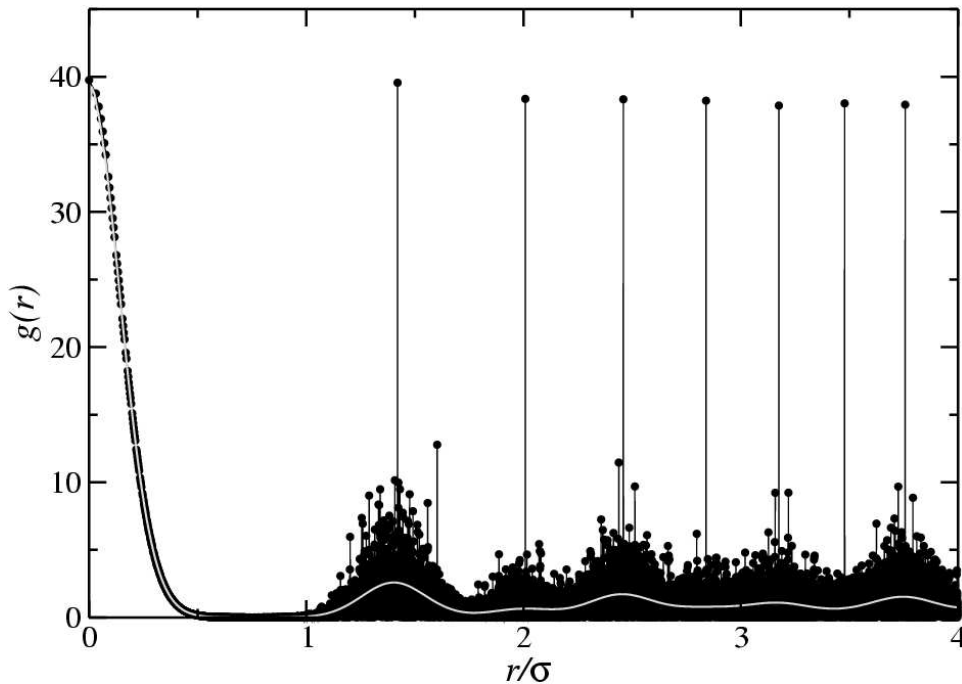


Figure 5.7: Simulation results of the RDF of a typical cluster solid as obtained by conventional MC (grey) and LMC (black). While the clustering phenomenon is reflected in the peak at $r = 0$, the crystal structure of the system can be seen from the pronounced peaks in the LMC data at certain distances.

5.4.3 Discretisation errors

By discretising the simulation cell as outlined in Sec. 5.4.1, we introduce two new kinds of errors to the determination of structural and thermodynamic properties of the system [92,93]. They are additional to the statistical error which is inherent to all MC simulations. The first error is a structural defect. It will be non-negligible in case the underlying grid is not sufficiently fine, as the use of discretised coordinates introduces anisotropies. However, the Shannon-Nyquist sampling theorem [95] tells us that discrete samples are a complete representation of the original property if we choose the lattice discretisation parameter $\zeta = 2^b/L$ sufficiently large so that all relevant wave-numbers of the structure factor of the system (which is proportional to the Fourier transform of the RDF) are captured. If this condition is fulfilled, the sampling of the structure of the system (i.e., the measurement of the RDF) is fine enough to contain all information [92].

The second error concerns the calculation of averages. Due to the underlying grid particle positions are no longer sampled from the continuous domain $[0, L) \times [0, L) \times [0, L)$ but rather from a set of discrete values $\{x_i, y_j, z_k\}$, with $i, j, k = 0, \dots, 2^b - 1$. Let $\delta = 1/\zeta$ be the mesh-size of the grid. Then, all possible positions in the volume element $[x_i - \delta/2, x_i + \delta/2) \times [y_j - \delta/2, y_j + \delta/2) \times [z_k - \delta/2, z_k + \delta/2)$ are mapped to the single point $\{x_i, y_j, z_k\}$. Taking averages of a property A , only the function values at these points are used. Therefore, in LMC simulations integrals are reduced to Riemann sums over all grid sites (cf. Fig. 5.8). Thus, we can conclude

that this discretisation error scales the same way as Riemann sums scale. It has to be stressed that even when performing an LMC simulation of *infinite* length, the final result would still be affected by this systematic error since the discretisation of the grid remains fixed throughout the simulation [49, 92].

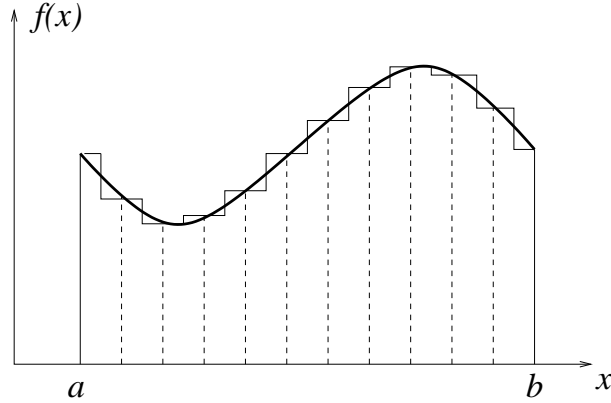


Figure 5.8: One-dimensional representation of the integration of some function f in the LMC scheme. Since only discrete positions (dashed lines) are allowed in the interval $[a, b)$, the MC summation converges towards the Riemann sum rather than the true integral.

5.4.4 Comparison conventional MC - LMC

First, we want to study the influence of the lattice discretisation parameter ζ , which is determined by the number of bits used per Cartesian dimension, on the structural properties in a qualitative way. Fig. 5.9 shows three simulation snapshots of a typical cluster solid (cf. Sec. 7.3). The upper left panel shows the system at a resolution of $b = 5$ bits (corresponding to $\zeta \sim 4$). In each direction, there are only 32 positions available, a limitation that strongly influences the structure of the system. Another snapshot of the same system is shown for a grid at $b = 6$ (corresponding to $\zeta \sim 8$, upper right panel). Now, the structure is already reproduced in a more appropriate way, though the effects of the grid are still visible. At $b = 8$ (corresponding to $\zeta \sim 32$, lower panel), the discretisation is sufficiently fine to obtain an acceptable resolution of the positions and reliable results for the structure.

In Fig. 5.10 we investigate the effects of LMC on the structure in a more quantitative way by calculating the RDF for the system presented in the snapshots in Fig. 5.9. Qualitative agreement with the data from conventional MC simulations is already achieved for a discretisation of 6 bits per direction, while at 8 bits, all the characteristic features of the RDF are fully captured. Since the data presented are for a GEM-4 system (cf. Sec. 2.5) frozen into an fcc crystal, the raw RDF measured in the LMC simulation exhibits sharp peaks at certain distances (cf. Fig. 5.7), while the data presented in Fig. 5.10 have already been smoothed. As can be seen in Fig. 5.11, in the fluid state the data for the RDF are much closer to conventional simulation data.

We conclude the discussion of structural properties by showing the RDF of the centres of mass

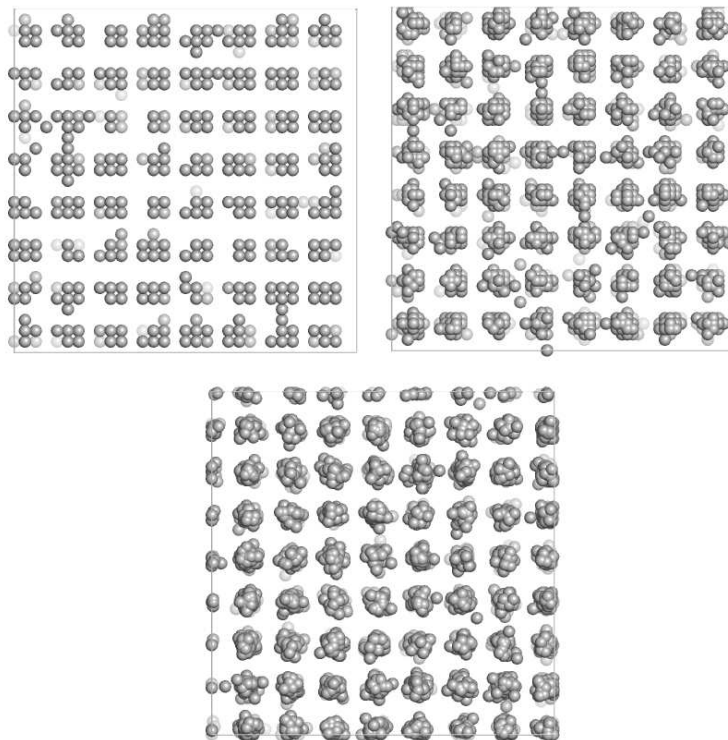


Figure 5.9: Snapshots from LMC simulations of a typical cluster solid (GEM-4, $\rho\sigma^3 = 9$, $k_{\text{B}}T/\varepsilon = 1$, fcc) for discretisations of $b = 5$ (upper left), 6 (upper right), and 8 (lower panel). Depth cueing is used to indicate the distribution of the particles in the direction perpendicular to the plane of the paper.

of the clusters (instead of the individual particles) in Fig. 5.12. It can be seen that already at very low values of b , we obtain qualitatively correct results. The curves obtained with $b = 7$, 8, and 9 coincide and reproduce the conventional-MC data perfectly.

Even though the results for the structural properties might suffer from small (fluid) to considerable (cluster solid) fluctuations, the situation is different for the *thermodynamic* properties, such as the pressure or the internal energy. They are calculated as configurational averages and hence are less affected by deficiencies in the details of the structural properties. From our results for different levels of discretisation and by comparing them to the results of the conventional MC approach, we conclude that 8 bits are sufficient to guarantee the required numerical accuracy in the structural and the thermodynamic properties. We want to stress that higher levels of discretisation go along with a considerably larger memory requirements, since the size of the array that stores all the possible interactions scales as $2^{2(b-1)}$ (cf. Sec. 5.4.1). Moreover, for these levels of discretisation, considerably increased array access times have to be taken into account once the lookup table exceeds the cache size.

Especially in the study of systems that show clustering behaviour, the LMC technique [augmented by the cell list method (cf. Sec. 5.3.2)] result in an average speed-up of ~ 15 , which brings extensive quantitative MC studies of these systems within reach.

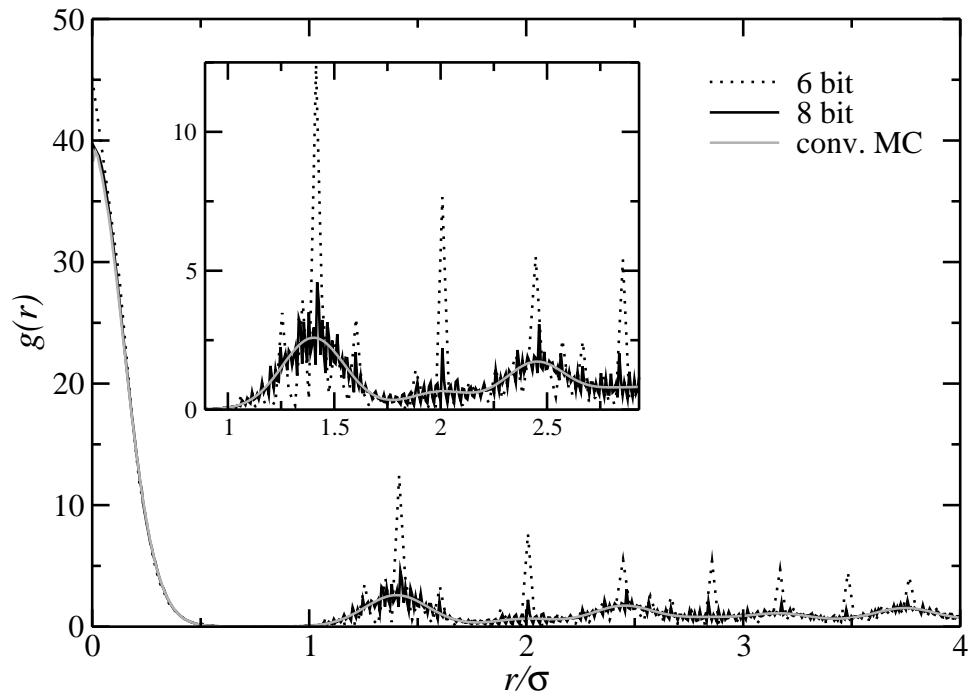


Figure 5.10: The RDF for a typical cluster solid (GEM-4, $\rho\sigma^3 = 9$, $k_B T/\varepsilon = 1$, fcc) as obtained by LMC simulations at $b = 6$ and 8 and compared to conventional MC simulation results.

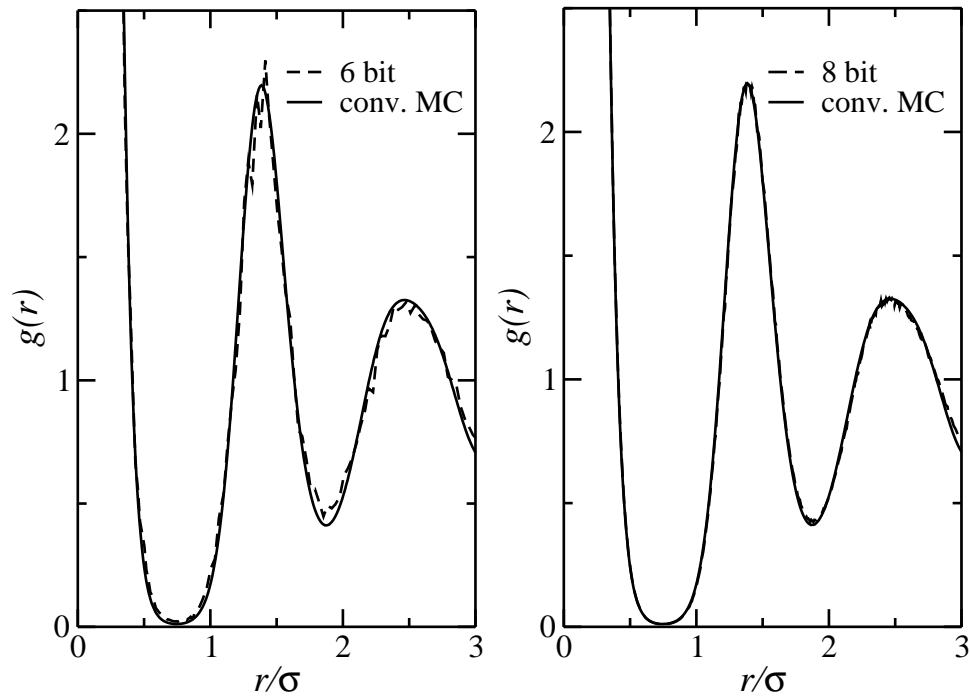


Figure 5.11: The RDF of a supercooled liquid (GEM-4, $\rho\sigma^3 = 9$, $k_B T/\varepsilon = 1$) as obtained by LMC simulations at $b = 6$ (left) and $b = 8$ (right) in comparison with conventional MC simulation results.

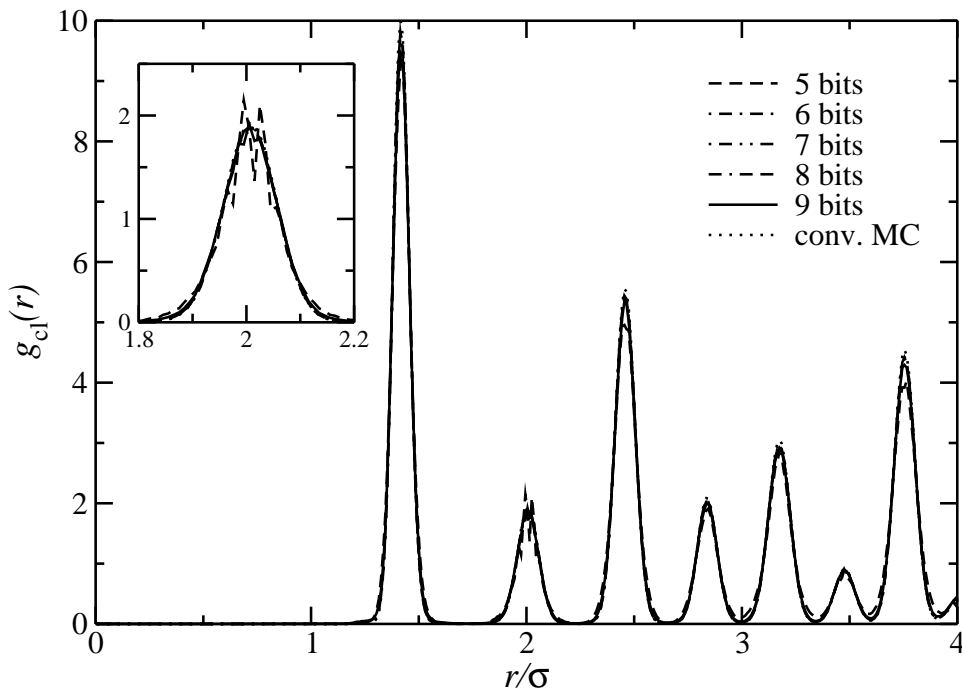


Figure 5.12: The RDF of the centres of mass of a typical cluster solid (GEM-4, $\rho\sigma^3 = 9$, $\beta\varepsilon = 1$, fcc) as obtained by LMC simulations at different levels of discretisation and compared to results of conventional MC simulations.

5.4.5 Isobaric-isothermal Lattice Monte Carlo simulations

Of course, the LMC technique is not limited to the canonical ensemble and can be generalised to the isobaric isothermal ensemble (cf. Sec. 3.3 and 5.2).

One possible implementation of LMC in the NPT ensemble could be based on discretised volume changes keeping the number of spatial grid points constant. Starting at volume V , the interaction array has to be computed and stored. Whenever the volume is modified during the simulation, the particles retain their position on the grid, but since the absolute grid spacing varies as $V^{1/3}$, all interparticle distances are rescaled. Thus, a new interaction array has to be determined, which will be stored for the case that the system visits this volume again. Since the volume normally fluctuates only slightly around its mean equilibrium value, only a small set of interaction arrays will be needed, keeping the memory requirement of the simulation at a reasonable level.

Another, computationally slightly more expensive implementation was suggested in [92]. While particle positions are discretised, volume moves are not. As before, each time we perform a volume change, ζ changes since we keep b fixed. At this point we have to recompute all interaction energies on the grid and store them in a second, provisional array. The outcome of the acceptance test of a volume move decides which interaction array will be kept. This approach only doubles the memory requirements to store all possible particle interactions. In terms of demand in CPU time,

this approach has proven reasonable. Note that the technique to measure the RDF discussed in Sec. 5.4.2 cannot be used for NPT -LMC since ζ is not fixed.

5.5 Free energies and phase equilibria in MC simulations

As already explained in Chap. 3, knowledge of the Helmholtz or Gibbs free energy comprises the knowledge of *all* thermodynamic properties of a system. In particular, if we know the free energy for a system, we can calculate its phase diagram. Unfortunately, it is not possible to measure free energies directly within simulations, since they are not averages of functions of the phase space coordinates. Rather, they are directly connected to the partition function Q of the system, and to determine this function we would need to count *all* states of the system [79].

Still, special techniques have been developed to make the free energies accessible also to MC simulations. In the following, we will present a few of them.

5.5.1 Widom or particle insertion method

In the canonical ensemble, the chemical potential μ is defined as [cf. Eq. (3.10)]

$$\mu = \left(\frac{\partial F}{\partial N} \right)_{V,T}. \quad (5.38)$$

With

$$F = -k_B T \log Q(N, V, T) \quad (5.39)$$

and $\mu \simeq F(N+1, V, T) - F(N, V, T)$ for large values of N , the chemical potential can be rewritten as

$$\mu = -k_B T \log (Q(N+1, V, T)/Q(N, V, T)). \quad (5.40)$$

Inserting Eq. (3.6), we find that

$$\mu = -k_B T \log \left(\frac{V}{\Lambda^3(N+1)} \right) - k_B T \log \left\{ \frac{\int d\mathbf{r}^{N+1} \exp[-\beta\Phi(\mathbf{r}^{N+1})]}{V \int d\mathbf{r}^N \exp[-\beta\Phi(\mathbf{r}^N)]} \right\}. \quad (5.41)$$

Here, the first term is the chemical potential of the ideal gas, μ^{id} , which can be calculated analytically. The second term is the excess part, μ^{ex} , and can be rewritten as

$$\mu^{\text{ex}} = -k_B T \log \langle \exp(-\beta\Delta\Phi) \rangle_N, \quad (5.42)$$

which now expresses the excess chemical potential as an ensemble average over an N -particle system that can easily be sampled. During a conventional NVT simulation, we periodically insert an additional particle at a uniformly distributed, random position within the simulation box and measure the difference in potential energy $\Delta\Phi$ caused by this process. Then, we compute

$\exp(-\beta\Delta\Phi)$ and average this quantity over all insertion positions and all configurations of the original N particles generated throughout the course of the simulation.

For the NPT ensemble, μ is defined by Eq. (3.27), which allows for an equivalent relation to be derived. Now, $\mu \simeq G(N+1, P, T) - G(N, P, T)$ for large N and therefore

$$\mu = k_{\text{B}}T \log(P\Lambda^3 / K_{\text{B}}T) - k_{\text{B}}T \log \frac{P}{(N+1)k_{\text{B}}T} \langle V \exp(-\beta\Delta\Phi) \rangle_{NPT}, \quad (5.43)$$

where the average is taken over the uniformly distributed random positions of a ghost particle and over all configurations of the original N particles and the volume. In contrast to Eq. (5.41), the first term corresponding to the ideal gas term is now defined at constant pressure rather than constant density.

Using the relation that at constant temperature

$$F = \mu N - PV, \quad (5.44)$$

we can then determine the free energy from simulations. Similarly, G can be determined via

$$G = \mu N. \quad (5.45)$$

Note that for systems that show cluster behaviour, special care has to be taken when using the last two formulae (cf. Sec. 7.2).

For systems where the pair potential ϕ diverges strongly at the origin the particle insertion method works well at moderate densities. In the case of bounded potentials the method also works for the solid phases since—in contrast to harshly repulsive potentials—overlaps of particles (which might occur upon the insertion) only cost a finite amount of energy.

5.5.2 Overlapping distribution method in the NVT ensemble

Of course, analogously to Eqs. (5.40) and (5.42), it is possible to express μ via

$$\begin{aligned} \mu &= -k_{\text{B}}T \log(Q_{N+1}/Q_N) \\ &= \mu^{\text{id}} + k_{\text{B}}T \log \langle \exp(+\beta\Delta\Phi) \rangle_{N+1}, \end{aligned} \quad (5.46)$$

where $\Delta\Phi$ now corresponds to the change in potential energy that stems from *removal* of one particle from the $(N+1)$ -particle system. Straightforward sampling of this equation, however, does not work. Significant contributions to the ensemble average in Eq. (5.46) correspond to configurations with very low Boltzmann weight, which is a measure of the probability of sampling this state during the course of the simulation. In other words, the important contributions to this average stem from configurations that are hardly ever visited [79].

Still, it is possible to measure the chemical potential by taking both particle insertions and

removals into account, a technique called overlapping distribution method (ODM) [96–98]. Consider two systems (labelled 0 and 1) at equal N , V and T and let all particles have the same mass. However, these systems interact via different pair potentials ϕ^0 and ϕ^1 and are characterised by the partition functions Q^0 and Q^1 . The difference in free energy between these two systems can be written in a similar way to Eq. (5.40)

$$\begin{aligned}\Delta F &= -k_{\text{B}}T \log(Q^1/Q^0) \\ &= -k_{\text{B}}T \log \left(\frac{\int d\mathbf{r}^N \exp[-\beta\Phi^1(\mathbf{r}^N)]}{\int d\mathbf{r}^N \exp[-\beta\Phi^0(\mathbf{r}^N)]} \right).\end{aligned}\quad (5.47)$$

Carrying out a standard NVT MC simulation for system 1, we can measure the potential energy difference $\Delta\Phi$ with respect to system 0 by also evaluating Φ^0 for the sampled configurations \mathbf{r}^N . Then, the probability density for this energy difference, $p^1(\Delta\Phi)$, is given by

$$p^1(\Delta\Phi) = \frac{1}{z_N^1} \int d\mathbf{r}^N \exp(-\beta\Phi^1) \delta(\Phi^1 - \Phi^0 - \Delta\Phi), \quad (5.48)$$

where z_N^1 is the configurational integral given by Eq. (3.13) and δ is the Dirac δ -function. This equation can then be simplified to

$$\begin{aligned}p^1(\Delta\Phi) &= \frac{1}{z_N^1} \int d\mathbf{r}^N \exp[-\beta(\Phi^0 + \Delta\Phi)] \delta(\Phi^1 - \Phi^0 - \Delta\Phi) \\ &= \frac{z_N^0}{z_N^1} \exp(-\beta\Delta\Phi) p^0(\Delta\Phi),\end{aligned}\quad (5.49)$$

where $p^0(\Delta\Phi)$ is the probability density to measure the same energy differences $\Delta\Phi$ when simulating system 0, i.e.,

$$p^0(\Delta\Phi) = \frac{1}{z_N^0} \int d\mathbf{r}^N \exp(-\beta\Phi^0) \delta(\Phi^1 - \Phi^0 - \Delta\Phi), \quad (5.50)$$

From Eqs. (5.47) and (5.49), we find that

$$\log p^1(\Delta\Phi) = \beta(\Delta F - \Delta\Phi) + \log p^0(\Delta\Phi) \quad (5.51)$$

It is convenient to define two functions² f^0 and f^1 as

$$\begin{aligned}f^0(\Delta\Phi) &= \log p^0(\Delta\Phi) - \frac{\beta\Delta\Phi}{2} \\ f^1(\Delta\Phi) &= \log p^1(\Delta\Phi) + \frac{\beta\Delta\Phi}{2}.\end{aligned}\quad (5.52)$$

We can then write

$$\beta\Delta F = f^1(\Delta\Phi) - f^0(\Delta\Phi). \quad (5.53)$$

²In the literature, these functions are sometimes also called g and f and the ODM is then referred to as f - g -sampling.

Note that f^0 and f^1 have to be measured in two separate simulations. This method can be used to calculate the chemical potential. Here, system 1 commonly consists of $N + 1$ interacting particles while system 0 contains N interacting particles plus one ideal gas particle. For system 1, $\Delta\Phi$ can be measured as the energy change due to a transformation of a random particle into an ideal gas particle. Similarly, in system 0, $\Delta\Phi$ can be obtained by turning the ideal gas particle into an interacting one. In both cases, we measure the histograms of the energy differences, which then can be used to calculate the functions f^0 and f^1 . Once we know the excess part of the chemical potential, which is given by

$$\Delta F = \beta\mu^{\text{ex}} = f^1(\Delta\Phi) - f^0(\Delta\Phi), \quad (5.54)$$

we can determine the free energy of the system via Eq. (5.44).

From Eq. (5.54) it is apparent that f^0 and f^1 have a constant offset equal to the excess chemical potential. To get good statistics, it is important that these two functions overlap on a significant range of the abscissa (cf. Fig. 7.47). Thereby, the overlapping distribution method can also serve as test of reliability of the Widom insertion method, hinting at possible sampling problems. This can be visualised in the following example. Consider a system that interacts via some hard-core potential. At high densities, it will be virtually impossible to insert test particles. Such trial insertions will always generate an overlap with the existing particles in the system, leading to high energy differences and thus to negligible Boltzmann factors. Only rarely will trial insertions find holes in the system large enough to accommodate a whole particle, which is necessary to make a relevant contribution to Eq. (5.42). In other words, the statistical accuracy of the particle insertion method will be poor in such cases. This will then also be reflected in the results of the ODM, since the functions f^0 and f^1 will hardly overlap.

5.5.3 Overlapping distribution method in the NPT ensemble

While the formalism of the ODM for the NPT ensemble [99,100] can be developed along the same lines as for the canonical ensemble, it is slightly more intricate due to the fluctuations in volume. Again, we have to perform two simulations: one simulation using a system of $(N + 1)$ particles interacting via potential Φ and a second one containing N interacting particles and one ideal gas particle.

For the system of $(N + 1)$ particles, the probability distribution of energy difference $\Delta\Phi$ with respect to the second system is given by

$$p_{N+1}(\Delta\Phi) = \frac{1}{z_{N+1,P,T}} \int dV e^{-\beta PV} \int dr^{N+1} e^{-\beta\Phi_{N+1}} \delta(\Phi_{N+1} - \Phi_N - \Delta\Phi), \quad (5.55)$$

where the configurational integral of an NPT system is given by

$$z_{N,P,T} = \int dV e^{-\beta PV} \int dr^N e^{-\beta\Phi_N}. \quad (5.56)$$

The probability distribution, $p_N(\Delta\Phi)$, for the system of N interacting particles and one ideal gas particle is given by

$$p_N(\Delta\Phi) = \frac{\int dV e^{-\beta PV} \int dr^{N+1} e^{-\beta\Phi_N} \delta(\Phi_{N+1} - \Phi_N - \Delta\Phi)}{\int dV e^{-\beta PV} \int dr^{N+1} e^{-\beta\Phi_N}}. \quad (5.57)$$

As we will show in more detail in Appendix B, the following relation can be derived

$$\begin{aligned} p_{N+1}(\Delta\Phi) &= \frac{z_{N,P,T}}{z_{N+1,P,T}} \langle V \rangle_{NPT} e^{-\beta\Delta\Phi} p_N(\Delta\Phi) = \\ &= e^{\beta\mu} \frac{\langle V \rangle_{NPT}}{\Lambda^3(N+1)} e^{-\beta\Delta\Phi} p_N(\Delta\Phi). \end{aligned} \quad (5.58)$$

Taking the logarithm of the last equation, we arrive at

$$\log p_{N+1}(\Delta\Phi) = \beta\mu + \log \frac{\langle V \rangle_{NPT}}{\Lambda^3(N+1)} - \beta\Delta\Phi + \log p_N(\Delta\Phi), \quad (5.59)$$

which can be rewritten as

$$\begin{aligned} \beta\mu &= \log(\beta P \Lambda^3) + \beta\Delta\Phi + \log[p_{N+1}(\Delta\Phi)] - \log \left[p_N(\Delta\Phi) \frac{\langle V \rangle_{NPT} \beta P}{(N+1)} \right] = \\ &= \beta\mu^{\text{id}} + \beta\Delta\Phi + \log[p_{N+1}(\Delta\Phi)] - \log \left[p_N(\Delta\Phi) \frac{\langle V \rangle_{NPT} \beta P}{(N+1)} \right]. \end{aligned} \quad (5.60)$$

The excess chemical potential is then given by

$$\beta\mu^{\text{ex}} = \beta\Delta\Phi + \log[p_{N+1}(\Delta\Phi)] - \log \left[p_N(\Delta\Phi) \frac{\langle V \rangle_{NPT} \beta P}{(N+1)} \right] \quad (5.61)$$

We define two functions, f^0 and f^1 by

$$\begin{aligned} f^0(\Delta\Phi) &= \log \left[p_N(\Delta\Phi) \frac{\langle V \rangle_{NPT} \beta P}{(N+1)} \right] - \frac{\beta\Delta\Phi}{2} \\ f^1(\Delta\Phi) &= \log[p_{N+1}(\Delta\Phi)] + \frac{\beta\Delta\Phi}{2}. \end{aligned} \quad (5.62)$$

Then, the excess part of the chemical potential can again be determined via

$$\beta\mu^{\text{ex}} = f^1(\Delta\Phi) - f^0(\Delta\Phi). \quad (5.63)$$

5.5.4 Non-Boltzmann sampling

Consider the following task: within simulations, we want to determine the effective potential between two interacting macromolecules as function of the separation R of their centres of mass. As they get closer to each other, the repulsion between these molecules increases, preventing further approach. Thus, in equilibrium the macromolecules will spend most of the simulation time at large separations, while short distances will be observed only rarely, leading to rather poor

statistics. However, some of the most valuable information can be obtained from the rare event of the macromolecules being close to each other. It is therefore necessary to focus attention on those events in order to obtain meaningful statistics without wasting time on irrelevant, though easily accessible configurations.

To overcome such bottlenecks, we can use non-Boltzmann sampling (also called umbrella sampling) [79,101]. Its idea is described in the following. In addition to the interactions acting between the macromolecules, we impose a so-called window or umbrella potential $W^i(R)$ on the centres of mass. This potential is defined as follows

$$W^i(R) = \begin{cases} 0 & R_{\min}^i < R < R_{\max}^i \\ \infty & \text{else} \end{cases} . \quad (5.64)$$

It forces the centres of mass to remain between the minimum and maximum distances, R_{\min} and R_{\max} , respectively. For this range of separations, a standard Metropolis MC simulation is carried out. If a trial move leads the system outside the prescribed distance range, the move is rejected and the old configuration is counted as a new one. By making a series of simulations using a sequence of umbrella potentials $W^i(R)$, we systematically vary the separations between the macromolecules. Now, also short distances will be probed often enough since the trajectory will be able to sample these regions efficiently. Since within each window states are sampled according to the Boltzmann distribution, this technique allows the system to move reversibly through all relevant states.

Within each of these windows i , a separate histogram of the probability of finding the molecules' centre of mass at a certain distance, $P^i(R)$, is recorded. At the end of the simulations, the effective potential $\Phi_{\text{eff}}(R)$ between the molecules is obtained by merging the effective potentials obtained within each window, $\Phi_{\text{eff}}^i(R)$

$$\beta\Phi_{\text{eff}}^i(R) = -\log [P^i(R)] + c_i, \quad (5.65)$$

where c_i is a normalisation constant. Since the c_i are initially unknown, the concatenation of $\Phi_{\text{eff}}^i(R)$ will display discontinuities at the windows' edges. To obtain a continuous $\Phi_{\text{eff}}(R)$ with $\Phi_{\text{eff}}(R \rightarrow \infty) = 0$, the c_i are chosen such that the data are aligned to each other at the edges of the windows and then $\Phi_{\text{eff}}(R = R_m)$ is subtracted for all R , where R_m is equal to R_{\max} of the outermost window. A schematic representation of this simulation procedure can be found in Fig. 5.13.

Using the non-Boltzmann sampling technique, care has to be taken on various levels. First, the variation of the effective interaction within each window should not exceed $1-2 k_B T$ to reliably sample the entire window. Further, statistics are usually poor at the edge of the windows [102], therefore, it is advisable to use overlapping windows and to smooth the data of each window using Savitzky-Golay filters [103] before constructing the continuous $\Phi_{\text{eff}}(r)$. Third, we have to make sure that R_m is chosen in a way that the effective interaction at this distance is really zero, which is usually the case if $[\partial\Phi_{\text{eff}}(R)/\partial R] \sim 0$ for $R \sim R_m$.

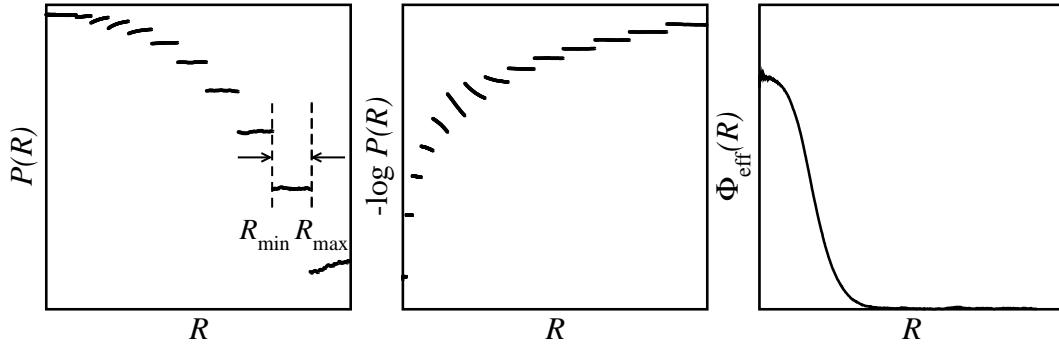


Figure 5.13: Schematic representation of umbrella sampling: In every window, we measure in a standard MC simulation the probability of the macromolecules being at distance R (left panel). After taking the logarithm (middle panel), the effective interaction $\Phi_{\text{eff}}(R)$ is obtained by aligning the data at the edges of the windows and shifting it so that $\Phi_{\text{eff}}(R_m) = 0$ (right panel).

5.5.5 Thermodynamic integration for cluster solids

Determination of the free energy in solids is usually more complicated than for fluids, since Widom's particle insertion method cannot be reliably used due to the complications of inserting particles into crystals. For such situations, Frenkel and Ladd [104] developed a simple technique of high accuracy. Assuming that the system of interest is governed by the interaction potential $\Phi(\mathbf{r}^N)$, they showed that its free energy at a given state point can be related to the known free energy of a reference system interacting via $\Phi_{\text{ref}}(\mathbf{r}^N)$. During the course of the simulations, the system's intermolecular interactions are slowly turned off while the interactions of the reference system are turned on at the same time. The easiest way to achieve this is to consider the linear potential energy function

$$\Phi_{\lambda}(\mathbf{r}^N) = (1 - \lambda)\Phi(\mathbf{r}^N) + \lambda\Phi_{\text{ref}}(\mathbf{r}^N), \quad (5.66)$$

where λ is the coupling parameter. For $\lambda = 0$, our system of interest is recovered, while for $\lambda = 1$, we deal with the reference system. The free energy of our system can be calculated via the coupling parameter formalism as

$$F = F_{\text{ref}} + \int_{\lambda=1}^{\lambda=0} d\lambda \left\langle \frac{\partial \Phi_{\lambda}}{\partial \lambda} \right\rangle. \quad (5.67)$$

Using Eq. (5.66), this last equation reduces to

$$F = F_{\text{ref}} + \int_{\lambda=1}^{\lambda=0} d\lambda [\Phi_{\text{ref}} - \Phi]. \quad (5.68)$$

This equation expresses the free energy difference as an ensemble average, which can be readily measured in MC simulations. Using the linear interpolation (5.66) is especially convenient since

we can then derive the Gibbs-Bogoliubov inequality [79]

$$\left(\frac{\partial^2 F}{\partial \lambda^2}\right)_{N,V,T} = -\beta \left\{ \langle (\Phi - \Phi_{\text{ref}})^2 \rangle_\lambda - \langle \Phi - \Phi_{\text{ref}} \rangle_\lambda^2 \right\} \leq 0, \quad (5.69)$$

i.e., $(\partial F/\partial \lambda)$ can never increase with λ . This can be used to check the accuracy of the simulation results.

In [104], the reference system was chosen to be an Einstein solid, where particles are connected to their respective lattice sites via harmonic springs [79]. This is a reasonable choice for perfect *single* occupancy crystals. However, in *multiple* occupancy crystals, several particles can be found per lattice site and particles can hop between lattice sites. In this case, a more convenient reference system is a system of ideal gas particles that move in potential wells centred around the lattice sites (cf. Fig. 5.14). A typical shape of the curve $\partial F/\partial \lambda$ can be seen in Fig. 5.15 for a cluster solid and a liquid system.

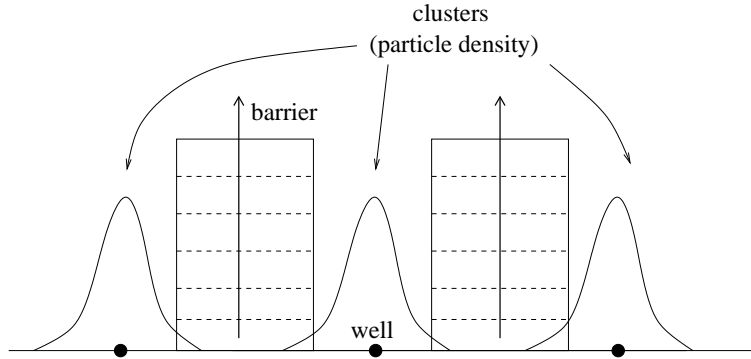


Figure 5.14: Schematic, one-dimensional representation of thermodynamic integration, confining particles in potential wells of increasing height. Lattice sites are indicated by black circles.

If we set,

$$\Phi_{\text{ref}}(\mathbf{r}) = \sum_{i=1}^N \phi_{\text{ref}}(\mathbf{r}_i) \quad (5.70)$$

where

$$\phi_{\text{ref}} = \begin{cases} 0 & \mathbf{r} \in \bigcup_{i=1}^{N_c} v_0(\mathbf{R}_i) \\ U_{\text{max}} & \text{else} \end{cases}, \quad (5.71)$$

with U_{max} being the maximal height of the potential barrier. Hereby, v_0 are small volumina centred around the N_c perfect lattice sites located at the lattice vectors \mathbf{R} of the crystal under study. The free energy calculation does not depend on the size or shape of these small regions v_0 , as long as they allow to construct a reversible path between the two systems. It is evident that the crystal structure will melt if these regions are too big, therefore the path would not be reversible anymore. Conveniently, the linear extent of the regions is chosen to roughly fit the width of the cluster density distribution, i.e., the distribution of particles around a lattice site (cf. Fig. 5.14).

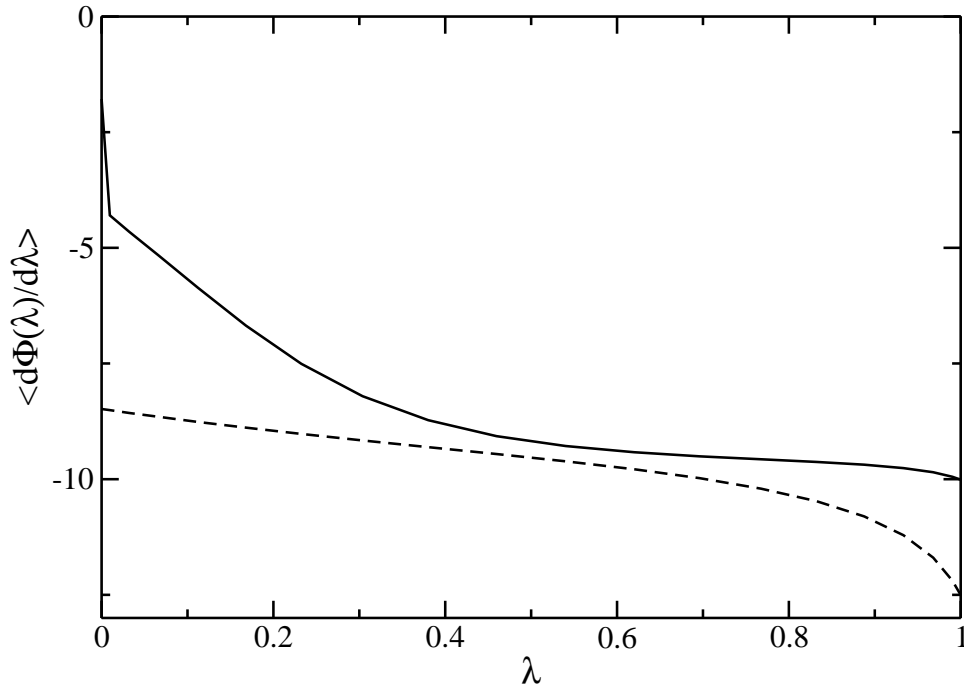


Figure 5.15: Typical progression of the curve $\partial F/\partial\lambda$ as function of λ for a cluster solid (GEM-4, $\rho\sigma^3 = 8.5$, $k_{\text{B}}T/\varepsilon = 1.1$, fcc; $U_{\text{max}} = 10k_{\text{B}}T$, cubic v_0 of box-length 0.1σ ; solid line) and a liquid, where an unconfined ideal gas was used as a reference system (GEM-4, $\rho\sigma^3 = 1.3$, $k_{\text{B}}T/\varepsilon = 0.2$, dashed line).

Since the height of the barrier between the lattice sites is finite, $U_{\text{max}} < \infty$, the partition function of the reference system is given as

$$Q_{\text{ref}} = \frac{1}{\Lambda^{3N} N!} (V_0 + V_{\text{barr}} e^{-\beta U_{\text{max}}})^N \quad (5.72)$$

where $V_0 = N_c v_0$ is the sum of all small volumina v_0 around the N_c lattice sites and $V_{\text{barr}} = V - V_0$ is the volume excluded by the barrier. Then, the reference free energy is obtained via

$$F = -k_{\text{B}}T \log Q_{\text{ref}}. \quad (5.73)$$

The integral in Eq. (5.68) can be evaluated via Gauss-Lobatto quadrature [105]. For every quadrature point λ , a separate Monte Carlo simulation in the NVT -ensemble has to be performed with particles interacting via Φ_λ given by Eq. (5.66), measuring $\langle \partial \Phi_\lambda / \partial \lambda \rangle$.

Apart from the standard particle moves, two additional trial moves are introduced to avoid sampling problems. At $\lambda = 0$, the barrier is completely turned off and has therefore no influence on the evolution of the system. Still, the barrier enters the formalism in the evaluation of Eq. (5.68). Since the system's centre of mass motion is not restricted, the system might exhibit a drift and particles can slowly move on top of the barrier. Therefore, $\langle \partial \Phi_\lambda / \partial \lambda \rangle_{\lambda=0} = \Phi_{\text{ref}} - \Phi$ can change quite drastically during the course of the simulation, resulting in large uncertainties

in $\langle \partial\Phi/\partial\lambda \rangle_{\lambda=0}$. To avoid this problem and to enhance statistics, we introduce a random move of the system's centre of mass via an arbitrary shift. Such a move does not change the potential energy of the system at $\lambda = 0$, thus, these moves will always be accepted. Another problem is encountered at the other end of the λ -range, i.e., for $\lambda \sim 1$. Now, the barrier might be so high that particles cannot cross from one potential well to a neighbouring one via standard MC moves. Therefore, we implement Widom-like moves, where a particle is moved to a completely random position within the simulation box. At $\lambda = 1$, these moves will be accepted with a probability given by the ratio V_0/V .

5.5.6 The Gibbs ensemble

Coexistence between two phases of a one-component system is possible if the chemical potentials μ , the temperature T and the pressures P of the respective phases are the same. Therefore, one might think that a constant μPT -ensemble would be the right means to study phase transitions. However, since all of these three variables are intensive, no such ensemble exists [79].

Panagiotopoulos [106–109] circumvented this problem and developed the so-called Gibbs ensemble method, which allows to simulate coexisting phases, i.e., at equal μ , P and T . This technique uses the trick to fix the two phases at constant difference in chemical potential, $\Delta\mu = 0$, while their absolute values are still undetermined [79].

The idea is to consider two simulation boxes, labelled 0 and 1, at constant temperature T , whose numbers of particles and volumes are allowed to fluctuate while the total particle number, $N_{\text{tot}} = N^0 + N^1$, and the total volume, $V_{\text{tot}} = V^0 + V^1$, remain fixed. This is achieved by implementing three different kinds of trial moves, which are illustrated in Fig. 5.16:

- Standard particle displacements: let ν be the configuration reached from configuration τ via displacement of some random particle in box 0. Then, the acceptance rule for this move is given by

$$a(\tau \rightarrow \nu) = \min(1, e^{-\beta\Delta\Phi}), \quad (5.74)$$

where $\Phi = \Phi(\mathbf{r}_\nu^{N^0}) - \Phi(\mathbf{r}_\tau^{N^0})$, i.e., the standard acceptance rule (5.27) already derived for the canonical ensemble.

- Volume changes: if, e.g., $V_\tau^0 \rightarrow V_\nu^0 = V_\tau^0 + \Delta V$, then at the same time $V_\tau^1 \rightarrow V_\nu^1 = V_\tau^1 - \Delta V$, thus keeping the total volume fixed. The acceptance rule is given by

$$a(\tau \rightarrow \nu) = \min \left\{ 1, \frac{(V_\nu^0)^{N^0} (V_\nu^1)^{N^1}}{(V_\tau^0)^{N^0} (V_\tau^1)^{N^1}} e^{-\beta[\Phi(r_\nu^{N_{\text{tot}}}) - \Phi(r_\tau^{N_{\text{tot}}})]} \right\}, \quad (5.75)$$

These moves eventually lead to $P^0 = P^1$.

- Random particle transfers between the boxes: assuming that a particle in box 1 gets trans-

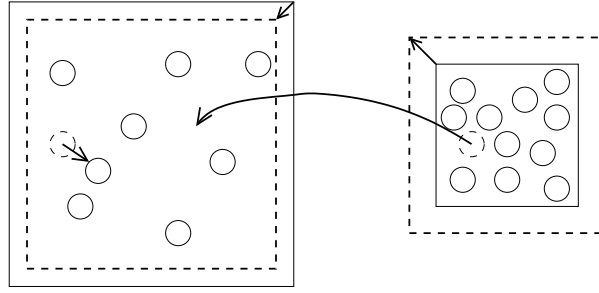


Figure 5.16: Sketch of the different moves leading to phase coexistence in the Gibbs ensemble: particle displacements, volume moves and particle transfers.

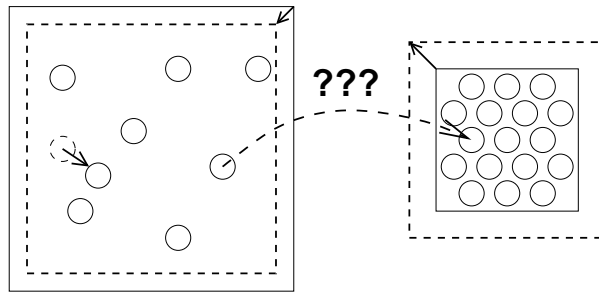


Figure 5.17: The Gibbs ensemble method fails when one of the studied phases is a single occupancy solid of harshly repulsive particles, since particle transfers will hardly ever get accepted.

ferred to box 0, the acceptance rule³ reads

$$a(\tau \rightarrow \nu) = \min \left\{ 1, \frac{N^1 V^0}{(N^0 + 1) V^1} e^{-\beta[\Phi(r_\nu^{N_{\text{tot}}}) - \Phi(r_\tau^{N_{\text{tot}}})]} \right\}, \quad (5.76)$$

These moves guarantee that $\mu^0 = \mu^1$.

To ensure detailed balance, the type of move executed at each step of the simulation is chosen at random with prescribed probabilities [79].

Monitoring the pressures and chemical potentials in the two boxes, the systems will slowly move to equilibrium, which is reached once the pressures and chemical potentials are equal. Then, each subsystem will be at its coexistence density, which can easily be measured and used to draw the phase diagram. Please note that special care has to be taken when the simulation is carried out close to a critical point, as the boxes might change identity [79].

The advantage of the Gibbs ensemble is that it needs only a *single* simulation to determine the coexistence densities at a given T . In the free energy simulations presented before we need to calculate the free energies for a range of densities (and at each density for several integration points) for the two phases of interest before the coexistence densities can be determined via the

³Note that this acceptance rule is only correct if first a box is chosen at random and then one of the particles is selected within this box. Just choosing a random particle from N_{tot} and transferring it to the other box would lead to a slightly different acceptance rule [79].

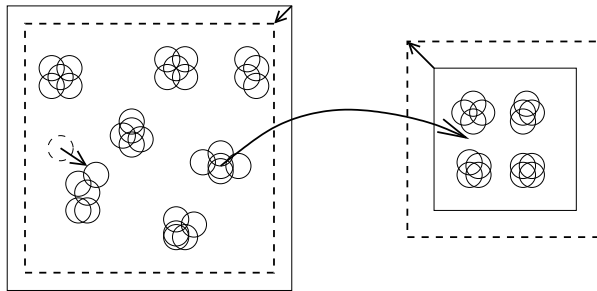


Figure 5.18: In cluster solids, particle transfers are possible due to the finite energy penalty for placing particles on top of each other.

common tangent construction. One disadvantage of the Gibbs ensemble technique, however, is that it fails when one of the coexisting phases is a solid. As illustrated in Fig. 5.17, particle transfers will be accepted only with very low probability, since vacancies in the crystal will be extremely rare [79]. Thus, the chemical potentials are not going to equilibrate. However, in crystals of particles interacting via bounded potential, i.e., especially in cluster solids, the situation is different (cf. Fig. 5.18). Now, transfer moves have a finite probability to be accepted since particles are allowed to sit on top of each other. Still, in this case extreme caution has to be exercised for other reasons, which will be discussed in Sec.7.2.

5.6 Data analysis

5.6.1 Cluster analysis

To study the properties of a clustered phase in detail, we first need a definition of a cluster. In Fig. 5.19, we show how a typical RDF of a clustered system varies with increasing density. One indicator of the clustering phenomenon is the rise of the value of $g(0)$. In a system where particles interact via a continuous potential, it is of course not possible to define sharp limits of a 'cluster' in the fluid phase. As we show in the inset of Fig. 5.19, the RDF does not completely vanish for this particular state-point, so that the location of the first minimum only gives an indication of the spatial extent of the clusters. However, as soon as the system freezes, the space between two clusters becomes nearly depleted, thereby allowing for a *definition* of the extent of a cluster. The cluster size, n_c , can then either be defined by integration of $g(r)$ up to its first minimum at r_c , i.e.,

$$n_c = 1 + 4\pi\rho \int_0^{r_c} dr r^2 g(r), \quad (5.77)$$

or via a cluster analysis, where r_c is used as a threshold value to group particles in clusters. In simulations, this is done as follows: Every particle in the simulation gets a label indicating its cluster identity. We start with particle 1 and calculate the distance to all other particles in the

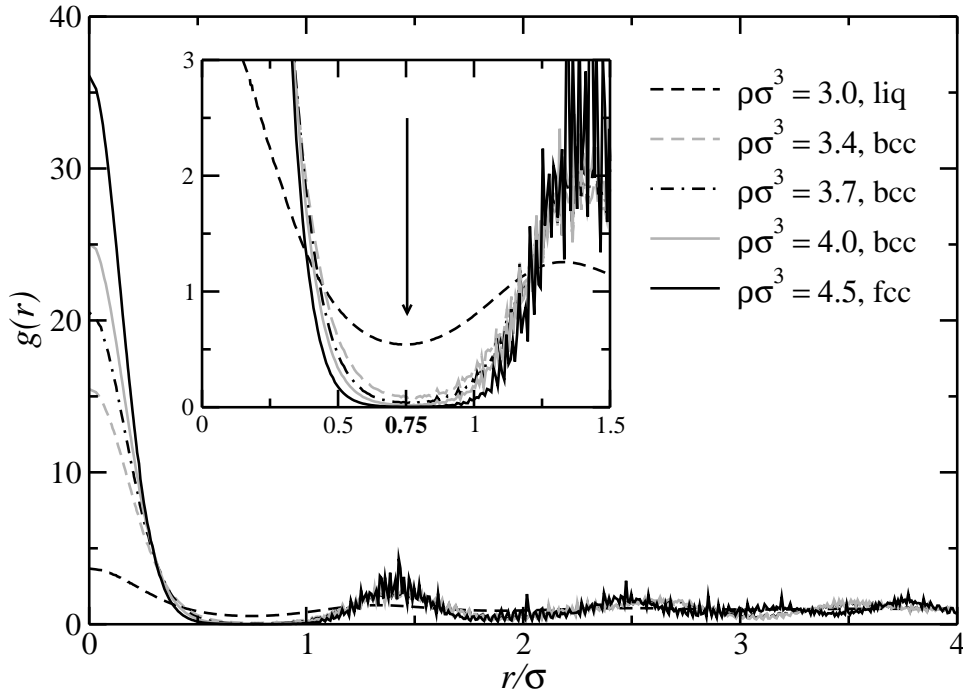


Figure 5.19: The RDF $g(r)$ as a function of r/σ of a clustering system (GEM-4, $k_B T/\varepsilon = 0.5$). With increasing density, the first minimum of $g(r)$ tends to zero at $r/\sigma \sim 0.75$, thus allowing for the definition of the spatial extend of a cluster.

system. Every particle within the threshold radius of r_c is considered to be part of the cluster and these particles themselves are again checked for other neighbouring particles within the threshold distance. When no more new neighbours are found, we proceed to the next particle that has not been labelled yet and repeat the procedure until every particle has been assigned a cluster identity. Of course, this algorithm does not work in all situations. Occasionally, particles hop between clusters and then might be located in between two clusters. Depending on the size of r_c , this algorithm will then either merge these two clusters or will eventually even issue three distinct cluster identities, where the intermediate particle is considered as a cluster of its own. There are various ways to fix these problems by keeping track of cluster sizes and/or modifying the threshold value during the cluster analysis. However, these additional manipulations render the analysis more expensive in time, while simply neglecting such rare events has little to no effect on the final result.

Once particles have been grouped to clusters, it is straightforward to determine their centres of mass and to perform analyses on the cluster level. It is then possible to calculate the RDF of the clusters, $g_{cl}(r)$, and to evaluate the distribution of particles around their respective centre of mass. In addition, the cluster size distribution as well as the mean cluster size can be determined. Finally, we can analyse the crystal structure of the system, as will be discussed in the next section.

5.6.2 Bond order parameters

To determine the full phase diagram of a system under consideration, it is indispensable to identify the structure of the system within the simulation box, i.e., whether the system is in the fluid or in some crystalline state. Depending on the density and the temperature, particles in (cluster) solids have a certain freedom to fluctuate around their equilibrium positions, i.e., the perfect lattice sites. Thus, we expect our crystals to be slightly distorted and we are therefore in need of a quantitative measure of the degree of “crystallinity” in our system. Such an analysis has to fulfil several requirements. First, it evidently has to be capable of unambiguously distinguishing between the fluid and a crystalline phase. Second, it has to be insensitive to the orientation of the crystal in space. Third, it has to be able to reliably identify the different crystal structures expected to occur in the phase diagram. And last, it should not be computationally too expensive.

In the search of such an identification tool it is important to recall the specific differences between a fluid and a crystal. These are the translational and orientational order that characterise the solid and are absent in the fluid phase. In other words, the particles form an infinite periodic array in three-dimensional space. At short range, every crystal can be characterised by the number of neighbours in a certain distance from a reference particle and their positions relative to this particle. Bond order parameters take advantage of these features [110–113], and are thereby indeed quantitative measures of crystallinity, meeting all the aforementioned prerequisites.

To calculate these bond order parameters, we first have to define the neighbours j of a tagged particle i , which are connected to this particle via bonds \mathbf{r}_{ij} . Then we search for an appropriate choice of the distance r_0 , which defines whether a particle is considered to be a neighbour or not. To this end we recall that the first peak of the RDF at non-zero distance corresponds to the location of the nearest neighbours. Thus, we choose r_0 to be slightly bigger than this distance, thereby assuring that also distorted crystals will still be correctly identified. In this thesis, we are going to concentrate on cubic crystals. In this case, care has to be taken to guarantee that in case of a bcc structure also the second coordination shell, which is situated very close to the first one, falls within the range of r_0 .

For every particle i and its corresponding bond \mathbf{r}_{ij} with neighbour j , we can then calculate the quantity

$$Q_{lm}(\hat{\mathbf{r}}_{ij}) = Y_{lm}[\vartheta(\hat{\mathbf{r}}_{ij}), \varphi(\hat{\mathbf{r}}_{ij})], \quad (5.78)$$

where Y_{lm} are spherical harmonics and $\vartheta(\hat{\mathbf{r}})$ and $\varphi(\hat{\mathbf{r}})$ are the polar and the azimuthal angles of the bond described by the unit vector $\hat{\mathbf{r}}$ with respect to an arbitrary reference coordinate system. We can average above parameters by summing over all bonds of particle i and obtain

$$\overline{Q}_{lm}(i) \equiv \frac{1}{N_b} \sum_{j=1}^{N_b} Q_{lm}(\hat{\mathbf{r}}_{ij}), \quad (5.79)$$

where the sum has to be taken over all N_b neighbours within r_0 . It can be shown that in the case

of cubic structures, the first nonzero values (apart from Q_{00}) occur for $l = 4$ [110]. As we will see, it is convenient to also use the $Q_{6m}(i)$ to distinguish different cubic structures in a reliable way.

Since above parameters also depend on the choice of the coordinate system, we construct rotationally invariant versions of second order of the $Q_{lm}(i)$ via

$$Q_l(i) \equiv \sqrt{\frac{4\pi}{2l+1} \sum_{m=-l}^l |\bar{Q}_{lm}(i)|^2} \quad (5.80)$$

and of third order via

$$\widehat{W}_l(i) \equiv \frac{\bar{W}_l(i)}{\left[\sum_{m=-l}^l |\bar{Q}_{lm}(i)|^2 \right]^{3/2}}, \quad (5.81)$$

where

$$\bar{W}_l(i) \equiv \sum_{\substack{m_1, m_2, m_3 \\ m_1 + m_2 + m_3 = 0}} \begin{pmatrix} l & l & l \\ m_1 & m_2 & m_3 \end{pmatrix} \bar{Q}_{lm_1}(i) \bar{Q}_{lm_2}(i) \bar{Q}_{lm_3}(i). \quad (5.82)$$

The term in brackets in the last equation is a Wigner $3j$ -symbol, which is related to the Clebsch-Gordan coefficients via

$$\begin{pmatrix} j_1 & j_2 & j_3 \\ m_1 & m_2 & m_3 \end{pmatrix} \equiv \frac{(-1)^{j_1 - j_2 - m_3}}{\sqrt{2j_3 + 1}} \langle j_1 m_1 j_2 m_2 | j_3 - m_3 \rangle. \quad (5.83)$$

They are implemented in **Mathematica** as `ThreeJSymbol` [114].

The bond order parameters described above represent a measure of the local order around a particle i . It is obvious that in a perfect Bravais crystal the contributions of all particles will be the same and thus we obtain global values for these parameters, characteristic for the crystal structure under consideration. In Tab. 5.1, we summarise these global bond order parameters for $l = 4$ and $l = 6$ for the fluid and for ideal cubic structures. In our simulations, however, the crystals will not be perfect but somewhat distorted. The neighbourhood of every particle will be slightly different, resulting in a distribution of Q_l and \widehat{W}_l values. We show typical distributions of these for cluster crystals in Fig. 5.20. Depending on the structure of our system, we expect these distributions to either have peaks around the values of the corresponding perfect crystal structures or, in case of the fluid, to be broadly distributed around zero. This reflects the important fact that also in the liquid, local order exists. In contrast to crystal structures, the global order parameters (i.e., summing over all particles in the system) vanish since all local order parameters add up in an incoherent way [111–113].

Though the probability densities of the bond order parameters might be rather broad, considerable differences between different structures are observed. Thus these distributions are fingerprints that enable us to not only distinguish crystals from the fluid but also to identify different crystal

geometry	Q_4	Q_6	\widehat{W}_4	\widehat{W}_6
fcc	0.191	0.575	-0.159	-0.013
bcc	0.036	0.511	0.159	0.013
sc	0.764	0.354	0.159	0.013
fluid	0	0	0	0

Table 5.1: Global bond order parameters for the fluid and different cubic Bravais lattices [111].

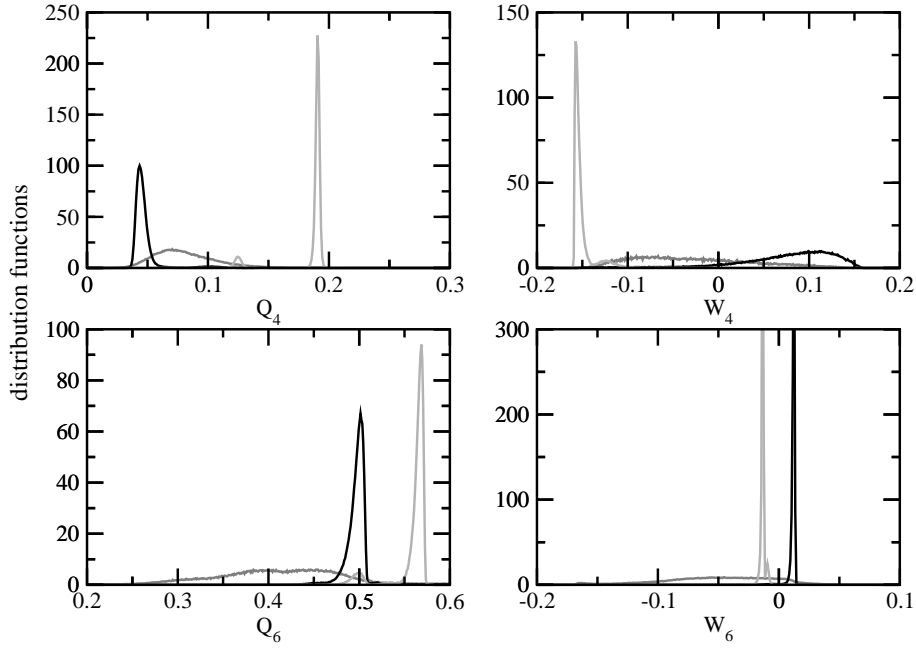


Figure 5.20: Typical bond order fingerprints of different cubic cluster crystals (black - bcc; light grey - fcc) and the fluid (dark grey).

structures. This can be done in the following way.

Let $\hat{\mathbf{v}}$ be a unit vector whose elements correspond to the concatenation of the histograms of all bond order parameters measured during a simulation. Then, the vector $\hat{\mathbf{v}}$ obtained for a particular system under study may be approximated by a linear combination of corresponding vectors for equilibrated crystal structures and the pure fluid by minimising equilibrated crystal structures and for the fluid by minimising

$$\Delta^2 = \left[\hat{\mathbf{v}} - \left(\sum_s f_s \hat{\mathbf{v}}_s \right) \right]^2 \quad (5.84)$$

where s corresponds to the structures under consideration. Therefore, $\hat{\mathbf{v}}_s$ are the vectors associated with the histograms of the equilibrated structures and the coefficients f_s are indicators of the crystal structure. The value Δ^2 is a measure of the quality of the fit. Decomposing such a fingerprint into a linear combination of the corresponding distributions of known structures allows

for a quantitative determination of the structure of the system in the simulation box [112, 113].

Chapter 6

Re-entrant melting

In Sec. 2.2, we introduced the phenomenon of re-entrant melting. A wide range of soft matter systems was found to show this sort of phase behaviour and we are going to present a few examples and theoretical studies of those in the following.

One of these systems are star polymers. Here, the macromolecules consist of a central core and a well-defined number, f , of polymer chains attached to it. By increasing f , one can vary the interpenetrability of these molecules and cover the range from the polymeric regime, where $f = 1$ or 2 to rather hard, colloidal particles for $f \gg 1$. It was shown in [3] that the effective interaction for these macromolecules may be approximated by a soft potential that diverges only logarithmically for short distances. In [23], the phase diagram for star polymer systems was determined and found to show the characteristic behaviour of re-entrant melting, where f acts as a control parameter equivalent to the inverse temperature in the GCM (cf. Sec. 2.2). Similar to the upper freezing temperature in the GCM, there exists a lower bound in f below which no solid structures are found and the system remains fluid at all densities.

Re-entrant melting was also found for microgels, i.e., mesoscopically sized, covalently linked polymer networks carrying a net charge Z . Like star polymers, these networks can be shown to interact via soft, Gaussian potentials that are charge- and density-dependent [12]. Here, the charge Z acts as the control parameter in the phase diagram, which again displays this specific phase behaviour [11].

As a last example we mention diblock copolymers, which are linear chain molecules consisting of two sub-chains that are linked covalently to each other and which were shown to interact via bounded effective interactions [115]. Here, re-entrant melting occurs upon lowering the temperature and upon constantly increasing the monomer fraction of one of the sub-chains [116].

These theoretical studies are complemented by experimental investigations. Re-entrant melting behaviour was observed in a series of small angle X-ray scattering (SAXS) experiments performed for copolymer micelles. Even a second freezing and re-entrant melting transition was found for a micellar solution which is physically very close to star polymers [117–119].

These examples establish re-entrant melting as a phase behaviour frequently encountered in soft matter systems.

6.1 The Gaussian core model as effective interaction

In Sec. 2.2, we have introduced the GCM as one of the most prominent model potentials in the class of bounded potentials that are known to show re-entrant melting behaviour. This model was studied extensively within theoretical approaches and computer simulations [25, 35–42], but still, one important question remains: how *realistic* is such an interaction?

In 1950, Flory proposed a Gaussian-like potential as effective interaction between polymer chains [120]. Some of the quantitative characteristics of this potential turned out to be wrong, such as the prediction that upon increasing the degree of polymerisation the interaction becomes steeper which is in disagreement with the later findings of [7]. The functional form of the potential, however, was shown in a series of theoretical studies as well as in on- and off-lattice simulations [6–8, 121–128] to be correct for good solvents. Most recently, Louis *et al.* [8] calculated the effective pair potential for systems consisting not only of two but considerably more polymer chains, covering a broad range of concentrations ranging from dilute solutions up to five times the overlap concentration. These authors confirmed the validity of the Gaussian shape of the interaction for this system and thus the pair potential picture for the whole concentration range, with only slight modifications of the length- and energy-scales beyond the overlap concentration [2, 8].

More recently, another class of macromolecules, namely so-called athermal dendrimers, were also shown to interact via Gaussian-shaped effective potentials [9, 129]. We are going to discuss these substances in more detail in Sec. 7.1.

Above examples give evidence that the GCM is indeed a realistic and important model for the effective interactions between various polymeric macromolecules. Therefore, it is essential to study its behaviour thoroughly.

As already mentioned before, both the fluid and the solid phases of the GCM were studied in detail, leading to the phase diagram of the GCM [40, 42].

In the following, we use the GCM and the detailed knowledge about its thermodynamic properties to test the applicability of the SCOZA scheme (cf. Sec. 4.1.6) to bounded potentials. We start with an MFA study of the GCM.

6.2 The MFA for the GCM

Within the framework of the MFA, the structural and thermodynamic properties of the GCM can be expressed semi-analytically to a large extent [40, 41, 46]. Here, we add a few details that have not been documented in the literature yet.

For the specific case of the GCM the MFA ansatz, Eq. (4.15) immediately leads to an analytic

expression for the static structure factor, $S(q)$,

$$S(q) = [1 - \varrho \tilde{c}(q)]^{-1} = \frac{1}{1 + \alpha \exp[-(q^2 \sigma^2/4)]}, \quad (6.1)$$

where $\alpha = \pi^{3/2} \varrho \sigma^3 \beta \varepsilon$. For the RDF, we find

$$g(r) = 1 - \frac{\alpha}{\varrho} \frac{1}{8\pi^3} \int d\mathbf{q} e^{-i\mathbf{q}\mathbf{r}} \frac{1}{e^{q^2 \sigma^2/4} + \alpha}. \quad (6.2)$$

In particular

$$g(0) = 1 + \frac{\beta \varepsilon}{\alpha} \text{Li}_{3/2}(-\alpha). \quad (6.3)$$

Here, $\text{Li}_n(x)$ is the polylogarithm of order n which is discussed in detail in Appendix A.

The thermodynamic properties of the GCM can be calculated semi-analytically using one of the three thermodynamic routes described in Sec. 4.1.1 or in [54]. The results for the dimensionless equation of state, $\beta P/\varrho$, obtained via the compressibility route ('C')

$$\left(\frac{\beta P}{\varrho}\right)^{\text{C}} = 1 + \frac{1}{2}\alpha \quad (6.4)$$

and the virial route ('V')

$$\left(\frac{\beta P}{\varrho}\right)^{\text{V}} = 1 + \frac{1}{2}\alpha - \beta \varepsilon \aleph(\alpha), \quad (6.5)$$

where

$$\aleph(\alpha) = \frac{1}{2\alpha} [\text{Li}_{3/2}(-\alpha) - \text{Li}_{1/2}(-\alpha)] \quad (6.6)$$

have already been reported in [40, 41].

The energy route ('E') has not been considered in the literature so far. To obtain $(\beta P/\varrho)^{\text{E}}$ we first calculate the excess (over ideal gas) internal energy per particle

$$\frac{\beta U^{\text{ex}}}{N} = 2\pi\beta\varrho \int_0^\infty dr \phi(r) g(r) r^2 = \frac{\alpha}{2} - \frac{\beta \varepsilon}{2\alpha} [\alpha + \text{Li}_{3/2}(-\alpha)], \quad (6.7)$$

from which we obtain the excess free energy per particle

$$\frac{\beta F^{\text{ex}}}{N} = \int_0^\beta d\beta' \frac{U^{\text{ex}}(\beta', \varrho)}{N} = \frac{\alpha}{2} - \frac{\beta \varepsilon}{2\alpha} [\alpha + \text{Li}_{5/2}(-\alpha)], \quad (6.8)$$

and, finally, the equation of state

$$\left(\frac{\beta P}{\varrho}\right)^{\text{E}} = 1 + \varrho \frac{\partial}{\partial \varrho} \left(\frac{\beta F^{\text{ex}}}{N}\right) = 1 + \frac{1}{2}\alpha - \beta \varepsilon \aleph(\alpha). \quad (6.9)$$

Thus we find that the virial (6.5) and energy route (6.9) lead *exactly* to the same expression for the dimensionless equation of state.

In our numerical investigations of similar bounded systems within the MFA, we have observed an analogous, remarkable coincidence of the virial and the energy route [47]. In fact, it was recently shown rigorously [130] that thermodynamic consistency between the energy and virial routes is not just guaranteed for the GCM within the MFA but for a whole set of “soft” potentials fulfilling the conditions

$$\lim_{r \rightarrow 0} r^3 \phi(r) = 0, \quad \lim_{r \rightarrow \infty} r^3 \phi(r) = 0. \quad (6.10)$$

and for a wider range of closure approximations of the form

$$\tilde{h}(q; \varrho, \beta) = \frac{1}{\varrho} \mathcal{G}(z), \quad \text{with } z \equiv \varrho \beta \tilde{\phi}(q), \quad (6.11)$$

where $\mathcal{G}(z)$ is an arbitrary function. The first condition in (6.10) defines how to interpret the term “soft” in this context. It not only includes bounded potentials but also logarithmically diverging potentials as well as potentials diverging weaker than r^{-3} . The second condition, on the other hand, requires the potential to be sufficiently short ranged.

6.3 The MFA-based SCOZA for the GCM

When applying the concept of the MFA-based SCOZA to systems with soft potentials, the GCM represents *the* ideal candidate. Based on the analytic expressions given by the MFA for the *energy* and the virial route of the GCM, it is possible to derive a partial differential equation (PDE) for the state-dependent function K_i introduced in the closure relation of the SCOZA which relates both density and temperature derivatives. Two alternative ways to enforce thermodynamic consistency can be formulated by using the virial and the *compressibility* route. On the one hand, this leads to an ordinary (ODE) that can be solved for each isotherm independently. On the other hand, we have proposed an integro-differential-equation (IDE) based formulation of the SCOZA, which has to be solved fully numerically on a T - ϱ grid (cf. Sec. 4.1.7).

The conventional formulation of the SCOZA presented here takes advantage of the availability of the semi-analytic solution of the MFA for the GCM discussed in Sec. 6.2. Therefore, closed expressions can be derived for the thermodynamic properties also within the MFA-based SCOZA. To simplify the notation we introduce a function $\hat{\alpha}_i(\varrho, \beta) = \pi^{3/2} \varrho \sigma^3 \beta \varepsilon K_i(\varrho, \beta) = \alpha K_i(\varrho, \beta)$, which is explicitly state-dependent, but for simplicity suppress the arguments of $\hat{\alpha}_i$ in the following. As already introduced in Sec. 4.1.6, $i = \text{EC}$ or VC , where the subscripts EC and VC specify whether the energy and the compressibility or the virial and the compressibility routes are used to enforce thermodynamic self-consistency. For the formulae common to both cases, the generic subscript i will be used.

According to the compressibility route the density derivative of the equation of state is given

by

$$(\kappa_{\text{red}}^{\text{C}})^{-1} = (\rho k_{\text{B}} T \kappa_{\text{T}}^{\text{C}})^{-1} = 1 - \rho \tilde{c}(0) = 1 - \hat{\alpha}_i, \quad (6.12)$$

where $\kappa_{\text{T}}^{\text{C}}$ is the isothermal compressibility and the reduced isothermal compressibility $\kappa_{\text{red}}^{\text{C}}$ is the zero wave-vector value of the structure factor $S(q)$.

Using the virial route one finds the following expression for the dimensionless equation of state

$$\left(\frac{\beta P}{\rho}\right)^{\text{V}} = 1 - \frac{2\pi}{3} \beta \rho \int_0^{\infty} dr r^2 \left[r \frac{d\phi(r)}{dr} \right] g(r) = 1 + \frac{1}{2} \alpha - \frac{\beta \varepsilon}{2 \hat{\alpha}_i} [\text{Li}_{5/2}(\hat{\alpha}_i) - \text{Li}_{3/2}(\hat{\alpha}_i)]. \quad (6.13)$$

Finally, according to the energy route the dimensionless excess energy per particle is given by

$$\frac{\beta U^{\text{ex}}}{N} = \frac{1}{2} \alpha + \frac{\beta \varepsilon}{2 \hat{\alpha}_i} [\text{Li}_{3/2}(\hat{\alpha}_i) - \hat{\alpha}_i]. \quad (6.14)$$

The thermodynamic inconsistency can be removed either via the energy/compressibility or via the virial/compressibility route. Both possibilities will be considered in the following subsections.

6.3.1 Energy and compressibility route

To enforce thermodynamic consistency between the energy and compressibility route we utilise the version of the MFA-based SCOZA-formalism proposed in [70, 131], which brought along a breakthrough of this concept for systems with repulsive potentials. From a historical perspective, this represents the conventional approach to the MFA-SCOZA. It is based on replacing the differential equation for $K_{\text{EC}}(\rho, \beta)$ by a differential equation for the excess energy density $u = U^{\text{ex}}/V$. To derive this equation, we consider the following thermodynamic relation (see, e.g., [132])

$$\frac{\partial}{\partial \beta} \left(\frac{1}{\kappa_{\text{red}}^{\text{E}}} \right) = \rho \frac{\partial^2 u}{\partial \rho^2}. \quad (6.15)$$

Expressing at constant density $\kappa_{\text{red}}^{\text{E}}$ as a function of u , the left hand side can be rewritten as

$$\frac{\partial}{\partial \beta} \left[\frac{1}{\kappa_{\text{red}}^{\text{E}}(u)} \right] = \frac{\partial}{\partial u} \left[\frac{1}{\kappa_{\text{red}}^{\text{E}}(u)} \right] \frac{\partial u}{\partial \beta}, \quad (6.16)$$

so that finally Eq. (6.15) becomes

$$\frac{\partial u}{\partial \beta} = \left\{ \frac{\partial}{\partial u} \left[\frac{1}{\kappa_{\text{red}}^{\text{E}}(u)} \right] \right\}^{-1} \rho \frac{\partial^2 u}{\partial \rho^2}. \quad (6.17)$$

This relation contains derivatives with respect to both ρ and β and is a PDE of the diffusion type. However, the diffusivity, $D(\rho, \beta) = \left\{ \frac{\partial}{\partial u} \rho \left[\frac{1}{\kappa_{\text{red}}^{\text{E}}(u)} \right] \right\}^{-1}$, is state-dependent¹ and turns out to be

¹Note, that the 'correct' diffusion equation for non-constant diffusivity $D(\rho, \beta)$ would read

$$\frac{\partial u}{\partial \beta} = \frac{\partial}{\partial \rho} \left[D(\rho, \beta) \frac{\partial u}{\partial \rho} \right].$$

negative. $\kappa_{\text{red}}(u)$ is now identified with the expression obtained by the compressibility route (6.12)

$$[\kappa_{\text{red}}^{\text{C}}(u)]^{-1} = 1 - \widehat{\alpha}_{\text{EC}}, \quad (6.18)$$

where $K_{\text{EC}}(u)$ is determined by inverting the result of the energy route

$$u = \frac{\varrho}{\beta} \left\{ \frac{1}{2} \alpha + \frac{\beta \varepsilon}{2 \widehat{\alpha}_{\text{EC}}} [\text{Li}_{3/2}(\widehat{\alpha}_{\text{EC}}) - \widehat{\alpha}_{\text{EC}}] \right\}. \quad (6.19)$$

From the numerical point of view, solving the diffusion-type MFA-based SCOZA-PDE (6.17) is a delicate task, as we have to face the problem of a state-dependent diffusivity $D(\varrho, \beta)$. Since this quantity is even negative (and one would obviously want to solve the parabolic equation starting at $\beta \varepsilon = 0$), not only the solution to the PDE but any numerical error incurred in obtaining it may be expected to grow exponentially. For example, small errors made in the formulation of the boundary conditions and the inversion of the highly non-linear relation (6.19) to determine $D(\varrho, \beta)$ will eventually become dominant. Together, these difficulties make it practically impossible to reliably solve this PDE. Reversing the direction in which the PDE is solved would represent a solution to this problem. Unfortunately, the initial condition for $\beta \varepsilon = \infty$ is not known.

6.3.2 Virial and compressibility route

As an alternative to the approach presented in the preceding subsection, we can calculate the compressibility via the *virial* route, $\kappa_{\mathcal{T}}^{\text{V}}$, which is achieved by differentiating Eq. (6.13) with respect to ϱ ,

$$\begin{aligned} \left(\frac{\partial \beta P}{\partial \varrho} \right)^{\text{V}} &= 1 + \alpha - \frac{1}{2 \sigma^3 \pi^{3/2} K_{\text{VC}}(\varrho, \beta)^2} \left\{ \frac{K_{\text{VC}}(\varrho, \beta)}{\varrho} [\text{Li}_{3/2}(\tilde{\alpha}_{\text{VC}}) - \text{Li}_{1/2}(\tilde{\alpha}_{\text{VC}})] \right. \\ &\quad \left. + \frac{\partial K_{\text{VC}}(\varrho, \beta)}{\partial \varrho} [2 \text{Li}_{3/2}(\tilde{\alpha}_{\text{VC}}) - \text{Li}_{5/2}(\tilde{\alpha}_{\text{VC}}) - \text{Li}_{1/2}(\tilde{\alpha}_{\text{VC}})] \right\}. \end{aligned} \quad (6.20)$$

Equating this result with the compressibility as obtained via the compressibility route (6.12) leads to the following ODE for the unknown function $K_{\text{VC}}(\varrho, \beta)$

$$\frac{\partial K_{\text{VC}}(\varrho, \beta)}{\partial \varrho} = \frac{K_{\text{VC}}(\varrho, \beta) \{ 2 \pi^3 \beta \varepsilon \varrho^2 \sigma^6 K_{\text{VC}}(\varrho, \beta) [K_{\text{VC}}(\varrho, \beta) + 1] - [\text{Li}_{3/2}(\widehat{\alpha}_{\text{VC}}) - \text{Li}_{1/2}(\widehat{\alpha}_{\text{VC}})] \}}{\varrho [2 \text{Li}_{3/2}(\widehat{\alpha}_{\text{VC}}) - \text{Li}_{5/2}(\widehat{\alpha}_{\text{VC}}) - \text{Li}_{1/2}(\widehat{\alpha}_{\text{VC}})]}. \quad (6.21)$$

Analysing the ODE, we note that the right hand side (RHS) of Eq. (6.21) contains two singularities. Obviously the denominator vanishes for $\varrho \rightarrow 0$, but expanding numerator and denominator around $\varrho = 0$, we find that

$$K_{\text{VC}}(\varrho = 0; \beta) = -\frac{4\sqrt{2}}{4\sqrt{2} + \beta \varepsilon}. \quad (6.22)$$

Further, the denominator also vanishes at $\hat{\alpha}_{\text{VC}} = \hat{\alpha}_{\text{VC},0} \approx -7.7982$, a singularity, which, however, turns out to be removable and which can be treated by appropriate means (see below).

This MFA-based SCOZA-ODE (6.21) has the attractive feature that it can be solved for each isotherm independently and represents thus a fast route to determine $K_{\text{VC}}(\varrho, \beta)$. We have used an implicit fourth-order Runge-Kutta algorithm [103] to solve this ODE numerically. In general, this approach works very well except for those state points where the expression in the square brackets of the denominator of the RHS of Eq. (6.21) vanishes. A closer analysis shows that this singularity at $\hat{\alpha}_{\text{VC}} = \hat{\alpha}_{\text{VC},0}$ is removable, since both numerator and denominator vanish simultaneously. In fact, splitting the density range in two regions, depending on whether $\hat{\alpha}_{\text{VC}}$ is smaller or larger than $\hat{\alpha}_{\text{VC},0}$, and integrating the ODE “forward” [starting at $\varrho = 0$ with initial value (6.22)] in the former and “backward” (from a sufficiently high density so that $K_{\text{VC}} = -1$) in the latter, we were able to smoothly join the partial solutions at $\hat{\alpha}_{\text{VC}} = \hat{\alpha}_{\text{VC},0}$ and thus to obtain $K_{\text{VC}}(\varrho, \beta)$ over the entire density range. We point out that reliable solutions of this ODE can only be obtained if an efficient and accurate evaluation of the polylogarithm is guaranteed (cf. Appendix A).

Alternatively, we have also solved this ODE with **MATHEMATICA** using a Livermore solver for ordinary differential equations with automatic method switching (LSODA) [133]. The polylogarithms encountered in the RHS of Eq. (6.21) are evaluated in **MATHEMATICA** with high accuracy (for details see [133]). Although the differential-equation-solver package is not able to deal properly with the removable singularity noted above and breaks down for $\hat{\alpha}_{\text{VC}} \sim \hat{\alpha}_{\text{VC},0}$, outside this small range, **MATHEMATICA** provides quasi-exact reference data for the function $K_{\text{VC}}(\varrho, \beta)$.

6.4 IDE SCOZA approach for the GCM

The IDE-based formulation of the SCOZA, i.e., Eq. (4.25) along with Eq. (4.24), has been solved iteratively using both the MFA-based and the HNC-based closure, i.e., Eq. (4.23) and Eq. (4.26), respectively. We introduce a density grid (with spacing $\Delta\varrho$) and assume a starting value $\bar{K} = -1$. We solve the OZE (4.9) with the appropriate closure relation using standard integral-equation solver algorithms for a given state point (i.e., we fix ϱ and β) and the neighbouring density values (i.e., for $\varrho \pm \Delta\varrho$). Thus, the derivatives on the RHS of Eq. (4.24) can be calculated numerically. Due to the presence of the derivative $\partial\bar{K}/\partial\varrho$, Eq. (4.24) has to be solved iteratively and leads to $\bar{K}(\varrho, \beta)$ for the *entire* density range considered. As a consequence of the iterative and purely numerical character of the solution strategy, this approach is more time consuming than the solution of the ODE (6.21).

6.5 Results of the different SCOZA approaches for the GCM

As a solution to the PDE could not be obtained, we concentrate our discussion on the results of the ODE and the IDE, which represent equivalent approaches to enforcing consistency between

the compressibility and virial routes. Thus, they are expected to lead to identical results. We start by specifying the range in (ϱ, β) -space where the MFA and the MFA-based SCOZA provide unphysical results, i.e., where $g(r)$ also attains negative values (cf. Fig. 6.1). While this failure of the MFA was briefly addressed in [41], we think that a more *quantitative* analysis is in order, since similar problems might be encountered in applications of the MFA (and of related concepts) to other systems with soft potentials. In fact, also for the MFA-based SCOZA unphysical results can be obtained for certain system parameter combinations. For the MFA the limits of this range of unphysical behaviour are easily determined via Eq. (6.3), and for the MFA-based SCOZA they are found from the equivalent, generalised expression (i.e., replacing α by $\hat{\alpha}_{\text{VC}}$). Results are shown in Fig. 6.1, indicating that at low temperatures the MFA and the MFA-SCOZA both become unphysical if the density becomes smaller than some threshold density $\varrho = \varrho(\beta)$. It is interesting to note that similar problems of unphysical solutions for the GCM and thus restricted applicability have also been reported for other self-consistent schemes, such as the RY- or the zero-separation concepts [40].

Detailed numerical investigations have shown that—as expected—the solution to the ODE provides indeed the same results as the one from the IDE. Thus, we present the state-dependent function $K_{\text{VC}}(\varrho, \beta) \equiv \bar{K}(\varrho, \beta)$ as obtained from the solution of the MFA-based SCOZA-PDE (6.21) [and the IDE approach to the MFA-based SCOZA closure (4.23), respectively] in Fig. 6.2 in a representative part of the parameter space. Bearing in mind that the MFA is recovered for $\bar{K}(\varrho, \beta) \equiv -1$, we observe that this function differs substantially from unity at low densities (with a pronounced temperature dependence), thus indicating those regions where the MFA is thermodynamically inconsistent. At high densities we confirm earlier results reported in [40, 41], which have stated that in this regime the MFA becomes exact and thus self-consistent. While in [41] this conclusion was based on an analysis of the high-density behaviour of the function $\aleph(\alpha)$ as defined in Eq. (6.6), our argumentation follows directly from a visual inspection of the function $\bar{K}(\varrho, \beta)$.

Taking into consideration that the virial and the energy route coincide within the MFA, an open question that remains is whether this also holds for the MFA-based SCOZA. In fact, when we take $K_{\text{VC}}(\varrho, \beta)$ as obtained from the ODE (6.21) and insert it into Eq. (6.17), we find that this relation is numerically fulfilled very accurately. This can be seen as an indication that $K_{\text{VC}}(\varrho, \beta)$ imposes thermodynamic consistency between *all three* thermodynamic routes. However, this fact cannot be proven analytically.

For the HNC-based SCOZA, the corresponding function, $\bar{K}_{\text{HNC}}(\varrho, \beta)$ is shown in Fig. 6.3. Taking the deviation of this function from -1 as a measure of the thermodynamic inconsistency of the simple HNC-approach (similar to the case of the MFA), we observe that the HNC is to a large degree self-consistent. It is only at small densities and low temperatures that $\bar{K}_{\text{HNC}}(\varrho, \beta)$ slightly deviates from -1 . This large degree of thermodynamic self-consistency of the HNC for systems with bounded potentials was already observed for selected state points in [40, 41], but was

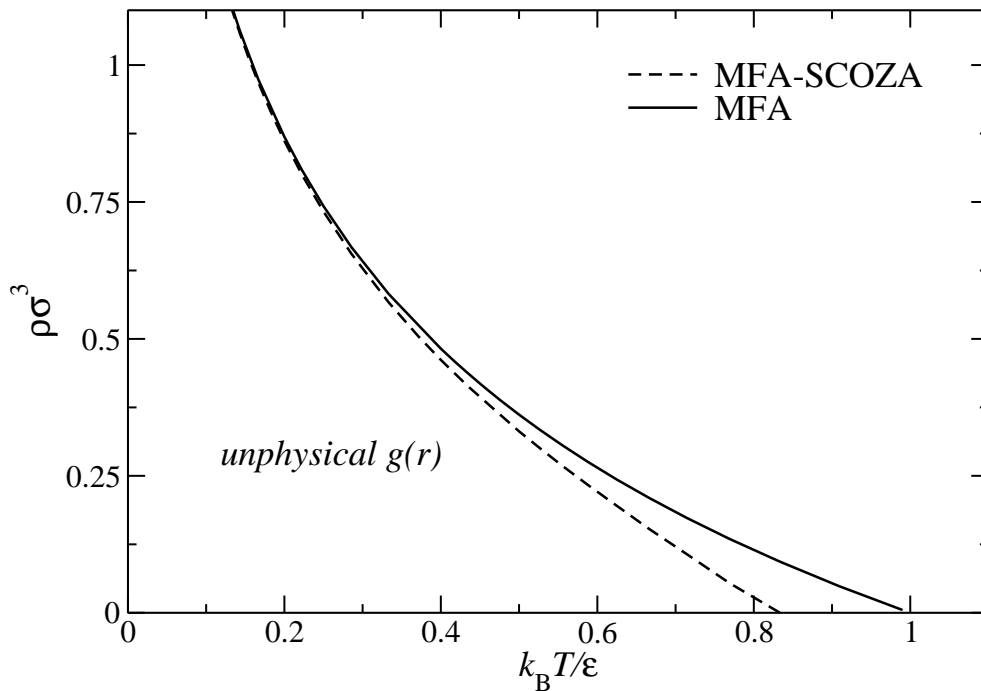


Figure 6.1: Region in the density-temperature space, where the MFA and the MFA-based SCOZA provide unphysical results, i.e., where $g(r)$ attains negative values.

never demonstrated on a quantitative level for a wider range of system parameters.

We conclude our discussion of the thermodynamic self-consistency of the MFA and HNC-based SCOZA concepts by a direct comparison between local and global self-consistency, as defined in Sec. 4.1.7. Let $\bar{K}_g(\varrho, \beta)$ denote the explicitly state-dependent function $\bar{K}(\varrho, \beta)$, as introduced to enforce thermodynamic self-consistency in the IDE formulation of the (MFA- or HNC-based) SCOZA (cf. Sec. 4.1.7). Thus, the subscript 'g' stands for *global* self-consistency. On the other hand, if the last term in Eq. (4.24) is neglected thermodynamic self-consistency is only enforced for a single, isolated state point, and in this case we denote the function by $\bar{K}_l(\varrho, \beta)$ (*local* self-consistency). In Fig. 6.4 we show the relative difference between these functions for the MFA-based SCOZA and we observe that it amounts to at most a few percent and is perceptible only for small densities, even down to intermediate temperatures. Fig. 6.5 shows the same function for the HNC-based SCOZA. Here, the differences become noticeable only at small densities and low temperatures. Thus, over a large parameter range *local* consistency is in both cases already a good substitute for *global* consistency.

We now turn to the structural properties of the GCM by comparing the RDFs for two different thermodynamic states. In Fig. 6.6, we have chosen a state-point ($\beta\varepsilon = 1.1$, $\varrho\sigma^3 = 0.04$) in the regime where MFA is already unphysical, while the MFA-based SCOZA is not (cf. Fig. 6.1). We observe that, compared to the MC reference data, the MFA-based SCOZA provides a slight improvement over the MFA. On the other hand, the results provided by the HNC and the HNC-

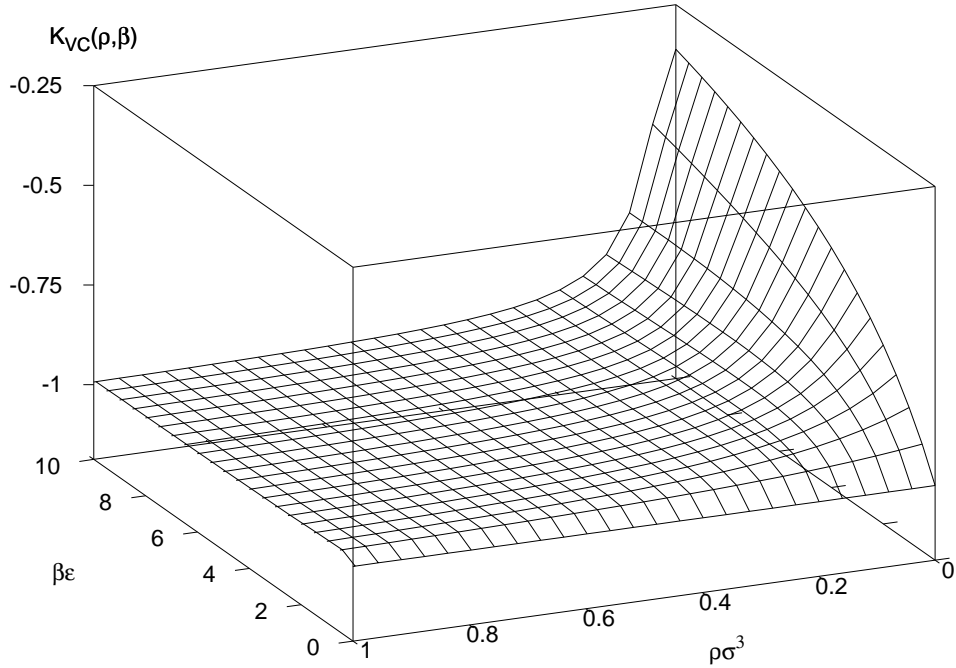


Figure 6.2: $K_{VC}(\rho, \beta) \equiv \bar{K}(\rho, \beta)$ as obtained from the solution of the SCOZA-PDE (6.21) [and the IDE approach to the MFA-based SCOZA closure (4.23), respectively] over a representative range of $\rho\sigma^3$ and $\beta\varepsilon$. Note that $\beta\varepsilon$ is the inverse reduced temperature, i.e., high values of $\beta\varepsilon$ correspond to low temperatures.

based SCOZA both reproduce the MC-data perfectly. Fig. 6.7 shows the RDF for the GCM at a low temperature and low density ($\beta\varepsilon = 10$ equiv. $k_B T = 0.1$, $\rho\sigma^3 = 0.14$). Here, we are in the regime where both the MFA and the MFA-based SCOZA yield unphysical results. We see that while the conventional HNC results already reproduce the MC data rather well, the HNC-based SCOZA leads to a perfect agreement with the simulations. We conclude that although the MFA-based SCOZA for the GCM does not bring along the same improvement for the structural properties as documented for HCY-systems the concept of self-consistency by itself proves to be of great value when used with a closure better adapted to bounded potentials, such as a HNC-based closure.

We conclude this section by examining thermodynamic properties and present the results for the dimensionless equation of state, $\beta P/\rho$, for two different temperatures, i.e., $k_B T/\varepsilon = 10$ (cf. Fig. 6.8) and $k_B T/\varepsilon = 0.1$ (cf. Fig. 6.9 and 6.10). For $k_B T/\varepsilon = 10$, we find that the SCOZA results coincide with high accuracy with the MC data. For $k_B T/\varepsilon = 0.1$ we observe (Fig. 6.9) that the MFA-based SCOZA provides data that are very close to those obtained by simulations, while the HNC-based SCOZA data fit them perfectly. A more detailed comparison, including now also other liquid state theories, such as the MFA, the PY, or the HNC approximations, is displayed on an enlarged scale in Fig. 6.10. We observe that also the virial route of the PY and of the HNC (as expected [40,41]) reproduce the MC data nicely. However, while the SCOZA is self-consistent, this is not the case for the conventional closure relations HNC and PY. Their respective compressibility

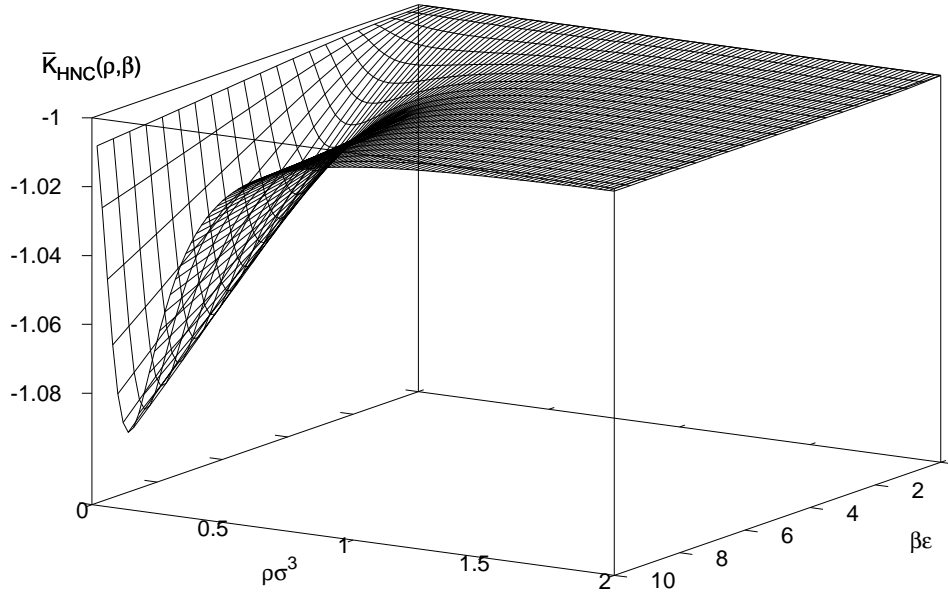


Figure 6.3: $\bar{K}_{\text{HNC}}(\varrho, \beta)$ as obtained from the solution of the IDE approach to the HNC-based SCOZA closure (4.26) over a representative range of $\varrho\sigma^3$ and $\beta\epsilon$. Note that to enhance visibility, the viewpoint is different from the one in Fig. 6.2.

data sometimes differ substantially from their virial and/or energy results (not shown in Fig. 6.10).

Thus, we can conclude that the general concept of the SCOZA *does* achieve an improvement over conventional liquid state theories for a thermodynamically consistent description of the properties of the GCM, in particular if used in combination with a modification of the HNC closure. It is especially remarkable that also the structural properties are enhanced, even though the SCOZA scheme only enforces self-consistency for the thermodynamic properties. Still, it has to be stressed that in contrast to systems with harshly repulsive potentials the improvement of the MFA-based SCOZA approach over the MFA data is less spectacular. While it coincides with the MFA results in the limiting case of high densities where the MFA is already self-consistent, the MFA-based SCOZA only represents a substantial improvement at small densities and low temperatures where the thermodynamic inconsistency of the MFA is more pronounced. Replacing the conventional SCOZA relation by an HNC-type closure that contains an analogous state-dependent function $\bar{K}_{\text{HNC}}(\varrho, \beta)$, we are able to improve the HNC-data for the structural as well as for the thermodynamic properties of the system. With this generalised approach we have not only demonstrated the flexibility and power of the IDE approach but have also proposed what may turn out to become a reliable liquid state theory for systems with bounded potentials.

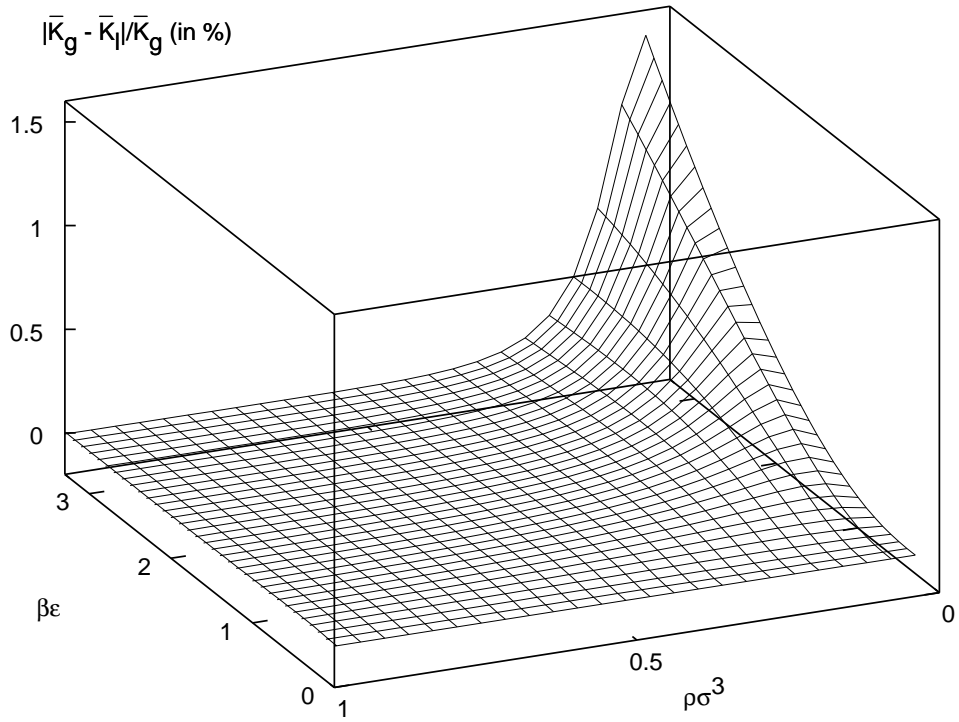


Figure 6.4: Relative difference between the functions $\bar{K}_g(\varrho, \beta)$ and $\bar{K}_l(\varrho, \beta)$ of the MFA-based SCOZA (as defined in the text) over a representative range of $\varrho\sigma^3$ and $\beta\epsilon$.

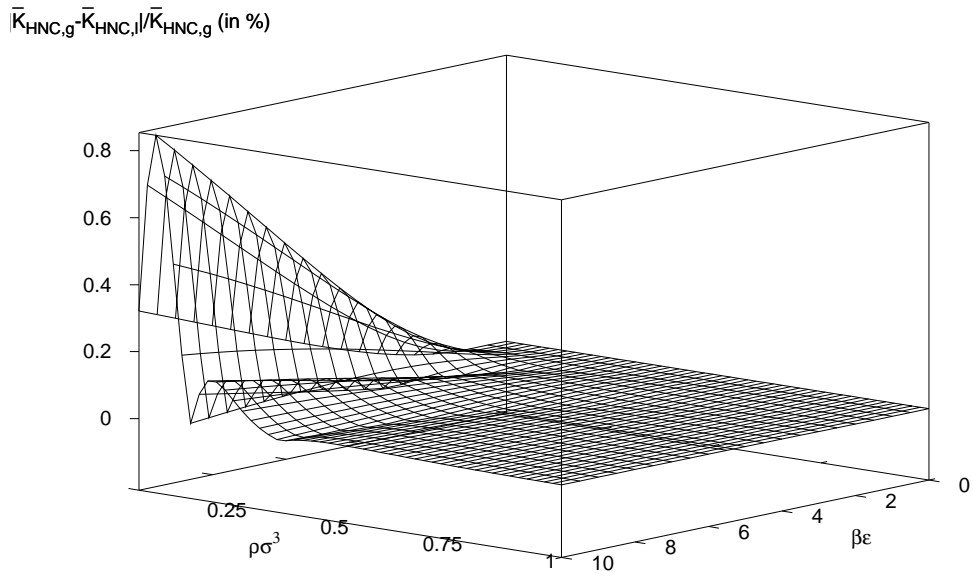


Figure 6.5: Relative difference between the functions $\bar{K}_{\text{HNC},g}$ and $\bar{K}_{\text{HNC},l}$ (as defined in the text) over a representative range of $\beta\epsilon$ and $\varrho\sigma^3$. Note that to enhance visibility, the viewpoint is different from the one in Fig. 6.4.

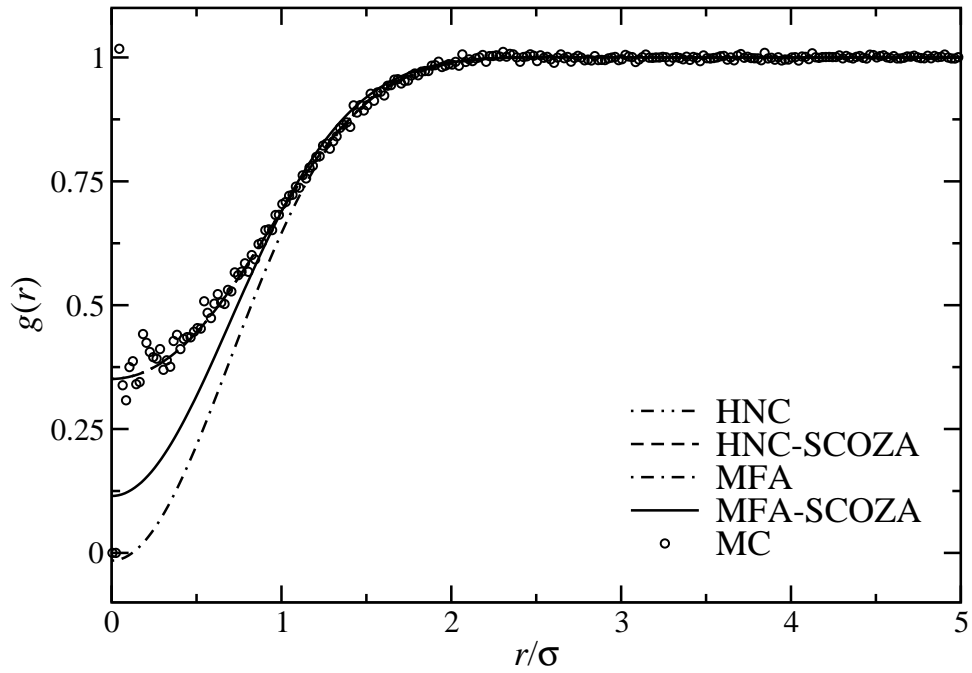


Figure 6.6: RDF $g(r)$ for the GCM at $\beta\varepsilon = 1.1$ and $\rho\sigma^3 = 0.04$. Note that the HNC and the HNC-based SCOZA curves coincide within line thickness.

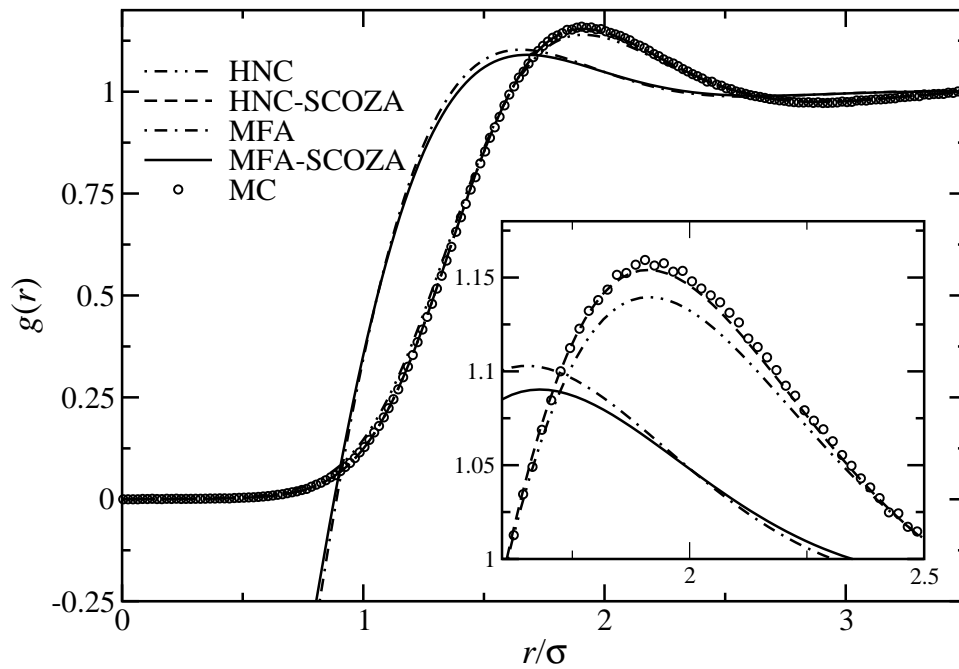


Figure 6.7: RDF $g(r)$ for the GCM at $k_B T / \varepsilon = 0.1$ and $\rho\sigma^3 = 0.14$.

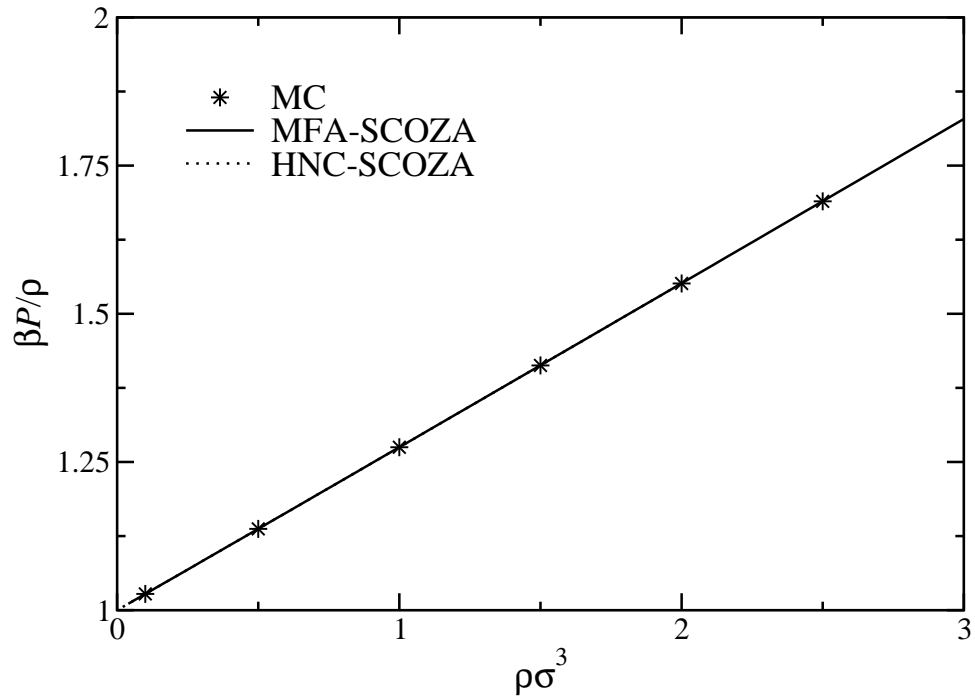


Figure 6.8: $\beta P/\rho$ as a function of $\rho\sigma^3$ for the GCM at $k_B T/\varepsilon = 10$. The results of the MFA- and HNC-based SCOZA coincide. Both SCOZA approaches provide physical data for the RDF [i.e., $g(r) > 0$] over the entire density-range.

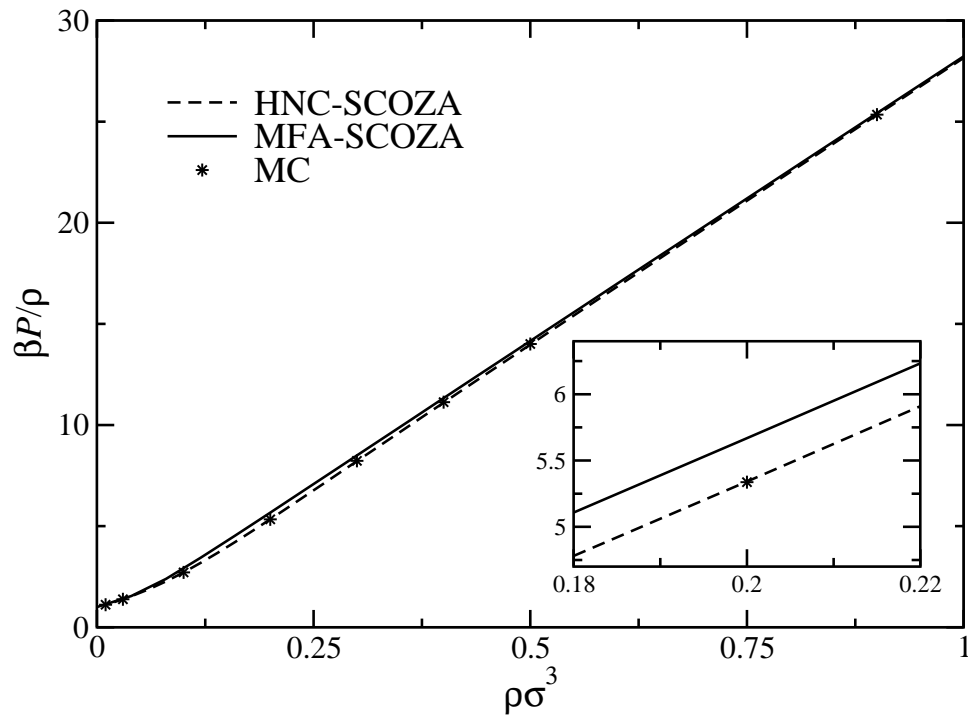


Figure 6.9: $\beta P/\rho$ as a function of $\rho\sigma^3$ at the GCM for $k_B T/\varepsilon = 0.1$. Note that the MFA-based SCOZA provides unphysical results for the RDF [i.e., $g(0) < 0$] for $\rho\sigma^3 \gtrsim 1.27$.

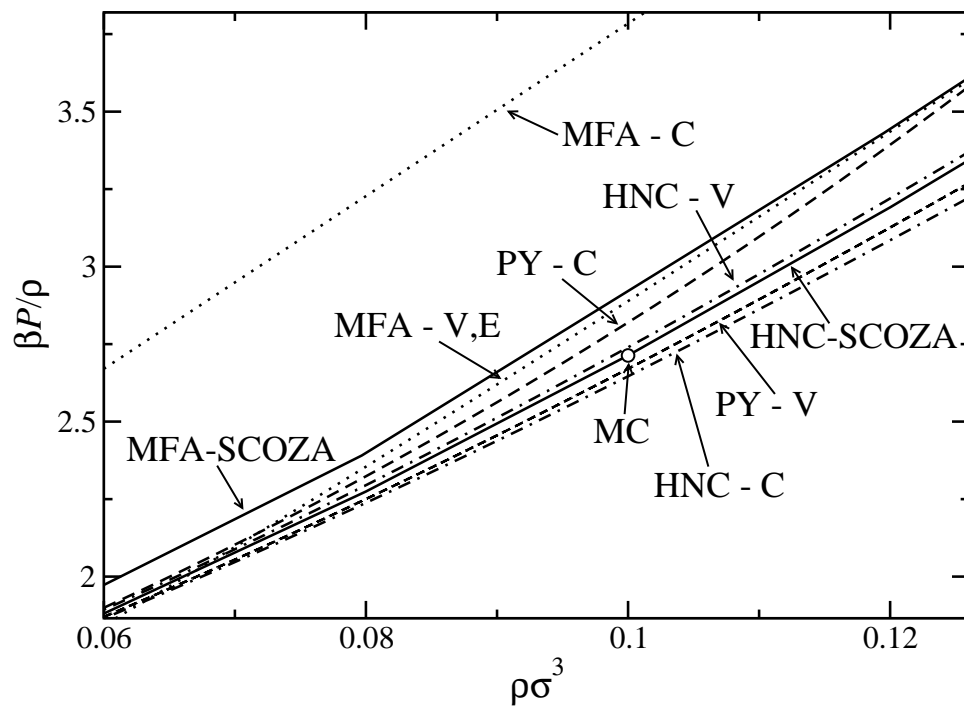


Figure 6.10: Same as Fig. 6.9, showing an enlarged view of a limited $\rho\sigma^3$ -range. Lines and symbols as labelled.

Chapter 7

Clustering

While re-entrant melting has been found in theoretical and experimental studies of various soft matter systems (cf. Sec. 6), clustering has not been observed in experiments or in simulations of monomer-resolved models of macromolecules up to date¹.

Thus, one key question that arises is whether it is possible to *tailor* substances that show clustering. In Sec. 2.5 we showed that the GCM represents the limit of re-entrant melting within the GEM- n family, while other members that are slightly steeper are expected to show clustering. With the aim of *designing* such interactions, we focus on a special class of macromolecules, so-called dendrimers, and investigate in Sec. 7.1 how modifications to the architecture of these substances can affect their interaction potentials and thus their phase behaviour.

In Sec. 7.2, we concentrate on the thermodynamics of clustering systems. Furthermore, in an effort to draw a comprehensive picture of such systems, we thoroughly investigate the properties of a representative model system that is expected to show clustering behaviour in Sec. 7.3.

7.1 Real systems - dendrimers

Dendrimers are synthetic macromolecules characterised by a high degree of monodispersity in both size and shape and a well-defined, highly branched internal structure. Hence their name, which stems from the Greek “ $\tau\delta\delta\acute{\epsilon}\nu\delta\rho\nu$ ”, meaning “tree”. A schematic representation of a dendrimer is shown in Fig. 7.1.

Ever since their first synthesis in 1978 by Vögtle and co-workers [135], dendrimers have rapidly become highly appreciated colloidal systems. One of the reasons for this growing interest in dendrimers was the conjecture that they show a so-called dense-shell conformation, where end-groups reside at the periphery of the macromolecule, leaving the inner part of the macromolecule hollow. This idea was supported by de Gennes *et al.* [136], who predicted this particular conformation

¹A possible verification of repulsion-induced clustering has been observed in two-dimensional electron systems in magnetic fields, with partially filled Landau levels. These give rise to soft effective potentials between the electrons [134], which lead to the formation of cluster or *bubble* solids.

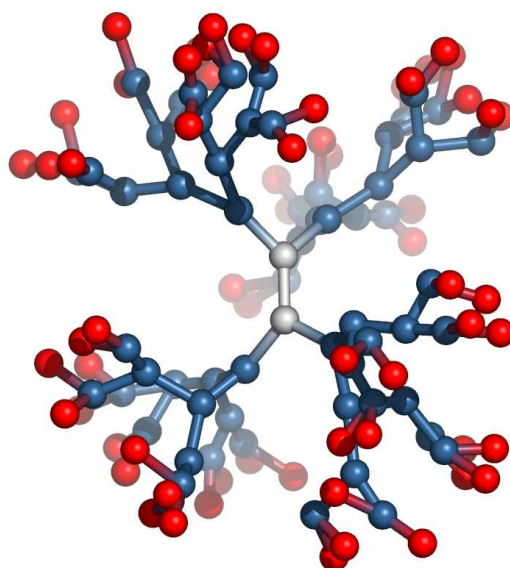


Figure 7.1: Schematic representation of a 5th generation dendrimer in dense-shell configuration.

based on theoretical considerations. Meanwhile, however, it was shown that this study was erroneous. Numerous theoretical and simulation studies confirmed that dendrimers with flexible bonds will exhibit a high degree of back-folding of their end-groups, which mix with the lower-generation monomers in the inner part of the molecule, thereby giving rise to the very compact, so-called dense-core structure [10, 137, 138]. These findings are further supported by a series of small angle neutron scattering (SANS) and SAXS experiments [139–141].

Progress in theory and simulations opened up the possibility to actually *design* dendrimers (and other macromolecules). The ability to directly map chemical structures onto simulation data [10] serves as a guide for synthesis in the lab. In these recent investigations, it was shown that dendrimers do not only exist in the dense-core, but also in the dense-shell conformation. Such an open structure can for instance be realised via the usage of stiff bonds [142], as also confirmed in experiments [143]. In addition, it was shown that changing the pH and/or the salt concentration of the solvent can bring about conformational changes from the dense-core to the dense-shell structure and vice versa [144], a fact which has also been corroborated in experiments [145, 146]. This new insight brought the synthesis of so-called dendritic boxes within reach, which can be used as carrier substances for smaller molecules, boosting once more interest in dendrimers.

Nowadays, dendrimers offer a wide range of technologically and medically relevant applications [147]. Their unique and perfect molecular composition and their high biocompatibility paired with low toxicity make them perfect candidates for use in humans. Typically, dendrimers are used for gene transduction and drug delivery, as bio-sensors or magnetic resonance imaging contrast agents or even for the prevention of infection with HIV or other sexually transmitted diseases [147–154].

Since the synthesis of dendrimers is rather time consuming and expensive, their commercial

availability is up to now limited to only a few substances [155]. Traditionally, dendrimers are grown in a repetitive process based on the activation of the end groups. This is either achieved in a divergent approach, i.e., growing from the central core unit outward, or in a convergent way [156], i.e., from the periphery inward. Especially for high generation dendrimers, this is a cumbersome technique because the chemistry needs to be quantitative since inefficient reactions lead to byproducts and imperfections, giving rise to tedious purification procedures. Recently, however, progress in the synthesis of dendrimers was achieved as it was shown that they can also be grown under accelerated conditions combining so-called Click chemistry [157] with traditional esterification and etherification reactions, where no purification steps are needed [155].

Let us now consider the special architecture of a single dendrimer [10]. Its centre, which represents the particles of generation 0, is a unit of functionality f , where most commonly $f = 3$. From there, f polymer chains consisting of P bonds branch out, where P is the so-called spacer length. At the end of each of these chains, we find another functional unit for the dendrimer to branch out and to build the next generation of monomers. The last-generation monomers are called end-groups. In summary, dendrimers are characterised by three numbers, i.e., the functionality f , the spacer length P and the total number of generations, denoted by G . Then, the total number of monomers forming the macromolecule can be determined via

$$N = 1 + fP \frac{(f-1)^{G+1} - 1}{f-2}. \quad (7.1)$$

The overall size of a dendrimer can be characterised by its radius of gyration, R_g . Let \mathbf{r}_i be the instantaneous positions of the monomers $i = 1, \dots, N$, and let \mathbf{R} be the coordinates of the centre of mass of the dendrimer, then

$$R_g^2 = \frac{1}{N} \left\langle \sum_{i=1}^N (\mathbf{r}_i - \mathbf{R})^2 \right\rangle. \quad (7.2)$$

This quantity can readily be measured in SANS experiments, therefore allowing for direct comparison between theory, simulations and experiments.

Insight into the conformation of the dendrimer, on the other hand, can be gained by studying the monomer density $\varrho(\mathbf{r})$, where \mathbf{r} is the vector connecting the centre of mass of the dendrimer to the reference point. It is given by

$$\varrho(\mathbf{r}) = \left\langle \sum_{i=1}^N \delta(\mathbf{r} - \mathbf{r}_i) \right\rangle, \quad (7.3)$$

where \mathbf{r}_i , $i = 1, \dots, N$, are the coordinates of the monomers of the dendrimer and the $\langle \dots \rangle$ denotes an average over different configurations. $\varrho(\mathbf{r})d\mathbf{r}$ can be interpreted as being proportional to the probability of finding a monomer in the infinitesimal volume $d\mathbf{r}$ around \mathbf{r} . Further, it is also possible to calculate generation resolved density profiles, where especially the end-group distribution contains valuable information on the conformation of the dendrimer, since it allows

to easily see whether the end-groups fold back or remain at the periphery of the molecule.

The form factor of the dendrimer allows for direct comparison between theoretical and experimental studies, since it can be directly measured in scattering experiments. It is defined as

$$F(\mathbf{q}) = 1 + \frac{1}{N} \left\langle \sum_{i=1}^N \sum_{j \neq i}^N e^{[-i\mathbf{q}(\mathbf{r} - \mathbf{r}_{ij})]} \right\rangle. \quad (7.4)$$

Introducing

$$\widehat{G}(\mathbf{r}) = \delta(\mathbf{r}) + \frac{1}{N} \left\langle \sum_{i=1}^N \sum_{j \neq i}^N \delta(\mathbf{r} - \mathbf{r}_{ij}) \right\rangle, \quad (7.5)$$

with \mathbf{r}_{ij} being the distance vector between monomers i and j , we obtain

$$F(\mathbf{q}) = \int d\mathbf{r} \widehat{G}(\mathbf{r}) e^{-i\mathbf{q}\mathbf{r}}. \quad (7.6)$$

7.1.1 Effective interactions

Due to their large number of constituent monomers, dendrimers (and macromolecules in general) are highly complex entities. To be able to gain insight into the equilibrium properties of such systems, one therefore has to resort to coarse-graining procedures [2, 9, 129] which help to reduce the degree of complexity and which we present in the following.

Dendrimers are usually dissolved in solvents of particles that are roughly three orders of magnitude smaller than these macromolecules themselves. We can coarse-grain the problem by treating the solvent as continuum. It is then considered as an effective medium and the solubility of the dendrimers can still be accounted for by a small set of parameters that affect the excluded volume or the form of the monomer-monomer interactions. However, we still have to take into account all microscopic degrees of freedom of the dendrimers themselves, which represents a level of detail we are not interested in. Therefore, it is convenient to choose a set of effective coordinates representing the macromolecule as a whole and average over the degrees of freedom of the constituent monomers. Thereafter, the dendrimers can be regarded as point particles interacting by means of an effective interaction (also called potential of mean force), which includes all effects of the monomers while preserving the thermodynamics of the system.

Let us consider two dendrimers, labelled $\tau = 1, 2$, each consisting of N monomers, labelled $i = 1, \dots, N$, positioned at $\mathbf{r}_{i\tau}$ and with momenta $\mathbf{p}_{i\tau}$. The Hamilton function \mathcal{H} of the system can be split according to

$$\mathcal{H}(\mathbf{r}_1^N, \mathbf{r}_2^N, \mathbf{p}_1^N, \mathbf{p}_2^N) = \mathcal{H}_{11}(\mathbf{r}_1^N, \mathbf{p}_1^N) + \mathcal{H}_{12}(\mathbf{r}_1^N, \mathbf{p}_1^N, \mathbf{r}_2^N, \mathbf{p}_2^N) + \mathcal{H}_{22}(\mathbf{r}_2^N, \mathbf{p}_2^N) \quad (7.7)$$

into the interactions between monomers of the same dendrimer, i.e., \mathcal{H}_{11} and \mathcal{H}_{22} , and a cross-term describing the interactions between monomers of different dendrimers, i.e., \mathcal{H}_{12} . The (canonical)

partition function of the system is given by

$$Q = \frac{1}{h^{6N}} \iint d\mathbf{p}_1^N d\mathbf{p}_2^N d\mathbf{r}_1^N d\mathbf{r}_2^N e^{-\beta\mathcal{H}}. \quad (7.8)$$

Let us now introduce the centre-of-mass densities

$$\hat{\rho}_\tau^{\text{CM}}(\mathbf{R}_\tau) = \delta\left(\mathbf{R}_\tau - \frac{1}{N} \sum_{i=1}^N \mathbf{r}_{i\tau}\right), \quad (7.9)$$

where \mathbf{R}_τ is the centre of mass of dendrimer τ . Keeping the \mathbf{R}_τ fixed at \mathbf{R}_1 and \mathbf{R}_2 , the effective interaction, $\Phi_{\text{eff}}(\mathbf{R}_1, \mathbf{R}_2)$, can be defined as [9]

$$\beta\Phi_{\text{eff}}(\mathbf{R}_1, \mathbf{R}_2) = -\log\left\{\frac{\Omega^2}{Q_1^2 h^{6N}} \iint d\mathbf{p}_1^N d\mathbf{p}_2^N d\mathbf{r}_1^N d\mathbf{r}_2^N \hat{\rho}_1^{\text{CM}}(\mathbf{R}_1) \hat{\rho}_2^{\text{CM}}(\mathbf{R}_2) e^{-\beta\mathcal{H}}\right\}, \quad (7.10)$$

where Ω is the volume of the system, while Q_1 is the partition function of a single dendrimer and is given by

$$Q_1 = \frac{1}{h^{3N}} \iint d\mathbf{p}_1^N d\mathbf{r}_1^N e^{-\beta\mathcal{H}_{11}}. \quad (7.11)$$

Combining Eqs. (7.8) and (7.10), we arrive at

$$Q = \frac{Q_1^2}{\Omega^2} \iint d\mathbf{R}_1 d\mathbf{R}_2 e^{-\beta\Phi_{\text{eff}}(\mathbf{R}_1, \mathbf{R}_2)}. \quad (7.12)$$

As the effective potential only depends on the separation $R = |\mathbf{R}_1 - \mathbf{R}_2|$ between two dendrimers, we can write $\Phi_{\text{eff}}(\mathbf{R}_1, \mathbf{R}_2) = \Phi_{\text{eff}}(R)$.

Since the effective potential has the form of a Landau free energy, it cannot be computed directly in simulations (cf. Sec. 5.5). Therefore, special techniques are required (cf. Sec. 5.5), such as relating $\Phi_{\text{eff}}(R)$ to the correlation function $G(R)$ between the centres of mass via

$$G(R) \propto e^{-\beta\Phi_{\text{eff}}(R)}. \quad (7.13)$$

This then allows for an efficient determination of $\Phi_{\text{eff}}(R)$ within simulations.

7.1.2 Athermal dendrimers

In the literature, several studies on so-called athermal dendrimers can be found. Here, bead-spring models were considered [9], where the monomer excluded volume was either modelled as a hard sphere or a Lennard Jones interaction, while the spacers were described via threads or a finite nonlinear extensible elastic model (see below). Computer simulations showed that the effective interactions of these macromolecules do not depend on the details of the model used and can be described by Gaussians with very high accuracy. The strength of the effective repulsion was found to be dependent on the spacer length, where shorter spacers bring about more repulsive potentials due to increased crowding in the centre of the macromolecule. This fact allows to

tune the interactions to a certain extent. Due to the Gaussian shape of the effective interaction, we expect these dendrimers to show re-entrant melting (cf. Sec. 6). Closely linked with these findings is the dense-core structure of these dendrimers, arising from back-folding of the terminal groups [9, 10, 138].

Since the calculation of the effective potential outlined in Sec. 7.1.1 is a *pair* potential approximation, the question of its validity arises. Which role do many-body forces play as soon as more than two dendrimers interact? In [158], Götze and Likos compared results from simulations of point particles interacting via the coarse-grained, Gaussian effective interaction with data obtained from monomer resolved simulations of several hundred athermal dendrimers. They found that similar to the case of polymer chains, the effective interaction describes the behaviour of dendrimers very well in the dilute regime. Beyond the overlap density the dendrimers slightly reduce their radius of gyration as a reaction to the diminished amount of space available to them, which has to be taken into account when setting the length-scale of the coarse-grained potential. This shows that the assumption of a pair potential as an effective interaction is successful even in highly concentrated dendrimer solutions [158].

Last, results for the structure factor obtained from simulations with the effective interaction are also in good agreement with SANS data [129], thus once more confirming the validity of the Gaussian shape of the effective interaction for this kind of dendrimers.

7.1.3 Amphiphilic Dendrimers

As we discussed in Sec. 2.2, clustering is predicted for purely repulsive, bounded potentials with *oscillatory* Fourier transforms. The intuitively expected formation of stable clusters in the presence of short-range attractions and long-range repulsions, as predicted by theory and simulations [159], has found experimental verification [160]. However, systems displaying solely *repulsion-induced* aggregation have not been discovered to-date. In this work, we show that dendrimers are suitable colloids for the experimental realisation of this phenomenon if their architecture is modified in suitable ways.

Our studies are motivated by the Flory theory for the effective interactions between athermal dendrimers [129], which is based on the fact that the monomer density profile of a single dendrimer, $\varrho(\mathbf{r})$, is a Gaussian. Considering two such dendrimers separated by distance \mathbf{R} and *assuming* that their profiles are not distorted by their mutual presence, the effective interaction between the two dendrimers takes the form

$$\Phi_{\text{eff}}(\mathbf{R}) = \iint d\mathbf{r}_1 d\mathbf{r}_2 \varrho(\mathbf{r}_1) \varrho(\mathbf{r}_2 - \mathbf{R}) \phi(|\mathbf{r}_1 - \mathbf{r}_2|), \quad (7.14)$$

where $\phi(|\mathbf{r}_1 - \mathbf{r}_2|)$ is the monomer-monomer interaction. By introducing a Flory-type interaction potential, $\beta\phi(|\mathbf{r}_1 - \mathbf{r}_2|) = v_0\delta(|\mathbf{r}_1 - \mathbf{r}_2|)$, with a monomer-monomer excluded volume parameter

$v_0 > 0$, the integral in Eq. (7.14) reduces to a simple convolution

$$\beta\Phi_{\text{eff}}(\mathbf{R}) = v_0 \int d\mathbf{r}_1 \varrho(\mathbf{r}_1) \varrho(\mathbf{r}_1 - \mathbf{R}). \quad (7.15)$$

Assuming radial symmetry, the Fourier transform of $\Phi_{\text{eff}}(R)$ has the form

$$\beta\tilde{\Phi}_{\text{eff}}(q) = v_0 \tilde{\varrho}^2(q). \quad (7.16)$$

From this equation it can be seen that due to the presence of the square on the right-hand side $\tilde{\Phi}_{\text{eff}}(q)$ is strictly positive, so there is no possibility of realising a Q^\pm -interaction within this framework.

In the following we want to generalise the Flory model to amphiphilic dendrimers, which consist of a solvophobic core that we label 'C' and a solvophilic shell, labelled 'S'. This means that we now have to introduce *three* different Flory potentials, characterised by the respective excluded volume parameters, v_{CC} , v_{CS} , and v_{SS} . Proceeding along similar lines as above leads to the Fourier transform of the effective interaction between our amphiphilic dendrimers

$$\beta\tilde{\Phi}_{\text{eff}}(q) = v_{CC}\tilde{\varrho}_C^2(q) + 2v_{CS}\tilde{\varrho}_C(q)\tilde{\varrho}_S(q) + v_{SS}\tilde{\varrho}_S^2(q), \quad (7.17)$$

where the $\tilde{\varrho}_\tau(q)$ are the Fourier transforms of the individual density profiles $\varrho_\tau(r)$, $\tau = C, S$. Due to their solvophobicity, the core regions try to arrange themselves close to each other in order to minimise their surface facing the solvent, thus, $v_{CC} < 0$. The other parameters are purely repulsive, i.e., v_{CS} and $v_{SS} > 0$. Therefore, $\tilde{\Phi}_{\text{eff}}(q)$ is not necessarily positive, offering the possibility to parameterise Q^\pm -interactions within our generalised Flory theory.

To justify our approach we recall that the Gaussian effective interaction is at the threshold to clustering (cf. Sec. 2.5). Thus, we require the following changes in $\Phi_{\text{eff}}(r)$ to achieve clustering behaviour: a flatter core region, such as those of, e.g., GEM- n potentials with $n > 2$, which—compared to a Gaussian—also display a steeper decay of the repulsion for larger separations. Alternatively, a positive effective interaction with a local *minimum* at $r = 0$ also leads to oscillations in $\tilde{\Phi}_{\text{eff}}(q)$, as we have $\Phi_{\text{eff}}''(r = 0) > 0$ in that case².

To realise this goal, we aim for a more open structure and stronger segregation between outer and inner particles. As we are going to show, this can be realised by assembling the aforementioned amphiphilic dendrimers. In Fig. 7.2, we qualitatively illustrate how our modifications lead in the correct direction. As the macromolecules start overlapping, the solvophilic, mutually repulsive shells cause a steeply increasing potential wall. This effect is reinforced upon further decreasing the distance since core and shell repel each other due to their different nature. Eventually, the attractive core regions overlap and slow down further growth of the repulsion, leading to a rather flat region or even a local minimum in $\Phi_{\text{eff}}(r)$ at small distances.

²These functional forms can be realised for instance by members of the double Gaussian core model (cf. Sec. 2.4).

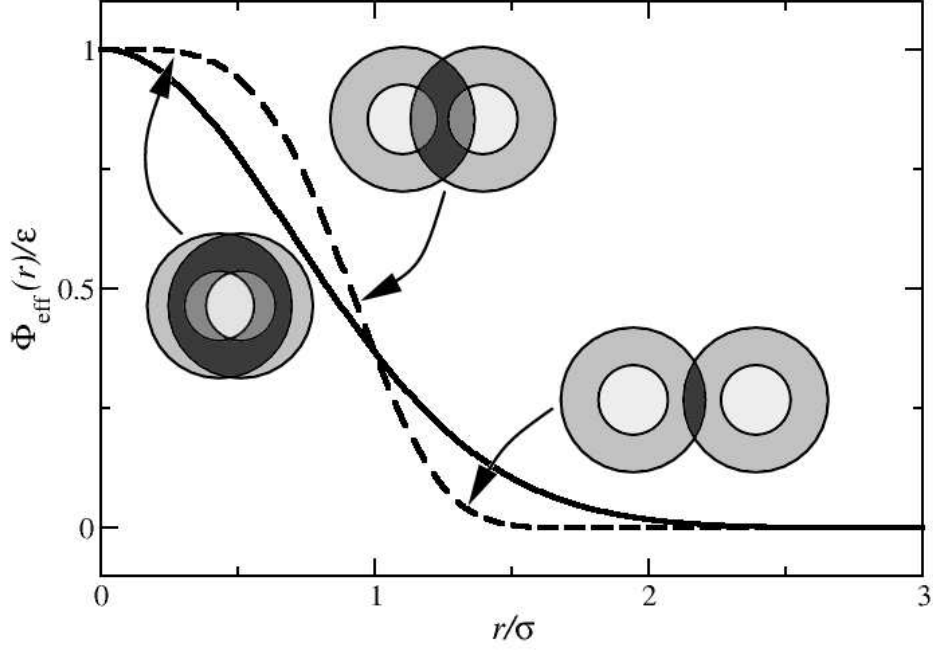


Figure 7.2: Different interactions between the solvophobic core (light grey) and the solvophilic shell (darker grey) region of our amphiphilic dendrimers lead to an effective interaction (dashed line) that is steeper than a Gaussian (solid line) at intermediate, and flatter at small distances. ε and σ are characteristic energy and length scales.

With this in mind we study the effective interactions between dendrimers in MC simulations. For this purpose, we decide to model second generation amphiphilic dendrimers (i.e., $G = 2$) consisting of *two* central units *in silico*. Further, we choose the spacer length to be $P = 1$ and the functionality as $f = 3$. Therefore, the number of particles in the macromolecule is given by

$$N = 2^{G+2} - 2. \quad (7.18)$$

We choose the end-groups to form the shell, while all inner monomers represent the core.

The bonds between monomers are modelled by the finitely extensible nonlinear elastic (FENE) potential [10, 144]

$$\beta\phi_{\tau\nu}^{\text{FENE}}(r) = -K_{\tau\nu}R_{\tau\nu}^2 \log \left[1 - \left(\frac{r - l_{\tau\nu}^0}{R_{\tau\nu}} \right)^2 \right], \quad \tau\nu = \text{CC}, \text{CS}, \quad (7.19)$$

which is similar to a harmonic spring potential but restricts the bond-length to be in the interval $[l_{\tau\nu}^{\text{max}}, l_{\tau\nu}^{\text{min}}]$. $K_{\tau\nu}$ is the spring constant and $R_{\tau\nu} = l_{\tau\nu}^{\text{max}} - l_{\tau\nu}^0$, with $l_{\tau\nu}^0 = (l_{\tau\nu}^{\text{max}} + l_{\tau\nu}^{\text{min}})/2$ being the equilibrium bond length. All other interactions between monomers separated by a distance r are

Morse	ε	αd_{CC}	d/d_{CC}
CC	0.714	6.4 ($D_1 - D_4, D_6, D_7$) 4.8 (D_5)	1
CS	0.014	19.2	1.5 ($D_3 - D_6$) 1.25 (D_1, D_2, D_7)
SS	0.014	19.2	2 ($D_3 - D_6$) 1.5 (D_1, D_2, D_7)
FENE	K/d_{CC}^2	l_0/d_{CC}	R/d_{CC}
CC	40 ($D_1, D_2, D_4 - D_7$) 80 (D_3)	1.875	0.375
CS	20	3.75 ($D_1 - D_6$) 2.8125 (D_7)	0.75 ($D_1 - D_6$) 0.5625 (D_7)
ZZ	40 ($D_1, D_2, D_4 - D_7$) 80 (D_3)	2.8125 ($D_1, D_3 - D_5$) 1.875 (D_2, D_6, D_7)	0.5625 ($D_1, D_3 - D_5$) 0.375 (D_2, D_6, D_7)

Table 7.1: Potential parameters [cf. Eqs. (7.19) and (7.20)] of the dendrimers considered in this work. Parameter sets are labelled D_1 to D_7 . ZZ refers to the two central monomers.

modelled by the Morse potential [10, 144]

$$\beta\phi_{\tau\nu}^{\text{Morse}}(r) = \varepsilon_{\tau\nu} \left\{ \left[e^{-\alpha_{\tau\nu}(r-d_{\tau\nu})} - 1 \right]^2 - 1 \right\}, \quad \tau\nu = \text{CC, CS, SS}, \quad (7.20)$$

which is characterised by a repulsive core at short and an attractive tail at long distances whose depth and range are parameterised by $\varepsilon_{\tau\nu}$ and $\alpha_{\tau\nu}$, respectively. The $d_{\tau\nu}$ are the monomer diameters. We modelled seven different dendrimers, labelled D_1 to D_7 , studying the influence of changes in, e.g., spacer-lengths or monomer size. The respective potential parameters are summarised in Tab. 7.1 and are within the limits of what can be realised experimentally [144]. A sketch of our dendrimer model can be seen in Fig. 7.3.

Employing Metropolis MC simulations of a single dendrimer, we can now measure the density profiles $\rho_C(r)$ and $\rho_S(r)$ which are depicted in Figs. 7.5, 7.9, 7.13, 7.17, 7.21, 7.25 and 7.29, for the dendrimers D_1 to D_7 . We observe that in all cases that both profiles can be approximated with high accuracy by a Gaussian shape.

Comparing the density profiles of amphiphilic and athermal dendrimers in Fig. 7.4, we find that due to the amphiphilic nature of our dendrimers and in striking contrast to the results of athermal dendrimers, the core and shell particles are *indeed* more segregated. The distributions of the core monomers have their maximum close to the origin, while the profiles of the shell particles are centred around $r \sim 0.85R_g$ to R_g (cf. Tab. 7.2). Thus, amphiphilicity prevents the end-groups from folding back to the centre, leading now to a rather open, dense-shell configuration. Snapshots of the various amphiphilic dendrimers, which are presented in Figs. 7.7, 7.11, 7.15, 7.19, 7.23, 7.27 and 7.31, illustrate the spherical shape of the molecules and thus justify the assumption of radially symmetric density profiles.

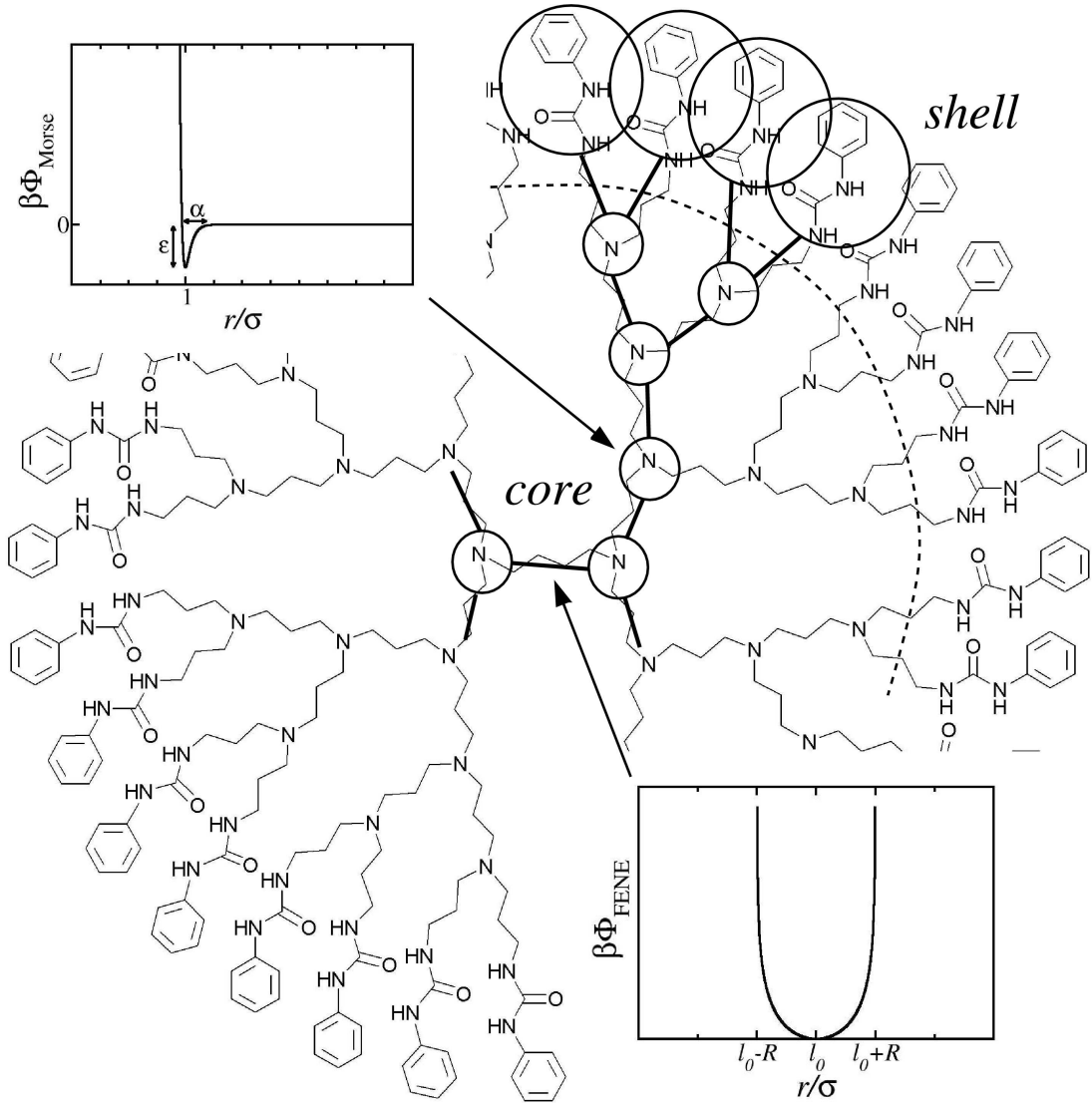


Figure 7.3: A sketch of the dendrimer model used in this work. We show a fourth generation dendrimer. The end-groups form the shell, while the inner monomers represent the core. Bonds are modelled via a FENE potential, while all other interactions are described by a Morse potential. In the background, we show the chemical structure of a real dendrimer (courtesy M. Ballauff [10]).

Encouraged by these results, we model the monomer densities $\varrho_\tau(\mathbf{r})$ within our generalised Flory theory as Gaussian functions

$$\varrho_\tau(r) = S_\tau e^{-\gamma_\tau(r-r_\tau)^2}, \quad (7.21)$$

$\tau = \text{C, S}$. The values for S_τ , γ_τ and r_τ are obtained by fits to the simulation data and are given

dendrimer	$S_\tau R_g^3$	$\gamma_\tau R_g^2$	r_τ/R_g	dendrimer	$S_\tau R_g^3$	$\gamma_\tau R_g^2$	r_τ/R_g
D_1 : ϱ_C	6.719	4.057	0.074	D_5 : ϱ_C	7.554	4.123	0.051
ϱ_S	0.681	2.917	0.873	ϱ_S	0.685	3.554	0.930
D_2 : ϱ_C	9.760	5.025	0.049	D_6 : ϱ_C	10.323	5.500	0.061
ϱ_S	0.666	3.751	0.958	ϱ_S	0.667	4.190	0.996
D_3 : ϱ_C	6.857	4.411	0.093	D_7 : ϱ_C	6.219	4.810	0.122
ϱ_S	0.683	3.450	0.924	ϱ_S	0.693	2.942	0.865
D_4 : ϱ_C	6.985	4.220	0.077				
ϱ_S	0.685	3.486	0.923				

Table 7.2: Fitting parameters for the density profiles of the core and the shell regions of the seven dendrimers considered, assuming a Gaussian profile, $\varrho_\tau(r) = S_\tau \exp[-\gamma_\tau(r - r_\tau)^2]$, $\tau = C, S$. The respective radii of gyration, R_g , of the dendrimers are given in Tab. 7.3.

	D_1	D_2	D_3	D_4	D_5	D_6	D_7
R_g/d_{CC}	3.54	3.36	3.61	3.62	3.59	3.43	2.91

Table 7.3: Radii of gyration R_g for the amphiphilic dendrimers D_1 to D_7 .

in Tab. 7.2. The Fourier transforms of these densities are approximately given by [161]

$$\tilde{\varrho}_\tau(q) = \tilde{\varrho}_\tau(0) \frac{e^{-\frac{q^2}{2\gamma_\tau}}}{\frac{1}{2\gamma_\tau} + r_\tau^2} \left[\frac{\cos(qr_\tau)}{2\gamma_\tau} + \frac{r_\tau^2 \sin(qr_\tau)}{qr_\tau} \right], \quad (7.22)$$

with

$$\tilde{\varrho}_\tau(0) = 2\pi S_\tau \left[\frac{r_\tau e^{-\gamma_\tau r_\tau^2}}{\gamma_\tau} + \frac{\sqrt{\pi} (1 + 2\gamma_\tau r_\tau^2) [1 + \text{erf}(\sqrt{\gamma_\tau r_\tau^2})]}{2\gamma_\tau^{3/2}} \right]. \quad (7.23)$$

The excluded volume parameters $v_{\tau\nu}$ with $\tau\nu = CC, CS,$ or SS in Eq. (7.17) are given by the second virial coefficients [162]

$$v_{\tau\nu} = \int d\mathbf{r} \left[1 - e^{-\beta\phi_{\tau\nu}(r)} \right], \quad (7.24)$$

where $\phi_{\tau\nu}(r)$ are the *non-bonded* monomer-monomer interactions. We find that $v_{CC}/d_{CC}^3 = -1.90$ ($D_1 - D_4, D_6, D_7$) or -4.33 (D_5). Further, $v_{SS}/d_{CC}^3 = 11.31$ (D_1, D_2) or 28.40 ($D_3 - D_7$). Finally, $v_{CS}/d_{CC}^3 = 6.25$ (D_1, D_2) or 11.31 ($D_3 - D_7$). Thus, we have all the ingredients to calculate $\tilde{\Phi}_{\text{eff}}(q)$ and hence $\Phi_{\text{eff}}(r)$ within the scope of the Flory theory [cf. Eq. (7.17)].

To put this extension of the Flory theory to the test, we perform umbrella sampling simulations as explained in Sec. 5.5.4. The maximum separation of the dendrimers is chosen to be $R_m = 5R_g$. For each of the 15 slightly overlapping umbrella windows, simulations of 2×10^8 MC sweeps are performed and $P(r)$ is determined to within an additive constant due to normalisation. Then, $\beta\Phi_{\text{eff}}(r)$ is evaluated via Eq. (5.65). The results for the seven dendrimers specified in Tab. 7.1 are shown in Figs. 7.7, 7.11, 7.15, 7.19, 7.23, 7.27 and 7.31.

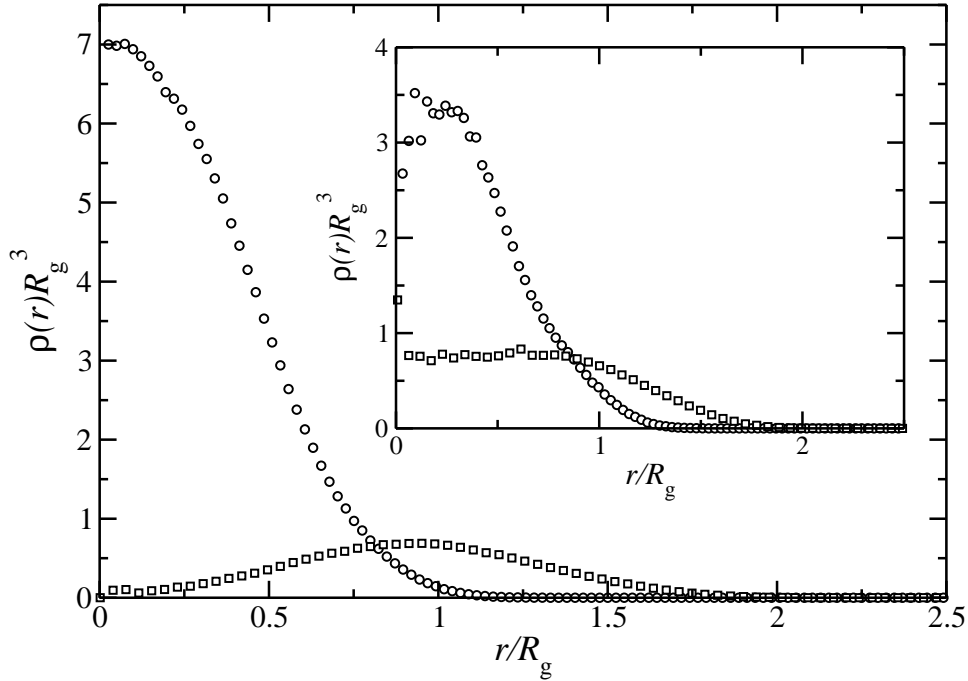


Figure 7.4: Monomer density profiles of the core (circles) and the shell region (squares) for a typical amphiphilic dendrimer (D_4) in comparison with an athermal dendrimer for $G = 2$ (inset). Distances are scaled to the respective radii of gyration.

dendrimer	$a/k_B T$	b/R_g	$c/k_B T$	d/R_g
D_1	7.544	1.149	6.291	1.004
D_2	27.77	1.098	26.693	1.049
D_5	22.773	1.158	20.468	1.066
D_6	36.702	1.159	33.741	1.096

Table 7.4: Fit parameters for the effective interactions of dendrimer D_1 , D_2 , D_5 and D_6 assuming a DGCM type of interaction with $\Phi(r) = a \exp[-(r/b)^2] - c \exp[-(r/d)^2]$.

The effective interactions indeed show a steep increase as the macromolecules approach each other and eventually become rather flat or even exhibit a locally attractive dip for smaller distances. To classify these interactions within known families of functional forms, we fit them to members of the GEM- n and DGCM potentials and present the fitting parameters in Tabs. 7.4 and 7.5. Since for all fits $\Phi''_{\text{eff}}(r=0) > 0$, the clustering character of these potentials is confirmed. This is further corroborated by the fact that the Fourier transforms exhibit negative components, as can easily be seen in Figs. 7.8, 7.12, 7.16, 7.20, 7.24, 7.28 and 7.32.

Finally, we compare our MC data to the results of the modified Flory theory. Differences between the two data sets can be attributed to the simplifying assumptions of Flory theory that the monomer densities of the isolated dendrimers do not change upon close interaction with other dendrimers and that the monomer-monomer interaction can be expressed by a Dirac delta function

dendrimer	$a/k_{\text{B}}T$	b/R_{g}	n
D_3	3.059	1.665	3.09
D_4	3.045	1.658	3.11
D_7	2.725	1.641	3.16

Table 7.5: Fit parameters for the effective interactions of dendrimer D_3 , D_4 and D_7 assuming a GEM- n type of interaction with $\Phi(r) = a \exp[-(r/b)^n]$.

weighted by the second virial coefficient of the full inter-monomer potential [162]. In view of these simplifying assumptions, the good qualitative agreement between simulations and theory is astonishing. Since the negative Fourier components, shown in Figs. 7.8, 7.12, 7.16, 7.20, 7.24, 7.28 and 7.32, are less pronounced within Flory theory than in the MC data, the former provides a comfortable lower threshold indicating the onset of the clustering phenomenon.

To motivate possible experimental realisations let us summarise our guidelines for assembling clustering dendrimers. In a first step, suitable solvophobic core and solvophilic shell groups have to be chosen, based on the expertise of experimentalists. For these, simulations on an isolated dendrimer are performed, leading to the core- and shell-density profiles. While Flory theory provides a reliable qualitative indicator whether the threshold to clustering has already been reached, full evidence can then be gathered by measuring the effective interactions in the more time-consuming simulations of two interacting dendrimers. From our observations for all dendrimers investigated, the following remarks on the trends of the effective interaction upon changing the dendrimers' architecture should prove useful:

- Bigger end-groups and/or shorter spacer lengths of the end-groups lead to a stronger repulsion in $\Phi_{\text{eff}}(r)$ at short distances.
- If the spacer length of the end-groups is increased and/or the distance between the two central particles and/or the end-group particle size is reduced, $\Phi_{\text{eff}}(r)$ becomes flatter or even develops a dip at small distances.
- Alternatively, if the range of the attraction is reduced and/or the size of the end-groups is reduced, $\Phi_{\text{eff}}(r)$ also becomes flatter or even develops a dip at small distances.

The fact that only a small number of generations is sufficient to lead to clustering is encouraging for experimentalists because it hints at a rather straightforward synthesis process [155]. Since $\Phi_{\text{eff}}(r=0) \sim k_{\text{B}}T$, clustering can easily be realised under ambient conditions in thermally activated processes.

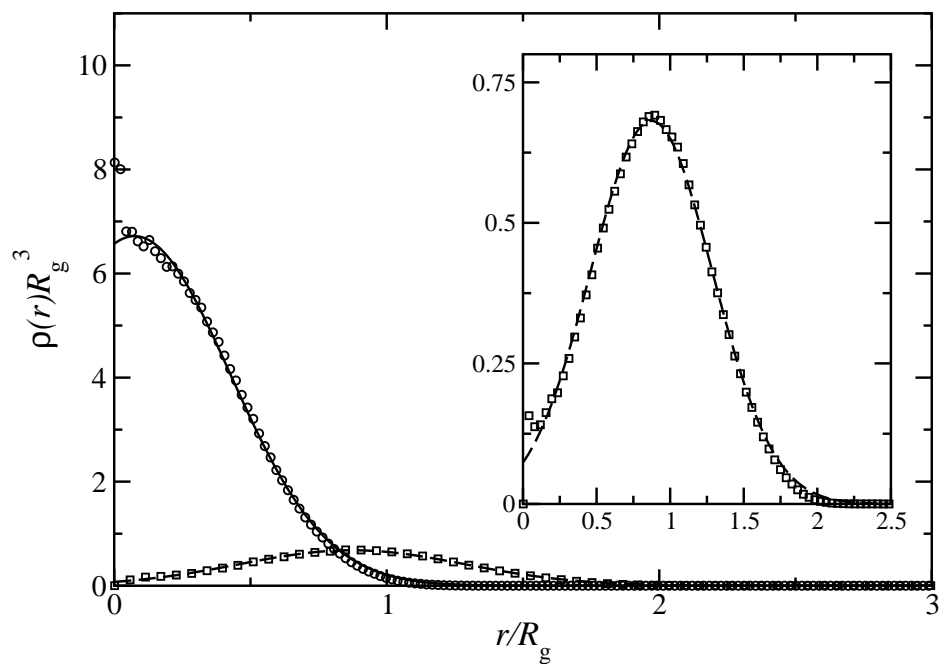


Figure 7.5: The density profiles of dendrimer D_1 for the core (circles) and the shell (squares) region according to MC simulations (symbols) and fitted to Gaussian functions (lines). The inset shows a close-up of the shell density profile.

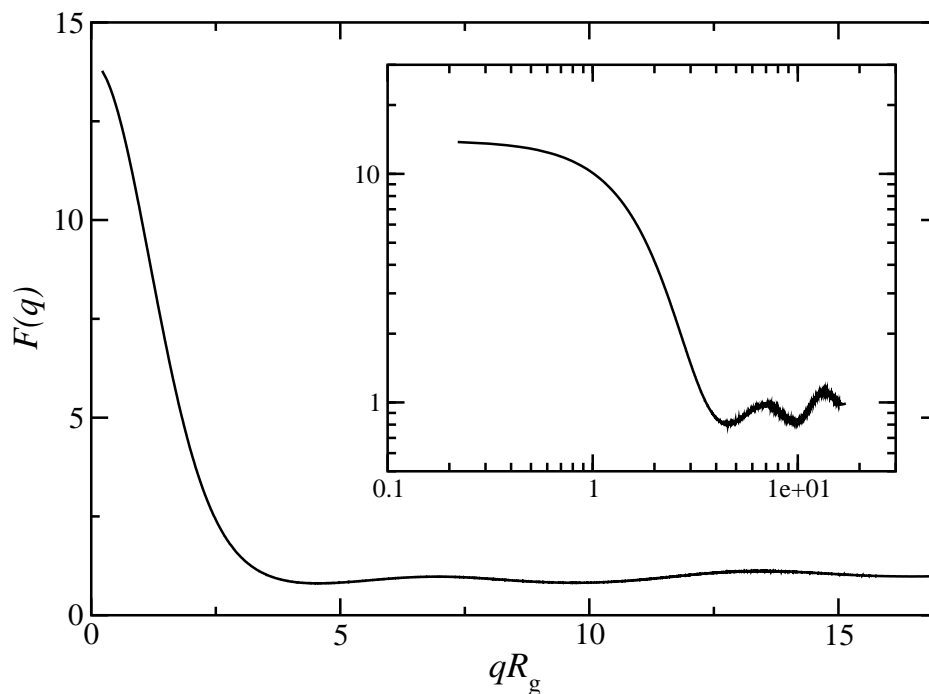


Figure 7.6: The form factor of dendrimer D_1 . The inset shows a close-up on the oscillations observed in a double logarithmic plot.

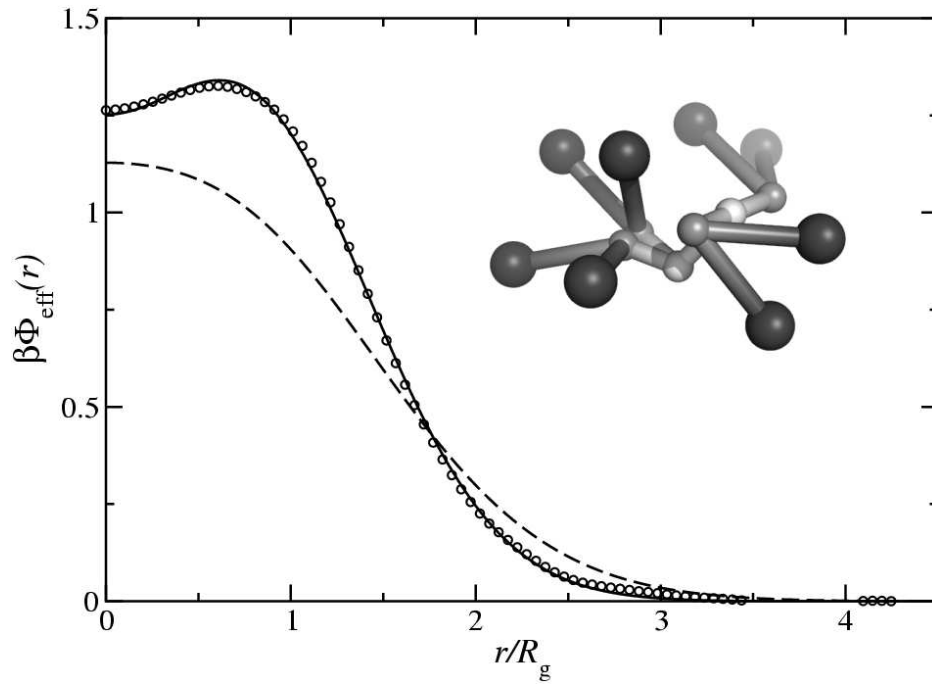


Figure 7.7: Dimensionless effective interaction $\beta\Phi_{\text{eff}}(r)$ between two D_1 dendrimers obtained by MC simulations [symbols, DGCM fit - solid line] and by the modified Flory theory (dashed line). The inset shows a simulation snapshot of a D_1 dendrimer. Particle diameters are drawn to scale.

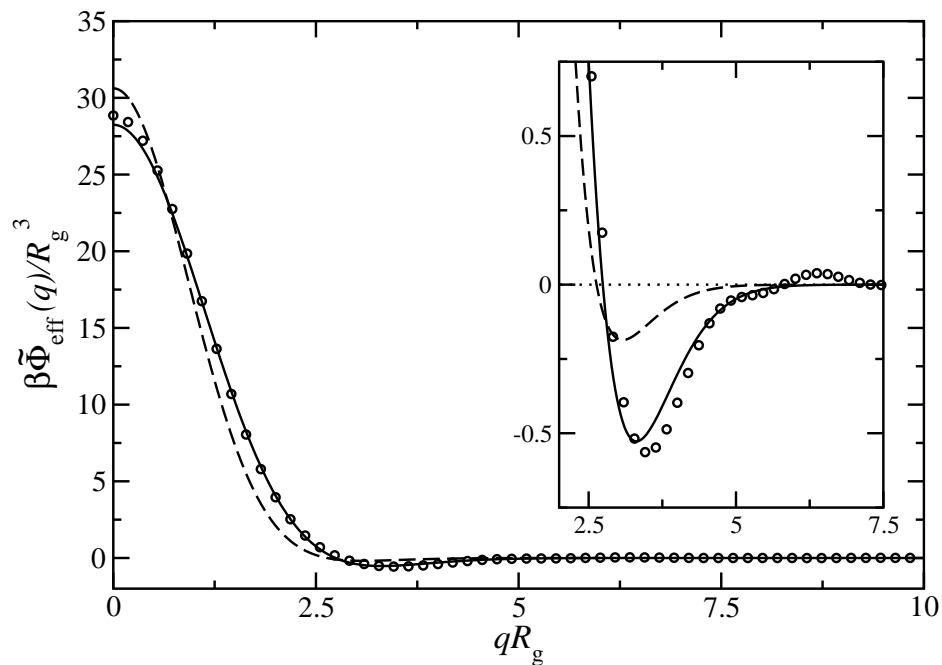


Figure 7.8: The Fourier transform of the effective interaction between two D_1 dendrimers obtained by MC simulations [symbols, DGCM fit - solid line] and by the modified Flory theory (dashed line).

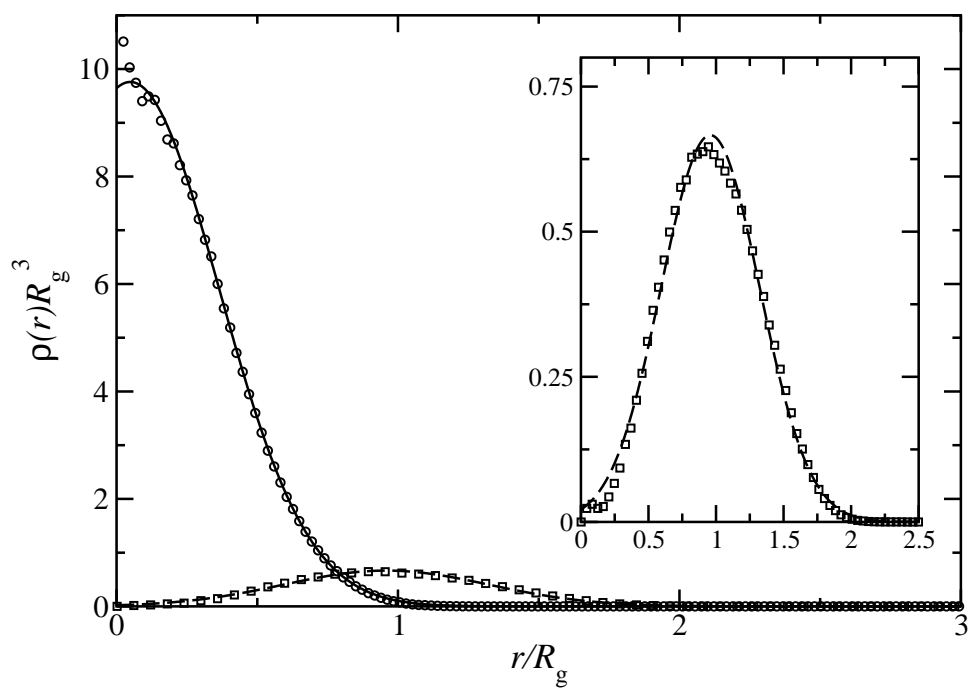


Figure 7.9: Same as Fig. 7.5 but for D_2 .

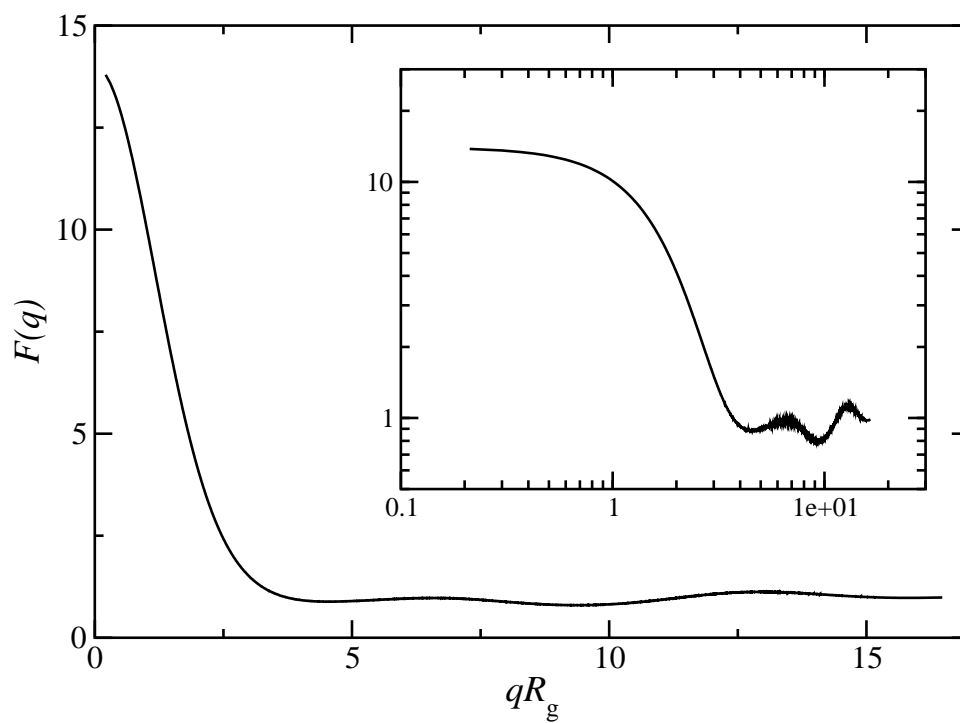


Figure 7.10: Same as Fig. 7.6 but for D_2 .

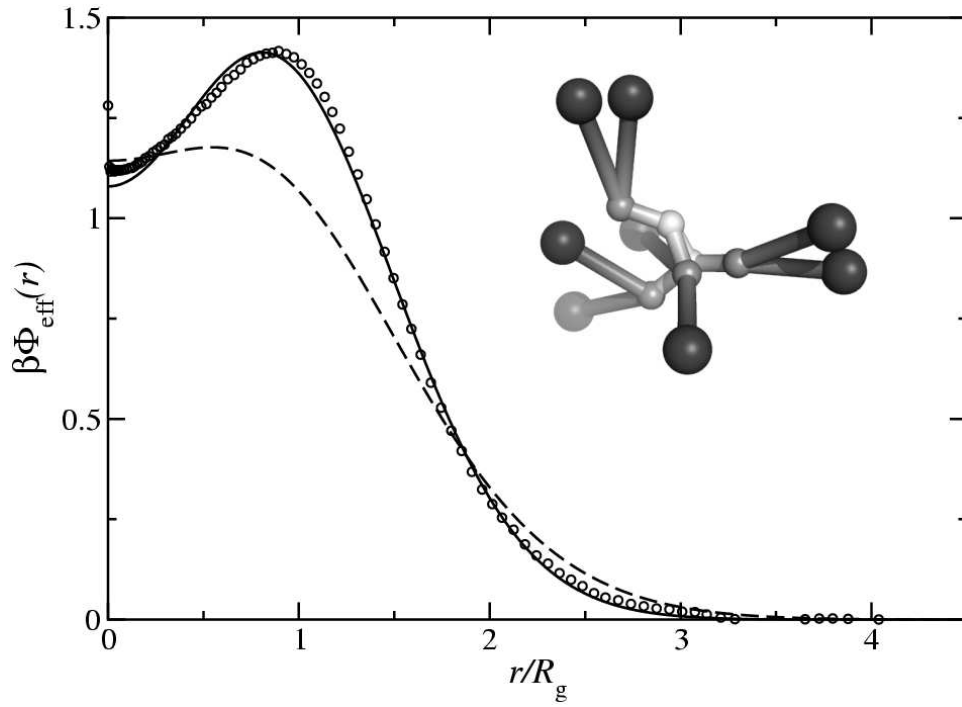


Figure 7.11: Same as Fig. 7.7 but for D_2 , using a DGCM fit.

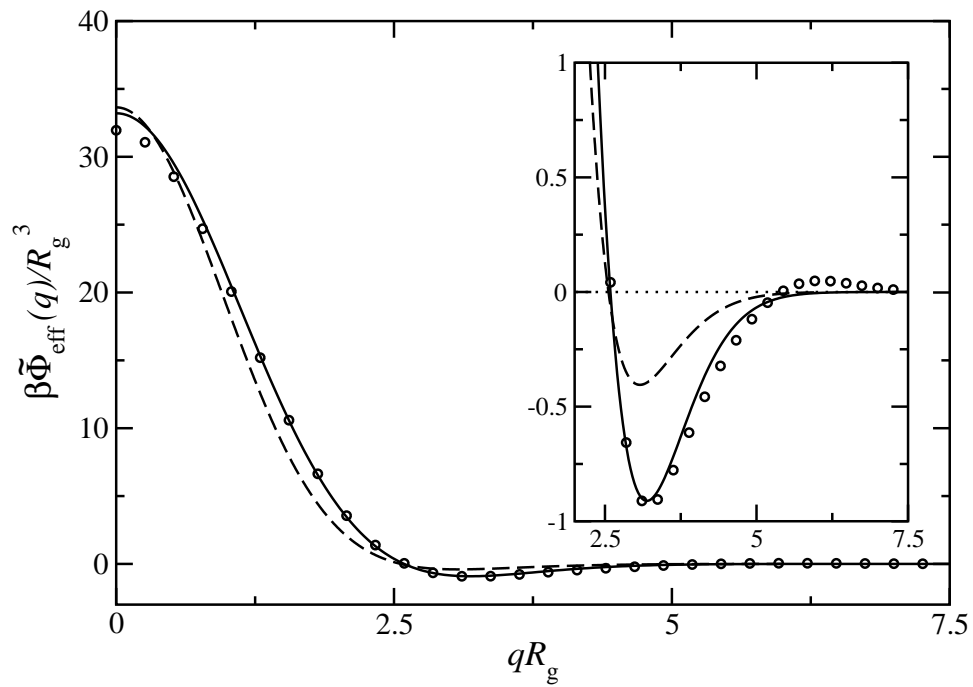


Figure 7.12: Same as Fig. 7.8 but for D_2 , using a DGCM fit.

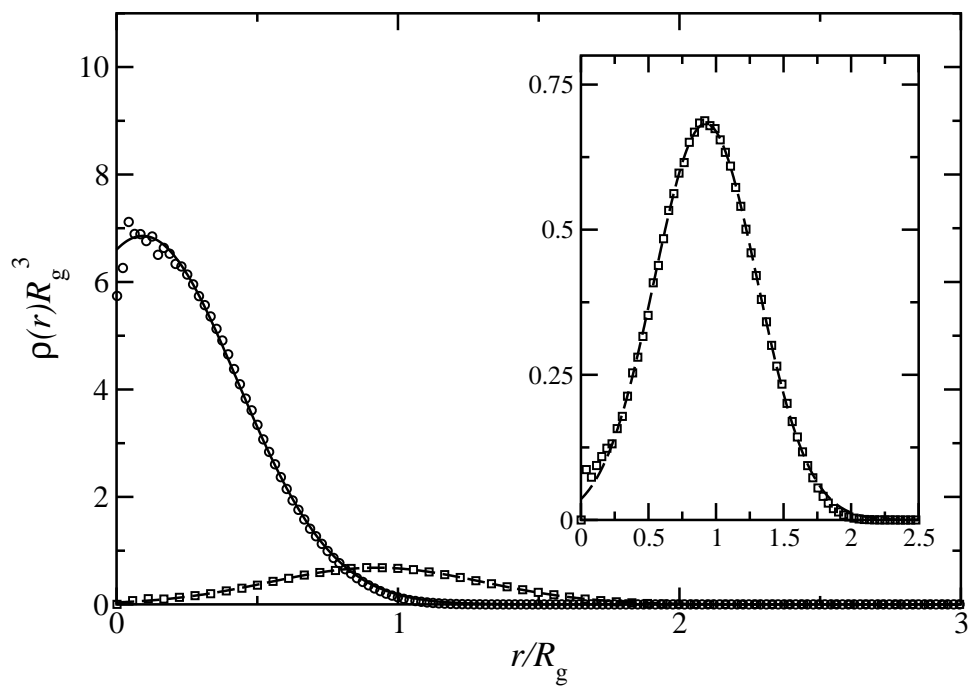


Figure 7.13: Same as Fig. 7.5 but for D_3 .

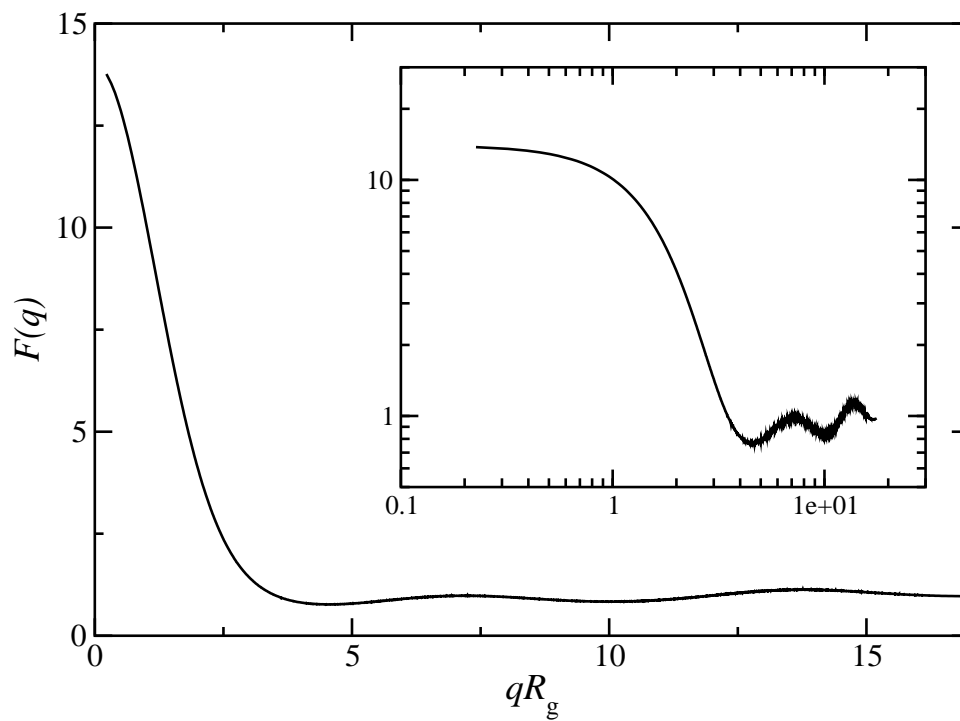


Figure 7.14: Same as Fig. 7.6 but for D_3 .

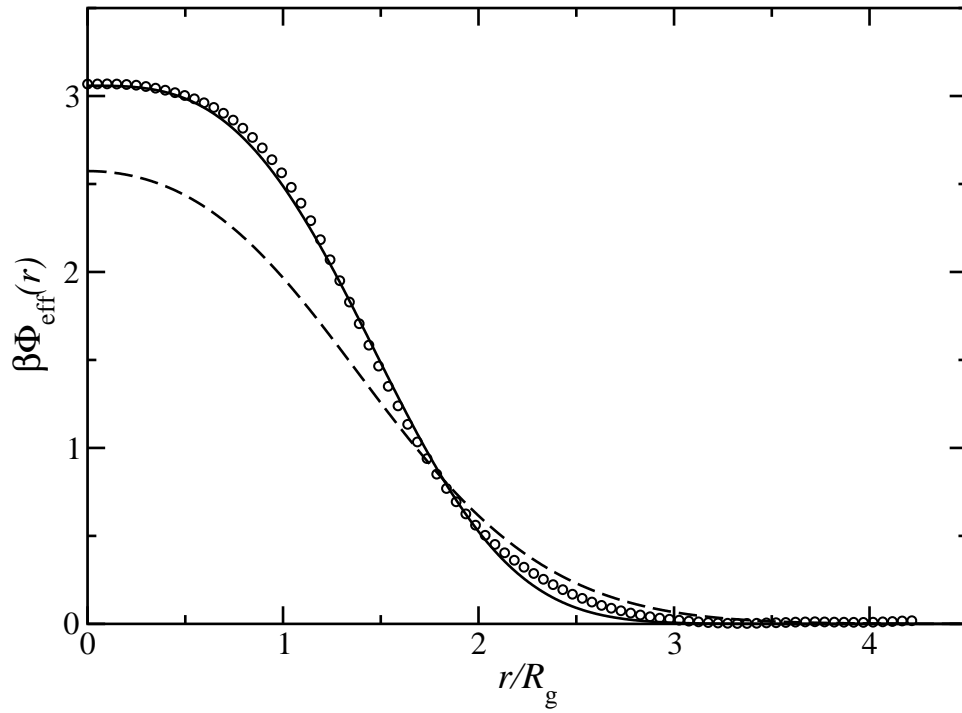


Figure 7.15: Same as Fig. 7.7 but for D_3 , using a GEM- n fit.

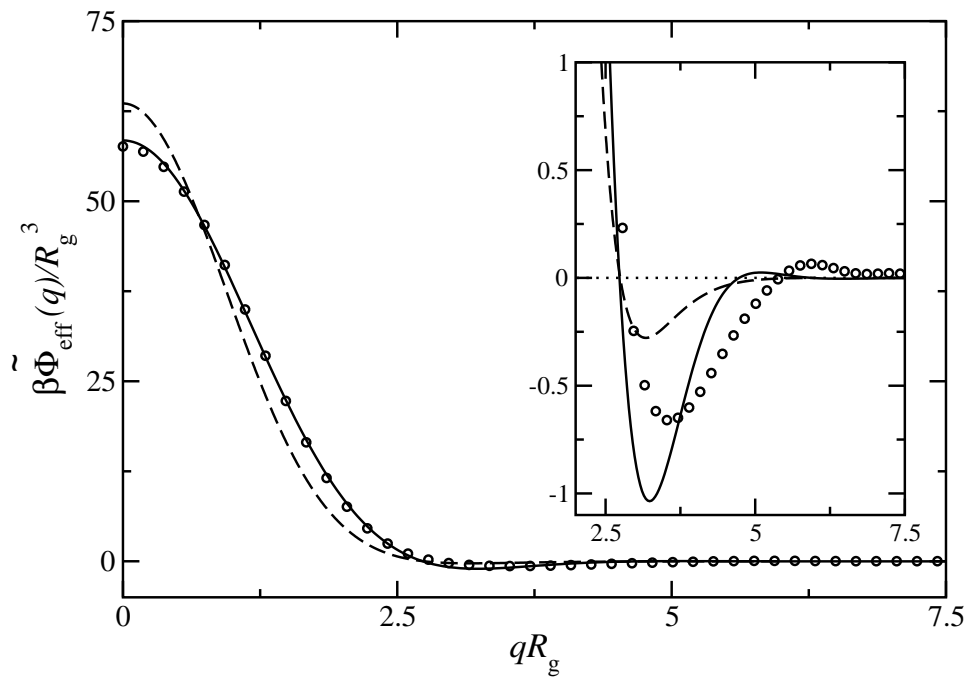


Figure 7.16: Same as Fig. 7.8 but for D_3 , using a GEM- n fit.

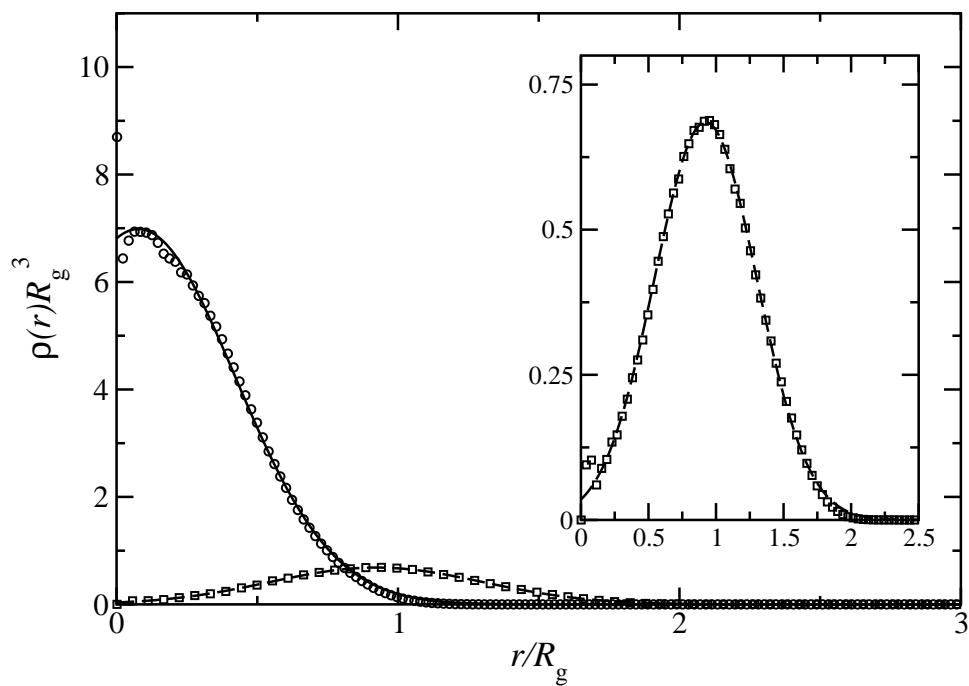


Figure 7.17: Same as Fig. 7.5 but for D_4 .

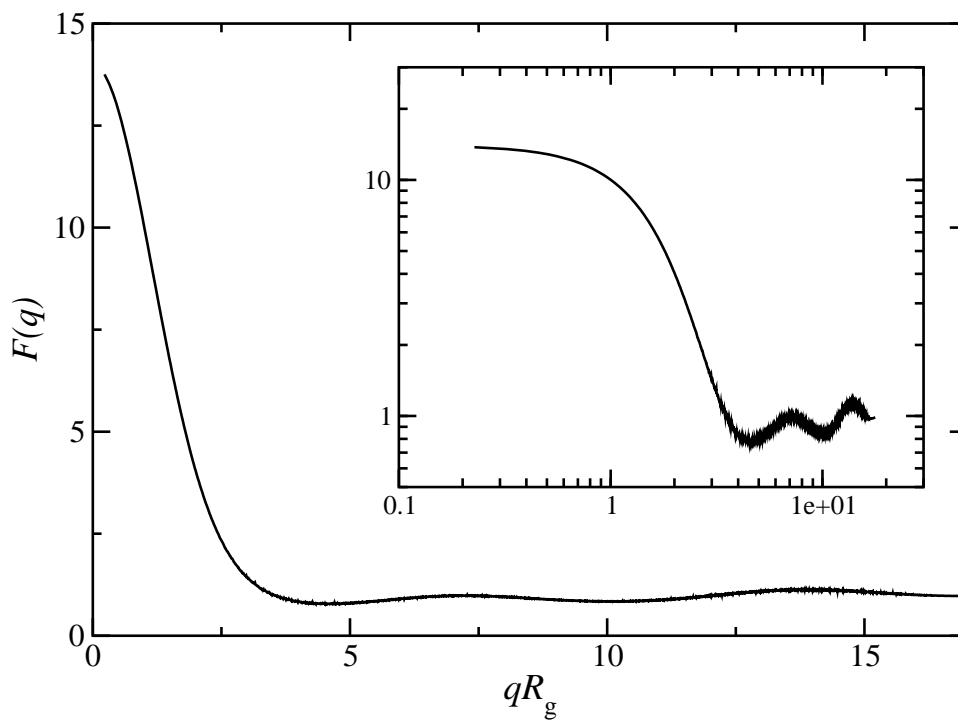


Figure 7.18: Same as Fig. 7.6 but for D_4 .

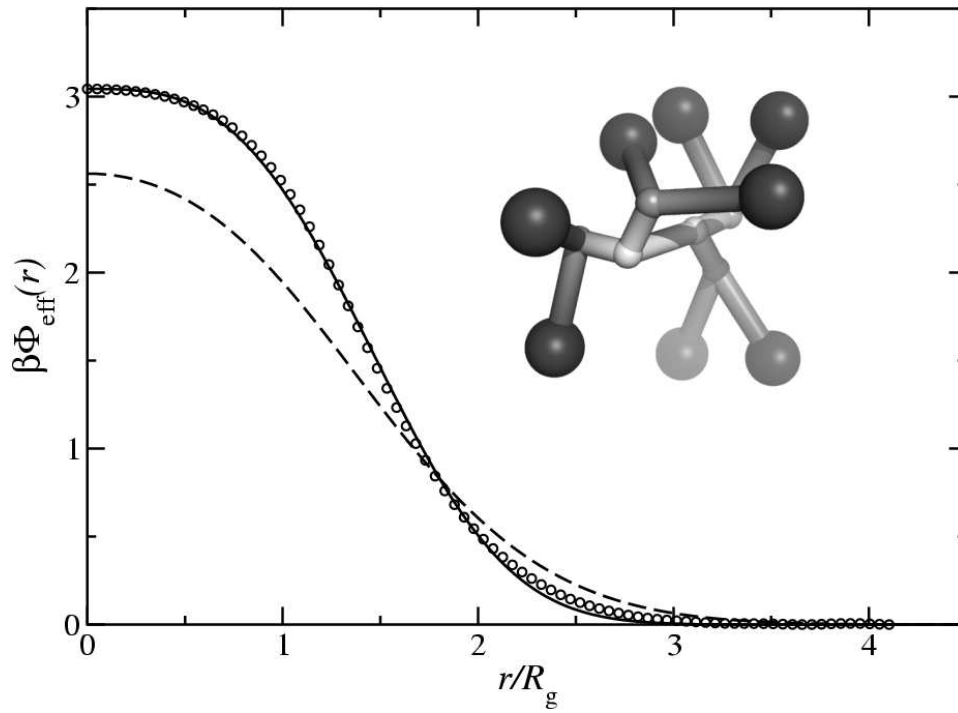


Figure 7.19: Same as Fig. 7.7 but for D_4 , using a GEM- n fit.

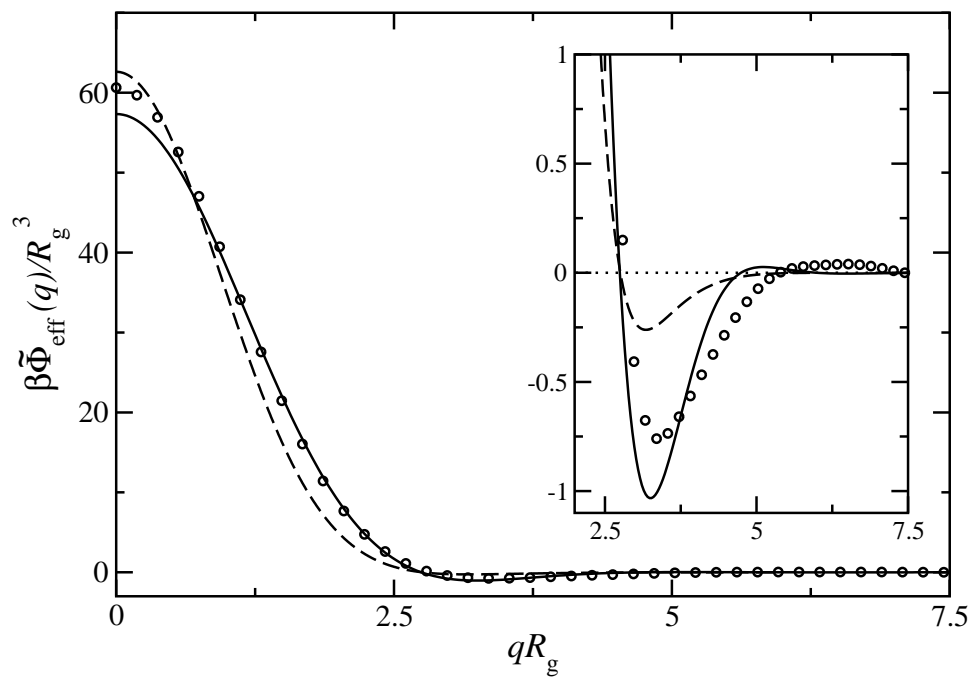


Figure 7.20: Same as Fig. 7.8 but for D_4 , using a GEM- n fit.

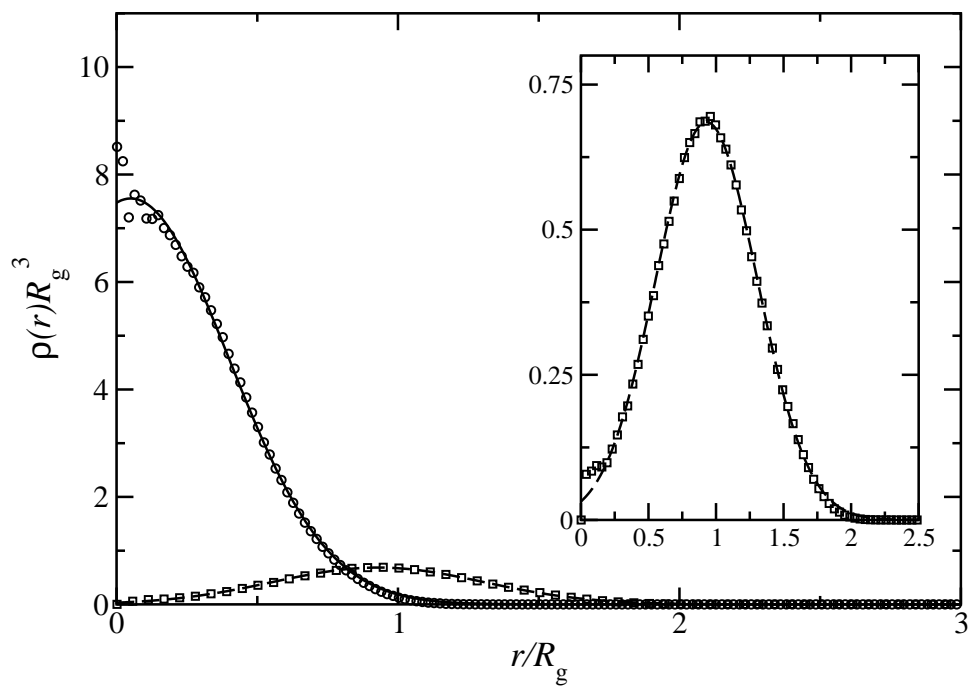


Figure 7.21: Same as Fig. 7.5 but for D_5 .

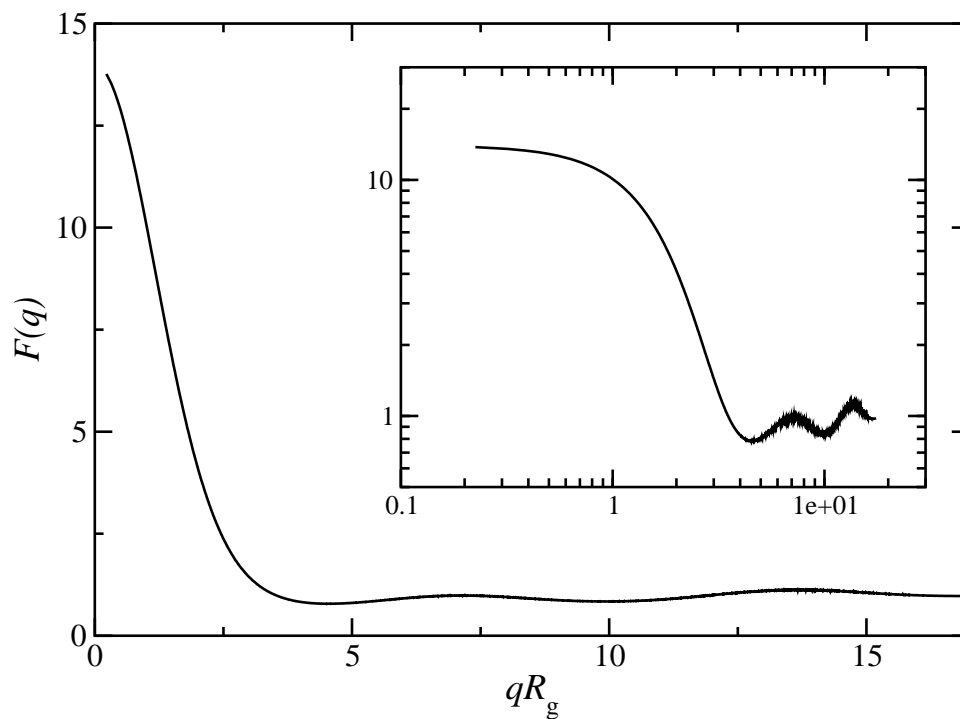


Figure 7.22: Same as Fig. 7.6 but for D_5 .

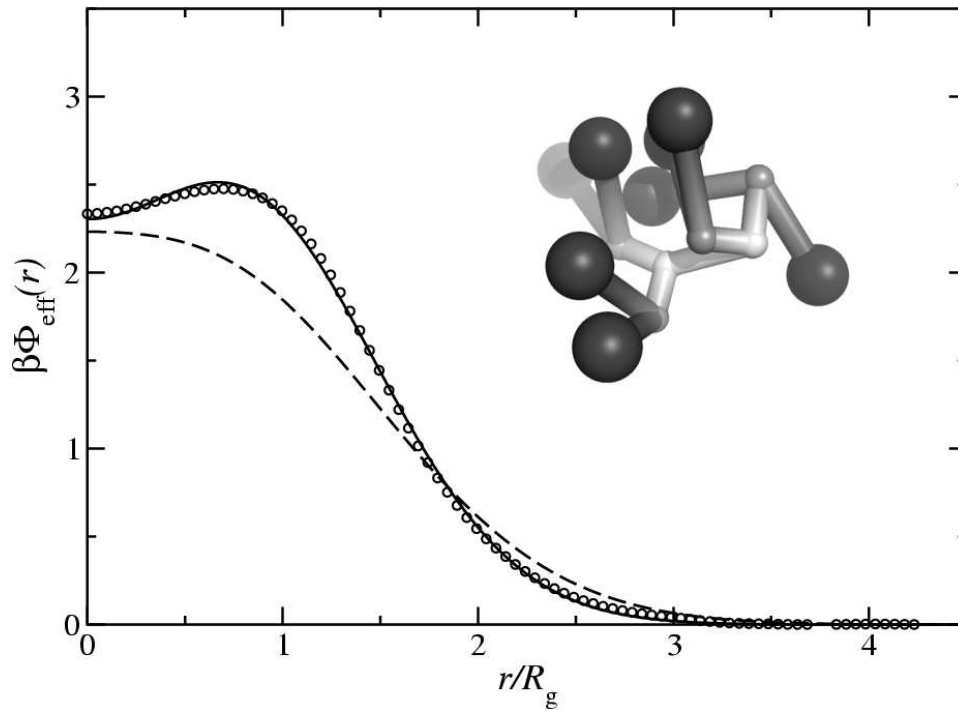


Figure 7.23: Same as Fig. 7.7 but for D_5 , using a DGCM fit..

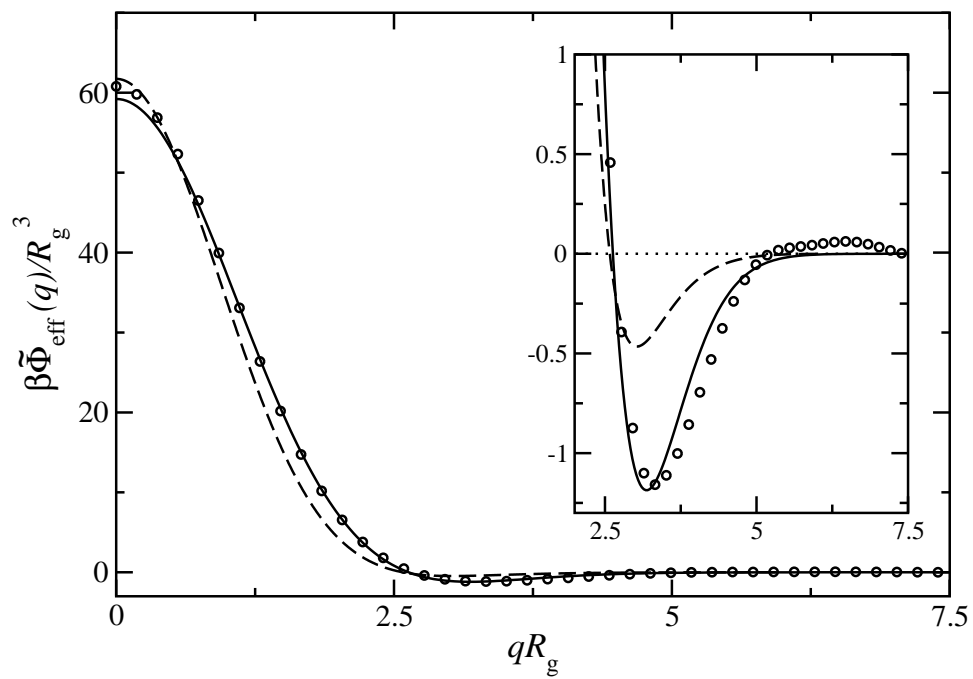


Figure 7.24: Same as Fig. 7.8 but for D_5 , using a DGCM fit..

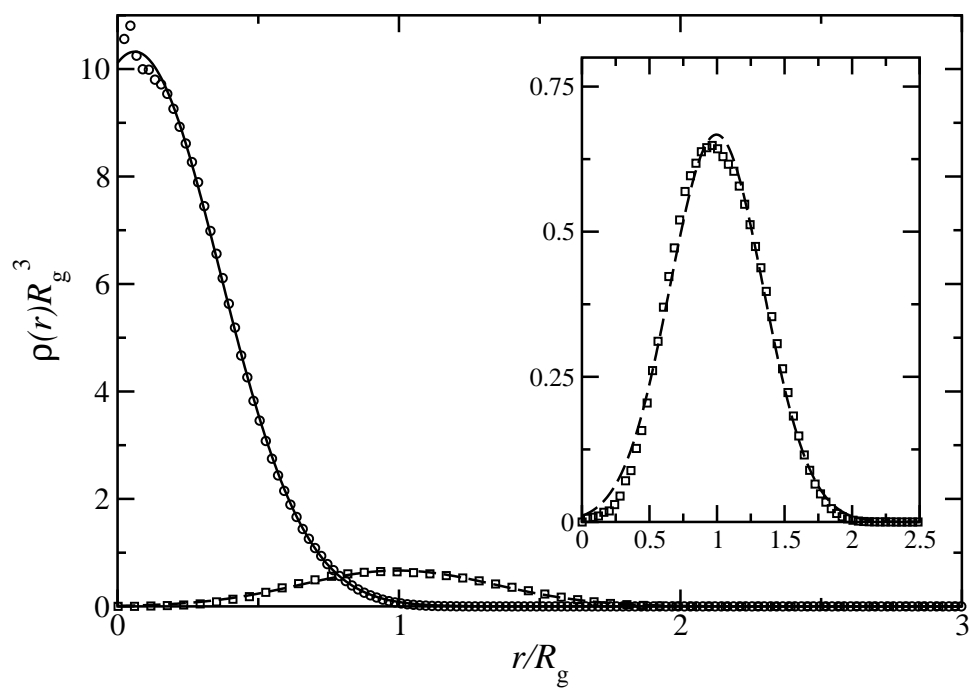


Figure 7.25: Same as Fig. 7.5 but for D_6 .

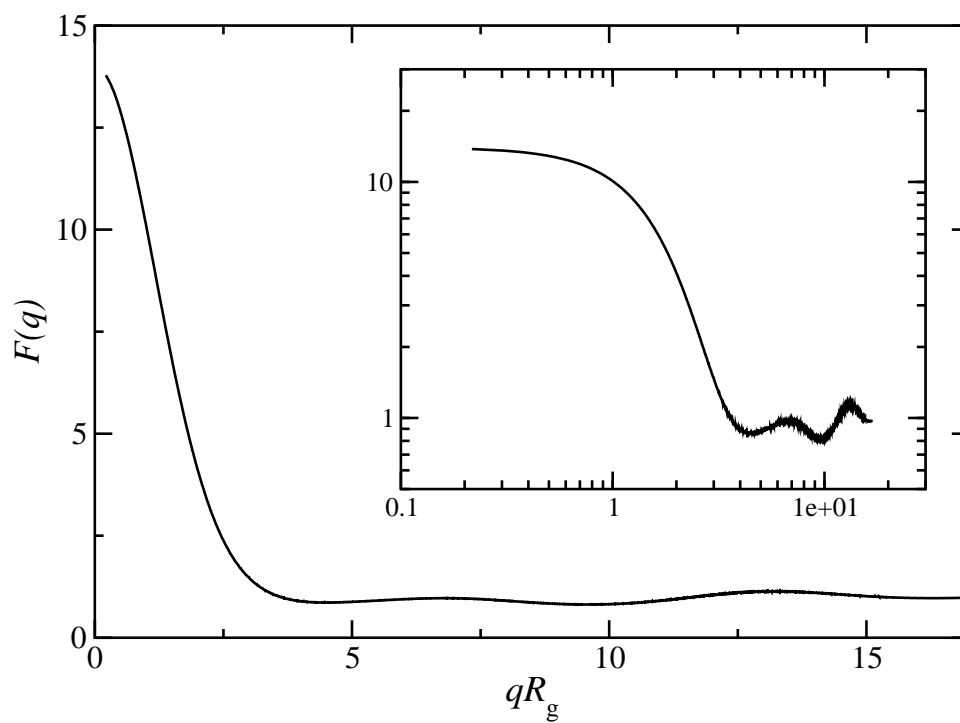


Figure 7.26: Same as Fig. 7.6 but for D_6 .

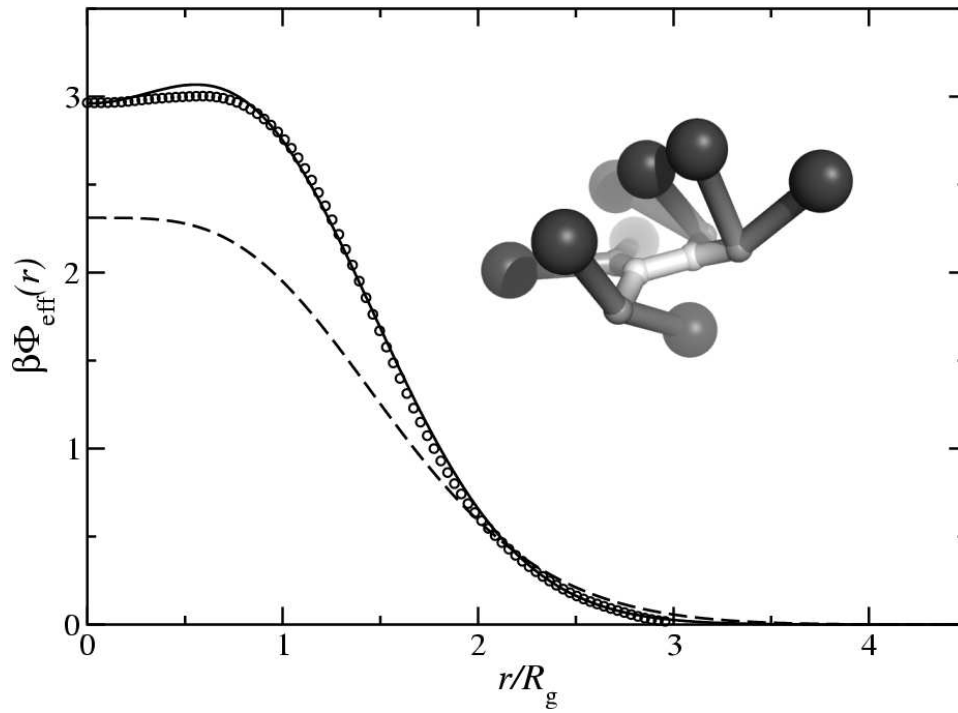


Figure 7.27: Same as Fig. 7.7 but for D_6 , using a DGCM fit..

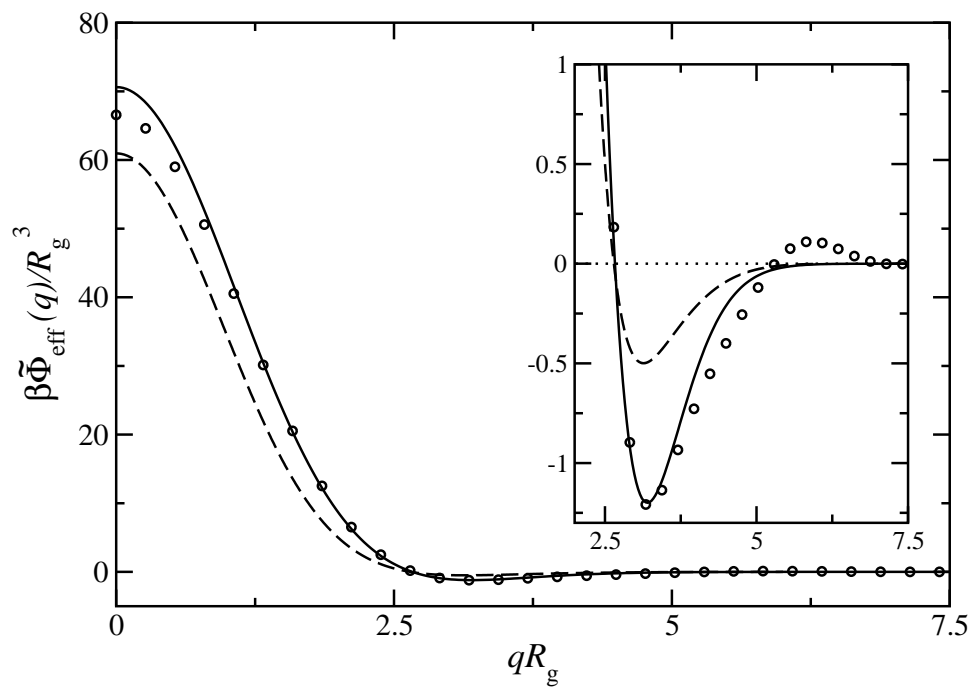


Figure 7.28: Same as Fig. 7.8 but for D_6 , using a DGCM fit..

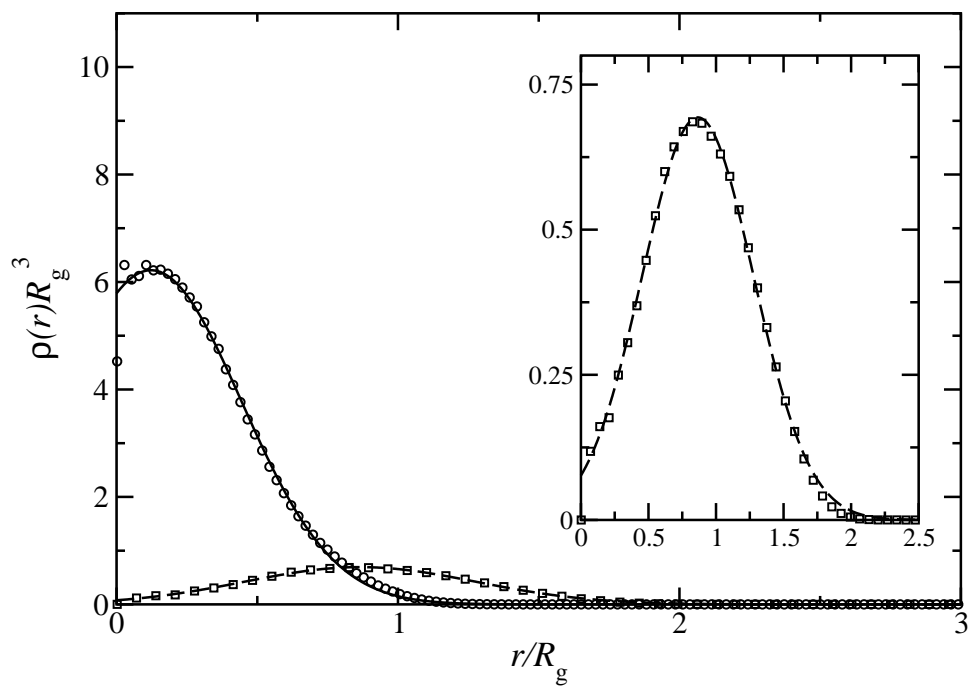


Figure 7.29: Same as Fig. 7.5 but for D_7 .

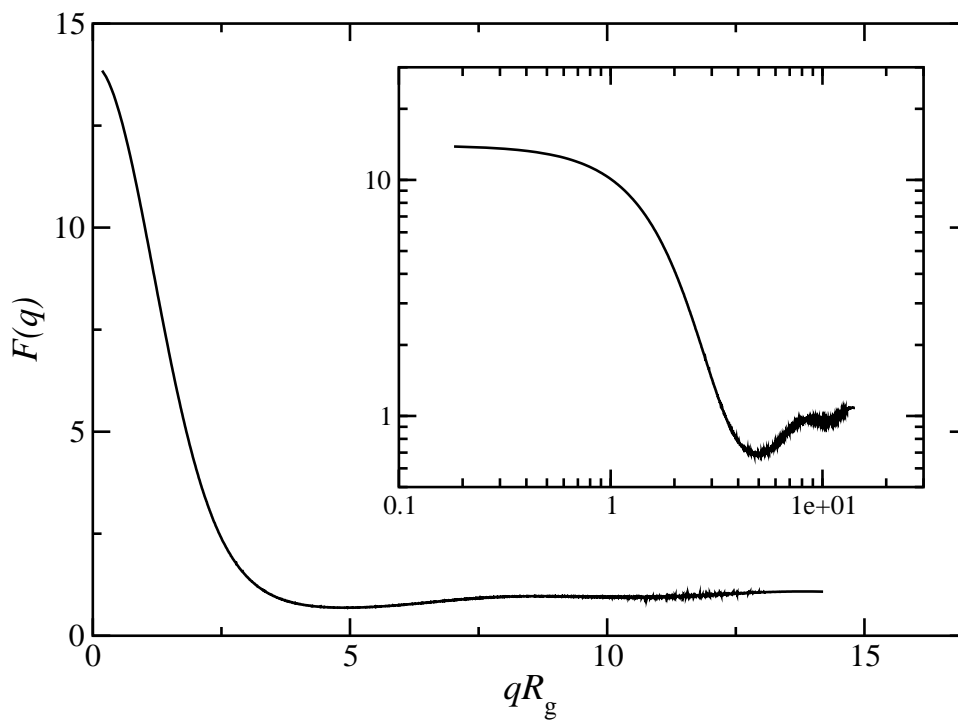


Figure 7.30: Same as Fig. 7.6 but for D_7 .

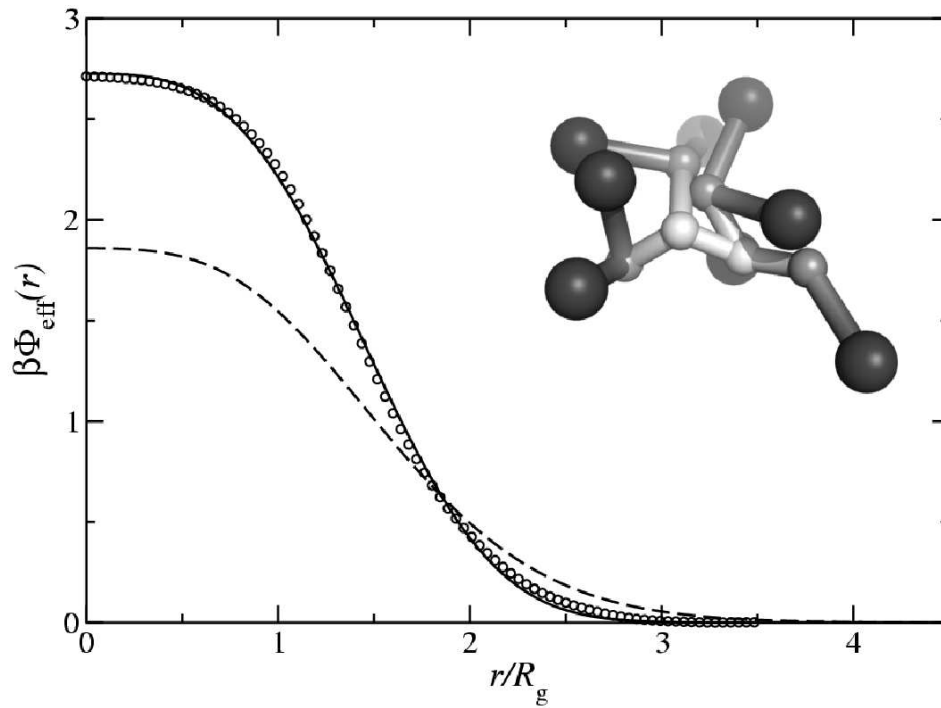


Figure 7.31: Same as Fig. 7.7 but for D_7 , using a GEM- n fit.

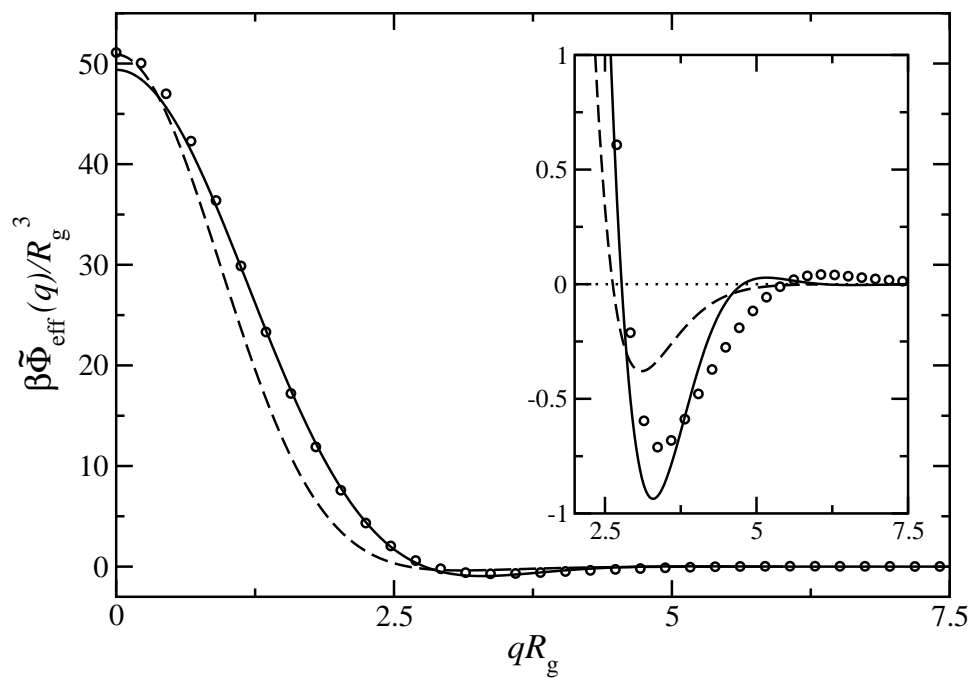


Figure 7.32: Same as Fig. 7.8 but for D_7 , using a GEM- n fit.

7.2 On the thermodynamics of cluster crystals

In equilibrium single-occupancy crystals the number of particles N is nearly equal, but usually smaller than the number of perfect lattice sites N_c in the system [79]. The principal contribution to the inequality is the finite-temperature concentration of vacancies and interstitials. This means that the ratio between N and N_c is not fixed by geometry alone. Swope and Andersen [163] developed a formalism to take this effect into account when determining the thermodynamic properties of a crystal through computer simulations. However, in simple crystals the equilibrium concentration of point defects is usually so low that their effect on the phase behaviour is negligible. For instance, at melting, the chemical potential of a hard-sphere crystal with vacancies roughly differs by as little as $10^{-3}k_B T$ from that of a defect-free crystal for which $N = N_c$ [164]. This is one of the reasons why the aforementioned formalism of Swope and Andersen has received little attention so far [165, 166]. However, for systems showing clustering behaviour, the usually subtle question of lattice-site occupancy takes on increasing importance for simulations since the particle number and the lattice-site count become completely decoupled at high densities ρ , with $N > N_c$.

In a bulk cluster crystal, the number of lattice sites changes until the free energy is minimised, which can be achieved by making adjustments at surfaces, interfaces, and boundaries. However, in a simulation box, where particle number N , volume V , and temperature T are fixed, the system is constrained by the initial choice of lattice geometry. In almost all simulations involving crystals, the average number of particles per primitive cell, $n_c = N/N_c$, is fixed at the outset of the simulation. The fixed volume and the use of periodic boundary conditions make the free-energy cost of creating a new lattice site too high to be observed on a simulation timescale, unless the system is very far from equilibrium [163]. The constrained free energy is determined not only by the conjugate variables entropy S / temperature T , pressure P / volume V , and chemical potential μ / particle number N , but also by the lattice site chemical potential μ_c / number of lattice sites N_c , where μ_c is the work necessary to introduce a new lattice site in the system. This last quantity does not introduce a new degree of freedom, but solely constrains the other variables. Accordingly, we can write an infinitesimal change in the constrained Helmholtz free energy, $F(\mu_c)$, as

$$dF(\mu_c) = -S(\mu_c)dT - P(\mu_c)dV + \mu(\mu_c)dN + \mu_c dN_c. \quad (7.25)$$

Then, the constrained pressure $P(\mu_c)$ is given by

$$P(\mu_c) = - \left(\frac{\partial F}{\partial V} \right)_{N, T, N_c}, \quad (7.26)$$

the constrained chemical potential $\mu(\mu_c)$ by

$$\mu(\mu_c) = \left(\frac{\partial F}{\partial N} \right)_{V, T, N_c}, \quad (7.27)$$

while the lattice site chemical potential μ_c is defined as

$$\mu_c = \left(\frac{\partial F}{\partial N_c} \right)_{V,T,N}. \quad (7.28)$$

Since no new thermodynamic quantity has been introduced, *equilibrium* properties are recovered when $\mu_c = \mu_c[N, V, T, N_c^{\text{eq}}(N, V, T)] = 0$, where N_c^{eq} is the equilibrium number of lattice sites. This condition can be tested using

$$\mu_c = \frac{F(\mu_c) + P(\mu_c)V - \mu(\mu_c)N}{N_c}. \quad (7.29)$$

Therefore, the equilibrium pressure P is related to the constrained pressure $P(\mu_c)$ via

$$P(N, V, T) = P(\mu_c = 0) = P[N, V, T, N_c^{\text{eq}}(N, V, T)] \quad (7.30)$$

and in a similar way, the equilibrium chemical potential μ is connected to the constrained one via

$$\mu(N, V, T) = \mu(\mu_c = 0) = \mu[N, V, T, N_c^{\text{eq}}(N, V, T)], \quad (7.31)$$

which provides the relation between the properties of the (small) constrained and the unconstrained (bulk) system.

In single occupancy crystals, the condition for phase coexistence in a one-component system is that values for the temperature, the pressure and the chemical potential of the respective systems have to be equal. In the following, let the labels 1 and 2 denote the systems involved. Plotting the specific free energy, F/N of these two systems as functions of the specific volume, V/N , we can determine the coexistence densities via the common tangent construction, where we consider tangents to the respective free energy curves, F/N vs. V/N . The requirement $P_1 = P_2$ states that the tangents have equal slopes, since $P = -(\partial F/\partial V)$. The condition $\mu_1 = \mu_2$, on the other hand, results in a common intercept, since $\mu = F/N + PV/N$ (cf. Fig. 7.33). The coexistence volumina are then given by the location of the points where the free energy curves touch the common tangent.

However, the situation is different when simulating cluster crystals. By fixing N_c (while varying V), we only determine the free energy curve of the *constrained* free energy, which will be different for different values of N_c . The equilibrium free energy may then be imagined as a sort of “envelope” to these curves, i.e., as those points where $\mu_c = 0$ (cf. Fig. 7.34).

If we consider these constrained free energy curves, F/N vs. V/N at fixed N_c , we find that the intercepts are given by $\mu_1 + \frac{\mu_{c,1}}{n_{c,1}}$ and $\mu_2 + \frac{\mu_{c,2}}{n_{c,2}}$. Requiring the chemical potentials of the two phases to be equal, the difference in the intercepts is

$$\Delta I = \frac{\mu_{c,1}}{n_{c,1}} - \frac{\mu_{c,2}}{n_{c,2}}. \quad (7.32)$$

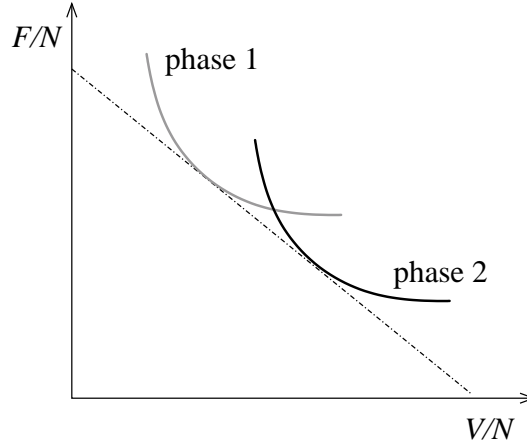


Figure 7.33: The common tangent construction in single occupancy crystals: the coexistence requirements of equal pressure and equal chemical potential result in a common tangent (dot-dashed line) to the free energy curves of the different phases (solid grey and black lines).

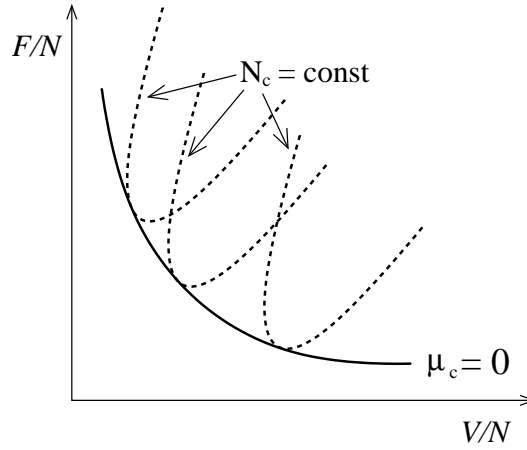


Figure 7.34: The equilibrium free energy curve of a cluster crystal can be found as those points of the constrained free energy curves ($N_c = \text{const.}$) where $\mu_c = 0$.

Hence, the common tangent construction is only correct when $\mu_c = 0$, i.e., only when it is applied to the *equilibrium* (i.e., unconstrained) free energy curves (see Fig. 7.35).

Due to the success of Widom's particle insertion method (cf. Sec. 5.5.1) for clustering systems, one could think of performing a kind of Gibbs-ensemble simulation where two systems exchange both particles and volume [106–109]. However, this is not thermodynamically appropriate when determining the fluid-solid or solid-solid phase coexistence in systems showing clustering behaviour. Setting up the two coupled simulation boxes (cf. Sec. 5.5.6) still leaves the *freedom* to lock into states where $\mu_c \neq 0$. Then, even though the phase coexistence conditions $P_1 = P_2$ and $\mu_1 = \mu_2$ are fulfilled, the intercepts are not the same anymore (see Fig. 7.36). One would need to be very lucky to prepare the Gibbs simulation such that $\mu_c = 0$ (see Fig. 7.37). Violating the condition $\mu_c = 0$ will allow to tune the location of the transition from one crystal phase to another at will.

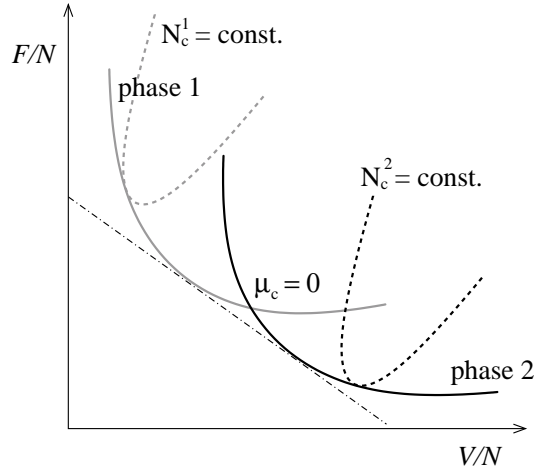


Figure 7.35: In the simulation of cluster crystals, the common tangent (dot-dashed line) construction is only correct if applied to the equilibrium free energy curves (solid grey and black lines) of the respective phases.

A similar phenomenon might even be observable in rapidly quenched experimental systems, if the resulting cluster crystals end up in states with $\mu_c \neq 0$. The long-lived non-equilibrium structures would then undergo phase transitions at different state points than those predicted by equilibrium thermodynamics.

The condition $\mu_c = 0$ is normally not considered in the discussion of the Gibbs phase rule. However, in his original formulation, Gibbs does allow for the possible existence of other thermodynamic “fields” in addition to μ , P and T [167].

Since thermodynamic equilibrium is only obtained when $\mu_c = 0$, it would appear that once the equilibrium points are found, all references to the artificial μ_c field can be discarded. Yet, for second derivatives of the constrained free energy, such as the bulk modulus B [cf. Eq.(3.11)], μ_c does matter, unless one already has the complete *equilibrium* free energy curve at hand. In single-occupancy crystals, $B = -V \left(\frac{\partial P}{\partial V} \right)_{N,T,N_c}$, which can be computed directly in simulations for a given state point through Eq. (5.11). For cluster crystals, however, the artificial system conditions further modify the bulk modulus. Starting from Eq. (7.30), we can write

$$\begin{aligned} B &\equiv -V \left[\frac{\partial P(N, V, T)}{\partial V} \right]_{N,T} \\ &= -V \left[\frac{\partial P(\mu_c = 0)}{\partial V} \right]_{N,T}. \end{aligned} \quad (7.33)$$

Deriving Eq. (7.30) with respect to V , we can rewrite this to

$$\begin{aligned} B &= -V \left[\frac{\partial P(\mu_c)}{\partial V} \right]_{N,T,N_c} - V \left[\frac{\partial P(\mu_c)}{\partial N_c} \right]_{N,T,V} \left(\frac{\partial N_c}{\partial V} \right)_{N,T} \\ &= B_{\text{vir}} - B_{\text{corr}}, \end{aligned} \quad (7.34)$$

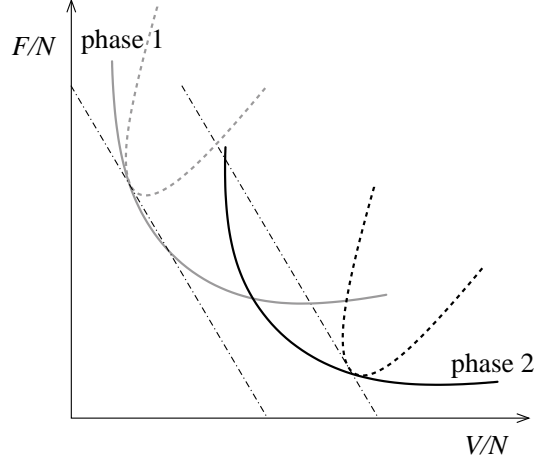


Figure 7.36: Setting up the two simulation boxes of the Gibbs ensemble leaves the freedom of locking into $\mu_c \neq 0$ states, resulting in an incorrect phase coexistence.

where the right hand side is evaluated at $\mu_c = 0$. The first term corresponds to a quenched system where particle rearrangements are not possible. Since obviously $B_{\text{corr}} > 0$, B_{vir} is an upper bound to B . As for B_{corr} , we can use a Maxwell relation to replace the first derivative by

$$\left[\frac{\partial P(\mu_c)}{\partial N_c} \right]_{N,T,V} = - \left(\frac{\partial \mu_c}{\partial V} \right)_{N,T,N_c}. \quad (7.35)$$

Introducing the volume of the primitive cell, $v_c = V/N_c$, we can rewrite the last factor in Eq. (7.34) as

$$\begin{aligned} \left(\frac{\partial N_c}{\partial V} \right)_{N,T} &= \frac{1}{v_c} - \frac{V}{v_c^2} \left(\frac{\partial v_c}{\partial V} \right)_{N,T} \\ &= \frac{1}{v_c} \left[1 - N_c \left(\frac{\partial v_c}{\partial V} \right)_{N,T} \right]. \end{aligned} \quad (7.36)$$

The correction term to the bulk modulus of clustering systems can then be obtained in simulations by evaluating

$$B_{\text{corr}} = \frac{\rho^2}{n_c} \left(\frac{\partial \mu_c}{\partial \rho} \right)_{T,n_c} \left[1 + \frac{\rho}{v_c} \left(\frac{\partial v_c}{\partial \rho} \right)_{T,\mu_c=0} \right], \quad (7.37)$$

where the partial derivatives are evaluated at an equilibrium state point.

If sound waves have a period shorter than the time it takes for particles to redistribute between primitive cells, then we can distinguish between two different sound modes in cluster solids. Density fluctuations stem either from changes to the primitive-cell volume v_c at fixed cluster occupancy n_c or from fluctuations in n_c at fixed v_c , as schematised in Fig. 7.38. To describe these fluctuations, we consider once more the variation in the free energy, given by Eq. (7.25). Keeping T and V

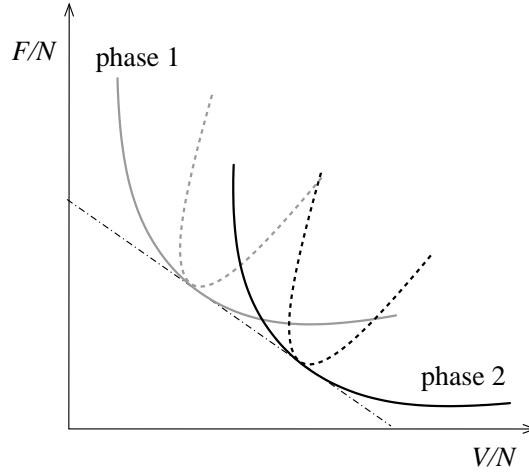


Figure 7.37: Using the Gibbs ensemble technique, one would need to be quite lucky to set up the boxes in a way that $\mu_c = 0$, which would allow to determine the correct phase coexistence.

constant and using the fact that $N = N_c n_c$, we can rewrite this as

$$dF = \mu N_c dn_c + (\mu_c + \mu n_c) dN_c \quad (7.38)$$

It is convenient to rather consider the total differential of the free energy density, $f \equiv F/V$, given by

$$df = \mu \varrho_c dn_c + (\mu_c + \mu n_c) d\varrho_c, \quad (7.39)$$

where $\varrho_c = N_c/V$ is the cluster density. Since the average value of the density fluctuations is zero, we consider the variation in f to second order, Δf , which is given by

$$\Delta f = c_{11} \varrho_c^2 (\Delta n_c)^2 + 2c_{12} \varrho_c n_c \Delta n_c \Delta \varrho_c + c_{22} n_c^2 (\Delta \varrho_c)^2, \quad (7.40)$$

where

$$\begin{aligned} c_{11} &= \frac{1}{2\varrho_c} \left(\frac{\partial \mu}{\partial n_c} \right)_{\varrho_c, T, V}, & c_{12} &= \frac{1}{2\varrho} \left[\frac{\partial(\mu \varrho_c)}{\partial \varrho_c} \right]_{n_c, T, V}, \\ c_{22} &= \frac{1}{2n_c^2} \left[\frac{\partial(\mu_c + \mu n_c)}{\partial \varrho_c} \right]_{n_c, T, V}. \end{aligned} \quad (7.41)$$

Especially in simulations, these coefficients can be obtained numerically via the following relations:

- c_{11} :

$$\left(\frac{\partial \mu}{\partial n_c} \right)_{\varrho_c, T, V} = \frac{N_c}{V} \left(\frac{\partial \mu}{\partial \varrho} \right)_{\varrho_c, T, V}. \quad (7.42)$$

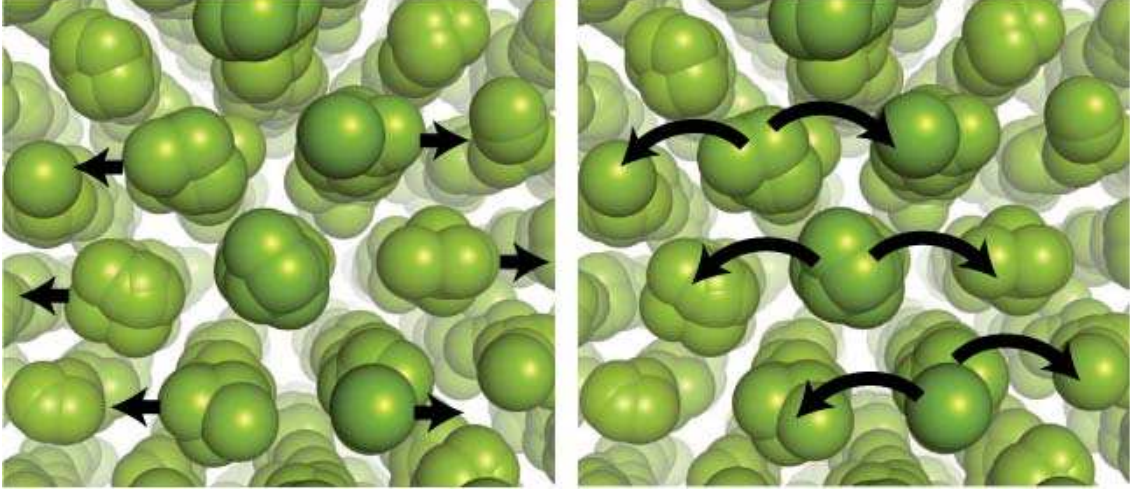


Figure 7.38: Density fluctuation contributions in multiple occupancy crystals either stem from fluctuations in the primitive-cell volume (left) or from rearrangements of particles between lattice sites (right).

- c_{12} : There are two equivalent possibilities to calculate the cross-term, i.e.,

$$\left[\frac{\partial(\mu \varrho_c)}{\partial \varrho_c} \right]_{n_c, T, V} = \left[\frac{\partial(\mu_c + \mu n_c)}{\partial n_c} \right]_{\varrho_c, T, V}. \quad (7.43)$$

This last version of the cross-term can be rewritten as

$$\left[\frac{\partial(\mu_c + \mu n_c)}{\partial n_c} \right]_{\varrho_c, T, V} = \mu + N_c \left(\frac{\partial \mu_c}{\partial N} \right)_{\varrho_c, T, V} + N \left(\frac{\partial \mu}{\partial N} \right)_{\varrho_c, T, V}. \quad (7.44)$$

- c_{22} :

$$\left(\frac{\partial \mu_c}{\partial \varrho_c} \right)_{n_c, T, V} = V \left(\frac{\partial \mu_c}{\partial N_c} \right)_{N, T, V}, \quad (7.45)$$

where the last derivative can be rewritten to

$$\begin{aligned} \left(\frac{\partial \mu_c}{\partial N_c} \right)_{T, N, V} &= - \frac{\left(\frac{\partial \mu_c}{\partial N} \right)_{N_c, T, V}}{\left(\frac{\partial N_c}{\partial N} \right)_{\mu_c, T, V}} \\ &= - \frac{\left(\frac{\partial \mu_c}{\partial N} \right)_{N_c, T, V}}{\left[\frac{\partial(1/v_c)}{\partial \varrho} \right]_{\mu_c, T}} \\ &= \frac{v_c^2}{V} \left(\frac{\partial \mu_c}{\partial \varrho} \right)_{\varrho_c, T} \left(\frac{\partial v_c}{\partial \varrho} \right)_{\mu_c, T}. \end{aligned} \quad (7.46)$$

Further, using Eq. (7.43) and the fact that

$$\left[\frac{\partial(\mu \varrho_c)}{\partial \varrho_c} \right]_{n_c, T, V} = \mu + \varrho_c \left(\frac{\partial \mu}{\partial \varrho_c} \right)_{n_c, T, V}, \quad (7.47)$$

we obtain

$$\left[\frac{\partial(\mu n_c)}{\partial \varrho_c} \right]_{n_c, T, V} = \frac{n_c}{\varrho_c} \left[N_c \left(\frac{\partial \mu_c}{\partial N} \right)_{\varrho_c, T, V} + N \left(\frac{\partial \mu}{\partial N} \right)_{\varrho_c, T, V} \right]. \quad (7.48)$$

Finally, a change of variables, $x_{\pm} = (\sqrt{c_{11}}\varrho_c \Delta n_c \pm \sqrt{c_{22}}n_c \Delta \varrho_c) / \sqrt{2}$, allows to diagonalise the second order variation of f as

$$\Delta f = (1 + \omega)x_{+}^2 + (1 - \omega)x_{-}^2, \quad (7.49)$$

where $\omega = c_{12} / \sqrt{c_{11}c_{22}}$. At the end of the following section, we are going to apply this formalism in the study of a representative model system that shows clustering behaviour.

7.3 Clustering model systems by example of the GEM-4

In Sec. 2.5, we showed that for the GEM- n family of potentials, clustering is expected for $n > 2$. Determining the zero-temperature phase diagram for this class for various potential indices n via the GA (cf. Sec. 4.2), we find that for this index range, only fcc and bcc lattices are realised (cf. Fig. 7.39), a result that is in full agreement with the predictions in [44]. This seems to indicate that the effective cluster-cluster interactions are harshly repulsive, a typical feature for systems that freeze into fcc and bcc solids, such as, e.g., the Lennard-Jones fluid. As we see from Fig. 7.40, for $n = 2$ (the GCM) the GA yields single-occupancy crystals, in agreement with the exact calculations of Stillinger [37]. We find that for low densities, $\varrho\sigma^3 \lesssim 0.2$, the GA predicts fcc to be the stable phase, in agreement with the results obtained by Stillinger in [37], which predict this phase for $\varrho\sigma^3 < \pi^{-3/2} \sim 0.18$. For higher densities, we obtain the bcc structure.

From the GA results shown in Fig. 7.39, we see that for the densities considered ($0.2 < \varrho\sigma^3 < 10$) the bcc structure is dominant for n -values close to the clustering threshold $n = 2$, while for $n \gtrsim 3$, fcc becomes more favourable. At the boundary between the two regimes ($n \sim 3$) the energy difference between the two structures is vanishingly small, resulting in the GA having considerable difficulties to decide unambiguously between the competing structures in this particular situation [75]. This is reflected in the small fluctuations in the data of the GEM-3 in Fig. 7.40. Of course, clustering (i.e., $n_c > 1$) is expected for all $n > 2$, a fact that is fully corroborated by the GA results for selected values of n (see Fig. 7.40). Further, in [44], it has been shown that n_c is proportional to ϱ/q_* , where q_* is the value of the wavenumber for which $\tilde{\phi}(q)$ has a minimum. The results of Fig. 7.40 fully confirm this proportionality relation for n up to 5. We note that the slope of the n_c vs. ϱ lines decreases with n . This is due to the fact that q_* grows with n , as can be easily verified from analysing $\tilde{\phi}(q)$.

Let us now turn to finite temperatures and start the discussion of the GEM-4 system by showing its phase diagram based on results from simulations and predictions from theory, depicted in Fig. 7.41. To give a qualitative understanding of the clustering phenomenon, we also show three simulation snapshots in the same Figure, all taken at the same temperature, i.e., $k_B T / \varepsilon = 1.1$,

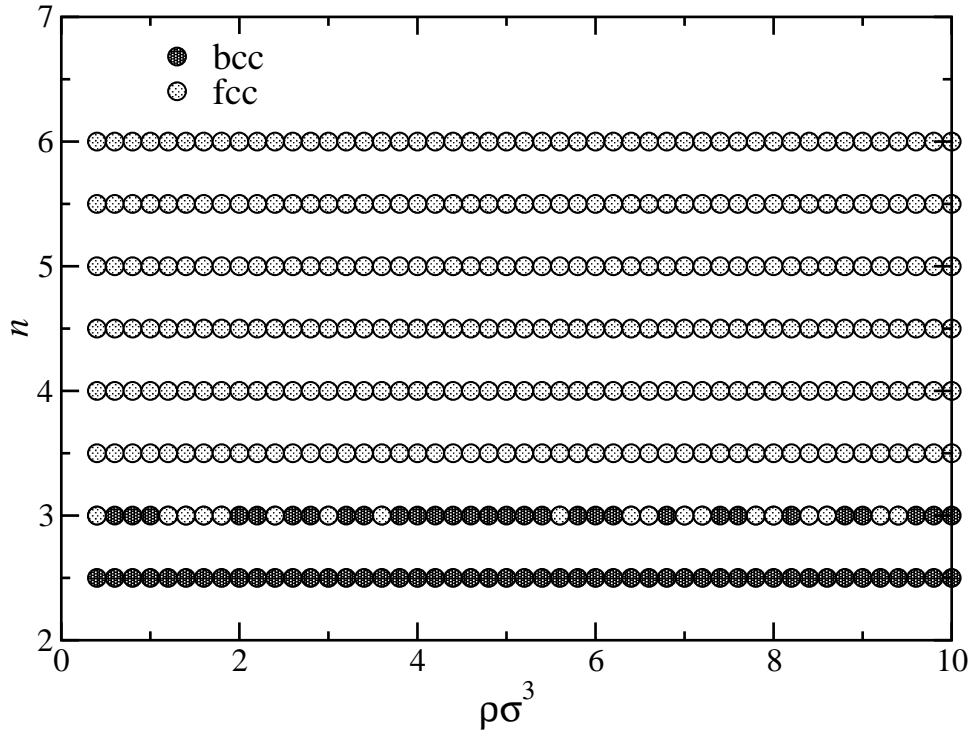


Figure 7.39: Zero temperature phase diagram of the GEM- n system showing the structures of the solid cluster phases as predicted by the GA as a function of $\rho\sigma^3$ and for a representative set of index values n . For key to symbols see legend.

but at different densities and in different phases. The explicit values for the densities are $\varrho\sigma^3 = 6$, where the system is evidently in the fluid phase, $\varrho\sigma^3 = 7.5$ for the cluster bcc and $\varrho\sigma^3 = 8.5$ for the cluster fcc phase.

In the following, we will focus on the different phases encountered in the phase diagram (cf. Fig. 7.41) and explain in detail how we determined the coexistence lines. We start by analysing the disordered, homogeneous phase. At $\varrho\sigma^3 = 6$ and $k_B T/\varepsilon = 1.1$ the system is already very close to the freezing line. A closer investigation of the particle positions shows that the fluid phase is actually a mixture of strongly aspherical clusters of particles with a vast variation of cluster sizes, n_c . The definition of a cluster in simulations is given in Sec. 5.6.1. From the RDF displayed in Fig. 7.42, we see that upon increasing the density, the value of $g(0)$ starts to rise. This maximum, which is already present in the RDF of the fluid, indicates that particles indeed agglomerate to clusters. As specified in the inset of the same figure, the space between two clusters becomes nearly depleted as soon as the system freezes. This depopulated region becomes broader as ϱ is increased, which reflects the tendency that at higher densities an increasing potential energy barrier between the clusters drives particles out of these interstitial regions and into the clusters. Such a behaviour seems completely counter-intuitive since this formation of stable clusters occurs in the complete absence of attraction. Nevertheless, it can be understood by considering the fact that full overlaps of particles create additional space for the *clusters*, thus offering the system a

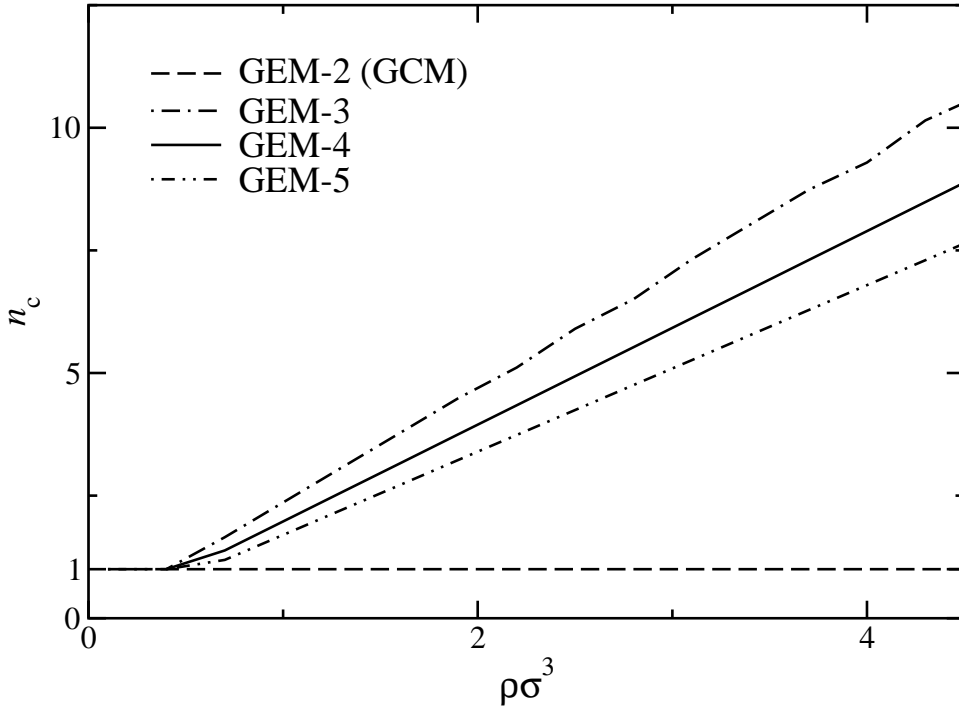


Figure 7.40: The cluster size n_c at $k_B T = 0$ as a function of density for different index values n of the GEM- n potentials as predicted by the GA. As we can see, the GA predicts $n_c = 1$ for all densities for the GCM. The small fluctuations in the data of the GEM-3 stem from the fact that the free energy differences between fcc and bcc are so small that the GA has difficulties to decide unambiguously between the competing structures.

possibility to increase its entropy. Moreover, above the overlap density, even an energetic gain may be achieved, since a single full overlap could be less expensive than the sum of the imminent costs due to the partial overlaps with the approximately 12 neighbours in a highly coordinated, dense fluid. This is most evident in the case of the PSM, for which the energy cost is independent of separation once the particles overlap. A detailed account of these contributions for the PSM is given in [24] in real space, whereas a more general argument based on reciprocal-space considerations can be found in [44].

In Fig. 7.43 we show the structure factor, $S(q)$, for the fluid phase according to MC simulations. We see that the first peak considerably exceeds the value of 2.85, which, according to the Hansen-Verlet criterion [168,169], indicates the freezing transition in harshly repulsive fluids. This demonstrates that the GEM-4 system can sustain a higher degree of spatial correlations than hard matter systems before it freezes.

Although the MFA does not capture the *structural* properties of clustering in the fluid phase on a quantitative level, it turns out that it can reproduce the increase in $g(0)$ on a qualitative level, which we show in the inset of Fig. 7.42. We can see that this feature is also predicted by the HNC or the PY approximations (cf. Secs. 4.1.4 and 4.1.5) with different levels of success. Moreover, the *thermodynamic* results obtained via the MFA energy route agree very well with

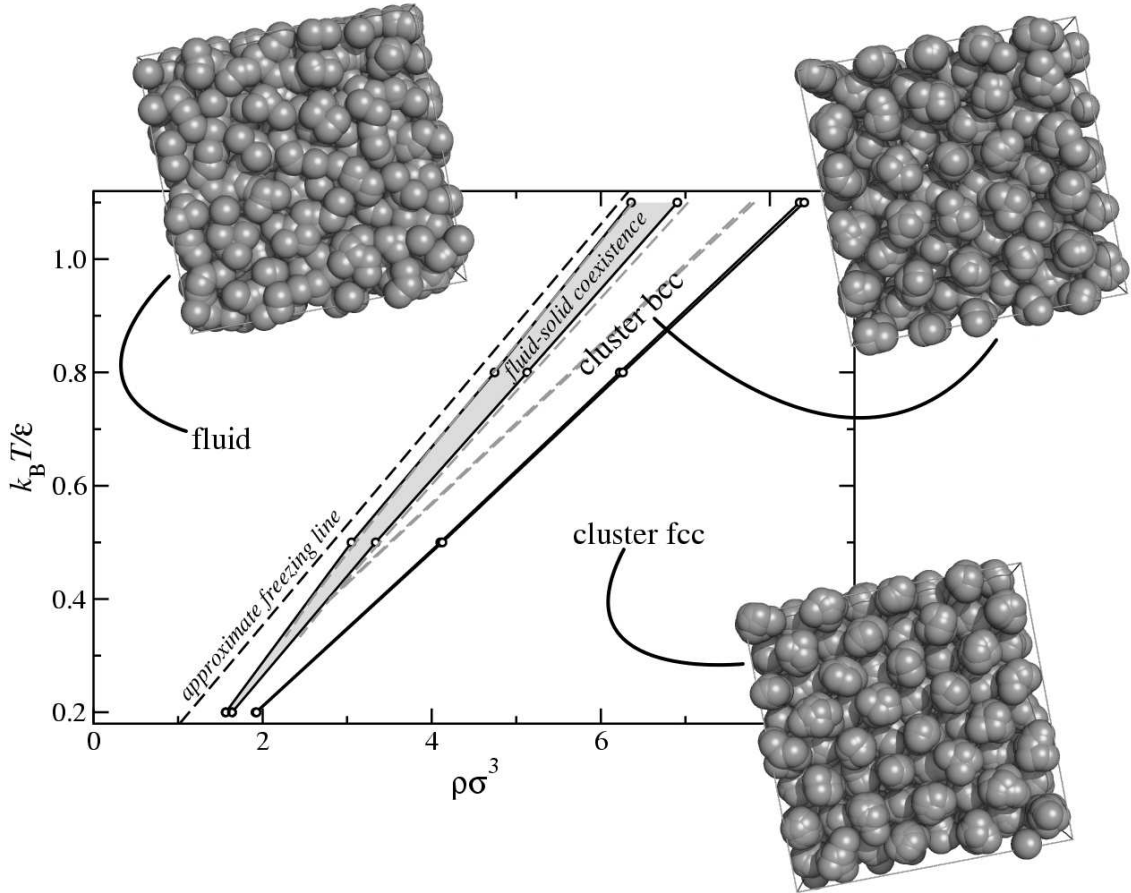


Figure 7.41: The phase diagram of the GEM-4 system (as discussed in the text). The circles are the coexistence points as obtained from MC simulations and the black solid lines serve as guide to the eye. The dashed grey lines show the MFA-DFT results. Please note that the bcc-fcc coexistence region is very narrow and not visible on the scale of the figure. The dashed black line shows the analytical prediction of the freezing line calculated in [44]. We also display three simulation snapshots of the system at $k_B T/\epsilon = 1.1$ for the fluid phase ($\rho\sigma^3 = 6$), the cluster bcc phase ($\rho\sigma^3 = 7.5$), and the cluster fcc phase ($\rho\sigma^3 = 8.5$). Note that for the two higher densities, every lattice site is multiply occupied. The particle diameters are not to scale and were chosen arbitrarily to optimise visibility.

results of computer simulations. To visualise this we present in Fig. 7.44 as an example the data for the reduced, dimensionless pressure, $\beta P/\rho$, for the GEM-4 at a rather low temperature of $k_B T/\epsilon = 0.5$. To put the success of the energy route of the MFA into a broader context, we also show in the same figure MFA results using different thermodynamic (i.e., virial or compressibility) routes, as well as data obtained by other liquid state theories, such as HNC or PY. We see that PY fails to reliably reproduce the simulation data especially at high densities. HNC, on the other hand, performs very well but breaks down (i.e., fails to converge) shortly after clustering sets in, i.e., where $g(0) \gtrsim 1$ and well before the actual transition to a cluster solid. The results of the virial and energy route of MFA lie on top of those of the virial route of HNC, while the MFA compressibility data lie close to those of the virial route of PY. Despite being the simplest among

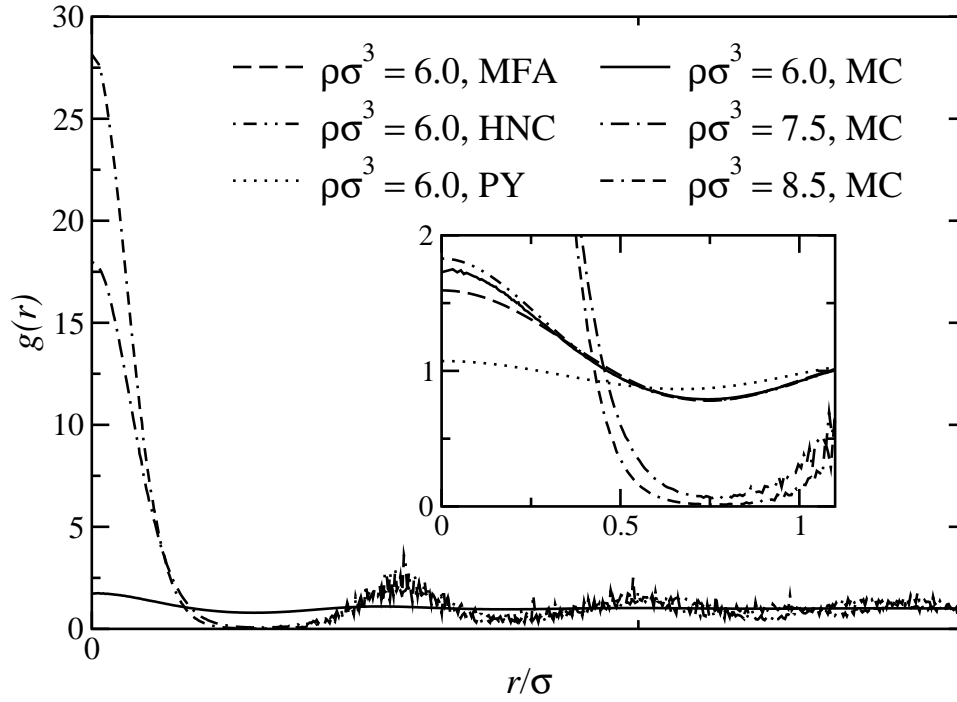


Figure 7.42: $g(r)$ as a function of r/σ for the GEM-4 system at $k_{\text{B}}T/\varepsilon = 1.1$ as determined from MC simulations for the states shown in the snapshots in Fig. 7.41. For the fluid phase at $\rho\sigma^3 = 6$, also results from MFA, HNC and PY are shown in the inset for a selected r -range.

the various closures to the OZ equation, the MFA outperforms all other closures since results can still be obtained when approaching the freezing transition. Note that at higher temperatures MFA reaches a level of accuracy close to the one of HNC in reproducing the data of simulations, as was shown in [44]. All these considerations leave the energy route of MFA as the best option to describe the thermodynamic and structural properties of the fluid. A more detailed analysis of MFA data in direct comparison with computer simulation results can be found in [46, 170].

Being able to calculate the equation of state, and hence the free energy of the fluid via MFA, we turn to the solid phases, which are treated within DFT. In Fig. 7.45 we show for a particular state point of the GEM-4 system the typical dependence of $f(n_c, \alpha)$, defined in Eq. (4.33), on n_c and α . It can be seen that the surface takes the shape of a trough that runs parallel to the α -axis, i.e., for each α the minimum with respect to n_c is located at a n_c -value that is α -independent. This is connected with the tendency of the system to adjust its lattice constant in such a way that the modulus of the first shell of reciprocal lattice vectors (RLVs) coincides with the value q_* at which $\tilde{\phi}(q)$ attains its negative minimum, confirming the analytical results of [44].

A detailed consideration of the separate contributions to $f(n_c, \alpha)$ [given by Eqs. (4.34) to (4.36)] as functions of n_c at fixed α (shown in Fig. 7.46) offers the key to understand the existence of stable clusters of finite size in this system. On increasing n_c , the lattice constant widens, the values of R in Eq. (4.35) grow and expensive close contacts with nearest neighbour clusters are

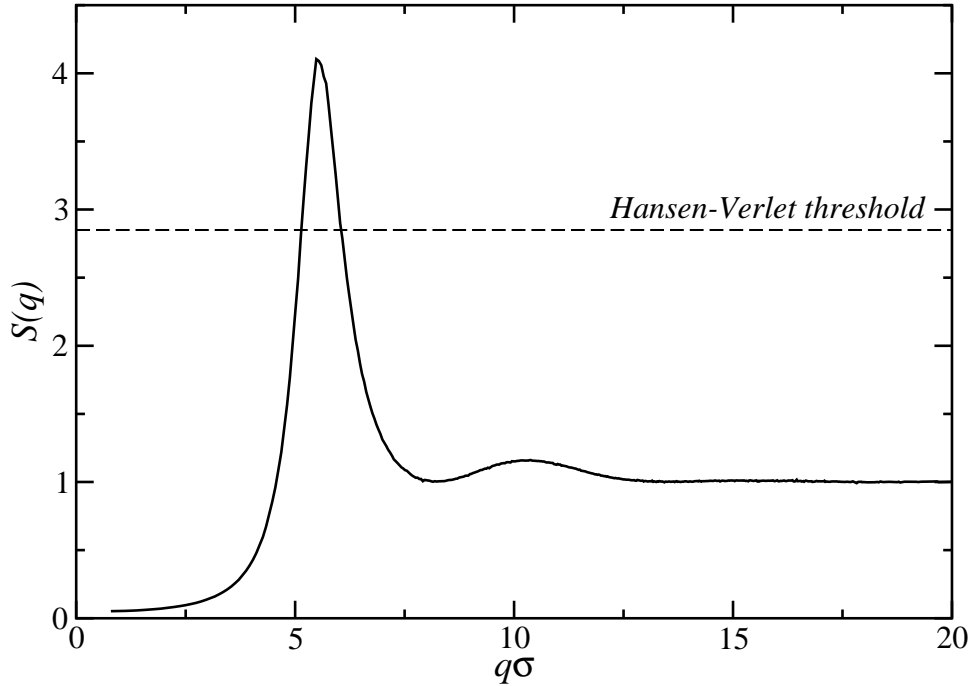


Figure 7.43: Structure factor $S(q)$ as a function of $q\sigma$ as obtained by MC simulations for a fluid GEM-4 system close to freezing, i.e., at $k_{\text{B}}T/\varepsilon = 1.1$ and $\rho\sigma^3 = 6$. The value of the first peak of $S(q)$ is considerably higher than the Hansen-Verlet threshold value that indicates freezing in systems interacting via harshly repulsive potentials.

avoided as shown by the fact that $f_{\text{inter}}(n_c)$ drops monotonically with n_c . On the other hand, the entropy loss due to particle aggregation, expressed by the term $\log n_c$ in Eq. (4.34), and the ‘self-interaction’ within the cluster, given by Eq. (4.36), both disfavour the formation of clusters, which can be seen from the monotonic increase of the respective terms with n_c . Nevertheless, very large values of n_c are unlikely because, at constant particle density, this would reduce the cluster density to such an extent that even the nearest neighbour distance between clusters exceeds the range of the potential $\phi(r)$. At this point, the entropic and self-interaction terms dominate and stop further aggregation. The interplay of these two competing contributions—*intra*-cluster interaction and entropy, on the one hand, and *inter*-cluster contribution, on the other hand—lead to an overall shape of $f(n_c, \alpha)$ which shows a global minimum at a finite value of $1 < n_c < \infty$, representing the optimal, equilibrium cluster size for this state point and rendering the clusters stable both against decomposition ($n_c = 1$) and unlimited growth ($n_c \rightarrow \infty$). Uncontrollable growth of n_c would be unfavourable not only on the basis of the thermodynamic arguments presented above but also on more fundamental, mechanical grounds. Indeed, should n_c and, correspondingly, the lattice constant, grow too large, there would be no appreciable restoring force from neighbouring clusters to provide the stabilisation mechanism against small lattice oscillations and the crystal would lose its ordered structure.

Since we are now able to calculate the free energy of the fluid and of the competing solid

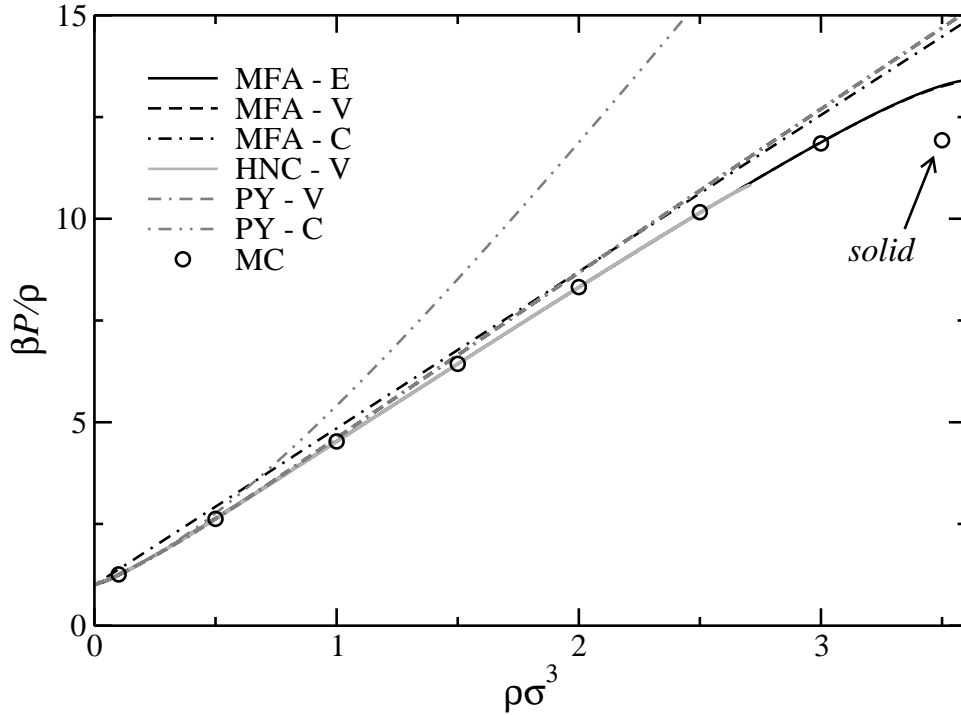


Figure 7.44: Reduced, dimensionless pressure, $\beta P/\rho$, as a function of $\rho\sigma^3$ for the GEM-4 system at $k_B T/\epsilon = 0.5$, calculated via different thermodynamic routes ('V' - virial, 'C' - compressibility, and 'E' - energy route) and using various IETs. MC simulation data are given by the symbols. While PY fails to reliably reproduce the simulation data especially at high densities, HNC initially provides a reasonable approximation but fails to converge well before the system crystallises at this temperature for densities around $\rho\sigma^3 \sim 3$. This leaves the energy route of the MFA as the best option to describe the properties of the fluid. Note that the MC data point at the highest density already corresponds to the solid phase.

structures (i.e., fcc and bcc) within the scope of the various accurate, yet in principle approximate theories, we turn to MC simulations for the determination of the exact free energy curves. Here, in accordance with Sec. 7.2, the locus $\mu_c = 0$ must be identified for each (ρ, T) state point. At given N, V, T , and N_c , the quantities $F(\mu_c)$, $P(\mu_c)$, and $\mu(\mu_c)$ may be directly computed from MC simulations, using thermodynamic integration (cf. Sec. 5.5.5), the virial equation [cf. Eq. (5.8)], and Widom's particle insertion method (cf. Sec. 5.5.1), respectively. Eq. (7.29) is used to check whether the chosen constraints correspond to the equilibrium conditions of the system (i.e., whether $\mu_c = 0$). This procedure is repeated for different N and V , keeping ρ and T constant, until the equilibrium configuration for the given state point is identified. We present our results for various temperatures and densities in Appendix C. The most computationally involved aspect is the determination of the free energy through thermodynamic integration. Due to clustering and particle hopping between lattice sites, an ideal gas in potential wells (cf. Sec. 5.5.5) proves to be a more appropriate reference state than the conventional Einstein crystal [79, 104]. As can be seen from Fig. 7.47, the validity of Widom's particle insertion method even at high densities can readily be verified with the help of the overlapping distribution method (cf. Sec. 5.5.2).

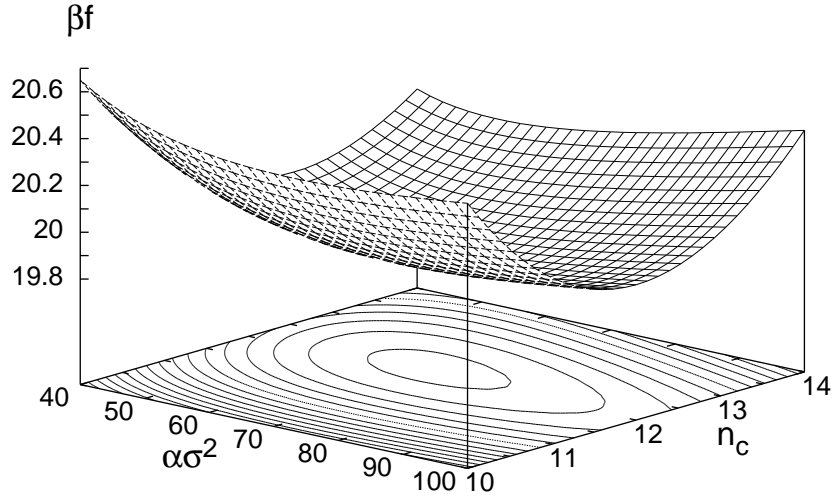


Figure 7.45: $\beta f(n_c, \alpha)$ given by Eq. (4.33) as a function of n_c and $\alpha\sigma^2$ for the GEM-4 system at $k_B T/\varepsilon = 0.5$ and $\rho\sigma^3 = 6$ in the fcc phase.

In Figs. 7.48 to 7.52 we show the modified (equilibrium) free energy density, $\beta\tilde{F}\sigma^3/V \equiv \beta F\sigma^3/V - K\rho\sigma^3$, for the different phases as a function of density at several fixed temperatures $k_B T/\varepsilon$. The terms $K\rho\sigma^3$, where the specific values of K are indicated in the captions of the plots, were added to enhance visibility, but they are irrelevant for the determination of the coexistence densities. From these figures it is apparent how small the energy differences between the competing solid cluster phases are. Therefore, simulation techniques that are able to determine the free energy with high accuracy are indispensable, and thermodynamic integration turned out to be a reliable tool to meet this requirement.

With the theoretical predictions and simulation data of the free energy at hand, we can now employ the common tangent construction to determine the coexistence densities and therefore the phase diagram, which was already shown in Fig. 7.41 and which we are going to discuss on a more quantitative level in the following. The approximate, analytical theory of [44] predicts for the freezing line ('f') a straight line of the form

$$\frac{k_B T_f}{\varepsilon} = 1.393|\tilde{\phi}(q_*)|_{\rho_f}\sigma^3 \approx 0.177\rho_f\sigma^3. \quad (7.50)$$

where $|\tilde{\phi}(q_*)| \sim 0.127$ is the absolute value of the negative minimum of the Fourier transform of the GEM-4 potential. Plotting the line specified in Eq. (7.50) in the phase diagram depicted in Fig. 7.41, we see that it lies reasonably close to the coexistence line predicted by the present full numerical MFA and DFT calculations. These data provide an almost straight line that can be

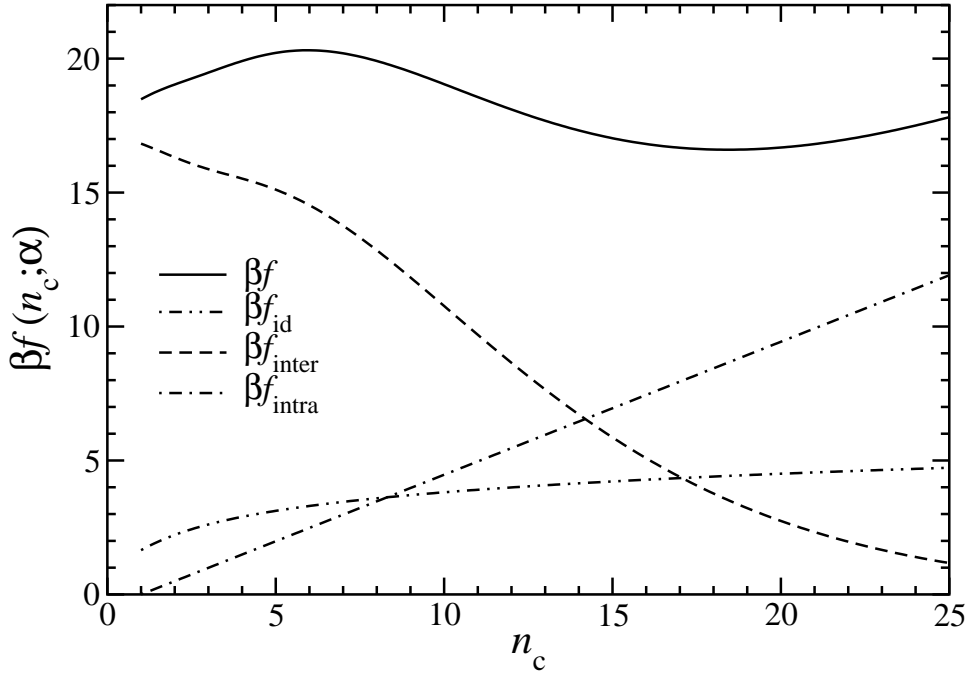


Figure 7.46: Contributions to $\beta f(n_c; \alpha)$ according to Eqs. (4.34) to (4.36) as functions of n_c for an fcc crystal formed in a GEM-4 system at $k_B T/\varepsilon = 1$, $\rho\sigma^3 = 9$ and $\alpha\sigma^2 = 45.51$, i.e., the α that minimises the free energy. The minimum in $\beta f(n_c; \alpha)$ is located at $n_c \sim 18.4$.

fitted by

$$\frac{k_B T_f}{\varepsilon} = 0.186(1)\rho_f\sigma^3 - 0.080(5). \quad (7.51)$$

MC simulations, on the other hand, give

$$\frac{k_B T_f}{\varepsilon} = 0.187(3)\rho_f\sigma^3 - 0.08(1), \quad (7.52)$$

and demonstrate the excellent accuracy of the full numerical MFA and DFT treatment in predicting the freezing transition. The approximate Eq. (7.50), on the other hand, slightly overestimates the region of stability of the solid because it neglects contributions from non-zero RLVs, resulting thereby in an artificial lowering of the free energy of the crystal.

Upon isothermal compression, the low-density fluid undergoes a first order transition into a cluster bcc phase, which occupies a wedge-like shape in the (T, ρ) -plane. As can be seen in Fig. 7.41, the prediction of MFA and DFT for the solidification line is only slightly different from the MC results. As the density is further increased, the system exhibits another first order transition into the cluster fcc phase which remains stable for all higher densities. Due to the small differences in the free energies and densities between the competing phases (shown in Figs. 7.48 to 7.52), this solid-solid transition becomes a stringent test for the accuracy of the DFT results. Indeed, we find that even though the DFT free-energy predictions are only off by a small amount, the location of the phase transition is shifted by roughly 10% in density. While the width of

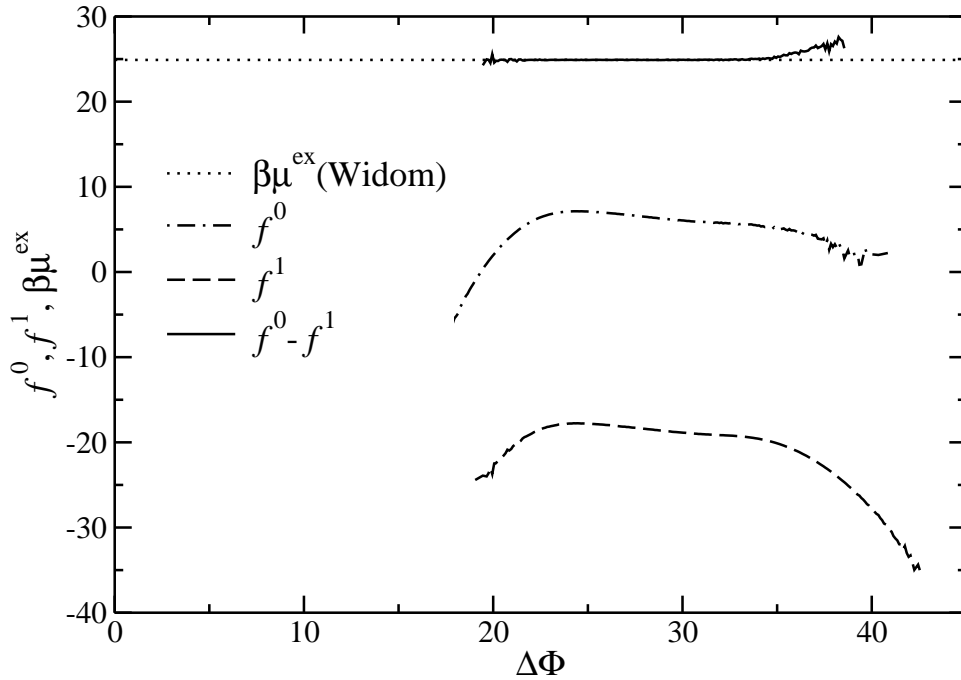


Figure 7.47: The validity of Widom's particle insertion method can easily be checked with the help of the overlapping distribution method, where $\beta\mu^{\text{ex}} = f^1 - f^0$ (cf. Sec. 5.5.2). Data is shown for an fcc crystal at $k_{\text{B}}T/\varepsilon = 1.1$ and $\rho\sigma^3 = 8.5$ in equilibrium (i.e., at $\mu_c = 0$).

the stable region of the bcc phase is underestimated by DFT, its prediction of the width of the bcc-fcc coexistence region is accurate and found to be very narrow and not visible on the scale of Fig. 7.41 in both approximations. This is confirmed on a quantitative level by the data of the coexistence densities as obtained by DFT and MC, presented in Tab. 7.6. Furthermore, MFA and DFT predict that at $k_{\text{B}}T/\varepsilon \sim 0.4$, the liquid and the two ordered cluster phases coexist at a triple point. Below this temperature, the bcc phase vanishes and the liquid freezes directly into the now thermodynamically more favourable cluster fcc crystals.

The P - T phase diagram, as obtained by MC simulations and shown in Fig. 7.53, displays the various state points considered, accompanied by tangents predicted by the Clausius-Clapeyron relation [79]. This equation is given by

$$\frac{dP}{dT} = \frac{\Delta s}{\Delta v}, \quad (7.53)$$

where Δs is the difference in entropy per particle, $s = S/N$, and Δv is the difference in specific volume, $v = V/N = 1/\rho$, between the two coexisting phases. Here, the entropy can readily be obtained from the simulation free energy and internal energy results via

$$S = \frac{U - F}{T}. \quad (7.54)$$

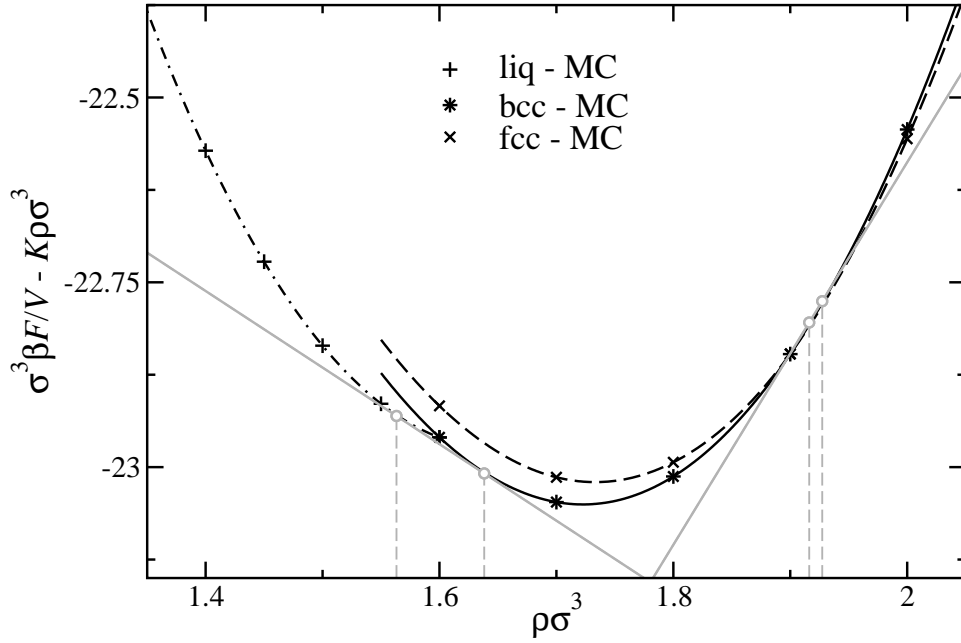


Figure 7.48: MC results of the modified free energy density $\beta \tilde{F} \sigma^3 / V \equiv \beta F \sigma^3 / V - K \rho \sigma^3$ of the GEM-4 system as function of $\rho \sigma^3$ at $k_B T / \epsilon = 0.2$ for the three coexisting phases. A term $K \rho \sigma^3$, with $K = 26$ and irrelevant for the determination of the coexistence densities, has been subtracted for clarity of presentation. The solid, dashed and dot-dashed curves interpolate the MC results and serve as guides to the eyes. The grey points and drop down lines indicate the coexistence densities, while the grey lines are the common tangents.

Inspecting the P - T phase diagram, the intersection point of the liquid-bcc and the bcc-fcc coexistence lines suggest a liquid-bcc-fcc triple point around $k_B T / \epsilon \sim 0.15$, which is less than half the DFT prediction. This dramatic shift is a consequence of the small differences between the slopes of the liquid-bcc and the bcc-fcc coexistence curves, which makes the location of the triple point very sensitive to any modification of these curves.

It is important to mention that—as already shown in [43]—the mean field assumption, which both the MFA and the DFT rest upon, breaks down at very low temperatures. Therefore, using the present theoretical methods, no reliable prediction of the location of the phase boundaries can be made for this region of phase space. At very low T and ρ , the GEM-4 can be approximated by soft-

$k_B T / \epsilon$	$\rho_{\text{liq}}^{\text{DFT}} \sigma^3$	$\rho_{\text{bcc}}^{\text{DFT}} \sigma^3$	$\rho_{\text{liq}}^{\text{MC}} \sigma^3$	$\rho_{\text{bcc}}^{\text{MC}} \sigma^3$	$\rho_{\text{bcc}}^{\text{DFT}} \sigma^3$	$\rho_{\text{fcc}}^{\text{DFT}} \sigma^3$	$\rho_{\text{bcc}}^{\text{MC}} \sigma^3$	$\rho_{\text{fcc}}^{\text{MC}} \sigma^3$
0.2	-	-	1.56	1.64	-	-	1.92	1.93
0.5	3.10	3.39	3.05	3.34	3.50	3.52	4.10	4.13
0.8	4.73	5.20	4.74	5.13	5.64	5.67	6.22	6.26
1.1	6.38	7.03	6.36	6.91	7.77	7.82	8.35	8.41

Table 7.6: Coexistence densities for the liquid('liq')-bcc and the bcc-fcc phase transitions as predicted by DFT and MC at various temperatures. For $k_B T / \epsilon = 0.2$, no DFT data is shown since the mean field assumption is not valid at such low temperatures.

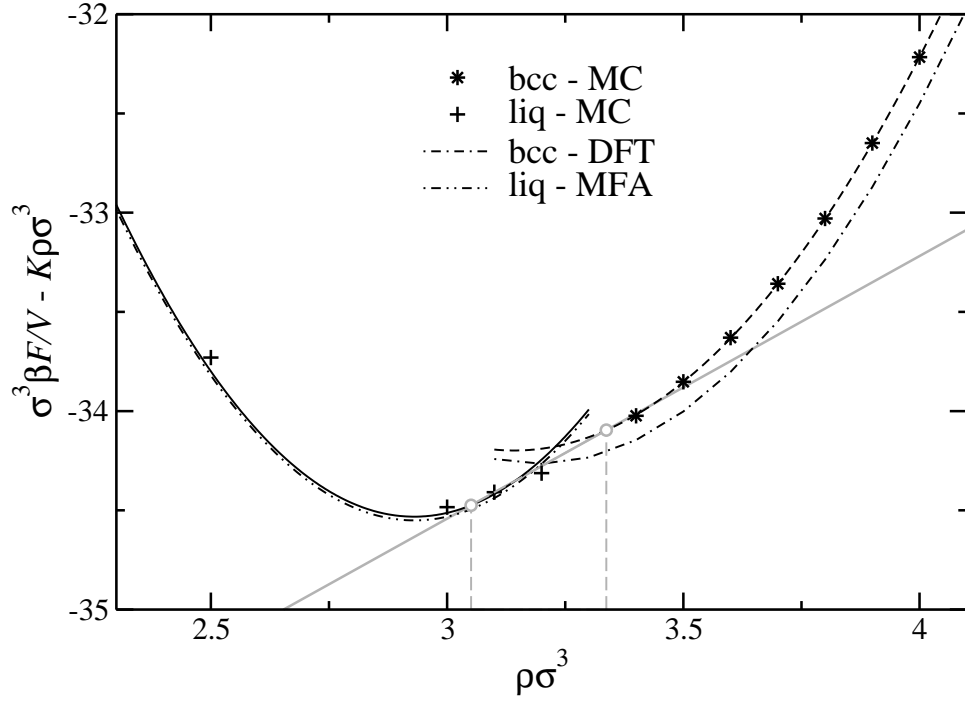


Figure 7.49: DFT and MC results of the modified free energy density $\beta \tilde{F} \sigma^3 / V \equiv \beta F \sigma^3 / V - K \rho \sigma^3$ of the GEM-4 system as function of $\rho \sigma^3$ at $k_B T / \varepsilon = 0.5$ for the fluid and the bcc phase. A term $K \rho \sigma^3$, with $K = 22$ and irrelevant for the determination of the coexistence densities, has been subtracted for clarity of presentation. The dashed and the solid lines serve as guide to the eye. All other lines and symbols as indicated in the plot. The grey points and drop down lines indicate the coexistence densities, while the grey line is the common tangent.

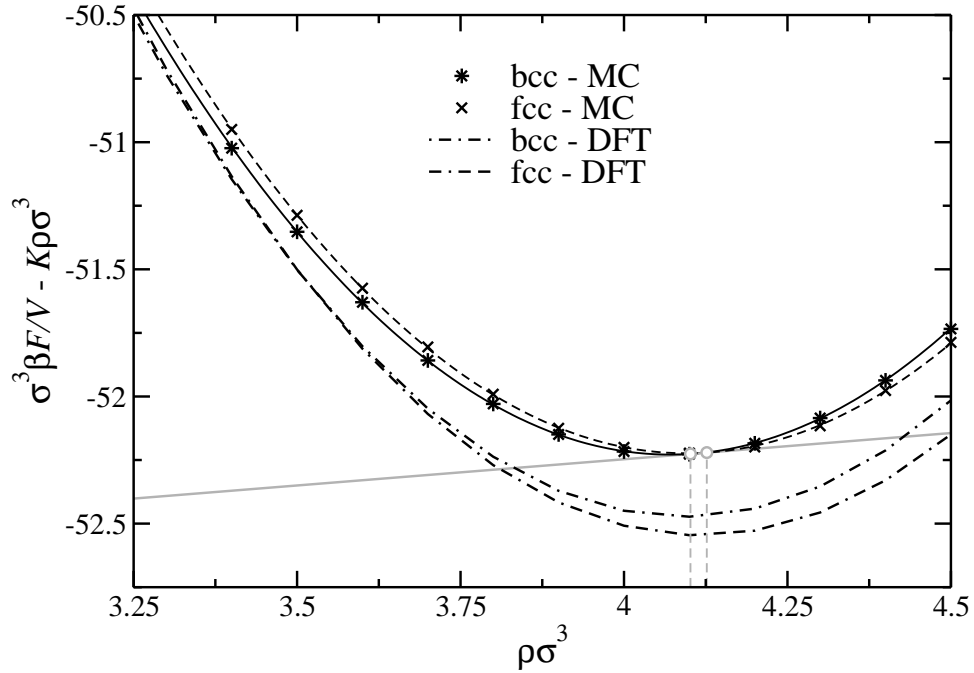


Figure 7.50: Same as Fig. 7.49 but for the bcc and fcc phases and for $K = 27$.

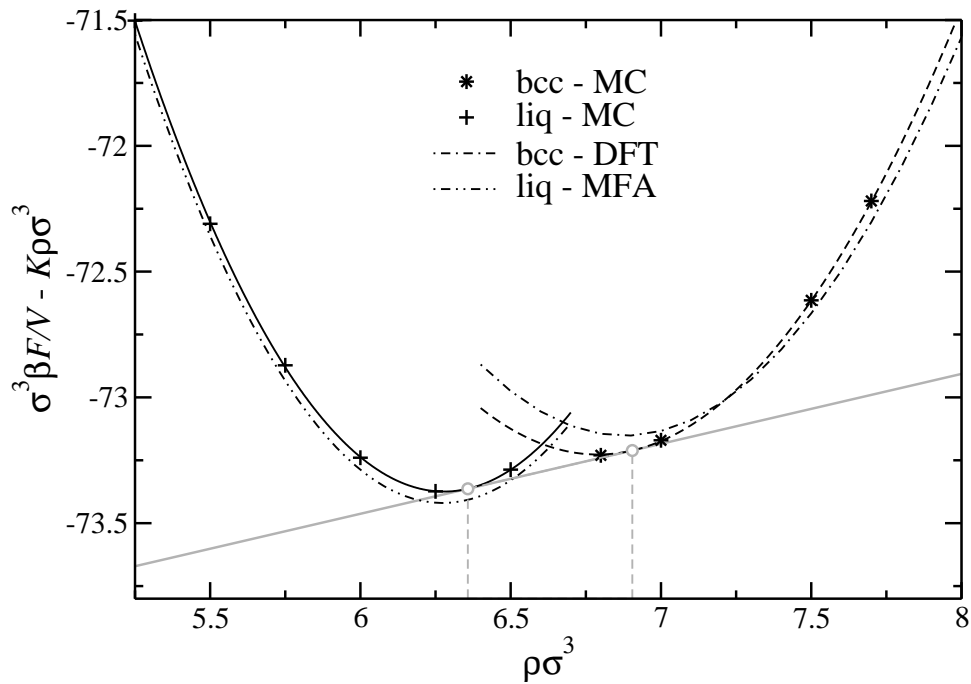


Figure 7.51: MC and DFT results of the modified free energy density $\beta \tilde{F} \sigma^3 / V \equiv \beta F \sigma^3 / V - K \rho \sigma^3$ of the GEM-4 system as function of $\rho \sigma^3$ at $k_B T / \varepsilon = 1.1$ for the fluid and the bcc phase. A term $K \rho \sigma^3$, with $K = 20$ and irrelevant for the determination of the coexistence densities, has been subtracted for clarity of presentation. The dashed and the solid lines serve as guide to the eye. All other lines and symbols as indicated in the plot. The grey points and drop down lines indicate the coexistence densities, while the grey line is the common tangent.

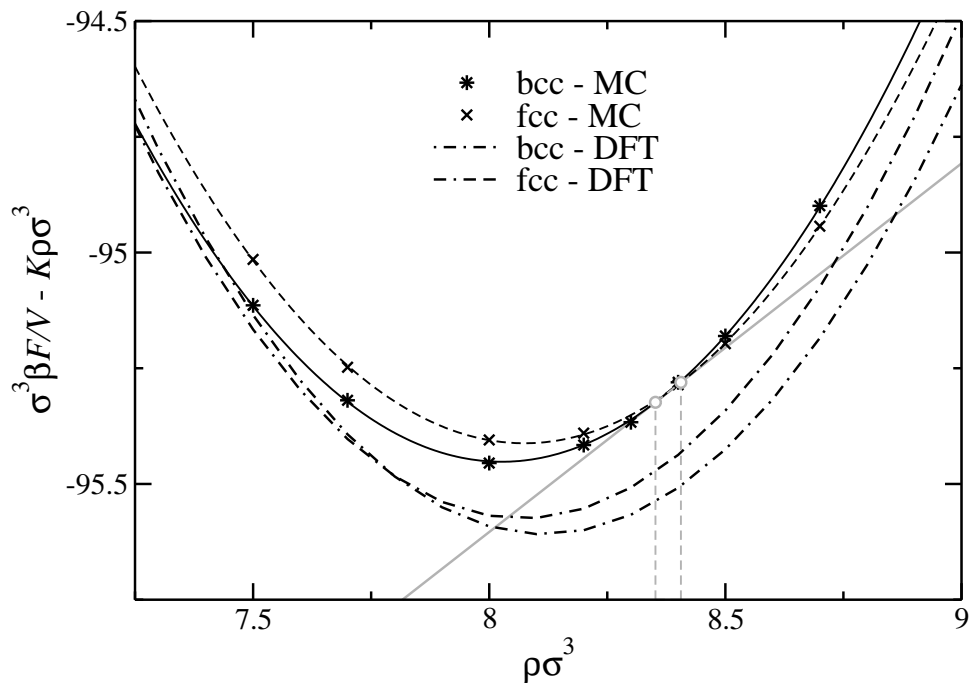


Figure 7.52: Same as Fig. 7.51 but for the bcc and fcc phases and for $K = 26$.

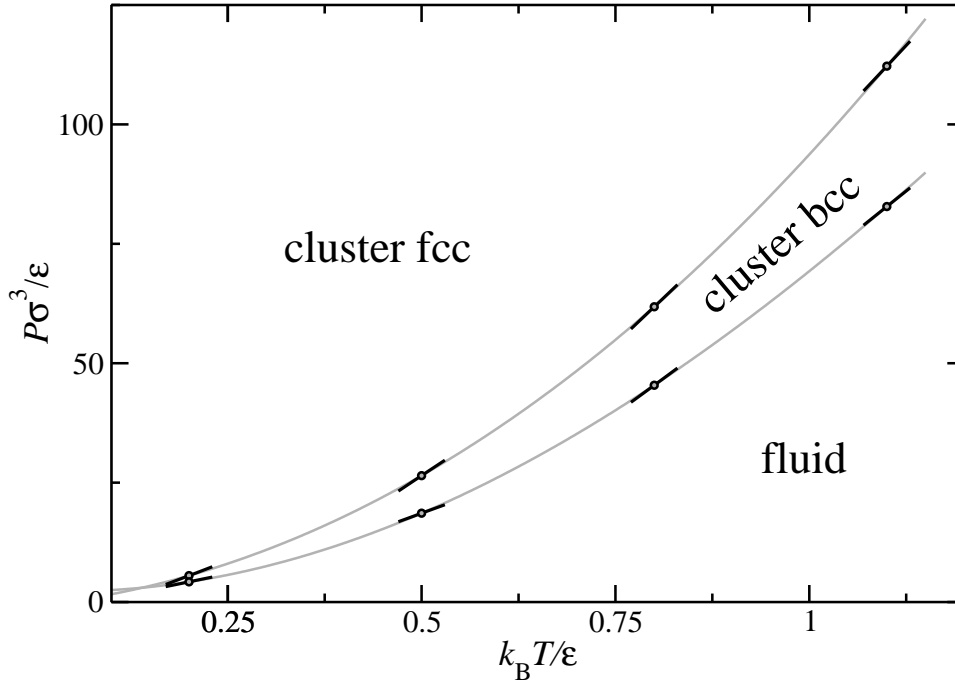


Figure 7.53: P - T phase diagram (points) as obtained from MC simulations with the corresponding Clausius-Clapeyron tangents (black segments) to the coexistence curve. The grey lines interpolate the simulation data and are guides to the eye. Their intersection point indicates a triple point at $k_B T/\epsilon \approx 0.15$.

sphere potentials, for which the phase diagrams are well known [171]. From these considerations, we expect for this temperature regime a phase transition between a liquid and a *single-occupancy* fcc crystal, while clustering only sets in after this freezing transition. These predictions have to be complemented by simulation results, which will be the topic of future work.

The use of MC simulations is indispensable to gain deeper insight into the clustering phenomenon, since they provide the connection between the microscopic details of the system and the (mean field) assumptions of the theories involved. Therefore, we proceed to a more detailed analysis of the clusters. Based on the data gathered for the three states corresponding to the simulation snapshots in Fig. 7.41 and an additional data set, we show in Fig. 7.54 how the cluster size distribution changes at fixed temperature when compressing the system. As already mentioned before, in the fluid phase ($\rho\sigma^3 = 6$) the cluster size distribution is very broad. This is also partly due to the difficulties to define clusters in an unambiguous manner (cf. Sec. 5.6.1). For the bcc structures formed at intermediate densities ($\rho\sigma^3 = 7$ and 7.5), the distribution of cluster sizes is already considerably narrower than in the fluid. Also, we see that the mean occupancy number increases upon compression. For the fcc phase at $\rho\sigma^3 = 8.5$, we see from the data in Fig. 7.54 that the mean cluster size has increased further and the cluster size distribution has become even narrower. This implies that the effective inter-cluster potential has become more repulsive with increasing ρ . Summarising, two tendencies are clearly visible with increasing density: the position of the maximum of these curves, indicating the most probable cluster size, shifts to higher values

while their width is reduced. This confirms on a more quantitative level the observations made at the beginning of this section that with increasing ρ the clusters become larger and more uniform in size.

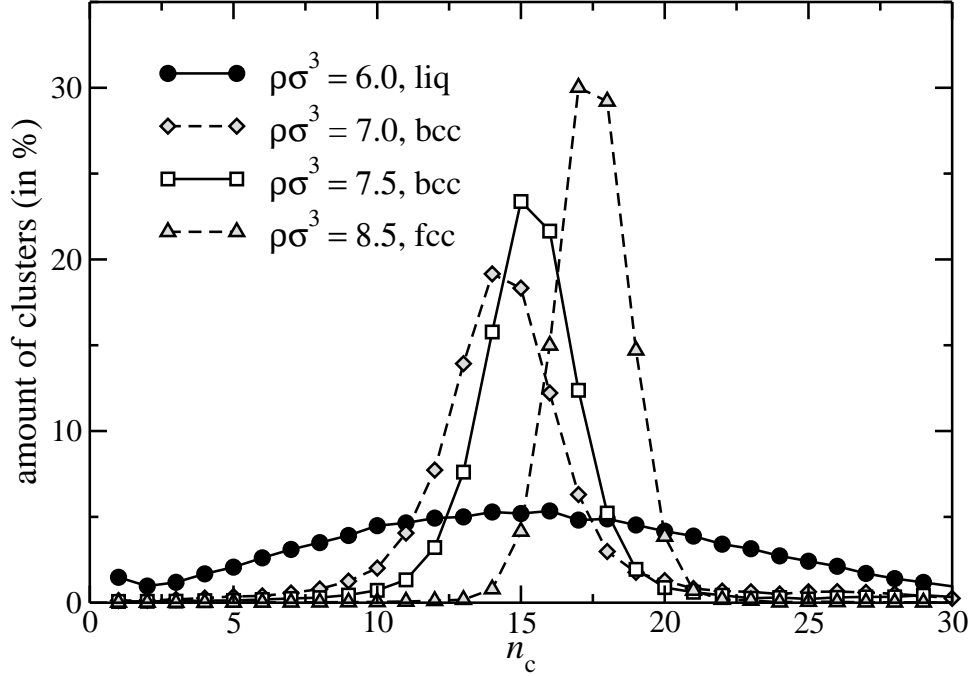


Figure 7.54: Probability distribution of cluster size n_c as obtained from MC simulations of a bcc phase at $\rho\sigma^3 = 7$ and the three states of the GEM-4 system shown in Fig. 7.41 (i.e., at $k_B T/\varepsilon = 1.1$). With increasing density, the maximum of n_c shifts to higher values and the distribution becomes narrower.

In Fig. 7.55, we plot the MC data for the mean value of n_c along the $k_B T/\varepsilon = 1.1$ isotherm as a function of ρ for the corresponding stable cluster solid. These data are complemented by the theoretical prediction of DFT, where n_c is the value minimising $f(n_c, \alpha)$ at a given state point. We point out that there is a discontinuity in n_c as the system undergoes a first order transition from the bcc to the fcc phase. Further, DFT predicts n_c to be *proportional* to the density, i.e., $n_c = c\rho\sigma^3$, c being a constant. This would have far-reaching consequences on the behaviour of our system, since then the lattice constant a of the conventional cubic unit cell can be expressed as

$$\frac{a}{\sigma} = \left(\frac{\gamma n_c}{\rho \sigma^3} \right)^{\frac{1}{3}} = (\gamma c)^{\frac{1}{3}} = \text{const.}, \quad (7.55)$$

where $\gamma = 2$ for bcc and $\gamma = 4$ for fcc crystals. This relation implies that the lattice constant should be *density-independent* and should not change under compression. This remarkable behaviour has already been predicted in [43] and has been put on a rigorous theoretical basis in [44]. It would mean that in striking contrast to harshly repulsive systems, the GEM-4 system should not react to an increase in density by diminishing its lattice constant. Rather, it is evidently more favourable for additional particles that are inserted into a fixed volume to join the clusters that have already

formed at the lattice sites while leaving the lattice constant unchanged. For the GEM-4, DFT predicts $a_{\text{bcc}} \sim 1.58\sigma$ and $a_{\text{fcc}} \sim 2.00\sigma$. In [44], it has been argued that the emergence of this single length scale is set by q_* , the location of the negative minimum in $\tilde{\phi}(q)$, i.e., it is a property solely determined by the functional form of the interaction potential. Using the values of the lattice constants quoted above, it is straightforward to show that the first non-vanishing RLVs of the bcc and fcc lattices have the magnitudes $\sigma q_{1,\text{fcc}} \sim 5.44$ and $\sigma q_{1,\text{bcc}} \sim 5.62$, respectively. Thus both lie very close to the value $\sigma q_* \sim 5.57$, in agreement with the arguments put forward in [44]. Within very good approximation, these values are constant at all densities, a feature that has also been seen in similar, two-dimensional models and has been termed ‘the unwavering magnitude of the wave vector’ [172].

It is interesting to compare this prediction of the DFT treatment to our MC results. DFT claims the lattice constant, and thereby primitive-cell volume volume, $v_c = V/N_c$, to be independent of density. This feature is known to break down in low-density crystals [93] and also within our MC simulations this prediction is found to be slightly violated at intermediate temperatures and densities. Though the linear relationship of n_c vs. ρ holds, the proportionality is shifted by a constant d , i.e., $n_c = c\rho\sigma^3 + d$. This then leads to a non-constant v_c , as can be gathered from Fig. 7.56, where we show that the change of v_c with density, $(\partial v_c/\partial \rho)_{T,\mu_c=0}$, is non-zero. However, it decreases with increasing T and ρ , suggesting that the DFT approximation is then *asymptotically* valid.

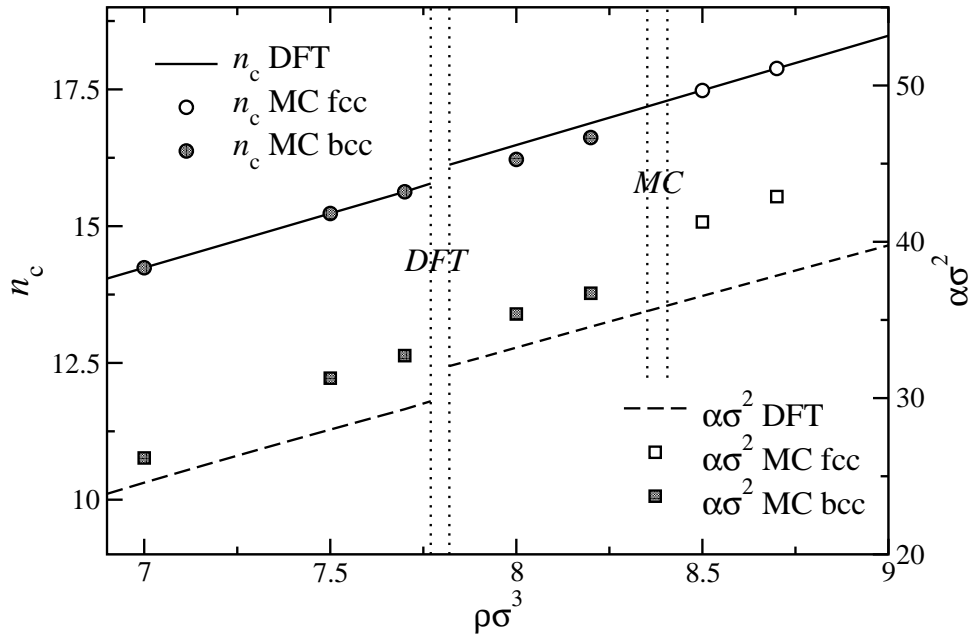


Figure 7.55: n_c and $\alpha\sigma^2$ as function of $\rho\sigma^3$ for the GEM-4 systems at $k_{\text{B}}T/\varepsilon = 1.1$. Discontinuities of both quantities at the density of the first order bcc-fcc phase transition are visible and indicated by dotted lines for both the DFT and MC prediction of the phase transition. Lines: DFT results, symbols: MC simulations.

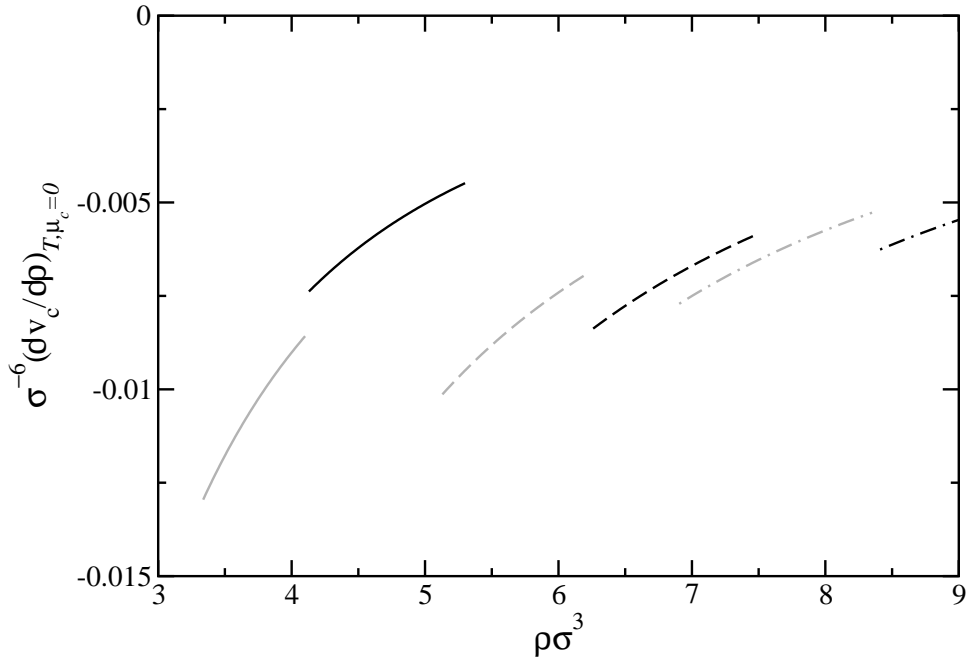


Figure 7.56: Variation of the primitive-cell volume, v_c , with density in equilibrium (i.e., at $\mu_c = 0$) for three different temperatures in the respective stable crystal structures [fcc (black) and bcc (grey) at $k_B T/\varepsilon = 0.5$ (solid line), $k_B T/\varepsilon = 0.8$ (dashed line), and at $k_B T/\varepsilon = 1.1$ (dot-dashed line)].

Let us return to Fig. 7.54, and investigate another characteristic feature of the system, namely the decrease of the width of the cluster size distribution with increasing density, which can be understood on energetic grounds. An increased density brings about a concomitant growth in the energetic barrier separating particles on one lattice site from those occupying another, neighbouring one. Thus, hopping between sites becomes prohibitively expensive and the clusters tend to show reduced “polydispersity” in occupancy. In addition, the localisation parameter α increases linearly with ϱ (cf. Fig. 7.55), i.e., the clusters become more compact as the density is increased, corresponding to a reduced polydispersity in size and shape. While the MC data for n_c nearly coincide with the DFT results, the agreement between the theoretical predictions for α and its corresponding value extracted from the simulations is slightly worse, while the tendencies are excellently reproduced on a qualitative level. We point out that the linear dependence of both n_c and α on ϱ has also been predicted in the theoretical framework presented in [44].

Finally, we proceed to a structure analysis of the clusters. In Fig. 7.57, we analyse the spherically averaged distribution $\varrho_{cl}(r)$ of the particles inside a cluster. Following the assumption made in the DFT calculations [cf. Eq. (4.31)] we fit the raw MC simulation data with a Gaussian shape for $\varrho(r)$, where α is now an adjustable parameter, while n_c is measured during the simulations. Though we observe small differences at small r (where the statistics of MC is, as expected, rather poor), the good qualitative agreement between simulation data and the fitted curve justifies *a posteriori* the assumption for the shape of the density profile $\varrho(r)$ postulated in Eq. (4.31).

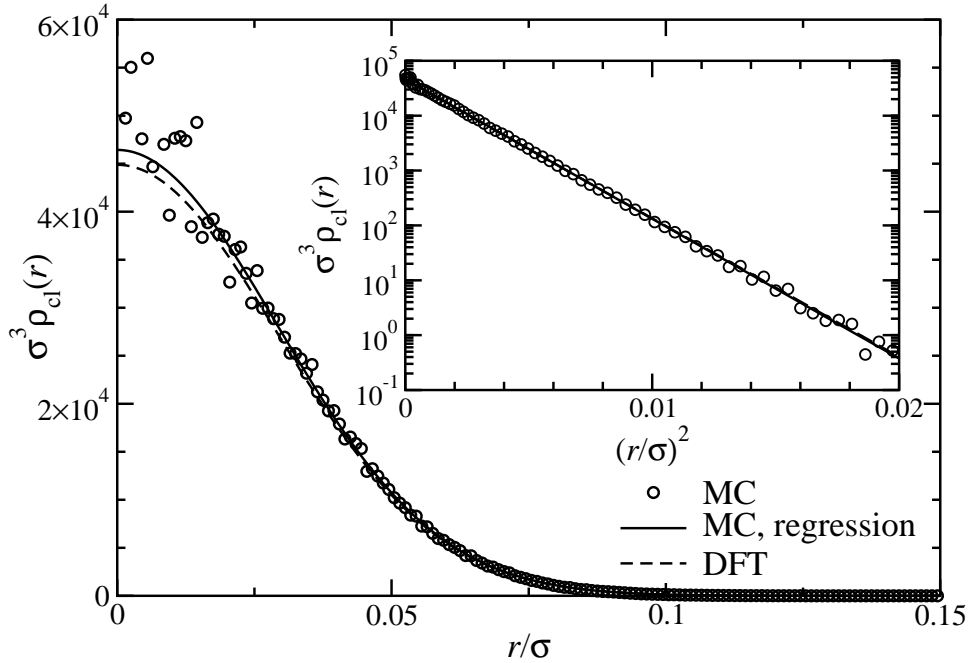


Figure 7.57: Cluster density profile $\rho_{cl}(r)$ for a cluster fcc crystal of the GEM-4 system at $k_B T/\varepsilon = 0.1$ and $\varrho\sigma^3 = 9$. The semi-logarithmic plot of $\rho_{cl}(r)$ vs. r^2/σ^2 in the inset corroborates the Gaussian shape of the distribution.

Due to the limitations of the MC simulations we use (i.e., fixed number of particles and constant box size and shape), spontaneous phase transitions from bcc to fcc are highly unlikely to take place. However, the spontaneous freezing of an initially liquid system as well as the melting of a crystal during the course of a simulation are observed. Thus, it is indispensable to unambiguously identify the crystalline structures within MC simulations. In Fig. 7.58 we show the RDF of the centres of mass of the clusters, i.e., $g_{cl}(r)$, for the three systems shown in Fig. 7.41. At $\varrho\sigma^3 = 6$, i.e., still in the fluid phase, $g_{cl}(r)$ shows a behaviour that is typical for a disordered phase. At the higher densities, $\varrho\sigma^3 = 7.5$ and $\varrho\sigma^3 = 8$, the occurrence of pronounced peaks is yet another imprint of the regular solid structures that the clusters have formed. The fact that these peaks become more pronounced at higher densities corroborates once more our observation that the lattice structure is then less distorted and thus better defined. The positions of the markers in Fig. 7.58 indicate the distances R_i^{fcc} or R_i^{bcc} of the different shells of neighbours around a central particle for the fcc or the bcc lattices. As expected, for $\varrho\sigma^3 = 7.5$, the positions of the peaks in $g_{cl}(r)$ coincide with the R_i^{bcc} of the bcc lattice, while for $\varrho\sigma^3 = 8.5$, they coincide with the fcc ones, confirming that the initial structures did not melt or transform. Also the height of the peaks of $g_{cl}(r)$ is correlated with the height of the respective markers. Thus, $g_{cl}(r)$ can serve as an indication of the respective crystalline structure of the systems.

As we can see from Fig. 7.57, the particles have a certain freedom to fluctuate around their equilibrium positions, i.e., the perfect lattice sites. These fluctuations are responsible that the

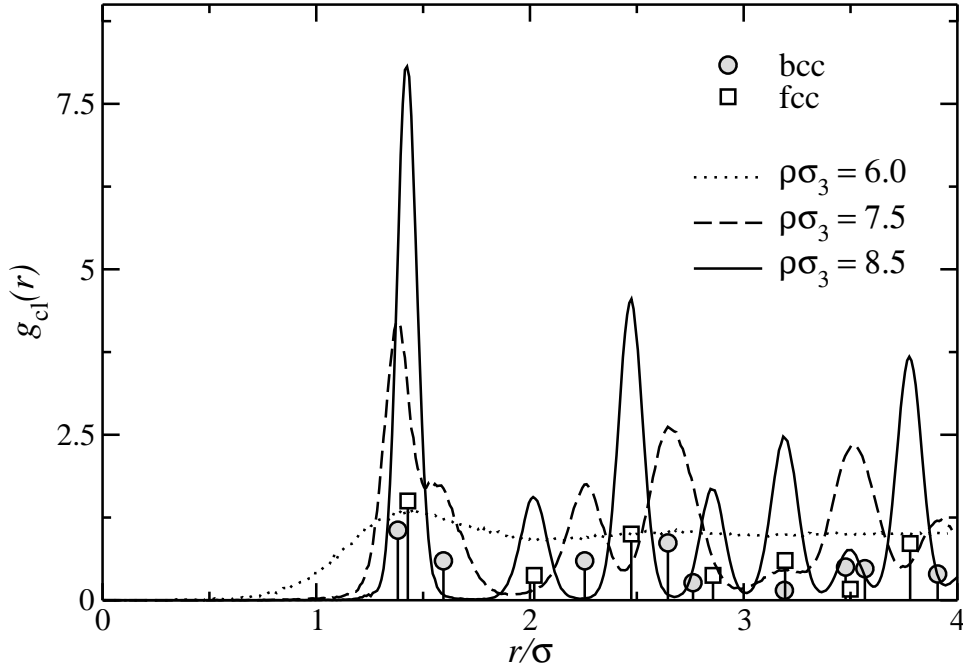


Figure 7.58: Radial distribution function $g_{cl}(r)$ of the centres of mass of the clusters for the three states of the GEM-4 system displayed in Fig. 7.41 (i.e., at $k_B T/\varepsilon = 1.1$). The markers indicate the positions of the various shells of neighbours of perfect bcc and fcc lattices.

perfect crystal is subject to slight distortions (see Fig. 7.59). Therefore, it is convenient to use bond order parameters (cf. Sec. 5.6.2) as a more quantitative measure of the degree of crystallinity in our system. In the case of our MC simulations for the GEM-4 system this tool has proven to be a reliable tool for unambiguously distinguishing between the liquid phase and the different hyper-crystals.

Finally, let us turn to the elastic behaviour of the GEM-4 system by studying the bulk modulus within MC simulations [cf. Sec. 7.2]. The results for B [obtained by Eq. (7.37)] for the respective stable solids at different temperatures (cf. Fig. 7.41) are compared in Fig. 7.60 to the values obtained by direct numerical differentiation of the equilibrium (i.e., $\mu_c = 0$) free energy results. A remarkable agreement is obtained between the two approaches. Being far from negligible, the correction to the “quenched” bulk modulus, B_{vir} , amounts to a reduction of over 40% of its value, as can be seen in Tab. 7.7 and in Fig. 7.60. The term $\frac{\rho^2}{n_c} \left(\frac{\partial \mu_c}{\partial \rho} \right)_{T, n_c}$ is the leading term in the correction to B [cf. Eq. (7.37)]. Therefore, we show how μ_c typically changes with density at constant T and n_c in Fig. 7.61. The other contribution to B_{corr} is at least an order of magnitude smaller. The nature of the leading term of the correction suggests that deletion of lattice sites substantially weakens the response of the system to compression compared to a simple affine transformation (which corresponds to the term B_{vir}). Going back to Fig. 7.60, we see that, as expected, an increase in density leads to an increase in the bulk modulus. The denser the system, the harder it is to compress. However, the temperature dependence is rather weak. Varying $k_B T/\varepsilon$

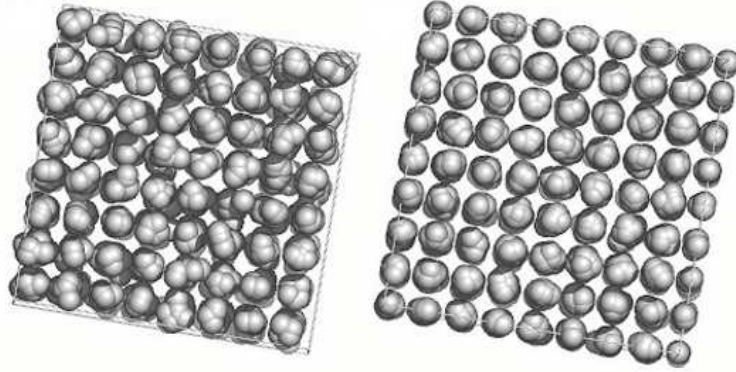


Figure 7.59: Snapshots from MC simulations of GEM-4 fcc crystals at $k_B T = 0.4$ and at $\varrho\sigma^3 = 3.5$ (left panel) and $\varrho\sigma^3 = 7$ (right panel). As we can see, the crystal structure becomes better defined at higher densities.

$k_B T/\varepsilon$	$\varrho\sigma^3$	$B_{\text{vir}}\varepsilon/\sigma^3$	$B_{\text{corr}}\varepsilon/\sigma^3$	$c_{11}\varepsilon\sigma^3$	$c_{12}\varepsilon\sigma^3$	$c_{22}\varepsilon\sigma^3$	ω
0.5	4.3	89.8	41.6	1.335	2.95	10.0	0.805
0.8	6.2	177	76.6	1.346	3.05	15.4	0.670
1.1	8.2	308	131	1.350	3.10	21.0	0.582

Table 7.7: Bulk modulus decomposition [cf. Eq.(7.37)] and sound mode coupling constants [cf. Eq.(7.40)] for three different multiply-occupied crystal state points.

from 0.5 to 1.1, all the respective curves of the bulk modulus seem to coincide with a single master curve, being only a function of ϱ . This suggests that entropic effects have little impact in this regime.

The coefficients c_{11} , c_{12} , and c_{22} of the sound modes [cf. Eq. (7.40)] can be obtained from numerical evaluation of the corresponding derivatives given by Eqs. (7.42) to (7.48). The main contributions in these formulae stem from the change of μ and μ_c with N at constant ϱ_c , therefore, we show the typical progression of these curves in Figs. 7.62 and 7.63. The results for the coefficients c_{11} , c_{12} , and c_{22} and the coupling constant ω of the density fluctuations are presented for three different state points in Tab. 7.7. Although these results are insufficient to draw the full picture, a few comments are still in order. First, c_{11} corresponds to the hopping of particles and the sound mode connected with this is expected to be heavily damped, while the sound wave associated with c_{22} is longitudinal and will propagate for long wavelengths. Second, for the temperature and density range studied, c_{11} and the cross term c_{12} increase only weakly with T and ϱ , while c_{22} grows by more than a factor of two. The increase in density as we proceed from one state point to the other is most certainly responsible for the increasing resistance of the system to this sort of density fluctuations. Higher temperatures, on the other hand, would rather *facilitate* lattice spacing fluctuations. To the best of our knowledge, no theoretical predictions exist with which to further compare these results.

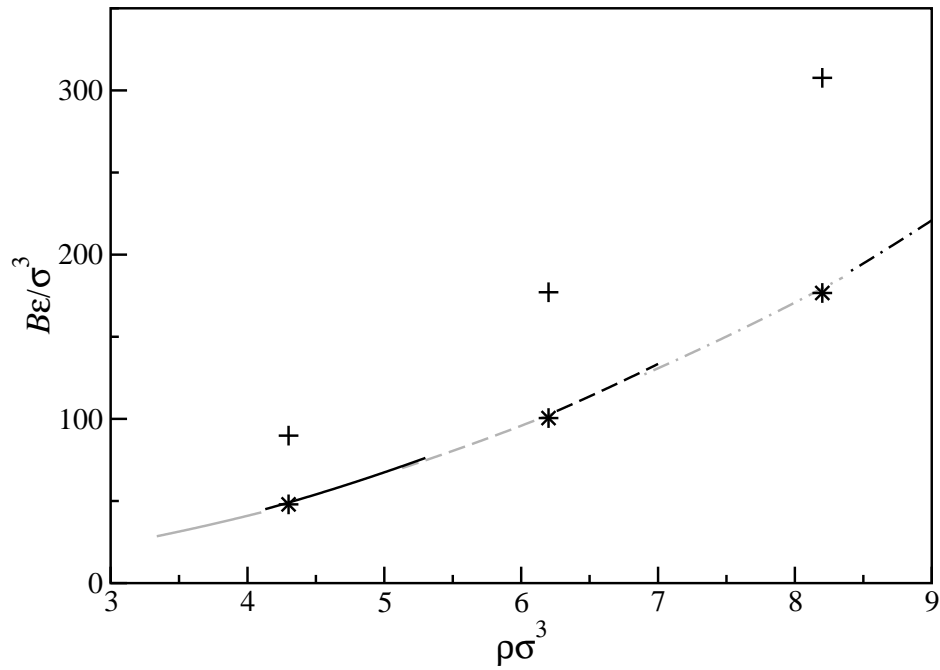


Figure 7.60: Results for the reduced dimensionless bulk modulus from direct differentiation of the free energy for three different temperatures in the stable crystal structures [fcc (black) and bcc (grey) at $k_B T/\varepsilon = 0.5$ (solid line), $k_B T/\varepsilon = 0.8$ (dashed line), and at $k_B T/\varepsilon = 1.1$ (dot-dashed line)], along with the values at three state points for B_{vir} (crosses) and $B = B_{\text{vir}} - B_{\text{corr}}$ (stars). The breakdown of the contributions to B is given in Tab. 7.7.

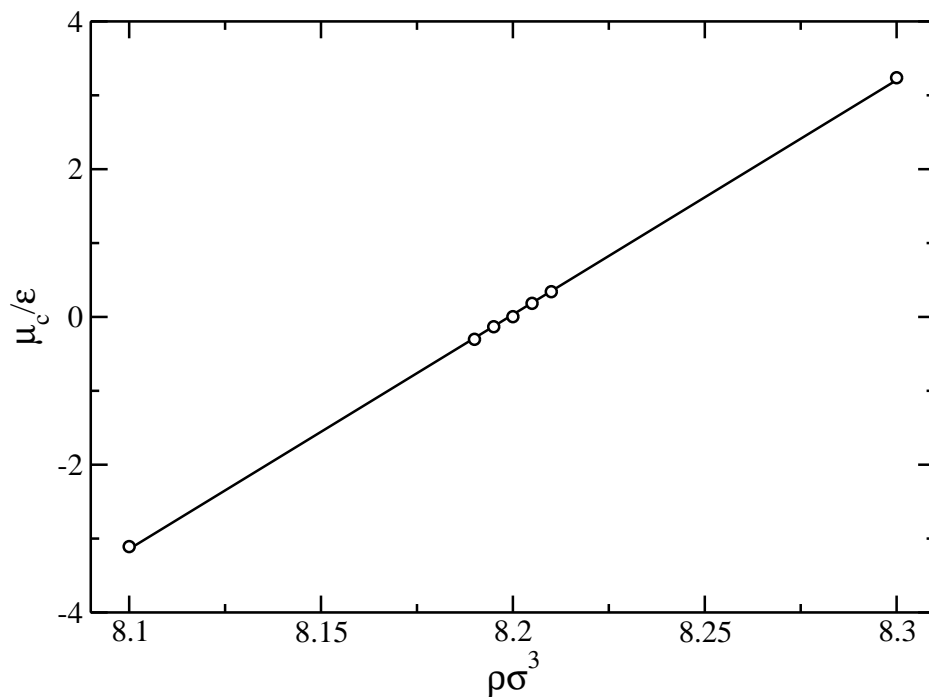


Figure 7.61: Typical progression of μ_c vs. ρ at constant ϱ_c . Data are shown for a GEM-4 bcc crystal at constant $N = 4155$, $N_c = 250$ and $k_B T/\varepsilon = 1.1$.

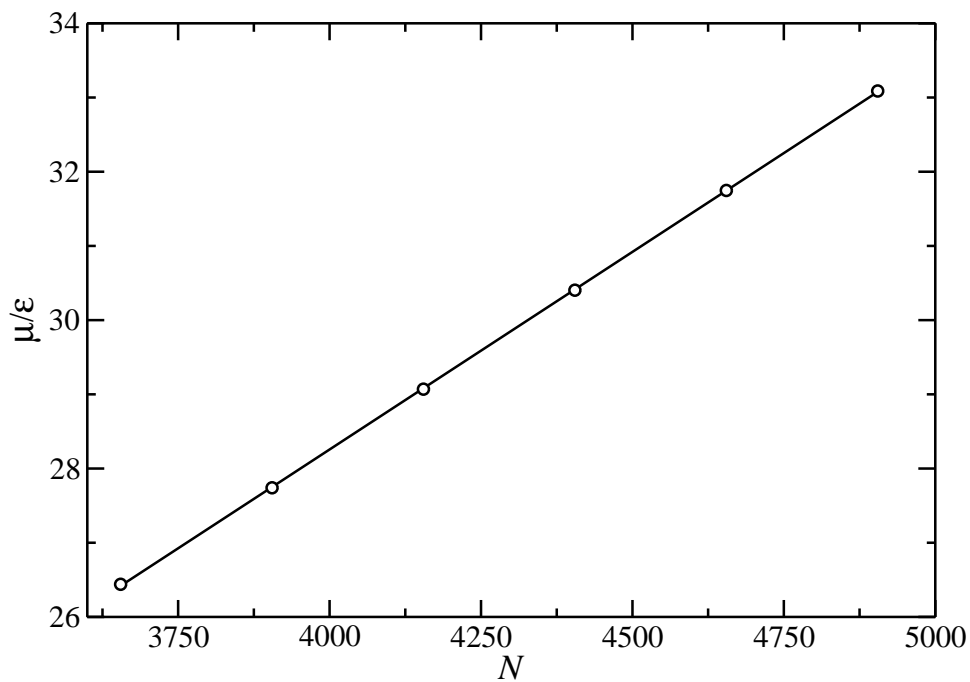


Figure 7.62: Typical progression of μ vs. N at constant ρ_c . Data are shown for a GEM-4 bcc crystal at constant $V = 506.70731$, $N_c = 250$ and $k_B T/\epsilon = 1.1$.

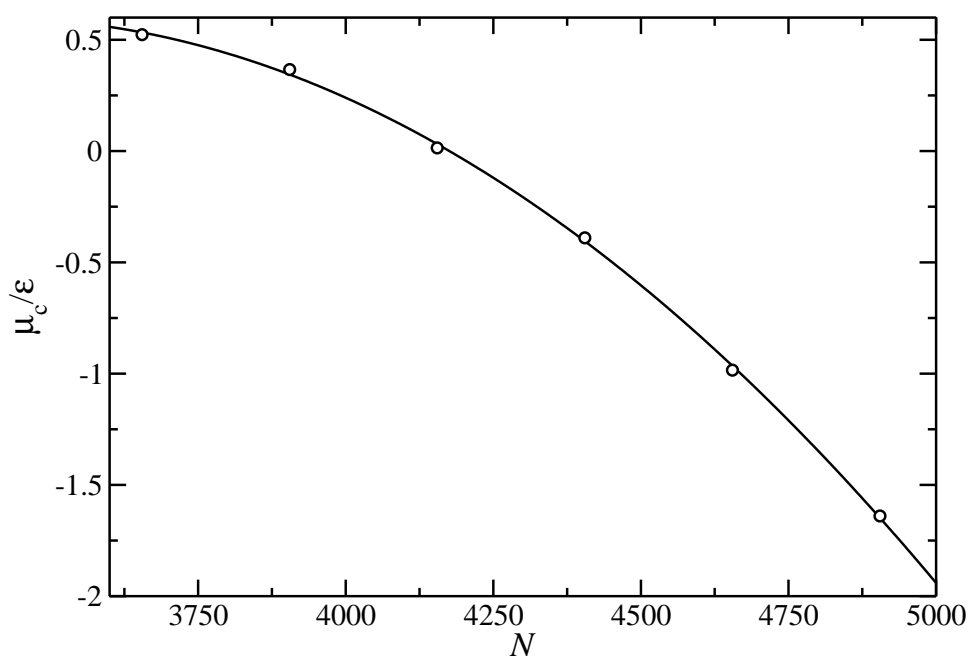


Figure 7.63: Typical progression of μ_c vs. N at constant ρ_c . Data are shown for a GEM-4 bcc crystal at constant $V = 506.70731$, $N_c = 250$ and $k_B T/\epsilon = 1.1$.

Chapter 8

Conclusion

In this work, we have studied the properties and the phase behaviour of systems where particles interact via purely repulsive, bounded effective potentials, which serve as model interactions of realistic soft-matter systems. We have shown that depending on whether the Fourier transform of such a potential is non-negative or oscillates between positive and negative values, re-entrant melting or clustering is expected as a phase behaviour. Re-entrant melting has already been investigated thoroughly. The clustering phenomenon however is much more intriguing for a couple of reasons. On the one hand, it is counterintuitive to find an effective attraction between purely repulsive particles. On the other hand, this behaviour has never been observed experimentally. Therefore, we have proposed guidelines for the synthesis of such substances. Here, we have designed amphiphilic dendrimers and have shown *in silico* how their effective interaction can be tuned by suitable modifications to their architecture.

Next, we have derived suitable statistical mechanical tools to describe the clustering phenomenon, thereby allowing for a thorough investigation of this remarkable phase behaviour. On the one hand, we have shown that the joint use of genetic algorithms, integral equation theories and density functional theory provides the proper theoretical framework to do so. On the other hand, we have developed new simulation techniques to determine the phase diagram of clustering potentials. Starting from the theoretical apparatus developed by Swope and Anderson [163], we have demonstrated how simulations and experiments of multiple-occupancy crystals critically depend on the chemical potential associated with the creation of a lattice site. Incorporating this into the simulation formalism allows for the precise determination of the thermodynamic phase diagram, which is much more complex than for traditional single-occupancy crystals. Even though the chemical potential connected to lattice site creation vanishes in equilibrium, derivatives of this property are non-zero, so it has considerable impact on second derivatives of the constrained free energy, as we have shown by example of the bulk modulus.

We have applied these techniques to a representative model potential for which clustering is expected, namely, the generalised exponential model of index 4. In particular, we have shown

that clustering occurs both in the dense fluid as well as in the ordered, solid phases. In the fluid phase, overlapping particles form clusters that are characterised by a broad cluster-size distribution. Upon increasing the density, first-order phase transitions occur where the clusters arrange themselves at the lattice sites of bcc and, upon further compression, fcc hyper-crystals. While the bcc structure is only stable in a narrow, wedge-like region of the (T, ρ) -plane, the fcc cluster crystals are stable in the overwhelming part of parameter space. In both solid phases, the respective lattice constant remains nearly unchanged upon compression of the system, so both the cluster population number and the width of the distribution of particles inside a cluster grow linearly with density. We demonstrated that the properties of the fluid phase can be reasonably well described by the mean field approximation. The solid cluster phases, on the other hand, can be treated within classical density functional theory using a mean-field simplification, as justified by theoretical considerations [44]. These data were checked against lattice Monte Carlo simulations results, showing both the strengths and deficiencies of the theoretical concepts.

Our guidelines on assembling amphiphilic dendrimers in the lab bear significance for soft-matter science and materials design at various levels. At the one-particle level, we have established that synthesising open dendrimers with a segregated core-shell structure requires neither stiff bonds nor electrostatic repulsions as commonly believed—amphiphilicity is sufficient. At the many-body level, solutions of such dendrimers will display pronounced correlations at a *single* length scale, independently of the density [44]. This allows for well-controlled spatial modulation of confined liquids and thus their local index of refraction, whose intensity can be tuned by changing the degree of confinement. Crystals formed by such systems will show lattice constants that are nearly density-*independent*, featuring thus a novel form of microscopic self-assembly. Moreover, clustering materials are quite unusual. They are diffusive on the single-particle level, which allows for mass transport. On the collective level however they are arrested, and thus rigid as a conventional solid [173].

Finally, on the fundamental level, we have demonstrated that within soft-matter physics, bounded effective interactions can be manipulated with the same degree of flexibility as diverging ones. This demonstrates that these systems have a lot of promising features in store that have not yet been discovered experimentally.

Appendix A

The Polylogarithm

The polylogarithm of order n , $\text{Li}_n(z)$, also known as Jonquière's function [174], is a complex valued function of complex argument z , defined by

$$\text{Li}_n(z) = \frac{z}{\Gamma(n)} \int_0^\infty dt \frac{t^{n-1}}{e^t - z}, \quad (\text{A.1})$$

where n is a positive, real parameter. If $z \in \mathbb{R} \setminus (1, \infty)$, then the polylogarithm is real-valued [175]. For $|z| < 1$ the polylogarithm can be evaluated as a power series

$$\text{Li}_n(z) = \sum_{k=1}^{\infty} \frac{z^k}{k^n}. \quad (\text{A.2})$$

A relation that turned out to be useful for the present application is

$$\frac{d}{dz} \text{Li}_n(z) = \frac{1}{z} \text{Li}_{n-1}(z). \quad (\text{A.3})$$

A detailed list of additional, helpful relations for this function can be found in [176].

The polylogarithm was introduced in the present context in [41] to calculate the thermodynamic properties of the GCM within the MFA where, obviously, expression (A.2) was used throughout. This was done even though there was no guarantee that for certain state points the modulus of the respective arguments $|z|$ does not exceed 1, violating thus the condition for the validity of Eq. (A.2). Since this function plays a central role in the formalism of the MFA and the SCOZA (see Sec. 4.1), a reliable evaluation of $\text{Li}_n(z)$ for arbitrary argument z is indispensable for a successful solution of the SCOZA-ODE and PDE. We therefore provide in the following a more detailed presentation of evaluation schemes and indicate how this function can be calculated in an accurate and efficient way for arbitrary argument z .

In its evaluation of $\text{Li}_n(z)$, the `MATHEMATICA` software relies on Euler-MacLaurin summation, expansions in terms of incomplete Gamma functions, and numerical quadrature [133]. Efficient *and* accurate C- or Fortran-based implementations, on the other hand, are more difficult to find.

First attempts to evaluate Eq. (A.1) directly by various numerical integration schemes turned out to be either too time-consuming or did not provide results of sufficient accuracy. Finally, we found that the following functional relation between the polylogarithm and the complete Fermi-Dirac function, $F_n(z)$,

$$F_n(z) = \frac{1}{\Gamma(n+1)} \int_0^\infty dt \frac{t^n}{e^{t-z} + 1} = -\text{Li}_{n+1}(-e^z) \quad (\text{A.4})$$

along with the accurate and efficient implementation of $F_n(z)$ via series and asymptotic expansions in combination with Chebyshev fits, as implemented in the GNU Scientific Library [177], provided the desired results, which finally brought the solution of the SCOZA differential equations within reach.

Appendix B

Overlapping distribution method in the NPT ensemble

Here, we derive the formalism of the overlapping distribution method in the NPT ensemble in more detail (cf. Sec. 5.5.3). We perform two simulations: one using a system of $(N + 1)$ particles interacting via potential Φ and the other containing N interacting particles and one ideal gas particle.

For the system of $(N + 1)$ particles, the probability distribution of energy difference $\Delta\Phi$ with respect to the second system is given by

$$p_{N+1}(\Delta\Phi) = \frac{1}{z_{N+1,P,T}} \int dV e^{-\beta PV} \int dr^{N+1} e^{-\beta\Phi_{N+1}} \delta(\Phi_{N+1} - \Phi_N - \Delta\Phi). \quad (\text{B.1})$$

where the configurational integral of an NPT system is given by

$$z_{N,P,T} = \int dV e^{-\beta PV} \int dr^N e^{-\beta\Phi_N}. \quad (\text{B.2})$$

The probability distribution, $p_N(\Delta\Phi)$, for the system of N interacting particles and one ideal gas particle is given by

$$p_N(\Delta\Phi) = \frac{\int dV e^{-\beta PV} \int dr^{N+1} e^{-\beta\Phi_N} \delta(\Phi_{N+1} - \Phi_N - \Delta\Phi)}{\int dV e^{-\beta PV} \int dr^{N+1} e^{-\beta\Phi_N}}. \quad (\text{B.3})$$

The normalisation factor of the term on the right hand side can be rewritten as follows

$$\begin{aligned}
\int dV e^{-\beta PV} \int dr^{N+1} e^{-\beta \Phi_N} &= \int dV e^{-\beta PV} \int dr_{N+1} \int dr^N e^{-\beta \Phi_N} \\
&= \int dV e^{-\beta PV} V \int dr^N e^{-\beta \Phi_N} \\
&= \frac{\int dV e^{-\beta PV} V \int dr^N e^{-\beta \Phi_N}}{\int dV e^{-\beta PV} \int dr^N e^{-\beta \Phi_N}} \int dV e^{-\beta PV} \int dr^N e^{-\beta \Phi_N} \\
&= \langle V \rangle_{NPT} z_{N,P,T} \tag{B.4}
\end{aligned}$$

Now, the probability distribution for the first system can be reformulated as

$$\begin{aligned}
p_{N+1}(\Delta\Phi) &= \frac{1}{z_{N+1,P,T}} \int dV e^{-\beta PV} dr^{N+1} e^{-\beta \Phi_{N+1}} \delta(\Phi_{N+1} - \Phi_N - \Delta\Phi) = \\
&= \frac{e^{-\beta \Delta\Phi}}{z_{N+1,P,T}} \int dV e^{-\beta PV} dr^{N+1} e^{-\beta PV} e^{-\beta \Phi_N} \delta(\Phi_{N+1} - \Phi_N - \Delta\Phi). \tag{B.5}
\end{aligned}$$

Using Eq. (B.4), this reduces to

$$\begin{aligned}
p_{N+1}(\Delta\Phi) &= \frac{z_{N,P,T}}{z_{N+1,P,T}} \langle V \rangle_{NPT} e^{-\beta \Delta\Phi} p_N(\Delta\Phi) = \\
&= \frac{Q_{N,P,T}}{Q_{N+1,P,T}} \frac{\Lambda^{3N} N!}{\Lambda^{3(N+1)} (N+1)!} \langle V \rangle_{NPT} e^{-\beta \Delta\Phi} p_N(\Delta\Phi) = \\
&= e^{\beta\mu} \frac{\langle V \rangle_{NPT}}{\Lambda^3 (N+1)} e^{-\beta \Delta\Phi} p_N(\Delta\Phi). \tag{B.6}
\end{aligned}$$

Taking the logarithm of the last equation, we arrive at

$$\ln p_{N+1}(\Delta\Phi) = \beta\mu + \ln \frac{\langle V \rangle_{NPT}}{\Lambda^3 (N+1)} - \beta \Delta\Phi + \ln p_N(\Delta\Phi), \tag{B.7}$$

which can be rewritten as

$$\begin{aligned}
\beta\mu &= \beta \Delta\Phi + \ln [p_{N+1}(\Delta\Phi)] - \ln \left[p_N(\Delta\Phi) \frac{\langle V \rangle_{NPT}}{\Lambda^3 (N+1)} \right] = \\
&= -\ln \left(\frac{1}{\beta P \Lambda^3} \right) + \beta \Delta\Phi + \ln [p_{N+1}(\Delta\Phi)] - \ln \left[p_N(\Delta\Phi) \frac{\langle V \rangle_{NPT} \beta P}{(N+1)} \right] = \\
&= \beta\mu^{\text{id}} + \beta \Delta\Phi + \ln [p_{N+1}(\Delta\Phi)] - \ln \left[p_N(\Delta\Phi) \frac{\langle V \rangle_{NPT} \beta P}{(N+1)} \right]. \tag{B.8}
\end{aligned}$$

The excess chemical potential is then given by

$$\beta\mu^{\text{ex}} = \beta \Delta\Phi + \ln [p_{N+1}(\Delta\Phi)] - \ln \left[p_N(\Delta\Phi) \frac{\langle V \rangle_{NPT} \beta P}{(N+1)} \right] \tag{B.9}$$

We define two functions, f^0 and f^1 , given by

$$\begin{aligned} f^0(\Delta\Phi) &= \log \left[p_N(\Delta\Phi) \frac{\langle V \rangle_{NPT} \beta P}{(N+1)} \right] - \frac{\beta \Delta\Phi}{2} \\ f^1(\Delta\Phi) &= \log [p_{N+1}(\Delta\Phi)] + \frac{\beta \Delta\Phi}{2}. \end{aligned} \tag{B.10}$$

Then, the excess part of the chemical potential can again be determined via Eq. (5.54).

Appendix C

Monte Carlo simulation data for the GEM-4

For every (T, ϱ) state point, simulations were carried out at different values of N , searching for the equilibrium configuration, i.e., $\mu_c = 0$. For this purpose, thermodynamic integration was carried out at 20 Gauss Lobatto integration points for each of these $N\varrho T$ combinations. In additional simulations, we measured P and μ for the same parameters. In total, determination of an equilibrium configuration at one specific (T, ϱ) point required an average of ~ 1200 CPU hours.

$k_{\text{B}}T/\varepsilon$	structure	$\rho\sigma^3$	n_c	$\beta F/N$	μ/ε	$P\sigma^3/\varepsilon$	
0.2	liq	1.2		8.023	3.86	2.71	
		1.3		8.958	4.20	3.14	
		1.4		9.877	4.52	3.57	
		1.45		10.330	4.67	3.79	
		1.5		10.776	4.81	4.00	
		1.55		11.217	4.95	4.21	
	bcc	1.6		11.650	5.08	4.41	
		1.6	3.241	11.650	4.90	4.11	
		1.7	3.444	12.443	5.14	4.52	
		1.8	3.657	13.215	5.39	4.95	
		1.9	3.850	13.975	5.66	5.45	
		2.0	4.037	14.728	5.94	5.99	
	fcc	2.1	4.220	15.476	6.22	6.57	
		2.2	4.428	16.217	6.48	7.11	
		1.6	3.278	11.677	4.88	4.08	
		1.7	3.494	12.463	5.12	4.46	
		1.8	3.710	13.226	5.36	4.89	
		1.9	3.908	13.975	5.63	5.38	
			2.0	4.086	14.722	5.91	5.94
			2.2	4.504	16.197	6.40	6.99

Table C.1: MC results for the cluster size n_c , free energy F , chemical potential μ and pressure P at fixed temperature $k_{\text{B}}T = 0.2$ for various densities and structures in equilibrium (i.e., $\mu_c = 0$). Error estimates in the various values are as follows: $n_c : \pm 0.005$, $\beta F/N : \pm 0.001$, $\mu/\varepsilon : \pm 0.02$, $P\sigma^3/\varepsilon : \pm 0.01$

$k_{\text{B}}T/\varepsilon$	structure	$\rho\sigma^3$	n_c	$\beta F/N$	μ/ε	$P\sigma^3/\varepsilon$	
0.5	liquid	0.5		-0.259	1.18	0.66	
		1.0		2.143	3.34	2.26	
		1.5		4.343	5.39	4.83	
		2.0		6.451	7.39	8.32	
		2.5		8.508	9.34	12.70	
		3.0		10.505	11.18	17.78	
		3.1		10.900	11.51	18.80	
		3.2		11.277	11.81	19.75	
		bcc	3.4	6.900	11.993	11.75	19.54
			3.5	7.096	12.328	12.00	20.42
			3.6	7.300	12.658	12.26	21.34
			3.7	7.492	12.984	12.52	22.31
			3.8	7.692	13.308	12.79	23.32
			3.9	7.892	13.628	13.05	24.33
	4.0		8.100	13.946	13.31	25.37	
	4.1		8.300	14.262	13.59	26.44	
	4.2		8.492	14.575	13.86	27.60	
	4.3		8.688	14.887	14.13	28.76	
	fcc	4.4	8.896	15.196	14.39	29.89	
		4.5	9.088	15.503	14.67	31.11	
		5.0	10.072	17.020	16.02	37.51	
		3.4	7.004	12.015	11.70	19.37	
		3.5	7.207	12.346	11.95	20.23	
		3.6	7.410	12.674	12.20	21.13	
		3.7	7.613	12.999	12.45	22.07	
		3.8	7.813	13.318	12.73	23.06	
		3.9	8.020	13.635	12.99	24.06	
		4.0	8.219	13.950	13.25	25.12	
		4.1	8.418	14.263	13.52	26.19	
		4.2	8.621	14.572	13.79	27.30	
	4.3	8.824	14.880	14.05	28.42		
	4.4	9.031	15.187	14.32	29.55		
4.5	9.230	15.492	14.58	30.72			

Table C.2: MC results for the cluster size n_c , free energy F , chemical potential μ and pressure P at fixed temperature $k_{\text{B}}T = 0.5$ for various densities and structures in equilibrium (i.e., $\mu_c = 0$). Error estimates in the various values are as follows: $n_c : \pm 0.005$, $\beta F/N : \pm 0.001$, $\mu/\varepsilon : \pm 0.02$, $P\sigma^3/\varepsilon : \pm 0.01$

$k_{\text{B}}T/\varepsilon$	structure	$\rho\sigma^3$	n_c	$\beta F/N$	μ/ε	$P\sigma^3/\varepsilon$
0.8	liquid	3.5		6.450	13.78	25.66
		3.75		6.970	14.77	29.24
		4.0		7.489	15.75	33.04
		4.2		7.901	16.53	36.23
		4.5		8.514	17.67	41.21
		4.75		9.014	18.59	45.47
		5.0	bcc	10.176	11.871	18.28
	5.5		11.176	12.938	19.53	50.47
	5.7		11.572	13.352	20.06	53.44
	6.0		12.164	13.963	20.86	58.17
	6.2		12.564	14.365	21.40	61.44
	6.3		12.760	14.564	21.67	63.13
	6.4		12.952	14.762	21.95	64.89
	6.5		13.152	14.960	22.21	66.63
	6.7		13.552	15.352	22.76	70.16
	5.5	fcc	11.352	12.953	19.45	49.99
	5.7		11.754	13.363	19.98	52.91
	6.0		12.359	13.968	20.77	57.54
	6.2		12.758	14.366	21.30	60.81
	6.3		12.957	14.563	21.57	62.48
	6.4		13.152	14.759	21.84	64.22
	6.5		13.368	14.955	22.10	65.85
	6.7	13.754	15.343	22.65	69.48	

Table C.3: MC results for the cluster size n_c , free energy F , chemical potential μ and pressure P at fixed temperature $k_{\text{B}}T = 0.8$ for various densities and structures in equilibrium (i.e., $\mu_c = 0$). Error estimates in the various values are as follows: $n_c : \pm 0.005$, $\beta F/N : \pm 0.001$, $\mu/\varepsilon : \pm 0.02$, $P\sigma^3/\varepsilon : \pm 0.01$

$k_{\text{B}}T/\varepsilon$	structure	$\rho\sigma^3$	n_c	$\beta F/N$	μ/ε	$P\sigma^3/\varepsilon$	
1.1	liquid	5.0		9.794	20.30	52.55	
		5.25		10.319	21.30	57.64	
		5.5		10.838	22.28	62.95	
		5.75		11.359	23.27	68.47	
		6.0		11.873	24.24	74.20	
		6.25		12.386	25.20	80.10	
		6.5		12.898	26.14	86.09	
		bcc	6.8	13.840	12.231	25.41	81.32
			7.0	14.240	12.547	25.90	84.68
			7.5	15.232	13.318	27.19	94.08
	7.7		15.628	13.621	27.73	98.12	
	8.0		16.220	14.068	28.53	104.47	
	8.2		16.620	14.364	29.07	108.81	
	8.3		16.820	14.510	29.34	111.02	
	fcc	8.4	17.012	14.657	29.61	113.33	
		8.5	17.212	14.802	29.88	115.61	
		8.7	17.604	15.092	30.43	120.31	
		7.5	15.477	13.331	27.09	93.17	
		7.7	15.879	13.630	27.61	97.16	
		8.0	16.484	14.074	28.40	103.37	
		8.2	16.887	14.367	28.94	107.69	
		8.4	17.285	14.656	29.47	112.14	
		8.5	17.480	14.800	29.74	114.45	
	8.7	17.883	15.087	30.28	119.05		

Table C.4: MC results for the cluster size n_c , free energy F , chemical potential μ and pressure P at fixed temperature $k_{\text{B}}T = 1.1$ for various densities and structures in equilibrium (i.e., $\mu_c = 0$). Error estimates in the various values are as follows: $n_c : \pm 0.005$, $\beta F/N : \pm 0.001$, $\mu/\varepsilon : \pm 0.02$, $P\sigma^3/\varepsilon : \pm 0.01$

The hidden chapter or The future of air travel

(and the dangers of applying science)

To save costs...



...airlines must increase the packing density of passengers.



They do this by decreasing the “lattice spacing”.
This is how most of us travel...



But if airlines ever find out about this work...

...the future could be far worse:



Text and drawings by Daan Frenkel.

Bibliography

- [1] Special Issue dedicated to the conference on "Colloidal dispersions in external fields", J. Phys.: Condens. Mat **16**, S3769 (2004).
- [2] C. N. Likos, Phys. Rep. **348**, 267 (2001).
- [3] C. N. Likos, H. Löwen, M. Watzlawek, B. Abbas, O. Jucknischke, J. Allgaier, and D. Richter, Phys. Rev. Lett. **80**, 4450 (1998).
- [4] A. R. Denton, Phys. Rev. E **67**, 11804 (2003).
- [5] A. R. Denton, Phys. Rev. E **68**, 49904 (2003), Erratum.
- [6] B. Krüger, L. Schäfer, and A. Baumgärtner, J. Phys. (France) **50**, 3191 (1989).
- [7] J. Dautenhahn and C. K. Hall, Macromolecules **27**, 5399 (1994).
- [8] A. A. Louis, P. G. Bolhuis, J.-P. Hansen, and E. J. Meijer, Phys. Rev. Lett. **85**, 2522 (2000).
- [9] I. O. Götze, H. M. Harreis, and C. N. Likos, J. Chem. Phys. **120**, 7761 (2004).
- [10] M. Ballauff and C. N. Likos, Angew. Chem. Int. Ed. **43**, 2998 (2004).
- [11] D. Gottwald, C. N. Likos, G. Kahl, and H. Löwen, Phys. Rev. Lett. **92**, 68301 (2004).
- [12] D. Gottwald, C. N. Likos, G. Kahl, and H. Löwen, J. Chem. Phys. **122**, 074903 (2005).
- [13] C. Pierleoni, C. Addison, J.-P. Hansen, and V. Krakoviack, Phys. Rev. Lett. **96**, 128302 (2006).
- [14] J.-P. Hansen and C. Pearson, Mol. Phys. **104**, 3389 (2006).
- [15] P. N. Pusey and W. van Meegen, Nature **320**, 340 (1986).
- [16] U. Gasser, E. R. Weeks, A. Schofield, P. N. Pusey, and D. A. Weitz, Science **292**, 258 (2001).
- [17] V. J. Anderson and H. N. W. Lekkerkerker, Nature **416**, 811 (2002).
- [18] P. Ziherl and R. D. Kamien, Phys. Rev. Lett. **85**, 3528 (2000).

- [19] M. E. Leunissen, C. G. Christova, A. P. Hynninen, C. P. Royall, A. I. Campbell, A. Imhof, M. Dijkstra, R. van Roij, and A. van Blaaderen, *Nature* **437**, 235 (2005).
 - [20] D. A. Hajduk, P. E. Harper, S. M. Gruner, C. C. Honeker, G. Kim, E. L. Thomas, and L. J. Fetters, *Macromolecules* **27**, 4063 (1994).
 - [21] W. M. Matsen, *J. Chem. Phys.* **108**, 785 (1998).
 - [22] C. K. Ullal, M. Maldovan, E. L. Thomas, G. Chen, Y. J. Han, and S. Yang, *Appl. Phys. Lett.* **84**, 5434 (2004).
 - [23] M. Watzlawek, C. N. Likos, and H. Löwen, *Phys. Rev. Lett.* **82**, 5289 (1999).
 - [24] C. N. Likos, M. Watzlawek, and H. Löwen, *Phys. Rev. E* **58**, 3135 (1998).
 - [25] F. H. Stillinger, *J. Chem. Phys.* **65**, 3968 (1976).
 - [26] M.-J. Feraud, E. Lomba, and L. L. Lee, *J. Chem. Phys.* **112**, 810 (2000).
 - [27] M. Schmidt, *J. Phys.: Condens. Matter* **11**, 10163 (1999).
 - [28] Y. Rosenfeld, M. Schmidt, M. Watzlawek, and H. Löwen, *Phys. Rev. E* **62**, 5006 (2000).
 - [29] L. Acedo and A. Santos, *Phys. Rev. A* **323**, 427 (2004).
 - [30] A. Santos, *Mol. Phys.* **104**, 3411 (2006).
 - [31] A. Malijevský and A. Santos, *J. Chem. Phys.* **124**, 074508 (2006).
 - [32] A. Santos and A. Malijevský, *Phys. Rev. E* **75**, 021210 (2007).
 - [33] A. Santos and A. Malijevský, *Phys. Rev. E* **75**, 049901 (2007).
 - [34] A. Malijevský, S. Yuste, and A. Santos, *Phys. Rev. E* **76**, 021504 (2007).
 - [35] F. H. Stillinger and T. A. Weber, *J. Chem. Phys.* **68**, 3837 (1978).
 - [36] F. H. Stillinger, *J. Chem. Phys.* **70**, 4067 (1979).
 - [37] F. H. Stillinger, *Phys. Rev. B* **20**, 299 (1979).
 - [38] F. H. Stillinger and T. A. Weber, *Phys. Rev. B* **22**, 3790 (1980).
 - [39] F. H. Stillinger and D. K. Stillinger, *Physica A* **244**, 358 (1997).
 - [40] A. Lang, C. N. Likos, M. Watzlawek, and H. Löwen, *J. Phys.: Condens. Matter* **12**, 5087 (2000).
 - [41] A. A. Louis, P. G. Bolhuis, and J.-P. Hansen, *Phys. Rev. E* **62**, 7961 (2000).
 - [42] S. Prestipino, F. Saija, and P. V. Giaquinta, *Phys. Rev. E* **71**, 50102 (2005).
-

-
- [43] C. N. Likos, A. Lang, M. Watzlawek, and H. Löwen, *Phys. Rev. E* **63**, 31206 (2001).
- [44] C. N. Likos, B. M. Mladek, D. Gottwald, and G. Kahl, *J. Chem. Phys.* **126**, 224502 (2007).
- [45] D. Ruelle, *Statistical Mechanics* (W. A. Benjamin, New York, 1969).
- [46] B. M. Mladek, *Integral Equation Theories and Computer Simulations for Systems with Bounded Potentials*, diploma thesis (Universität Wien, unpublished), 2003.
- [47] B. M. Mladek, M.-J. Feraud, G. Kahl, and M. Neumann, *Condens. Matter Phys.* **8**, 135 (2005).
- [48] B. M. Mladek, D. Gottwald, G. Kahl, M. Neumann, and C. N. Likos, *Phys. Rev. Lett.* **96**, 45701 (2006).
- [49] H. Fragner, *Phys. Rev. E* **75**, 061402 (2007).
- [50] K. Huang, *Statistical Mechanics* (John Wiley and Sons, New York, 1963).
- [51] R. Kubo, *Statistical Mechanics* (North-Holland Publishing Company, Amsterdam, 1965).
- [52] D. A. McQuarrie, *Statistical Mechanics* (University Science Books, Sausalito, 2000).
- [53] C. Kittel and H. Kroemer, *Thermal Physics*, 2nd ed. (W. H. Freeman and Company, New York, 1995).
- [54] J.-P. Hansen and I. R. McDonald, *Theory of Simple Liquids*, 3rd ed. (Academic Press, London, 2006).
- [55] M. P. Allen and D. J. Tildesley, *Computer Simulation of Liquids* (Clarendon Press, Oxford, 1990).
- [56] L. S. Ornstein and F. Zernike, *Proc. Akad. Sci. (Amsterdam)* **17**, 793 (1914).
- [57] J. L. Lebowitz and J. Percus, *Phys. Rev.* **144**, 217 (1966).
- [58] D. Henderson, E. Waisman, J. L. Lebowitz, and L. Blum, *Mol. Phys.* **35**, 241 (1978).
- [59] J. M. J. van Leeuwen, J. Groeneveld, and J. de Boer, *Physica* **25**, 792 (1959).
- [60] J. K. Percus and G. J. Yevick, *Phys. Rev.* **110**, 1 (1958).
- [61] F. J. Rogers and D. A. Young, *Phys. Rev. A* **30**, 999 (1984).
- [62] Y. Rosenfeld and N. W. Ashcroft, *Phys. Rev. A* **20**, 1208 (1979).
- [63] J.-P. Hansen and G. Zerah, *Phys. Lett.* **108**, 277 (1985).
- [64] G. Zerah and J.-P. Hansen, *J. Chem. Phys.* **84**, 2336 (1986).
-

- [65] J. S. Høye and G. Stell, *Mol. Phys.* **52**, 1071 (1984).
 - [66] J. S. Høye and G. Stell, *J. Chem. Phys.* **67**, 439 (1977).
 - [67] A. Parola and L. Reatto, *Adv. Phys.* **44**, 211 (1995).
 - [68] A. Reiner and G. Kahl, *Phys. Rev. E* **65**, 46701 (2002).
 - [69] A. Reiner and G. Kahl, *J. Chem. Phys.* **117**, 4925 (2002).
 - [70] D. Pini, G. Stell, and N. B. Wilding, *Mol. Phys.* **95**, 483 (1998).
 - [71] D. Pini, G. Stell, and N. B. Wilding, *J. Chem. Phys.* **115**, 2702 (2001).
 - [72] E. Schöll-Paschinger, *J. Chem. Phys.* **120**, 11698 (2004).
 - [73] L. Blum and J. S. Høye, *J. Stat. Phys.* **19**, 317 (1978).
 - [74] E. Arrieta, C. Jedrzejek, and K. N. Marsh, *J. Chem. Phys.* **95**, 6806 (1991).
 - [75] D. Gottwald, G. Kahl, and C. N. Likos, *J. Chem. Phys.* **122**, 204503 (2005).
 - [76] D. Gottwald, *Genetic Algorithms in Condensed Matter Theory*, PhD thesis (TU Wien, unpublished), 2005.
 - [77] R. Evans, in *Fundamentals of Inhomogeneous Fluids* (Marcel Dekker, New York, 1992), Chap. Density Functionals in Nonuniform Fluids.
 - [78] B. M. Mladek, D. Gottwald, G. Kahl, M. Neumann, and C. N. Likos, *Clustering in the absence of attractions: density functional theory and computer simulations*, *J. Phys. Chem. B*, 2007, in press.
 - [79] D. Frenkel and B. Smit, *Understanding Molecular Simulation*, 2nd ed. (Academic Press, London, 2002).
 - [80] M. E. J. Newman and G. T. Barkema, *Monte Carlo Methods in Statistical Physics* (Clarendon Press, Oxford, 1999).
 - [81] D. P. Landau and K. Binder, *A guide to Monte Carlo simulations in statistical physics* (Cambridge University Press, Cambridge, 2000).
 - [82] P. S. Y. Cheung, *Mol. Phys.* **33**, 519 (1977).
 - [83] J. S. Rowlinson, *Liquids and liquid mixtures* (Butterworths Scientific Publications, London, 1959).
 - [84] J. M. Yeomans, *Statistical Mechanics of Phase Transitions* (Clarendon Press, Oxford, 1992).
 - [85] S. Lipschutz, *Schaum's Outline of Theory and Problems of Probability* (McGraw-Hill Book Company, New York, 1968).
-

-
- [86] N. G. van Kampen, *Stochastic Processes in Physics and Chemistry* (North-Holland Physics Publishing, Amsterdam, 1981).
- [87] N. Metropolis, A. W. Rosenbluth, M. N. Rosenbluth, A. H. Teller, and E. Teller, *J. Chem. Phys.* **21**, 1087 (1953).
- [88] W. W. Wood, *J. Chem. Phys.* **48**, 415 (1968).
- [89] I. R. McDonald, *Mol. Phys.* **23**, 41 (1972).
- [90] R. Eppinga and D. Frenkel, *Mol. Phys.* **52**, 1303 (1984).
- [91] B. Quentrec and C. Brot, *J. Comput. Phys.* **13**, 430 (1975).
- [92] H. Fragner, *Lattice Monte Carlo Simulationen mit rekonfigurierbaren Prozessoren*, PhD thesis (Universität Wien, unpublished), 2005.
- [93] H. Fragner, *Comput. Phys. Commun.* **176**, 327 (2007).
- [94] A. Z. Panagiotopoulos, *J. Chem. Phys.* **112**, 7132 (2000).
- [95] C. E. Shannon, *Proc. Institute of Radio Engineers* **37**, 10 (1949).
- [96] K. S. Shing and K. E. Gubbins, *Mol. Phys.* **46**, 1109 (1982).
- [97] K. S. Shing and K. E. Gubbins, *Mol. Phys.* **49**, 1121 (1983).
- [98] C. H. Bennett, *J. Comp. Phys.* **22**, 245 (1976).
- [99] M. J. Vlot, S. Claassen, H. E. A. Huitema, and J. P. van der Eerden, *Mol. Phys.* **91**, 19 (1997).
- [100] D. Paschek, *J. Chem. Phys.* **120**, 6674 (2004).
- [101] D. Chandler, *Introduction to Modern Statistical Mechanics* (Oxford University Press, Oxford, 1987).
- [102] B. J. Schulz, K. Binder, M. Müller, and D. P. Landau, *Phys. Rev. E* **67**, 067102 (2003).
- [103] W. H. Press, S. A. Teukolsky, W. T. Vetterling, and B. P. Flannery, *Numerical Recipes in FORTRAN: The Art of Scientific Computing*, 2nd ed. (Cambridge University Press, Cambridge, 1992).
- [104] D. Frenkel and A. J. C. Ladd, *J. Chem. Phys.* **81**, 3188 (1984).
- [105] M. Abramowitz and I. A. Stegun, *Handbook of Mathematical Functions with Formulas, Graphs, and Mathematical Tables*, 9th ed. (Dover, New York, 1972).
- [106] A. Z. Panagiotopoulos, *Mol. Phys.* **61**, 813 (1987).
-

- [107] A. Z. Panagiotopoulos, N. Quirke, M. R. Stapleton, and D. J. Tildesley, *Mol. Phys.* **63**, 527 (1988).
- [108] B. Smit, Ph. de Smedt, and D. Frenkel, *Mol. Phys.* **68**, 931 (1989).
- [109] A. Z. Panagiotopoulos, *Mol. Simul.* **9**, 1 (1992).
- [110] P. J. Steinhart, D. R. Nelson, and M. Ronchetti, *Phys. Rev. B* **28**, 784 (1983).
- [111] J. S. van Duijneveldt and D. Frenkel, *J. Chem. Phys.* **96**, 4655 (1992).
- [112] P. R. ten Wolde, M. J. Ruiz-Montero, and D. Frenkel, *Phys. Rev. Lett.* **75**, 2714 (1995).
- [113] P. R. ten Wolde, M. J. Ruiz-Montero, and D. Frenkel, *J. Chem. Phys.* **104**, 9932 (1996).
- [114] Wolfram MathWorld: <http://mathworld.wolfram.com/Wigner3j-Symbol.html>.
- [115] C. I. Addison, J.-P. Hansen, V. Krakoviack, and A. A. Louis, *Mol. Phys.* **103**, 2045 (2005).
- [116] M. W. Matsen and M. Schick, *Phys. Rev. Lett.* **72**, 2660 (1994).
- [117] G. A. McConnell and A. P. Gast, *Phys. Rev. E* **54**, 5447 (1996).
- [118] G. A. McConnell and A. P. Gast, *Macromolecules* **30**, 435 (1997).
- [119] A. P. Gast, *Curr. Opinion Colloid Interface Sci.* **2**, 258 (1997).
- [120] P. J. Flory and W. R. Krigbaum, *J. Chem. Phys.* **18**, 1086 (1950).
- [121] O. F. Olaj and K. H. Pelinka, *Macromol. Chem.* **177**, 3413 (1976).
- [122] O. F. Olaj, *Macromol. Chem.* **177**, 3427 (1976).
- [123] O. F. Olaj and W. Lantschbauer, *Ber. Bunsen-Ges. Physik. Chem.* **81**, 985 (1977).
- [124] O. F. Olaj, W. Lantschbauer, and K. H. Pelinka, *Macromolecules* **13**, 299 (1980).
- [125] A. Y. Grosberg, P. G. Khalatur, and A. R. Khokhlov, *Makromol. Chem.* **3**, 709 (1982).
- [126] O. F. Olaj, G. Zifferer, and H. Rhemann, *Monatsh. Chem.* **116**, 1395 (1985).
- [127] L. Schäfer and A. Baumgärtner, *J. Phys. (Paris)* **47**, 1431 (1986).
- [128] R. Czech and C. K. Hall, *Macromolecules* **24**, 1535 (1991).
- [129] C. N. Likos, S. Rosenfeldt, N. Dingenouts, M. Ballauff, P. Lindner, N. Werner, and F. Vögtle, *J. Chem. Phys.* **117**, 1869 (2002).
- [130] A. Santos, *J. Chem. Phys.* **126**, 116101 (2007).
- [131] E. Schöll-Paschinger, *Phase Behaviour of Simple Fluids and Their Mixtures*, PhD Thesis (TU Wien, unpublished), 2002.
-

-
- [132] C. Caccamo, G. Pellicane, D. Costa, D. Pini, and G. Stell, *Phys. Rev. E* **60**, 5533 (1999).
- [133] S. Wolfram, *The Mathematica Book*, 5th ed. (Wolfram Media Inc., Champaign, 2003).
- [134] M. O. Goerbig, P. Lederer, and C. Morais Smith, *Phys. Rev. B* **69**, 115327 (2004).
- [135] E. Buhleier, W. Wehner, and F. Vögtle, *Synthesis-Stuttgart* **2**, 155 (1978).
- [136] P.G. de Gennes and H. Hervet, *J. Phys. Lett.* **44**, L351 (1983).
- [137] R. L. Lescanec and M. Muthukumar, *Macromolecules* **23**, 2280 (1990).
- [138] T. C. Zook and G. T. Pickett, *Phys. Rev. Lett.* **90**, 015502 (2003).
- [139] B. J. Bauer, B. Hammouda, R. Briber, and D. A. Tomalia, *Polym. Mater. Sci. Eng.* **67**, 340 (1992).
- [140] T. J. Prosa, B. J. Bauer, E. J. Amis, D. A. Tomalia, and R. Scherrenberg, *J. Polym. Sci., Part B: Polym. Phys.* **35**, 2913 (1997).
- [141] D. Poetschke and M. Ballauff, *Structure of Dendrimers in Solution as Probed by Scattering Experiments*, in *Structure and Dynamics of Polymer and Colloidal Systems* (Kluwer, Dordrecht, 2002).
- [142] C. N. Likos and M. Ballauff, in *Functional Molecular Nanostructures of the Series Topics in Current Chemistry* (Springer-Verlag, Berlin, 2005), Chap. Equilibrium Structure of Dendrimers - Results and Open Questions.
- [143] S. Rosenfeldt, N. Dingenouts, D. Pötschke, M. Ballauff, A. J. Beeresheim, K. Müllen, and P. Linder, *Angew. Chem.* **116**, 111 (2004).
- [144] P. Welch and M. Muthukumar, *Macromolecules* **31**, 5892 (1998).
- [145] J. K. Young, G. R. Baker, G. R. Newkome, K. F. Morris, and C. S. Johnson, *Macromolecules* **27**, 3464 (1994).
- [146] R. Briber, B. Bauer, B. Hammouda, and D. Tomalia, *Polym. Mater. Sci. Eng.* **67**, 430 (1992).
- [147] B. Helms and E. W. Meijer, *Science* **313**, 929 (2006).
- [148] L. J. Twyman, A. E. Beezer, R. Esfand, M. J. Hardy, and J. C. Mitchell, *Tetrahedron Lett.* **40**, 1743 (1999).
- [149] N. Malik, R. Wiwattanapatapee, R. Klopsch, K. Lorenz, H. Frey, J. W. Weener, E. W. Meijer, W. Paulus, and R. Duncan, *J. Control. Release* **65**, 133 (2000).
- [150] A. E. Beezer, A. S. H. King, I. K. Martin, J. C. Mitchel, L. J. Twyman, and C. F. Wain, *Tetrahedron* **59**, 3873 (2003).
-

- [151] F. Aulenta, W. Hayes, and S. Rannard, *Eur. Polym. J.* **39**, 1741 (2003).
- [152] N. Nishiyama, A. Iriyama, W. D. Jang, K. Miyata, K. Itaka, Y. Inoue, H. Takahashi, Y. Yanagi, Y. Tamaki, H. Koyama, and K. Kataoka, *Nat. Mater.* **4**, 934 (2005).
- [153] C. C. Lee, J. A. MacKay, J. M. J. Frechet, and F. C. Szoka, *Nat. Biotechnol.* **23**, 1517 (2005).
- [154] T. D. McCarthy, P. Karellas, S. A. Henderson, M. Giannis, D. F. O'Keefe, G. Heery, J. R. A. Paull, B. R. Matthews, and G. Holan, *Mol. Pharmaceutics* **2**, 312 (2005).
- [155] P. Antoni, D. Nyström, C. J. Hawker, A. Hult, and M. Malkoch, *Chem. Commun.* 2249 (2007).
- [156] C. Hawker and J. M. J. Fréchet, *J. Am. Chem. Soc.* **112**, 7638 (1990).
- [157] H. C. Kolb, M. G. Finn, and K. B. Sharpless, *Angew. Chemie Intl. English Ed.* **40**, 2004 (2001).
- [158] I. O. Götze and C. N. Likos, *J. Phys.: Condens. Matter* **17**, S1777 (2005).
- [159] F. Sciortino, S. Mossa, E. Zaccarelli, and P. Tartaglia, *Phys. Rev. Lett.* **93**, 055701 (2004).
- [160] A. Stradner, H. Sedgwick, F. Cardinaux, W. C. K. Poon, S. U. Egelhaaf, and P. Schurtenberger, *Nature* **432**, 492 (2004).
- [161] J.-P. Hansen and C. Pearson, *Mol. Phys.* **104**, 3389 (2007).
- [162] M. Doi and S. F. Edwards, *The Theory of Polymer Dynamics* (Clarendon Press, Oxford, 2003).
- [163] W. C. Swope and H. C. Andersen, *Phys. Rev. A* **46**, 4539 (1992).
- [164] S. Pronk and D. Frenkel, *J. Phys. Chem. B* **105**, 6722 (2001).
- [165] P. A. Monson and D. A. Kofke, in *Advances in Chemical Physics* (John Wiley & Sons, New York, 2000), Chap. Solid-fluid equilibrium: insights from simple molecular models.
- [166] D. Tanguy and M. Mareschal, *Phys. Rev. B* **72**, 174116 (2005).
- [167] J. W. Gibbs, *The Scientific Papers of J. Willard Gibbs, Volume 1: Thermodynamics* (Ox Bow Press, Woodbridge, 1993).
- [168] J.-P. Hansen and L. Verlet, *Phys. Rev.* **84**, 151 (1969).
- [169] J.-P. Hansen and D. Schiff, *Mol. Phys.* **25**, 1281 (1973).
- [170] B. M. Mladek, G. Kahl, and C. N. Likos, *Computer Assembly of Cluster-Forming Amphiphilic Dendrimers*, arXiv:0708.4380.
-

-
- [171] R. Agrawal and D. A. Kofke, *Mol. Phys.* **85**, 23 (1995).
- [172] M. A. Glaser, G. M. Grason, R. D. Kamien, A. Košmrlj, C. D. Santagelo, and P. Ziherl, *Europhys. Lett.* **78**, 46004 (2007).
- [173] A. J. Moreno and C. N. Likos, *Diffusion and relaxation dynamics in cluster crystals*, *Phys. Rev. Lett.*, 2007, in press.
- [174] Wolfram MathWorld: mathworld.wolfram.com/Polylogarithm.html.
- [175] D. C. Wood, *The Computation of Polylogarithms*, <http://www.cs.ukc.ac.uk/pubs/1992/110>, 1992.
- [176] Wolfram Research: <http://functions.wolfram.com/ZetaFunctionsandPolylogarithms/PolyLog/>.
- [177] M. Galassi, J. Davies, J. Theiler, B. Gough, G. Jungman, M. Booth, and F. Rossi, *GNU Scientific Library: Reference Manual*, 2nd ed. (Network Theory Ltd., Bristol, 2005).
-

The work presented here resulted in the following original publications:

1. B. M. Mladek, M.-J. Feraud, G. Kahl, and M. Neumann
On the thermodynamic properties of the generalized Gaussian core model.
Condens. Matt. Phys. **8**, 135 (2005).
2. B. M. Mladek, D. Gottwald, G. Kahl, M. Neumann, and C. N. Likos
Formation of polymorphic cluster phases for purely repulsive soft spheres.
Phys. Rev. Lett. **96**, 045701 (2006).
3. B. M. Mladek, G. Kahl, and M. Neumann
Thermodynamically self-consistent liquid state theories for systems with bounded potentials.
J. Chem. Phys. **124**, 064503 (2006).
4. C. N. Likos, B. M. Mladek, D. Gottwald, and G. Kahl
Why do ultrasoft repulsive particles cluster and crystallize? Analytical results from density functional theory.
J. Chem. Phys. **126**, 224502 (2007).
5. B. M. Mladek, D. Gottwald, G. Kahl, M. Neumann, and C. N. Likos
Clustering in the absence of attractions: density functional theory and computer simulations.
to appear in J. Phys. Chem. B.
6. B. M. Mladek, P. Charbonneau, and D. Frenkel
Phase coexistence of cluster crystals: beyond the Gibbs phase rule.
submitted, arXiv:0708.2979.
7. B. M. Mladek, G. Kahl, and C. N. Likos
Computer assembly of cluster-forming amphiphilic dendrimers.
submitted, arXiv:0708.4380.
8. C. N. Likos, B. M. Mladek, A. J. Moreno, D. Gottwald, and G. Kahl
Cluster-forming systems of ultrasoft repulsive particles: statics and dynamics.
submitted.

This work was supported by the Österreichische Forschungsfond (FWF) under Project Nos. P15758 and P17823. Further financial support by the following institutions is gratefully acknowledged: TU Wien, Erwin Schrödinger International Institute for Mathematical Physics, Gemeinde Wien (Project No. H-1080/2002), COST-P13 (MOLSIMU), and Österreichische Forschungsgemeinschaft. Part of this work was carried out under the HPC-EUROPA project (RII3-CT-2003-506079), with the support of the European Community - Research Infrastructure Action of the FP6.

Computer time on “Phoenix” (TU Wien), “Schrödinger” (Universität Wien), “Dudo” (Heinrich-Heine-Universität Düsseldorf) and the facilities of the Dutch centre for high-performance computing SARA is gratefully acknowledged.

Further, the author would like to acknowledge that all data obtained by genetic algorithms and density functional theory presented in this work were kindly provided by Dieter Gottwald.

Acknowledgements

Danke... Thanks... Bedankt... *Ευχαριστώ*... Grazie... Gracias... Obri-gada... Merci... Mamnoon... Gràcies... Hvala... Takk... Kiitos...

- **Gerhard Kahl** for being not only a supervisor but also a friend. Furthermore that you gave me the chance and freedom to explore my own ideas, both in Vienna and abroad.
- **Martin Neumann** for your support with MC simulations and for sharing your passion for music and especially U2.
- **Christos Likos and Daan Frenkel** for your enthusiasm and energy when it comes to physics, which can only be infectious. Christos—for being a great friend and for having faith in me. Daan—for your endless patience in explaining things to me.
- **Dieter Gottwald and Patrick Charbonneau** for fruitful and enjoyable collaborations. Without the two of you some of this thesis might not exist. Furthermore, for your friendship.
- **Christoph Dellago and Roland Roth** for helpful discussions. Roland—for being the inspiration for lots of hypotheses.
- **My colleagues at TU Wien: María José Fernaund Espinosa, Julia Fornleitner, Gernot Pauschenwein, Dieter Schwanzner, Georg Falkinger, Mario Kahn, Svetlana Mihajlovic and Jürgen Köfinger** for providing a great working atmosphere and for always being ready to help. Especially MJ—you are a most valuable friend. And Julia—it was a pleasure to get to know you better in Rome and Sicily.
- **My friends from Uni Wien: Claudia Zechmann, Christina Hirschl, Herbert Richter and Harald Oberhofer** for moral support and friendship. Especially Claudia—for being a friend one can always count on.
- **My friends from Heinrich-Heine-Universität Düsseldorf: Federica Lo Verso and Rik Wensink** for your very special friendship. Rik—for giving me the motivation to finish this thesis.
- **Rhoda Hawkins, Beatrice Marino, Marina Soares e Silva, Behnaz Bozorgui, Chantal Valeriani, Fabiana Diotallevi, Live Rekvig, Erynn Sarno, Paolo Scalia, Koos van Meel, Marco Morelli, Josep Pàmies, Domenico Paparo, Christian Tischer, Eduardo Sanz and all my other friends at AMOLF and in Amsterdam** for cooking sessions with great food and cinema nights, for boat trips, ice-skating and common holiday trips, for visits to the museum and shopping tours. Most of all, for laughing together. Especially Rhoda—for always being there for me. Koos—for helping me out with CPU hours. Pep—for helping me with everything that is connected to thermodynamic integration. Bea and Marina—you are like the sisters I never had. Last but not least: Paolo—malgrado tutto, grazie di tutto.
- **Meiner Familie: Annemarie, Georg und Claudio, Rosmarie und Lisl** für Eure Unterstützung und Eure Liebe.

Curriculum Vitae

Personal Data

Name: Bianca M. Mladek

Birth Date: July 2nd, 1980

Birth Place: Vienna, Austria

Citizenship: Austrian

Educational History

1986 - 1990 Evangelische Volksschule am Karlsplatz, Vienna

1990 - 1998 Bundesrealgymnasium BG IX, Wasagasse, Vienna

1998 - 2004 Studies of Physics at the University of Vienna

2003 - Studies of Medical Computer Science at the Vienna University of Technology

2004 - 2007 PhD in Physics at the Vienna University of Technology

Employment History

2000 - 2003 Tutor at the "Department of Mathematics", University of Vienna

2004 - Webmaster for the Faculty of Physics at the Vienna University of Technology

2004 - 2007 PhD position funded by the FWF

2004 Tutor at the "Institute for Theoretical Physics", Vienna University of Technology

2007 - University assistant in the "Computational Physics" group, University of Vienna